ATMOSPHERE – CRYOSPHERE INTERACTION IN THE ARCTIC, AT HIGH LATITUDES AND MOUNTAINS WITH FOCUS ON TRANSPORT, DEPOSITION AND EFFECTS OF DUST, BLACK CARBON, AND OTHER AEROSOLS

EDITED BY: Pavla Dagsson-Waldhauserova and Outi Meinander
PUBLISHED IN: Frontiers in Earth Science

frontiers Research Topics

frontiers

ISSN 1664-8714
ISBN 978-2-88963-504-7
DOI 10.3389/978-2-88963-504-7

About Frontiers

Frontiers is more than just an open-access publisher of scholarly articles: it is a pioneering approach to the world of academia, radically improving the way scholarly research is managed. The grand vision of Frontiers is a world where all people have an equal opportunity to seek, share and generate knowledge. Frontiers provides immediate and permanent online open access to all its publications, but this alone is not enough to realize our grand goals.

Frontiers Journal Series

The Frontiers Journal Series is a multi-tier and interdisciplinary set of open-access, online journals, promising a paradigm shift from the current review, selection and dissemination processes in academic publishing. All Frontiers journals are driven by researchers for researchers; therefore, they constitute a service to the scholarly community. At the same time, the Frontiers Journal Series operates on a revolutionary invention, the tiered publishing system, initially addressing specific communities of scholars, and gradually climbing up to broader public understanding, thus serving the interests of the lay society, too.

Dedication to Quality

Each Frontiers article is a landmark of the highest quality, thanks to genuinely collaborative interactions between authors and review editors, who include some of the world's best academicians. Research must be certified by peers before entering a stream of knowledge that may eventually reach the public - and shape society; therefore, Frontiers only applies the most rigorous and unbiased reviews.
Frontiers revolutionizes research publishing by freely delivering the most outstanding research, evaluated with no bias from both the academic and social point of view. By applying the most advanced information technologies, Frontiers is catapulting scholarly publishing into a new generation.

What are Frontiers Research Topics?

Frontiers Research Topics are very popular trademarks of the Frontiers Journals Series: they are collections of at least ten articles, all centered on a particular subject. With their unique mix of varied contributions from Original Research to Review Articles, Frontiers Research Topics unify the most influential researchers, the latest key findings and historical advances in a hot research area! Find out more on how to host your own Frontiers Research Topic or contribute to one as an author by contacting the Frontiers Editorial Office: researchtopics@frontiersin.org

ATMOSPHERE – CRYOSPHERE INTERACTION IN THE ARCTIC, AT HIGH LATITUDES AND MOUNTAINS WITH FOCUS ON TRANSPORT, DEPOSITION AND EFFECTS OF DUST, BLACK CARBON, AND OTHER AEROSOLS

Topic Editors:
Pavla Dagsson-Waldhauserova, Agricultural University of Iceland, Iceland
Outi Meinander, Finnish Meteorological Institute, Finland

Image by Pavla Dagsson Waldhauserova

Citation: Dagsson-Waldhauserova, P., Meinander, O., eds. (2020). Atmosphere – Cryosphere Interaction in the Arctic, at High Latitudes and Mountains With Focus on Transport, Deposition and Effects of Dust, Black Carbon, and Other Aerosols. Lausanne: Frontiers Media SA.
doi: 10.3389/978-2-88963-504-7

Table of Contents

frontiers in Earth Science

EDITORIAL
published: 18 December 2019
doi: 10.3389/feart.2019.00337

Editorial: Atmosphere—Cryosphere Interaction in the Arctic, at High Latitudes and Mountains With Focus on Transport, Deposition, and Effects of Dust, Black Carbon, and Other Aerosols

Pavla Dagsson-Waldhauserova[1,2]* *and Outi Meinander*[3]

[1] Agricultural University of Iceland, Borgarnes, Iceland, [2] Faculty of Environmental Sciences, Czech University of Life Sciences Prague, Prague, Czechia, [3] Climate Research Programme, Atmospheric Composition Research Unit, Finnish Meteorological Institute, Helsinki, Finland

Keywords: aerosol, light absorbing impurity, cold regions, climate, Arctic

Editorial on the Research Topic

Atmosphere—Cryosphere Interaction in the Arctic, at High Latitudes and Mountains With Focus on Transport, Deposition, and Effects of Dust, Black Carbon, and Other Aerosols

OPEN ACCESS

Edited and reviewed by:
Eugene V. Rozanov, Physikalisch-Meteorologisches Observatorium Davos, Switzerland

***Correspondence:**
Pavla Dagsson-Waldhauserova
pavla@lbhi.is

Specialty section:
This article was submitted to Atmospheric Science, a section of the journal Frontiers in Earth Science

Received: *07 November 2019*
Accepted: *02 December 2019*
Published: *18 December 2019*

Citation:
Dagsson-Waldhauserova P and Meinander O (2019) Editorial: Atmosphere—Cryosphere Interaction in the Arctic, at High Latitudes and Mountains With Focus on Transport, Deposition, and Effects of Dust, Black Carbon, and Other Aerosols. Front. Earth Sci. 7:337. doi: 10.3389/feart.2019.00337

Atmosphere and cryosphere are closely linked and therefore need to be investigated as an interdisciplinary subject. Most of the cryospheric areas have undergone severe changes in recent decades, while such areas have been more fragile and less adaptable to global climate change (Boy et al., 2019). Atmospheric air pollutants, in particular black carbon (BC) and dust, are deposited on clean snow, land ice or sea ice surfaces, and decrease their albedo. Due to albedo-feedback, snow and ice are melting faster and seasonal snow cover earlier. Impacts of ice loss include reduction in the Earth's albedo and, as a positive feedback, this leads to further warming (Flanner et al., 2007), as for example in the Arctic region. Albedo is wavelength dependent and typically very high for clean snow, and decreases as a function of snow age, snow grain size, and impurity content (e.g., Warren and Wiscombe, 1980; Aoki et al., 2000; Gardner and Sharp, 2010). It is estimated that Arctic snow albedo is reduced primarily due to BC, but other impurities can also contribute to absorption, such as organic or brown carbon (Doherty et al., 2010). Surface albedo feedback has been found as the second main contributor to Arctic amplification (Pithan and Mauritsen, 2014), and BC deposition to snow and ice can strongly contribute to the darkening via black-carbon-on-snow forcing (Bond et al., 2013). The role of BC in snow and ice has been widely investigated, and detailed scientific assessments have been presented in Bond et al. (2013), Intergovernmental Panel on Climate Change (IPCC) (2013), and AMAP (2015). Seemingly small amounts of BC in snow, of the order of 10–100 parts per billion by mass (ppb), have shown to decrease its albedo by 1–5% (Hadley and Kirchstetter, 2012). A reduction in snow-surface density due to light absorbing impurities has been documented (Meinander et al., 2014; Skiles and Painter, 2017), and BC has also been suggested as disturbing the water holding capacity of snow (Meinander et al., 2014).

Dust has been identified as reducing snow albedo in many parts of the world, for example the Chilean Andes, European Alps, Greenland, Himalaya, Iceland, Caucasus Mountains, North America, and Antarctica (e.g., Painter et al., 2007; Kutuzov et al., 2013; Meinander et al., 2016; Svensson et al., 2018; Bergstrom et al., 2019; Di Mauro et al., 2019; Rowe et al., 2019). In Iceland, dust events have been observed to decrease snow and ice albedo on average by 0.18,

and dust deposition has been estimated to cause an additional 1.1 m w.e. (water equivalent) of snowmelt (or 42% of the 2.8 m w.e. total melt) compared to a hypothetical clean glacier surface (Wittmann et al., 2017). Extreme snow dust storms (Dagsson-Waldhauserova et al., 2015) can lead to insulation effect instead of snow melting (Dragosics et al., 2016; Möller et al., 2016) or to albedo decrease via a clumping mechanism, where small particles form larger particles in snow (Dagsson-Waldhauserova et al., 2015; Peltoniemi et al., 2015; Möller et al., 2019). Experiments have shown that volcanic dust (Iceland) can reduce albedo of snow similarly to BC (Peltoniemi et al., 2015; Zubko et al., 2019). Albedo changes on snow surface can also be caused by pigmented algae (Benning et al., 2014; Lutz et al., 2016), or cryoconite, a mixture of dust, pebbles, soot, and microbes (Di Mauro et al., 2017). All LAI have an important role in enhanced warming via feedback mechanisms. They reduce the albedo of highly reflective surfaces and increase absorption of solar radiation.

The atmosphere, such as over the Arctic, is influenced by air pollution from distant anthropogenic sources, but not all local and foremost natural sources of air pollution are well-known or monitored. For example, anthropogenic pollutants from residential heating (domestic combustion), land transport, industrial production, and biomass burning, accumulate during the winter and spring in the stable Arctic atmosphere resulting in a local phenomenon, Arctic haze. Arctic haze is predominantly caused by sulfate and organic carbon particles and, to a lesser extent, by ammonium, nitrate, BC, and dust (Hyslop, 2009). There are also local anthropogenic sources of air pollution in the Arctic such as shipping, smelters, flaring in the oil and gas industry, air traffic and radioactive waste disposal. BC is the most powerful light absorbing aerosol with climate warming potential of all aerosol types. Significant natural air pollution sources, such as dry riverbeds, volcanoes, high latitude deserts and dust sources, biogenic sources, and oceans, are located at high latitudes. For example, high latitude dust (HLD) sources are estimated to contribute about 3–5% of the global dust budget (Bullard et al., 2016; Groot Zwaaftink et al., 2016). Mineral dust is considered mainly a light-scattering particle in the atmosphere, but a light-absorbing particle when deposited on snow or ice [Intergovernmental Panel on Climate Change (IPCC), 2013]. Volcanic dust is, contrarily, a strongly absorbing particle with a spectral reflectance of 0.03 (Ovadnevaite et al., 2009; Peltoniemi et al., 2015; Zubko et al., 2019). In the Arctic, volcanic dust can reach altitudes of several kilometers and travel distances over 1,000 km (Arnalds et al., 2016; Dagsson-Waldhauserova et al., 2019). Aerosols in cold regions have direct impacts on climate, but their forcing effects can rapidly increase via indirect forcing when aerosols interact with the cryosphere, such as via deposition on snow, ice, sea ice, and other bright surfaces. Dust has been recognized as an important climate driver, causing snow darkening and melting in polar regions [Intergovernmental Panel on Climate Change (IPCC), 2019].

In this Research Topic, the main objective was to fill some of the gaps in our understanding of HLD sources, local sources of BC and other air pollutants in high latitudes, as well as long-range transport of air pollution from lower latitudes. The impacts of air pollutants on the cryosphere and the identification of LAI in snow pack are crucial to understand the atmosphere—cryosphere interaction and climate.

WHAT DID WE NOT KNOW BEFORE THIS RESEARCH TOPIC AND WHAT DO WE KNOW NOW?

The main findings of the papers published in this Research Topic include:

BC from cropland burning is entering Arctic snow areas from latitudes as low as 40°N in the spring. Some of these emissions can be deposited beyond 80°N despite the low injection heights associated with cropland burning (Hall and Loboda).

Local emission of BC have been identified from the snow samples in Antarctica. Antarctic BC originates from human activities such as local combustion of fossil fuels as well as regional wildfires from the South American continent (Khan et al.).

A 31-year study of Alpine snow pack showed an occurrence of about 0.75 dust on snow deposition events on average. Saharan dust layers can be defined by snow pH > 5.6 together with a Ca^{2+} concentration >10 μeq/l, with increased Mg^{2+} by 25% and Ca^{2+} by 35% (Greilinger et al.).

What are the light absorbing impurities (LAI)? The story of LAI in snow as a journey of one science field and the remarkable scientist behind it. What was the past and what are the needs in the future? (Warren).

Radon concentrations on the Antarctic Plateau have increased due to subsidence of terrestrially influenced tropospheric air (long distance air pollution) while radon concentrations at coastal Antarctic sites have increased from local radon sources in summer and tropospheric subsidence. An Antarctic and Southern Ocean radon overview is provided by Chambers et al.

Dust storms are frequently occurring in Antarctica's ice-free area where the mean PM_{10} concentrations are similar to those reported from background North-European stations (Kavan et al.).

First study provides an evidence of long range transport of Icelandic volcanic dust toward the High Arctic, >2,000 km. This is also the first documented study on long range transport of HLD inside the Arctic (Moroni et al.).

HLD can be transported toward Europe, traveling over 3,000 km (Dordevic et al.).

There are 128 dust days annually reported in Iceland based on the 60 years SYNOP data analysis (Nakashima and Dagsson-Waldhauserova).

Nepal experiences heavy spring dust loads from north-west reflected in high AOD observations, which can be estimated using linear regression model (Bhattarai et al.).

This Research Topic offers new findings on aerosols and air pollutants such as BC, dust, radon, and ozone. These air constituents were identified as having different origins: BC from low latitude crop burning, combustion of fossil fuels in Antarctica and wild fires in South America; dust from the Sahara and high latitudes such as volcanic dust from Iceland and Antarctic dust. Light absorbing impurities, aerosols and air pollutants were

reported from the Russian Arctic, the European Alps, Svalbard, Antarctica, South America, Southern Ocean, and Himalaya, as well as Icelandic dust detected in Balkan Peninsula in Europe.

The long-range transport of air pollutants toward fragile pristine areas of our planet is the main link between most of the studies in this Research Topic. Transport of HLD as an air pollutant toward inhabited areas of Europe is another transport pathway which needs to be considered. Local sources of air pollution inside the polar and mountain regions as well as their long-range travel capabilities inside such regions need to be taken into account in assessing their various impacts. These studies provide evidence of the presence of BC, dust, radon in previously not known remote locations. Great interest has arisen and a large amount of work has been done to understand the direct and indirect impacts of BC on climate as well as BC source identification. There are, however, great gaps in current understanding of BC, for example in wet and dry deposition rates as well as seasonal and temporal variability of BC in the cryosphere, and of dust (crustal desert dust as well as HLD) sources, (re)suspension/deposition processes, and climate impacts (albedo changes/snow melt, atmospheric chemistry, cloud microphysics, etc.) currently missing in climate models.

Scientific research is a long journey for individuals, institutions, and worldwide networks for better understanding of our planet. Such a scientific journey is full of surprises of great importance and following two sentences from Professor Steve Warren's life and contribution to this Research Topic (Warren), dated decades ago, perfectly describe the meaning of it: "I could hardly imagine anything more boring than atmospheric dust," and "What's that light-absorber you're finding in the atmospheric aerosol? Bob revealed his not-yet-published secret, whispering in our ears: 'It's carbon!'"

AUTHOR CONTRIBUTIONS

PD-W coordinated the writing of the editorial. OM made original plans for the topical conference session and consequently Research Topic and provided large inputs for the editorial.

ACKNOWLEDGMENTS

The Nordic Center of Excellence CRAICC Cryosphere–Atmosphere Interactions in a Changing Arctic Climate supported the initial work and co-operation of PD-W and OM. The work of PD-W was partly funded by the Czech Science Foundation under the HLD-CHANGE project The role of High Latitude Dust in changing climate (No. 20-06168Y). The work of OM was funded by the Ministry for Foreign Affairs of Finland IBA-project Black Carbon in the Arctic and significance compared to dust sources (No. PC0TQ4BT-25), and the Academy of Finland NABCEA-project Novel Assessment of Black Carbon in the Eurasian Arctic (No. 296302). OM was also supported by the EU-Interact-BLACK-project Black Carbon in snow and water (H2020 Grant Agreement No. 730938) and Academy of Finland Center of Excellence program The Centre of Excellence in Atmospheric Science - From Molecular and Biological processes to The Global Climate (No. 272041). The Friends of Vatnajökull supported this work as well. We thank Mark Francis Sixsmith for his proofreading of this work.

REFERENCES

AMAP (2015). *Black Carbon and Ozone as Arctic Climate Forcers.* Arctic Monitoring and Assessment Programme (AMAP), Oslo, 116.

Aoki, T., Fukabori, M., Hachikubo, A., Tachibana, Y., and Nishio, F. (2000). Effects of snow physical parameters on spectral albedo and bidirectional reflectance of snow. *J. Geophys. Res*. 105, 10219–10236. doi: 10.1029/1999JD901122

Arnalds, O., Dagsson-Waldhauserova, P., and Olafsson, H. (2016). The Icelandic volcanic aeolian environment: processes and impacts—a review. *Aeolian Res.* 20, 176–195. doi: 10.1016/j.aeolia.2016.01.004

Benning, L. G., Anesio, A. M., Lutz, S., and Tranter, M. (2014). Biological impact on Greenland's albedo. *Nature Geosci.* 7:691. doi: 10.1038/ngeo2260

Bergstrom, A., Gooseff, M., Myers, M., and Doran, P. T. (2019). The seasonal evolution of albedo across glaciers and the surrounding landscape of the Taylor Valley, Antarctica. *Cryosphere Discuss.* doi: 10.5194/tc-2019-146

Bond, T. C., Doherty, S. J., Fahey, D. W., Forster, P. M., Berntsen, T., DeAngelo, B. J., et al. (2013). Bounding the role of black carbon in the climate system: a scientific assessment. *J. Geophys. Res. Atmos*. 188, 5380–5552. doi: 10.1002/jgrd.50171

Boy, M., Thomson, E. S., Acosta Navarro, J.-C., Arnalds, O., Batchvarova, E., Bäck, J., et al. (2019). Interactions between the atmosphere, cryosphere, and ecosystems at northern high latitudes. *Atmos. Chem. Phys*. 19, 2015–2061. doi: 10.5194/acp-19-2015-2019

Bullard, J. E., Baddock, M., Bradwell, T., Crusius, J., Darlington, E., Gaiero, D., et al. (2016). High-latitude dust in the Earth system. *Rev. Geophys*. 54, 447–485. doi: 10.1002/2016RG000518

Dagsson-Waldhauserova, P., Arnalds, O., Olafsson, H., Hladil, J., Skala, R., Navratil, T., et al. (2015). Snow-dust storm: unique case study from Iceland, March 6-7, 2013. *Aeolian Res.* 16, 69–74. doi: 10.1016/j.aeolia.2014.11.001

Dagsson-Waldhauserova, P., Renard, J.-B., Olafsson, H., Vignelles, D., Berthet, G., Verdier, N., et al. (2019). Vertical distribution of aerosols in dust storms during the Arctic winter. *Sci. Rep*. 9, 1–11. doi: 10.1038/s41598-019-51764-y

Di Mauro, B., Baccolo, G., Garzonio, R., Giardino, C., Massabò, D., Piazzalunga, A., et al. (2017). Impact of impurities and cryoconite on the optical properties of the Morteratsch Glacier (Swiss Alps). *Cryosphere* 11, 2393–2409. doi: 10.5194/tc-11-2393-2017

Di Mauro, B., Garzonio, R., Rossini, M., Filippa, G., Pogliotti, P., Galvagno, M., et al. (2019). Saharan dust events in the European Alps: role in snowmelt and geochemical characterization. *Cryosphere* 13, 1147–1165. doi: 10.5194/tc-13-1147-2019

Doherty, S. J., Warren, S. G., Grenfell, T. C., Clarke, A. D., and Brandt, R. E. (2010). Light-absorbing impurities in Arctic snow. *Atmos. Chem. Phys*. 10, 11647–11680. doi: 10.5194/acp-10-11647-2010

Dragosics, M., Meinander, O., Jónsdóttir, T., Dürig, T., De Leeuw, G., Pálsson, F., et al. (2016). Insulation effects of Icelandic dust and volcanic ash on snow and ice. *Arabian J. Geosci*. 9, 126. doi: 10.1007/s12517-015-2224-6

Flanner, M. G., Zender, C. S., Randerson, J. T., and Rasch, P. T. (2007). Present day climate forcing and response from black carbon in snow. *J. Geophys. Res.* 112:D11202. doi: 10.1029/2006JD008003

Gardner, A. S., and Sharp, M. J. (2010). A review of snow and ice albedo and the development of a new physically based broadband albedo parameterization. *J. Geophys. Res.* 115:F01009. doi: 10.1029/2009JF001444

Groot Zwaaftink, C. D., Grythe, H., Skov, H., and Stohl, A. (2016). Substantial contribution of northern high-latitude sources to mineral dust in the Arctic. *J. Geophys. Res. Atmos.* 121, 13678–13697. doi: 10.1002/2016JD025482

Hadley, O., and Kirchstetter, T. (2012). Black-Carbon reduction of snow albedo. *Nat. Clim. Change* 2, 437–440. doi: 10.1038/nclimate1433

Hyslop, N. P. (2009). Impaired visibility: the air pollution people see. *Atmos. Environ*. 43, 182–195. doi: 10.1016/j.atmosenv.2008.09.067

Intergovernmental Panel on Climate Change (IPCC) (2013). *The Fifth Assessment Report of the Intergovernmental Panel on Climate Change*, eds T. F. Stocker, D. Qin, G.-K. Plattner, M. Tignor, S. K. Allen, J. Boschung, A. Nauels, Y. Xia, V. Bex and P. M. Midgley. Cambridge; New York, NY: Cambridge University Press.

Intergovernmental Panel on Climate Change (IPCC) (2019). "Summary for policymakers," in *IPCC Special Report on the Ocean and Cryosphere in a Changing Climate,* eds H.-O. Pörtner, D. C. Roberts, V. Masson-Delmotte, P. Zhai, M. Tignor, E. Poloczanska, K. Mintenbeck, M. Nicolai, A. Okem, J. Petzold, B. Rama, and N. Weyer. Available online at: https://www.ipcc.ch/srocc/chapter/summary-for-policymakers/

Kutuzov, S., Shahgedanova, M., Mikhalenko, V., Ginot, P., Lavrentiev, I., and Kemp, S. (2013). High-resolution provenance of desert dust deposited on Mt. Elbrus, Caucasus in 2009–2012 using snow pit and firn core records. *Cryosphere* 7, 1481–1498. doi: 10.5194/tc-7-1481-2013

Lutz, S., Anesio, A. M., Raiswell, R., Edwards, A., Newton, R. J., Gill, F., et al. (2016). The biogeography of red snow microbiomes and their role in melting arctic glaciers. *Nat. Commun.* 7:11968. doi: 10.1038/ncomms11968

Meinander, O., Dagsson-Waldhauserova, P., and Arnalds, O. (2016). Icelandic volcanic dust can have a significant influence on the cryosphere in Greenland and elsewhere. *Polar Res.* 35:31313. doi: 10.3402/polar.v35.31313

Meinander, O., Kontu, A., Virkkula, A., Arola, A., Backman, L., Dagsson-Waldhauserová, P., et al. (2014). Brief communication: light-absorbing impurities can reduce the density of melting snow. *Cryosphere* 8, 991–995. doi: 10.5194/tc-8-991-2014

Möller, R., Dagsson-Waldhauserova, P., Möller, M., Kukla, P., Schneider, C., and Gudmundsson, M. T. (2019). Persistent albedo reduction on southern Icelandic glaciers due to ashfall from the 2010 Eyjafjallajökull eruption. *Remote Sens. Environ*. 233, 111396. doi: 10.1016/j.rse.2019.111396

Möller, R., Möller, M., Kukla, P. A., and Schneider, C. (2016). Impact of supraglacial deposits of tephra from Grimsvötn volcano, Iceland, on glacier ablation. *J. Glaciol*. 62, 933–943. doi: 10.1017/jog.2016.82

Ovadnevaite, J., Ceburnis, D., Plauskaite-Sukiene, K., Modini, R., Dupuy, R., Rimselyte, I., et al. (2009). Volcanic sulfate and arctic dust plumes over the North Atlantic Ocean. *Atmos. Environ.* 43, 4968–4974. doi: 10.1016/j.atmosenv.2009.07.007

Painter, T. H., Barrett, A. P., Landry, C. C., Neff, J. C., Cassidy, M. P., Lawrence, C. R., et al. (2007). Impact of disturbed desert soils on duration of mountain snow cover. *Geophys. Res. Lett*. 34:L12502. doi: 10.1029/2007GL030284

Peltoniemi, J. I., Gritsevich, M., Hakala, T., Dagsson-Waldhauserová, P., Arnalds, Ó., Anttila, K., et al. (2015). Soot on Snow experiment: bidirectional reflectance factor measurements of contaminated snow. *Cryosphere* 9, 2323–2337. doi: 10.5194/tc-9-2323-2015

Pithan, F., and Mauritsen, T. (2014). Arctic amplification dominated by temperature feedbacks in contemporary climate models. *Nat. Geosci.* 7, 181–184. doi: 10.1038/ngeo2071

Rowe, P. M., Cordero, R. R., Warren, S. G., Stewart, E., Doherty, S. J., Pankow, A., et al. (2019). Black carbon and other light-absorbing impurities in snow in the Chilean Andes. *Sci. Rep.* 9:4008. doi: 10.1038/s41598-019-39312-0

Skiles, M. K., and Painter, T. (2017). Daily evolution in dust and black carbon content, snow grain size, and snow albedo during snowmelt, Rocky Mountains, Colorado. *J. Glaciol*. 63, 118–132. doi: 10.1017/jog.2016.125

Svensson, J., Ström, J., Kivekäs, N., Dkhar, N. B., Tayal, S., Sharma, V. P., et al. (2018). Light-absorption of dust and elemental carbon in snow in the Indian Himalayas and the Finnish Arctic. *Atmos. Meas. Tech*. 11, 1403–1416. doi: 10.5194/amt-11-1403-2018

Warren, S., and Wiscombe, W. A. (1980). Model for the spectral Albedo of snow. II: snow containing atmospheric aerosols. *J. Atmos. Sci.* 37, 2734–2745.

Wittmann, M., Groot Zwaaftink, C. D., Steffensen Schmidt, L., Guð*mundsson, S., Pálsson, F., Arnalds, O., et al. (2017). Impact of dust deposition on the albedo of Vatnajökull ice cap, Iceland. *Cryosphere* 11, 741–754. doi: 10.5194/tc-11-741-2017

Zubko, N., Muñoz, O., Zubko, E., Gritsevich, M., Escobar-Cerezo, J., and Berg, J. (2019). Light scattering from volcanic-sand particles in deposited and aerosol form. *Atmos. Env.* 215:116813. doi: 10.1016/j.atmosenv.2019.06.051

Conflict of Interest: The authors declare that the research was conducted in the absence of any commercial or financial relationships that could be construed as a potential conflict of interest.

frontiers in Earth Science

ORIGINAL RESEARCH
published: 22 December 2017
doi: 10.3389/feart.2017.00109

Quantifying the Potential for Low-Level Transport of Black Carbon Emissions from Cropland Burning in Russia to the Snow-Covered Arctic

Joanne V. Hall and Tatiana V. Loboda*

Department of Geographical Sciences, University of Maryland, College Park, MD, United States

Short lived aerosols and pollutants transported from northern mid-latitudes have amplified the short term warming in the Arctic region. Among those black carbon is recognized as the second most important human emission in regards to climate forcing, behind carbon dioxide, with a total climate forcing of +1.1 Wm^{-2}. Studies have suggested that cropland burning may be a large contributor to the black carbon emissions which are directly deposited on the snow in the Arctic. However, commonly applied atmospheric transport models rely on estimates of black carbon emissions from cropland burning which are known to be highly inaccurate in both the amount and the timing of release. Instead, this study quantifies the potential for the deposition of hypothetical black carbon emissions from known cropland burning in Russia, identified by the Moderate Resolution Imaging Spectroradiometer (MODIS) active fire detections, through low-level transport to the snow in the Arctic using wind vectors from the European Centre for Medium-Range Weather Forecasts' ERA-Interim Reanalysis product. Our results confirm that Russian cropland burning is a potentially significant source of black carbon deposition on the Arctic snow in the spring despite the low injection heights associated with cropland burning. Approximately 10% of the observed spring (March–May) cropland active fires (7% annual) likely contribute to black carbon deposition on the Arctic snow from as far south as at least 40°N. Furthermore, our results show that potential spring black carbon emissions from cropland burning in Russia can be deposited beyond 80°N, however, the majority (∼90%-depending on injection height) of all potential spring deposition occurs below 75°N.

Keywords: low-level atmospheric transport, black carbon, cropland burning, Russia, Moderate Resolution Imaging Spectroradiometer (MODIS)

OPEN ACCESS

Edited by:
Pavla Dagsson-Waldhauserova, University of Iceland, Iceland

Reviewed by:
Ernesto Dos Santos Caetano Neto, Universidad Nacional Autónoma de México, Mexico
Bijoy Vengasseril Thampi, Science Systems and Applications, Inc., United States
Aki Virkkula, Finnish Meteorological Institute, Finland

****Correspondence:***
Joanne V. Hall
jhall1@umd.edu

Specialty section:
This article was submitted to Atmospheric Science, a section of the journal Frontiers in Earth Science

Received: *20 September 2017*
Accepted: *08 December 2017*
Published: *22 December 2017*

Citation:
Hall JV and Loboda TV (2017) Quantifying the Potential for Low-Level Transport of Black Carbon Emissions from Cropland Burning in Russia to the Snow-Covered Arctic. Front. Earth Sci. 5:109. doi: 10.3389/feart.2017.00109

INTRODUCTION

Over the past 30 years, the Arctic surface air temperature has risen at rates more than double of those anywhere else on Earth (NOAA, 2017). This has resulted in the drastic loss of sea ice, increased release of stored carbon and methane from melting permafrost, and substantial impacts on migratory patterns of birds and animals among many other environmental changes (EPA, 2016; NOAA, 2017; NSIDC, 2017[1]). However, arguably one of the most important consequences of the

[1]https://nsidc.org/cryosphere/arctic-meteorology/index.html (Accessed Mar 11, 2017).

amplified warming of the Arctic is its impact on the Earth's radiation budget through the decrease in snow and ice albedo which further drives increases in regional and global temperatures via a positive feedback loop within the climate system (Wexler, 1953; Chapin et al., 2005). While the reported increases in annual and especially cold-season temperatures (NOAA, 2017) are large enough to directly result in the loss of surface snow and sea ice, atmospheric pollutants—and especially black carbon (BC) deposition on the snow and ice surface—have contributed to the changes in snow/ice albedo and the subsequent accelerated rate of melting (Ramanathan and Carmichael, 2008; Dou and Xiao, 2016).

While remote and largely inaccessible, the Arctic is a known pollutant receptor region as the majority of pollution is transported via oceanic and atmospheric circulation from outside source regions, yet there are also important local sources including pollution from gas and oil exploration, shipping, and emissions from boreal forest fires (Law and Stohl, 2007; Arnold et al., 2016). The release of long-lived greenhouses gases, such as carbon dioxide, are responsible for the longer-term warming of the Earth, however, emitted short-lived aerosols and pollutants are key drivers impacting the Arctic climate. Specifically, short-lived pollutants, for example methane and BC, primarily emitted from open-source biomass burning have a large influence on regional warming (EPA, 2016). BC—the absorptive byproduct of the incomplete combustion of carbonaceous fuels—has received a great deal of attention due to its absorptive efficiency (Quinn et al., 2011) and its fairly complex influence on the climate with both direct (increased absorption of shortwave radiation in the atmosphere) and indirect (changes in the surface albedo; changes in emissivity; and impacts on the distribution and properties of clouds) effects. The short atmospheric lifetime of BC, on average approximately 1 week (Koch and Hansen, 2005; Cape et al., 2012), fluctuates with variations related to the type of deposition (wet or dry) and atmospheric processes, for instance, mixing with other aerosol compounds. Atmospheric removal of BC occurs within several days to weeks and the mixing of BC with other substances occurs within 1–5 days (Jacobson, 2001; Bond et al., 2013). Although air pollution in the Arctic is comprised of several other components, including, ozone, sulfate aerosols, and methane, BC is of particular importance primarily due to the effectiveness of its absorptive properties. A new international initiative PACES (air Pollution in the Arctic: Climate Environment and Societies) under the partnership of the International Global Atmospheric Chemistry Project and the International Arctic Science Committee emphasizes the importance of studying processes controlling Arctic air pollution with a focus on accurately identifying the potential BC source locations and the relative contributions to the potential deposition on the Arctic snow (Arnold et al., 2016).

Biomass burning (forests, grasslands, and croplands), gas flaring, and transportation emissions within East- and South Asia and Russia have been identified as the dominant sources of BC within the Arctic (e.g., Klonecki et al., 2003; Stohl et al., 2006; AMAP, 2015; Evangeliou et al., 2016; Winiger et al., 2017). Specifically, several studies have indicated that biomass burning sources as far south as 40°N are assumed to significantly impact the Arctic region (e.g., Warneke et al., 2010; Quinn et al., 2011; Sharma et al., 2013; Cheng, 2014; Liu et al., 2015). However, the relative importance of these various sources is dependent on their seasonal patterns as the timing of the burning plays a key role in determining the efficacy of BC in the Arctic (Doherty et al., 2015). The largest impact on the snow/ice albedo in the Arctic from BC deposition occurs during spring when the solar energy is increasing while still retaining the maximum snow cover extent (Quinn et al., 2011). Despite the vast circumpolar extent of the boreal forest, the majority of forest fires occur during the summer months (Groisman et al., 2007); whereas cropland burning in Russia predominantly occurs within spring and fall months–related to the harvest cycles (**Figure 1**).

Russia is the world's fifth-largest wheat exporter with a cropland area of approximately 215×10^4 km^2, primarily located between 40 and 55°N (FAOSTAT, 2015)[2]. Although federal laws banning open-source burning are established in Russia it is still a common practice often used to clear, predominantly wheat, residue after harvest and before the next planting (Hall J. V. et al., 2016). Grains, specifically spring and winter wheat, are the major crop types in Russia and account for the majority of crop residue burning (USDA FAS, 2016). Typically, winter wheat is sown in fall, while spring wheat is sown in April and the burning of crop residue stubble usually occurs before planting to remove excess waste and pests from the field (McCarty et al., 2012).

Unlike forest fires, crop residue fires are typically low intensity, short-lived events with low injection heights ranging between 500 and 1,500 m (Ichoku and Kaufman, 2005; Martin et al., 2010; Soja et al., 2012). Although forest fires produce substantially more emissions than cropland fires due to higher biomass loading, Russian cropland burning occurs during the crucial time period for impacts on the Arctic snow/ice albedo. Despite the ongoing scientific progress, major challenges lie in the inability to accurately simulate the temporal and spatial variations in Arctic air pollution and to accurately quantify the contribution of air pollution from these source regions (Shindell et al., 2008; Hirdman et al., 2010; Monks et al., 2015). For example, a recent study focused on Siberian Arctic BC sources (Winiger et al., 2017) found gas flaring and biomass burning to be far less significant than transportation and domestic emissions—findings which are in contrast to other BC source contribution studies (e.g., AMAP, 2015). The majority of previous studies have utilized atmospheric chemical-transport models to quantify the contribution of BC emissions from northern mid-latitude source locations to the Arctic (e.g., Qi et al., 2017). Some have focused on modeled trajectories from atmospheric trajectory model outputs, such as NOAA's Hybrid Single Particle Lagrangian Integrated Trajectory (HYSPLIT) model, to identify potential source regions (e.g., Stohl et al., 2007; Larkin et al., 2012). Both atmospheric chemical-transport models (e.g., GEOS-Chem) and trajectory models (e.g., HYSPLIT) incorporate cropland burning emissions estimates, which are quite uncertain in the amount and timing of emissions. At present, crop residue emission estimates are notoriously difficult to quantify accurately. Typically, emission estimates are

[2]http://faostat3.fao.org/browse/T/TP/E (Accessed Aug 22, 2015).

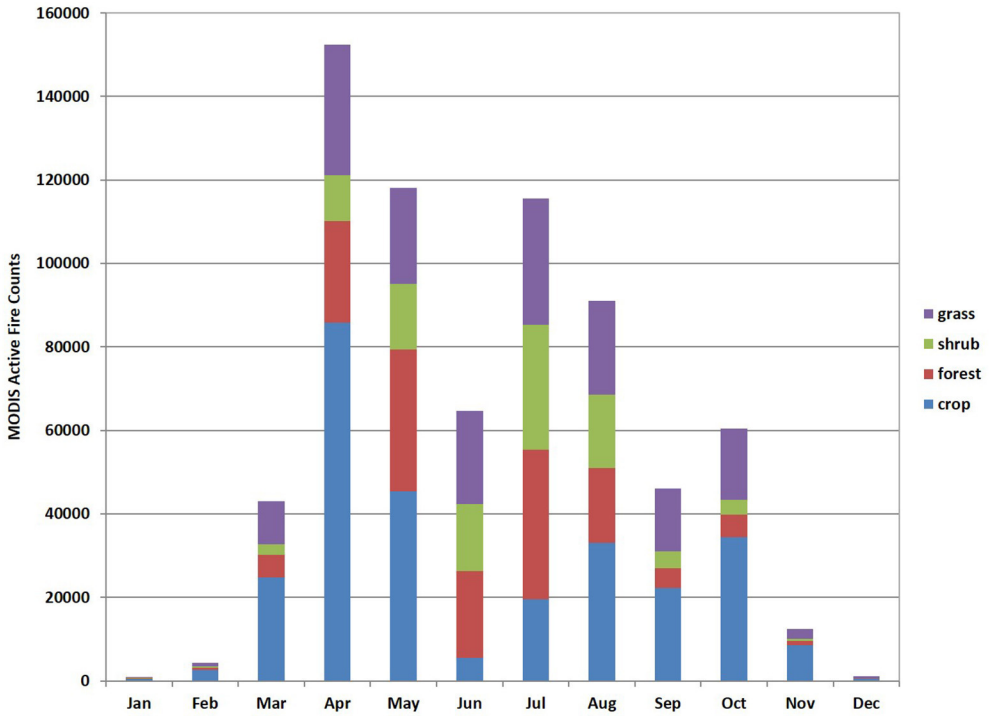

FIGURE 1 | Average monthly MODIS active fire counts (2003–2015) within Russian grasslands, shrublands, forest and croplands as defined by the International Geosphere-Biosphere Programme (IGBP) land cover type data layer (MCD12Q1; Friedl et al., 2010).

calculated following the equation originally developed by Seiler and Crutzen (1980):

$$\text{Emissions} = A * B * CE * ei \quad (1)$$

Here, A represents the extent of burned area, B is the fuel load estimate, CE is the combustion efficiency, and *ei* is the emission factor for the specific species of interest. Cropland burned area (A) is a key requirement in the calculation; however, as shown in Hall J. V. et al. (2016), global publicly available and regionally-adjusted coarse resolution burned area products are unable to map burned area even within comparatively large and contiguous Russian croplands. Cropland burns differ dramatically from other types of natural and managed fire events and require a high frequency of observation which currently can only be met by coarse resolution satellite systems. Furthermore, the relatively small scale of individual burns (0.005–4 km^2) and the low pre-fire biomass accumulations lead to comparatively minor changes in surface reflectance within coarse resolution pixels following a fire event, which are easily masked by bidirectional reflectance-induced changes in the recorded signal (Hall J. V. et al., 2016). In addition, all satellite-derived burned area maps carry an uncertainty of several days around the date of mapping resulting from missed observations due to cloud cover and high concentrations of atmospheric aerosols (Roy et al., 2008; Giglio et al., 2009; Hall J. V. et al., 2016). This inability to map cropland burned area accurately has large implications in both the magnitude and timing of calculated emissions.

Fuel loads (B) are typically derived from yield statistics using a yield-to-residue coefficient factor. The accuracy of these data are dependent on both the data source and the spatial resolution. For Russia, the yield data are typically produced at the oblast (administrative regions) level; however, variations between state official statistics and local expert data (compiled by USDA Foreign Agricultural Service, Mark Lindeman pers.comm.) has been identified in the yield tables. Finally, the values for the combustion efficiency (CE) and the emission factor for species i (*ei*) are usually based on laboratory and experimental analyses with a number of emission based studies (e.g., Wiedinmyer et al., 2011; McCarty et al., 2012) using the value quoted in a study by Andreae and Merlet (2001) which is defined by the authors as "best guess."

Atmospheric chemical-transport models (e.g., GEOS-Chem) utilize biomass burning emission estimates from sources such as the Global Fire Emissions Database (GFED; Giglio et al., 2013). The updated GFEDv4 has been released to include small fires (detailed in Randerson et al., 2012) and crop residue coefficient factors from Akagi et al. (2011); however, the underlying cropland burned area and emission coefficients are still plagued with the previously addressed uncertainties. Atmospheric trajectory models (e.g., HYSPLIT) are the other main type of model used in studies identifying potential BC emission transport to the Arctic through simulating atmospheric trajectories, primarily back trajectories, and dispersions (Stein et al., 2015). However, these models also rely on emission estimates to monitor air pollutant concentration information

over the course of the trajectory and require accurate estimates of the timings of those emissions to allow for proper transport and dispersion patterns within rapidly changing atmospheric conditions.

This inability to accurately quantify crop residue emissions or determine their spatial and temporal variability is a key weakness in these atmospheric transport models. The added complexity produces a sense of precision and accuracy which cannot be easily verified at any level. Furthermore, although numerous estimates of BC emissions from cropland burning in Russia have appeared in the scientific literature (e.g., McCarty et al., 2012; Hao et al., 2016), the inaccuracies within the current emission estimates inputs (e.g., burned area) lead to an imprecise representation of the timing and amount of cropland burning emissions. Given the combination of uncertainty surrounding the cropland burned area estimates, the yield values, and the coefficient factors, this study does not attempt to include any quantification of the magnitude of successfully transported cropland emission estimates to the Arctic. Instead, the purpose of this study is to quantify the fraction of cropland burning in Russia that potentially contributes to the deposition of BC on the Arctic snow with a particular focus on the spatial and temporal variability of the transport patterns. Here we present a simple transport model based on wind fields and the precipitation estimates of the European Centre for Medium-Range Weather Forecasts' ERA-Interim Reanalysis product (Berrisford et al., 2011). The model ingests the locations of known flaming cropland burning events and transports the "potential" BC emissions of unspecified amount following established wind patterns at varying injection heights. Using the developed transport trajectories, we are able to quantify the potential for contribution of BC generated by cropland burning in Russia observed between 2003 and 2015 to deposition on snow and ice above 60°N taking into account the spatio-temporal dynamics of both fire occurrence and snow cover.

STUDY AREA

This study focuses on the contribution of cropland burning in Russia to the snow in the Eastern Hemisphere of the circumpolar region between 0–180°E and 60–90°N. The Russian croplands are defined by the MODIS land cover classification dataset (MCD12Q1; Friedl et al., 2010) cropland and cropland/natural vegetation mosaic classes (IGBP legend classes 12 and 14, respectively). While cropped areas are found across Russia, including regions above 60°N, the majority of croplands (∼70%) are distributed along the southern boundary of the country roughly between ∼40 and 55° N (**Figure 2**). In this study, Arctic snow and ice are defined as any permanent or seasonal snow and ice cover over land above 60°N.

DATA AND METHODS

Our main research objective is to evaluate whether large-scale wind patterns in the low levels of the troposphere coupled with observed precipitation patterns can support the transport and eventual deposition of a hypothetical parcel of BC emissions, which originates from cropland fires, to the snow above 60°N. This approach combines satellite-derived observations of cropped areas (0.5 km grid cell), fire occurrence (∼1 km grid cell), and snow cover (0.05° grid cell) and climatological ERA-Interim reanalysis (0.75° grid cell) data between 2003 and 2015. The transport model is driven by ERA-Interim meteorology and operates at a 0.75° resolution between 0–180°E and 30–90°N. Other components are incorporated into the model at their native resolution (fire and cropped areas) or as a fractional representation within the 0.75° grid (snow cover). Sections Cropland Burning Source Locations, Arctic Snow Cover Extent, and Transport Algorithm Development below detail the development of the modeling framework and its components.

Cropland Burning Source Locations

The active fire (MCD14ML; Giglio et al., 2003) collection 6 product was used to identify ongoing burning within the Russian croplands between 2003 and 2015. As discussed in the introduction, current burned area products provide very poor estimates of the magnitude and timing of cropland burning (Hall J. V. et al., 2016). While active fire detections offer no improvement over the burned area products in the amount of area burned, they accurately estimate the timing of burning as the flaming front is detected during the satellite overpass. In this study, the MODIS active fire dataset represents a fraction of burning within the Russian croplands observable by satellites. The MODIS orbital overlap provides the opportunity for much more frequent observations of fire activity on the land surface than the nominal twice daily (from each of the two MODIS instruments) temporal scales. The date and time of fire detections were utilized to create hourly depictions of cropland burning between 30–90°N and 0–180°E within the 0.75° grid. Each 1 km MODIS active fire detection that intersected the 500 m cropland layer was considered a "cropland fire event." The specific time of each detection was rounded to the nearest full hour. Finally, the number of active fire detections within the 0.75° grid was recorded in hourly layers depicting both binary fire/no fire and number of events attributes. These source regions represent the starting burn locations and times for the transport algorithm.

Arctic Snow Cover Extent

The goal of this assessment is to quantify the potential deposition over snow and ice covered ground in the Arctic (here defined as above 60°N). Therefore, daily Arctic snow layers were developed for the period between January 1, 2003 and December 31, 2015 using the standard daily, MOD/MYD10C1 collection 6 MODIS snow cover product at climate modeling grid (0.05°) resolution (Hall D. et al., 2016). Primarily the Terra-based product (MOD10C1) was used in the construction of the snow layers while the Aqua-based product (MYD10C1), impacted by the non-functional detectors in band 6 (Riggs and Hall, 2015), was used to supplement any missing dates.

The Arctic region remains snow-covered during a large portion of the year with a relatively short snow-free season,

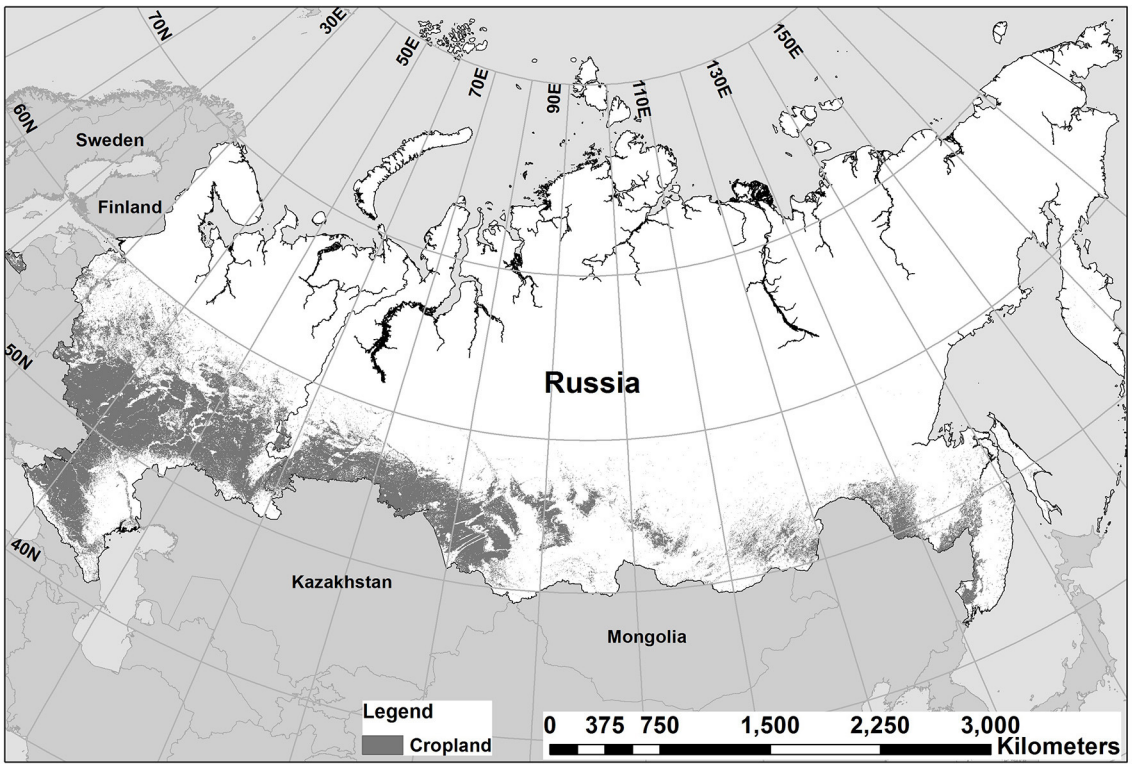

FIGURE 2 | Russian cropland area as defined by the IGBP cropland/ natural vegetation mosaic.

except for regions surrounding the pole where permanent ice and snow cover are present. The spectral signature of snow and ice is distinct and allows for strong differentiation from other land surface covers (Dozier, 1989; Satterwhite et al., 2003). However, the daily MODIS snow cover estimates are strongly impacted by gaps in observations: amongst the most substantial is the absence of solar irradiance during the polar nights and the substantial cloud cover in the Arctic regions during the sunlit period (Schiffer and Rossow, 1983). In this analysis, snow cover is considered absent until five consecutive clear (i.e., not impacted by cloud cover) land surface observations within a given grid cell remain snow-free. A 5 day window was chosen based on the observed persistent cloud cover patterns with the need to avoid late spring and early fall snow events which do not represent established seasonal snow cover. Similarly, snow cover is considered present until five consecutive clear land surface observations within a given grid cell show the presence of snow. These two periods are subsequently referred to as "snow cover melt" and "snow cover establishment" with the details of the methodology developed to extract these values described below.

Creation of the snow cover extent required the snow cover percentage (DayCMGSnowCover), cloud cover percentage (DayCMGCloudObscured) and the quality assessment (SnowSpatialQA) layers from the MOD/MYD10C1 datasets. The daily snow cover percentage layer was filtered using the quality assessment layer to retain only values of "best" and "good" quality ($QA \leq 2$). All grid cells impacted by polar night conditions were considered snow covered. All grid cells not impacted by the lack of solar irradiance were subsequently classified as:

- Snow (1): filtered snow layer value $\geq$50% (majority snow cover).
- Cloud (2): filtered snow layer value $<$50% and cloud percentage $\geq$50%.
- Water (3): values in any of the 3 original layers that were flagged as ocean, cloud obscured water, inland water, or lake ice.
- Fill (4): QA $>$ 2 or any of the layers that were flagged as fill, no retrieval, or not mapped.
- No Snow/Clear (5): filtered snow layer value $<$ 50% and cloud percentage $<$ 50%.

Snow melt date is recorded within each 0.05° grid cell as the first date of a five consecutive clear (not cloud impacted) period of observations where land surface is reported as snow-free. A grid cell is considered permanently covered by snow if it does not reach the snow melt criteria by October 1 (Day of Year 274 or 275 for leap year) after the sea ice extent in the Arctic reaches its lowest annual extent in mid-September and begins to grow (NSIDC, 2017)[3]. The snow establishment date must follow the snow melt date and is recorded as the first date of a five consecutive clear period of observations where land surface is reported as snow covered. If the algorithm fails to determine the

[3]http://nsidc.org/arcticseaicenews/sea-ice-tools/ (Accessed July 9, 2017).

snow establishment date by Day of Year 360, it is automatically assigned a snow establishment date of 365 (or 366 for leap year). The output contains values for each grid cell that represent either a Day of Year or a reserved value indicating water or permanent snow cover. The values of 0.05° grids are scaled up to 0.75° to match the resolution of the meteorological variables from ERA-Interim Reanalysis product where the median Day of Year value for the date of snow melt and establishment of the 15 × 15 0.05° snow layer grid cells is recorded into the corresponding 0.75° grid cell.

Transport Algorithm Development

Our simplified transport algorithm takes into consideration a variety of potential injection heights, wind speed, wind direction, and precipitation provided within the European Centre for Medium-Range Weather Forecasts' daily, 0.75° resolution ERA-Interim Reanalysis product (Berrisford et al., 2011). Specifically, we ingest U- and V-Wind layers at the following five pressure levels: 1,000 mb (∼110 m altitude), 975 mb (∼323 m altitude), 950 mb (∼540 m altitude), 925 mb (∼762 m altitude), and 900 mb (∼914 m altitude) to account for the reported variability of cropland burning emission injection heights (Ichoku and Kaufman, 2005; Martin et al., 2010; Soja et al., 2012). Total Precipitation (mm) was evaluated at the surface level only. Daily averages of wind direction (d, units: rad) and speed (s, units: ms^{-1}) were computed using the U- and V-Wind vectors.

The transport algorithm was designed to quantify potential low-level, long distance transport within 96 h. This 96 h cut off reflects the atmospheric lifetime of BC used in a previous study (Larkin et al., 2012) focused on transport of BC from Russia to the Arctic. The algorithm records the transport time (hours) from each cropland burning source grid cell to the first instance of reaching snow-covered ground in the Arctic. Furthermore, the algorithm records the trajectory of the parcel, estimated by connecting the center points of the 0.75° grid cells, beyond the first instance of arriving on snow-covered ground above 60°N. The trajectory is tracked until either 96 h has elapsed or if the parcel encounters precipitation. For all analyses, we assume a total washout of BC from the atmospheric column if precipitation of any amount is encountered. If the precipitation is encountered over snow-covered ground above 60°N, the transport will be terminated; however, the mapped output will indicate a successful event (assumed wet deposition on snow) and the time to that snow-covered grid cell will be recorded in the source cell.

The time of travel is calculated using the daily average, computed from 6 h ERA-Interim data, wind speed (ms^{-1}) and the great circle distance (m) between the center longitude and latitude values of the starting grid cell and the next grid cell. The longitude and latitude values of the next grid cell were determined through the wind direction using the following directional criteria: north (>337.5 to ≤22.5°); north-east (>22.5 to ≤67.5°); east (>67.5 to ≤112.5°); south-east (>112.5 to ≤157.5); south (>157.5 to ≤202.5°); south-west (>202.5 to ≤247.5°); west (>247.5 to ≤292.5°); north-west (>292.5 to ≤337.5°). The time (distance/speed) is then added to the starting UTC time taken from the hourly cropland burning source locations, which continues until the cumulative time has crossed the following day's threshold when meteorological parameters and snow date are extracted from the following date. This process continues until the parcel reaches snow-covered ground beyond 60°N (within the allowed 96 h period). The time at this point would be recorded in the starting source grid cell in the mapped output. If no precipitation was encountered or if the time had not exceeded 96 h, then the trajectory will be continuously tracked until the 96 h threshold is reached. If precipitation was encountered or if the parcel did not reach snow above 60°N within 96 h, then it is assigned a fill value and considered a "failed" transporting event.

This analysis was carried out at the hourly time step between 2003 and 2015 for each of the five pressure levels (1,000, 975, 950, 925, and 900 mb). The final outputs of the transport model include: (1) a binary successful/failed transport event for each cropland burning source grid cell, (2) time (up to 96 h) from each cropland burning source grid cell to the first instance of reaching snow-covered ground in the Arctic; (3) 96 h transport trajectories from the cropland burning source grid cells.

RESULTS

Our results show that a substantial fraction of individual cropland burning events can be deposited on the Arctic snow. As expected, this fraction is the greatest (7.2%-annual average over 13 years) at higher injection heights (900 mb) and diminishes gradually from 7.0% (925 mb), to 6.4% (950 mb), to 5.3% (975 mb) to 2.9% at the lowest injection height (1,000 mb). Our analysis on the seasonal fractions of successful cropland burning events illustrates the importance of spring (March, April, and May) burning contributions to deposition on the Arctic snow. **Table 1** summarizes the total cropland active fires and the successful active fire counts per atmospheric pressure level averaged between 2003 and 2015. Annual tables are available in the Supplementary Material (Table S1).

Based on these values, on average between 2003 and 2015, approximately 4–10% of the March, April, and May observed fire occurrences (depending on injection height) are within regions with successful transport to the Arctic. These results represent a unique quantification of the fraction of observed burning within Russian croplands which are potentially able to contribute to the deposition of BC on the Arctic snow. The observed decrease in successful transport events is likely the result of increased interaction with the surface layer at 1,000 mb as compared to 900 mb, causing lower horizontal wind speeds, and therefore increased likelihood of trajectories failing to reach the snow in the Arctic within 96 h. **Figure 3** illustrates the change in density of the successful trajectories at varying assumed injection heights.

Seasonal Patterns of Successful Transport Potential

Our analysis reveals a large inter-annual and seasonal variability in the success rate of transport of hypothetical BC emission

TABLE 1 | Monthly average (2003–2015) successfully transported and total active fire counts within the Russian croplands.

	All active fires	Successful active fire counts				
	Total	900 mb	925 mb	950 mb	975 mb	1,000 mb
Jan	109	5	4	3	1	0
Feb	763	79	85	74	52	32
Mar	11,840	962	843	774	668	389
Apr	66,335	7,840	7,966	7,395	6,285	3,677
May	44,994	4,076	3,953	3,493	2,735	1,154
Jun	5,545	49	48	28	11	5
Jul	10,621	0	0	0	0	0
Aug	16,564	3	3	1	0	0
Sep	13,623	28	14	9	0	0
Oct	16,027	296	300	238	209	119
Nov	2,385	30	29	25	28	17
Dec	189	4	2	2	1	1

parcels to the Arctic. The largest overall number of successful trajectories (4,645 at 925 mb) were recorded in 2008 and the least (107 at 1,000 mb) in 2013 with the largest (2,246 at 900 mb) monthly contribution of successful trajectories recorded in April 2010 (Table S2). This variability is driven by the confluence of respective variabilities in atmospheric conditions, fire activity, and snow cover extent (Figure S1). In this part of the analysis we assess generalized monthly patterns of transport potential through trajectory densities at various injection heights over the 13 year time frame (**Figure 4** and Figures S2–S5). The general temporal pattern of successful transport events is stable across all injection heights, therefore, in this section we discuss findings for trajectory patterns only at 925 mb. Monthly snow extent maps are also produced to help interpret these successful transport patterns (Figure S1).

Generally, in December, January and February the few (on average 1, 2, and 19, respectively) successful events predominantly originate in the south-western regions of Russia in the Northern Caucasus (∼45°N, 40°E). The few fires that occurred in the winter months are unlikely to represent crop residue burning in preparation for planting; however, they may be associated with other types of burning, including bonfires or pile burning of agricultural waste. March, April and May saw the largest number of successful transport events (on average 198, 1,197, and 839, respectively), often several orders of magnitude higher than other months. The very large number of successful trajectories in the spring result from not only the overall large amount of residue management fires (on average ∼12,000, ∼66,000, and ∼45,000 for March, April, and May, respectively) but also largely from the coincidental maximal extent of snow cover above 60°N. In contrast, while the total monthly cropland burning activity in August (monthly average ∼17,000 per year between 2003 and 2015) begins to increase in response to the wheat harvest cycles, snow extent in the Arctic is at its minimum (Figure S1), hence, substantially limiting the potential for cropland burning-resultant BC deposition on snow.

While in general, spring cropland burning appears to have the greatest potential to result in BC deposition on the Arctic snow, there is a considerable difference in the amount and spatial patterns of trajectory densities among March, April and May. In March, the hotspot in the density of overlapping trajectories is typically located along the western edge of Russia. This hotspot migrates east with time and reaches 80°E by May. By June, the number of successful transport trajectories is substantially reduced (on average 18 year^{-1}) with the highest density located around 90°E. July and August on average have very few successful transport events, depending on the pressure level and year (on average <1 successful event per year). The number of successful events gradually increases in September (on average 5 year^{-1}) and has a minor peak in October (on average 77 year^{-1}), which is mostly associated with a rapid establishment of snow cover in the Arctic. The total number of successful trajectories quickly drops in November (on average 15 year^{-1}) driven by the overall decrease in crop residue burning.

Further analysis of the full extent of the transport trajectories within the 96 h window show that BC emissions from cropland burning in Russia can be transported beyond 80°N. This potential for reaching far into the Arctic indicates that cropland burning has an impact not only on snow-covered land but also on sea ice. To determine how far north these successful trajectories can reach, the northern most latitude for each trajectory was recorded and summed over several latitude bands (60–65°N, 65–70°N, 70–75°N, 75–80°N, and 80–90°N) for every month between 2003 and 2015. The starting latitude was also recorded to help identify how far south within Russia a potential cropland burning emission source could be located to potentially deposit BC within each of these latitude bands (**Figure 5**). In this section we discuss only the results for March, April, and May–months with the larger number of successful transport events as compared with other months.

The results show that BC emissions from as far south as 45°N (in March at the highest injection height) and 50°N (April and May at almost all injection heights) can potentially be transported as far north as 80–90°N. Deposition of BC this far north has important implications for the permanent sea ice cover in the Arctic. Furthermore, the trajectories indicate that cropland burning BC from as far south as 40–45°N can be transported and deposited on the Arctic snow (in some cases up to 70–75°N) during March, April and May and for nearly all injection heights.

Spatial Patterns of BC Transport to the Arctic Snow

Quantifying the transport time is an important element in identifying the relative importance of the burning source regions to their potential contribution to the BC deposition on snow in the Arctic. The exact impact of deposited BC on Arctic snow relies on the microphysical properties of the BC particle and the various chemical and turbulent processes within the atmosphere; however, as a general rule, the longer a molecule remains in the atmosphere the more mixing and alterations it will undergo before it is ultimately removed via wet or dry deposition.

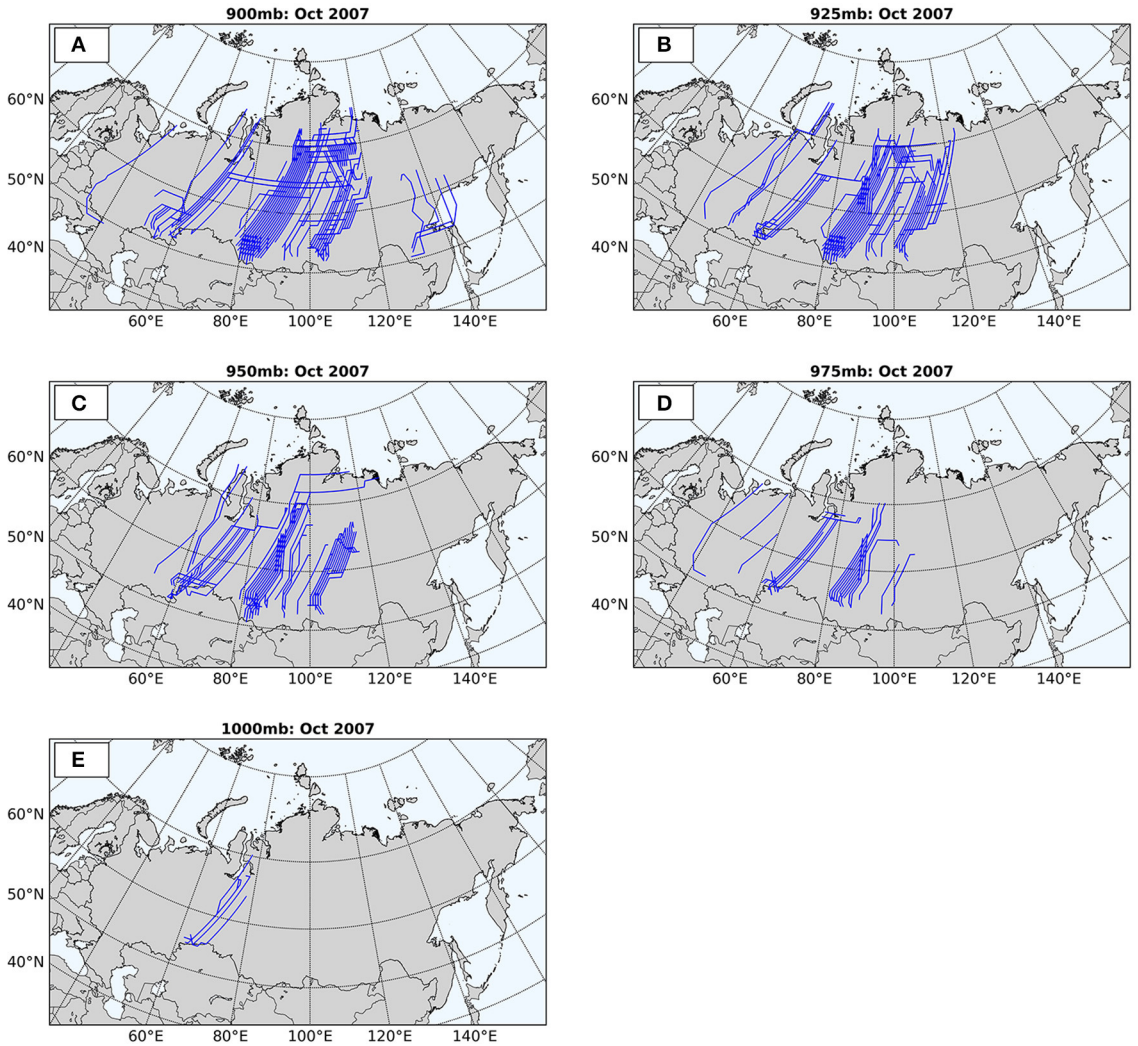

FIGURE 3 | Transport trajectory line maps for successful events for October 2007 at five different pressure levels: 900 mb **(A)**; 925 mb **(B)**; 950 mb **(C)**; 975 mb **(D)**; 1,000 mb **(E)**. For illustration purposes only October 2007 is shown, but the pattern is representative of the generally observed decrease in the number of successful events with shallower injection heights across all months and years.

We analyzed the average transport time (hours), the success (%) of each starting location, and the number of active fires within each grid cell of origin for a successful transport event to quantify the fraction of the potential contributions of BC deposition and to characterize the cropland burning source regions. While we discuss the findings of this analysis for all months (Figures S6–S14), we graphically show only results from March, April, and May (2003–2015) at 900 mb and 1,000 mb as the majority of the successful fires occur during these months (**Figures 6**–**8**). The 900 and 1,000 mb results are shown to illustrate the two extremes of the injection height range used in this study.

On average, fire occurrence in January and February is very low with only 1 active fire per grid cell per year on average between 2003 and 2015 predominantly located in the south-western region of European Russia (45°N, 50°E). The few locations with successful transport were able to reach the snow-covered Arctic on average within approximately 50 h (January) and 40 h (February), depending on the injection height. By March, the total number of cropland fires increased to approximately 5–15 active fires per successful grid cell, while also increasing in spatial extent (**Figure 6**). As expected the success rate of potential crop residue emission transport decreases while transport time increases with lower injection heights; however, an interesting anomalous pattern occurs in March in the north-west region (centered on 55°N, 45°E) of the transport map. Instead of the transport time increasing with lower injection heights, the transport time actually decreases from approximately 40–50 h to approximately 10–30 h on average to the Arctic. Analysis of the transport pathways found this anomalous pattern resulted from longer trajectories at higher injection heights seemingly associated with a more circular pattern as compared to more straight northerly trajectories at lower injection heights.

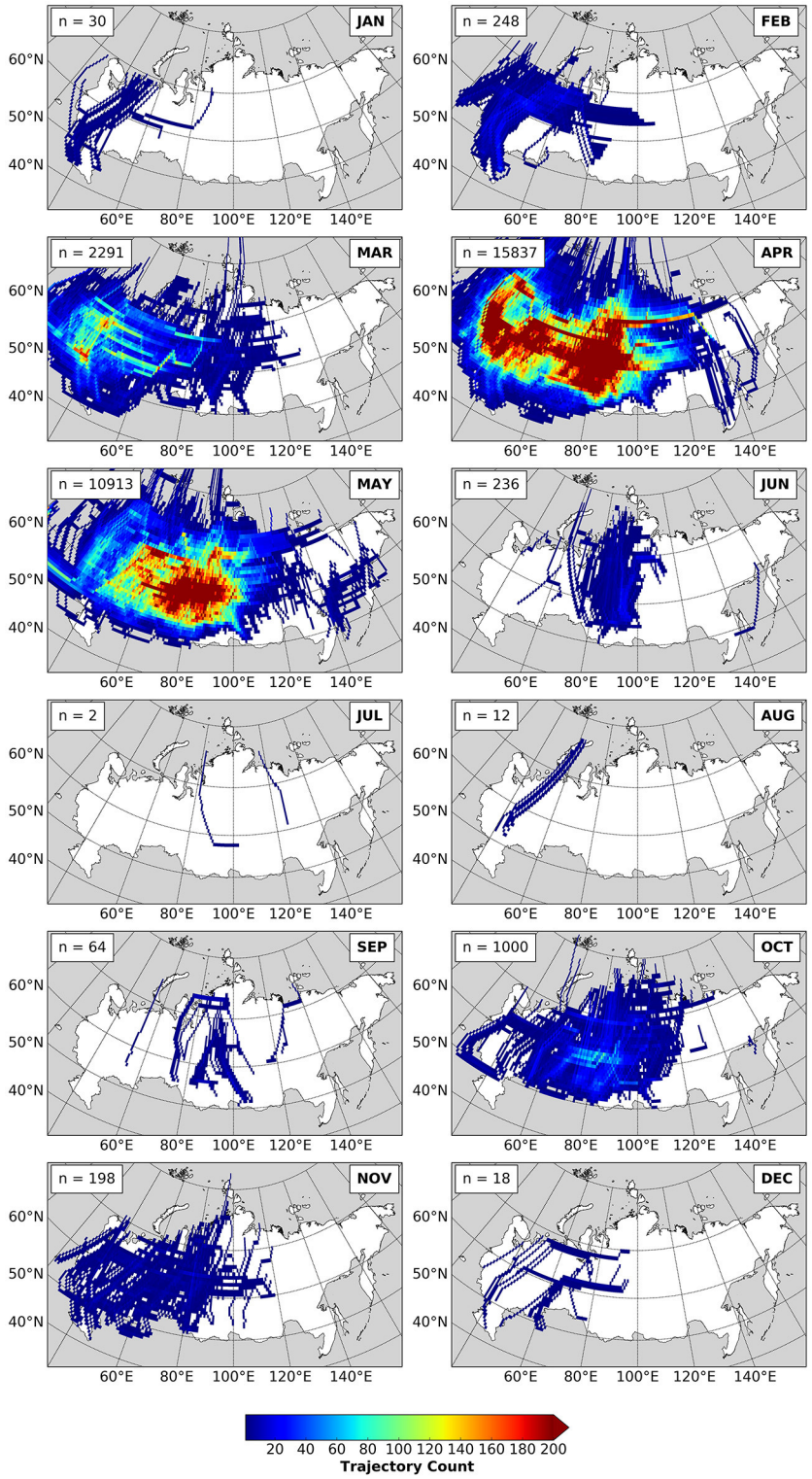

FIGURE 4 | The cumulative number of successful trajectories between 2003 and 2015 monthly at 925 mb. See Figures S2–S5 for accompanying maps for cumulative trajectories at other injection heights examined within this study.

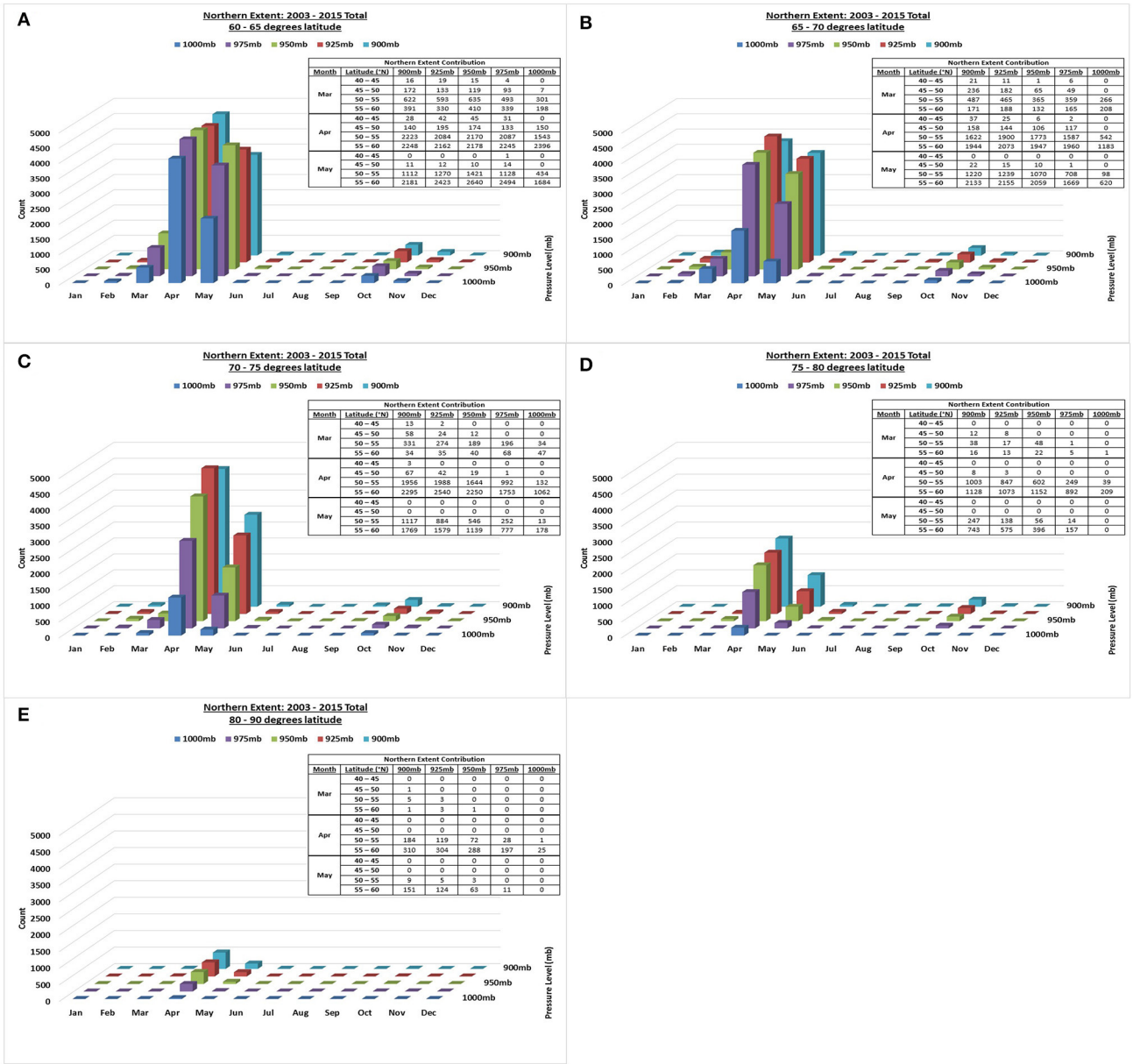

FIGURE 5 | Total number of successful events (monthly) between 2003 and 2015 that reach snow cover between 60–65°N **(A)**, 65–70°N **(B)**, 70–75°N **(C)**, 75–80°N **(D)**, 80–90°N **(E)** as their northern-most extent per injection height. The inset table represents the contribution from the lower latitude bands (40–45°N, 45–50°N, 50–55°N, 55–60°N) for March, April and May.

In April, the successfully transported fire load reached a peak (100–130 active fires per grid cell–**Figure 7**) between 70 and 80°E. Although this area has low success rates, the transport time to the Arctic remains relatively low in comparison to the surrounding regions even at low injection heights. A slightly smaller peak in fire occurrence is located in the north-west corner (approximately 55°N, 35°E) with a coincidental increase in success rate. Transport times for both clusters vary between <10 and 50 h, therefore the emissions from these higher fire loads will likely encounter less mixing and fall out than emissions with longer atmospheric residence times. Furthermore, at higher injection heights, successful transport of potential emissions can originate at least as far south as approximately 40°N, which is the limit of the Russian croplands.

In May, the success rate along the southern edge of the Russian croplands, particularly at lower injection heights, drops significantly except for the region located between 70 and 80°E (**Figure 8**). As with April, this same area has slightly lower transport times to the Arctic as compared to the surrounding regions. Analysis of the transport pathways does not explain the decrease in transport time in that region. A possible explanation lies in the higher number of successful burning locations (see

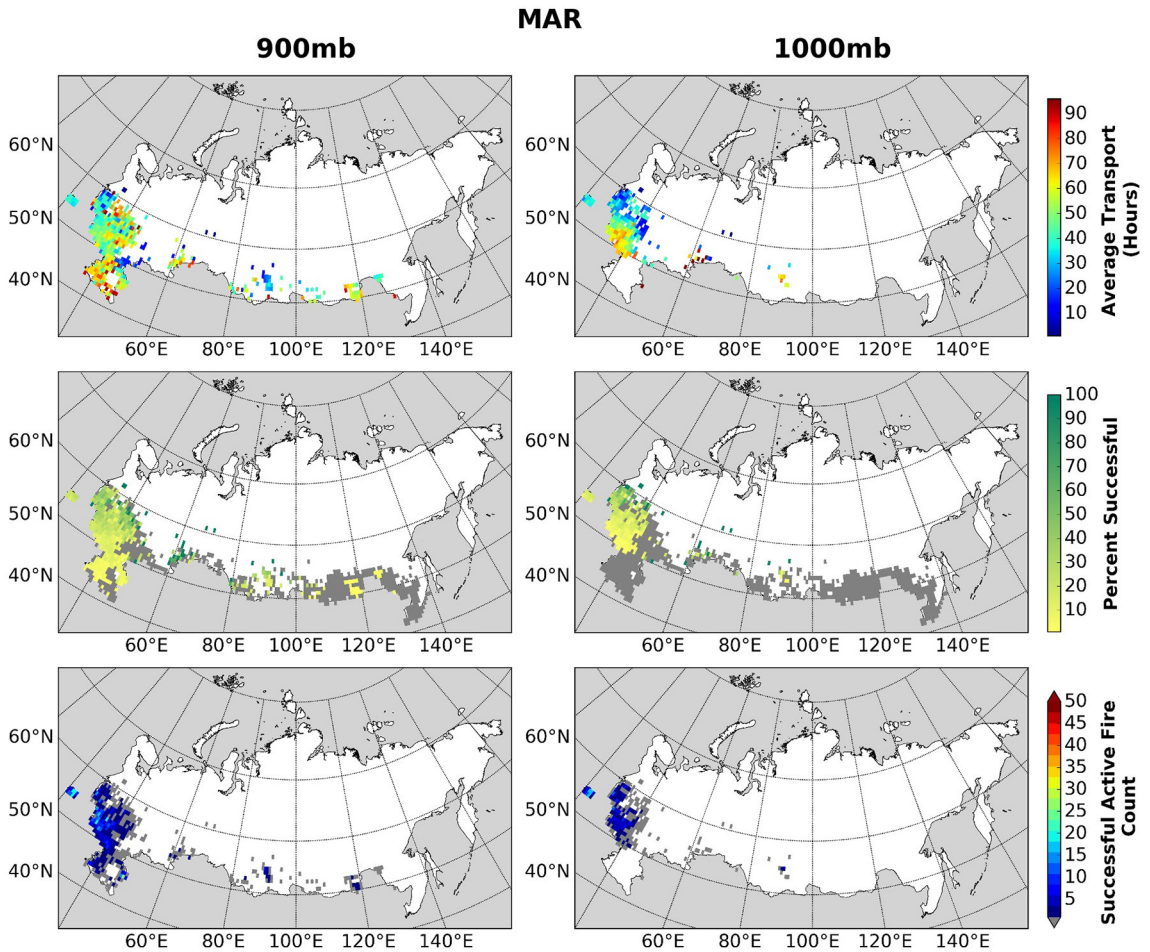

FIGURE 6 | 900 and 1,000 mb March 2003–2015 average transport (hours), percent successful and active fires potentially contributing to BC deposition on snow in the Arctic. The dark gray color in the percent successful maps (middle) represents the starting fire locations which were unsuccessful at reaching the snow in the Arctic within 96 h.

bottom map in **Figures 7**, **8**) in that area as compared to other areas in the Russian croplands. These maps show the average transport times which are more likely to be influenced by outliers within the regions with fewer successful fires as compared to the region located between 70° and 80°E.

The highest density of cropland fires occurs in the spring in the southern portion of the cropland in the Far East (approximately between 40–55°N and 110–130°E); however, there are very few fires with successfully transported emissions within this region. Specifically, the success rate of fires east of 95°E are severely reduced with lower injection heights in comparison to the cropland fires within European Russia at similar latitudes. Analysis of the trajectories originating in the Far East croplands reveal short pathways often flowing toward the east over the Sea of Okhotsk (away from the snow extent), whereas the European Russian trajectories are much longer and tend to flow north. These differences are likely due to the varying atmospheric circulation patterns observed across Russia.

DISCUSSION

Sources of Uncertainty

Quantifying the fraction of BC emitted from cropland burning in Russia that is deposited on snow in the Arctic is a difficult task due to the inherent challenges associated with the underlying input datasets. As previously mentioned, existing satellite-based estimates of area burned in croplands are very poor (Hall J. V. et al., 2016) which results in highly inaccurate cropland burning emissions inventories. This study assumes emissions of a hypothetical parcel of BC of unknown amount from cropland burning using the MODIS active fire detections. The orbital overlap that is achieved at the latitude of Russian croplands allows for more frequent observations of fire activity than the nominal twice daily from each of the two MODIS-carrying satellites. While it has not been established quantitatively (because there are currently no accurate estimates of cropland area burned), we assume active fire observations to be generally representative of

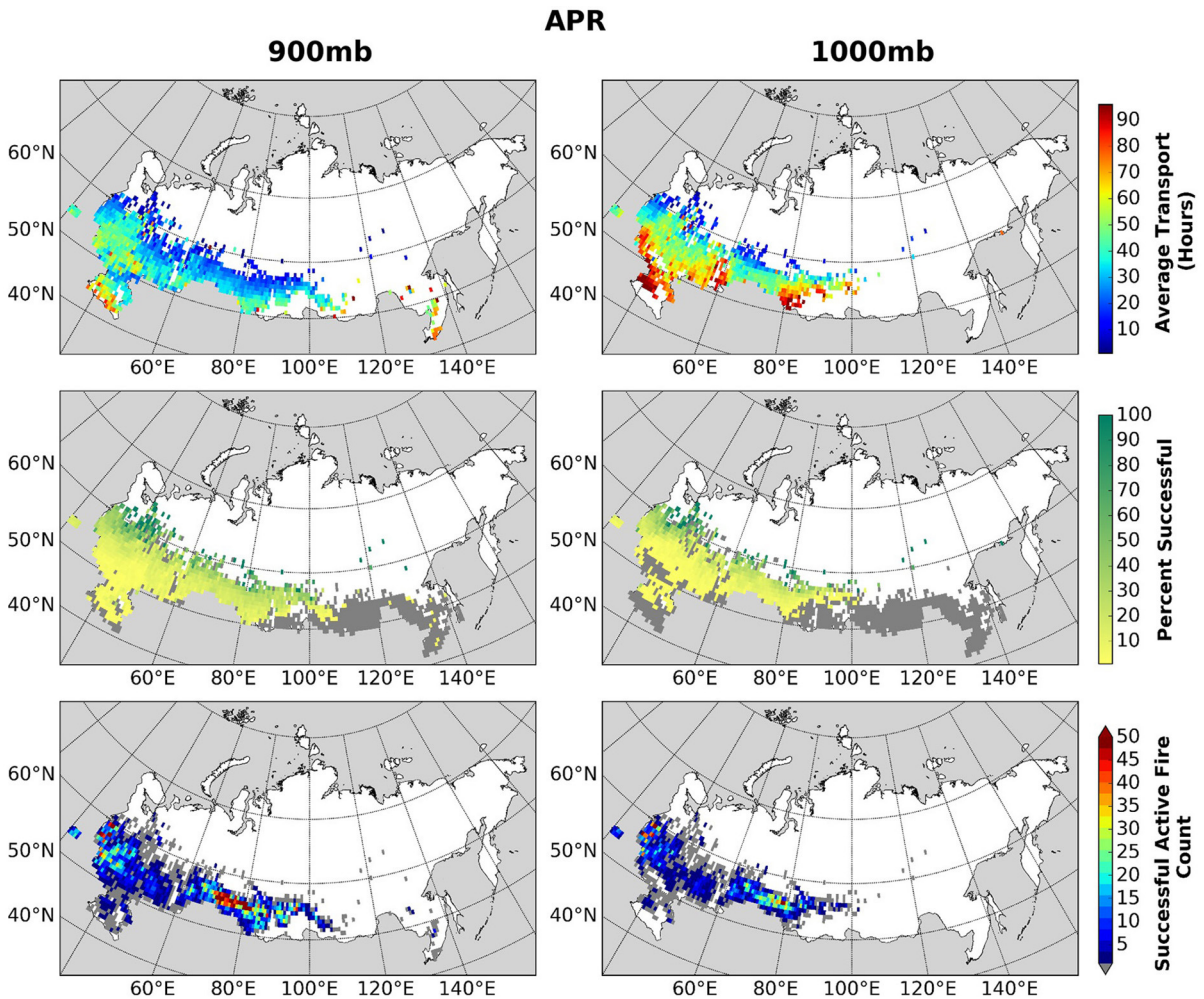

FIGURE 7 | 900 and 1,000 mb April 2003–2015 average transport (hours), percent successful and active fires potentially contributing to BC deposition on snow in the Arctic. The dark gray color in the percent successful maps (middle) represents the starting fire locations which were unsuccessful at reaching the snow in the Arctic within 96 h.

the spatio-temporal patterns of biomass burning within Russian croplands.

The spatial scale of the meteorological data used in this transport model determines the spatial granularity of resultant trajectories which were restricted to tracking the centers of the individual grid cells rather than the actual locations of the active fires. While very coarse compared to the 1 km MODIS active fire pixels, ERA-Interim meteorological data (at 0.75°) records parameters at a finer scale than the more commonly used, in previous studies, 2.5° resolution NCEP/NCAR (National Centers for Environmental Prediction–National Center for Atmospheric Research Global Reanalysis; Kalnay et al., 1996) dataset. For example, the coarser NCEP/NCAR meteorological data is frequently used to drive HYSPLIT trajectory models (e.g., Treffeisen et al., 2007; Huang et al., 2010; Larkin et al., 2012). Additionally, 6 h ERA-Interim wind and precipitation data fields were aggregated to daily values. While ideally, hourly wind and precipitation data would more accurately represent the actual meteorological conditions throughout the transport pathway, it is difficult to quantify how much actual precision is lost in using daily vs. 6 hourly data within a 0.75° grid cell. The general weather patterns across Russia's mid-latitudes are primarily influenced by cyclonic and anticyclonic activity which most frequently last more than 1 day (Lebedeva et al., 2015). It is likely that the aggregation of meteorological parameters to a daily temporal scale has impacted trajectories for fire events that occurred during the stages when the weather patterns were shifting between cyclones and anticyclones. However, it is expected that most of the burning occurs during anticyclonic weather patterns when the meteorological conditions produce drier fuels (a particularly limiting parameter for fire spread during post snow-melt conditions in the spring) that can support fire spread more readily. Furthermore, this simplified transport model assumes the only vertical transport occurs at the point

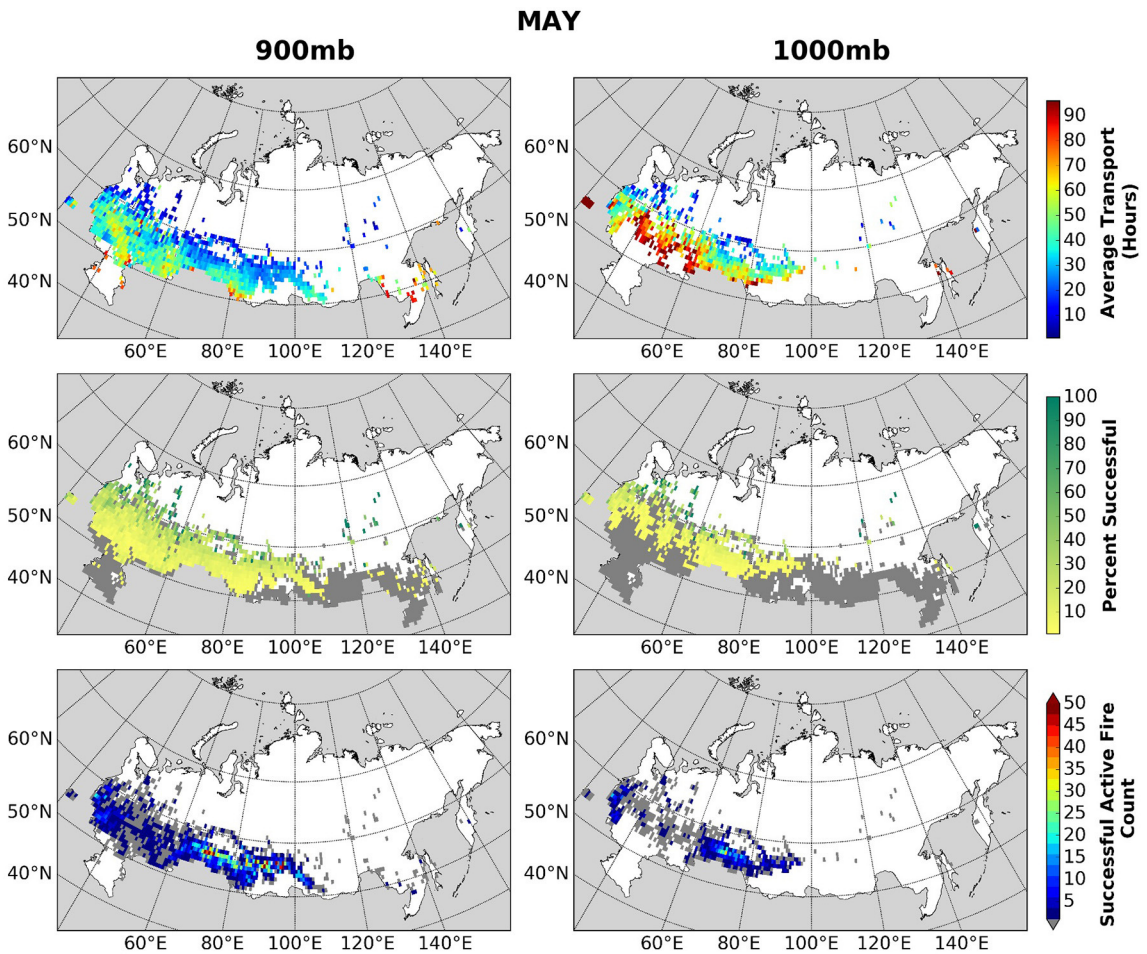

FIGURE 8 | 900 and 1,000 mb May 2003–2015 average transport (hours), percent successful and active fires potentially contributing to BC deposition on snow in the Arctic. The dark gray color in the percent successful maps (middle) represents the starting fire locations which were unsuccessful at reaching the snow in the Arctic within 96 h.

of BC injection from cropland burning and all subsequent transport occurs via horizontal wind vectors. Due to the vertical atmospheric stratification and dominant horizontal advection motions, this assumption is not a severe constraint on the model; however, future work focusing on the variability within the planetary boundary layer could be undertaken to improve the understanding of how BC is transported from cropland burning in Russia to the Arctic snow.

An additional source of uncertainty is related to the satellite-based estimates of snow cover extent used in this study. The high northern latitudes are plagued with persistent cloud cover during the sunlit period and an absence of solar irradiance during the polar nights. Therefore, several assumptions had to be defined in order to create snow melt and snow establishment layers. The inability to observe surface conditions due to cloud presence introduces a considerable amount of uncertainty in identifying the exact date of snow melt and snow establishment. Quantifying the difference between the 0.75° aggregated snow establishment and snow melt dates (calculated as the median of the 0.05° grid cells–see section Arctic Snow Cover Extent) and the dates of the individual 0.05° grid cells found that on average (2003–2015) the difference was <1 day for both the snow melt and snow establishment periods with a standard deviation of 6 and 7 days, respectively, with the majority of the variability stemming from grid cells below 65°N.

Finally, transport trajectories and the resultant outputs generated by this methodology are consistent (although not directly comparable) with those produced within previously published studies. Several previous studies have indicated that biomass burning sources from northern mid-latitudes significantly impact the Arctic region (e.g., Warneke et al., 2010; Quinn et al., 2011; Larkin et al., 2012; Sharma et al., 2013; Cheng, 2014; Liu et al., 2015). Comparison of this study's results with previous studies (focused on air pollution transport from northern mid-latitudes to the Arctic) has demonstrated that the simple form of the transport model, developed within this study, has represented the key meteorological drivers

appropriately and that the interpretation of the results is meaningful.

Significance of BC Deposition from Cropland Burning on the Arctic Snow

A key attribute of this study is focused on BC deposition on the snow in the Arctic. This nuance has important implications for the timing of burning. Although forest fires produce substantially more emissions than cropland fires due to higher biomass loading (e.g., Hao et al., 2016), the timing of the burning largely determines the relative importance of these source emissions to BC deposition on Arctic snow. Forest fires typically occur in the summer, when high temperatures, low humidity, and little precipitation drive the increase in forest flammability. On the other hand, crop residue burning in Russia usually follows the crop planting and harvest cycles. Analysis of the active fire dataset between 2003 and 2015 found two peaks in cropland fires – one in April/May and another smaller peak in August/September (Hall J. V. et al., 2016) consistent with winter and spring planting and harvesting dates in Russia (USDA FAS, 2016). Despite the peak in summer cropland fires, the contribution to BC deposition on the Arctic snow is negligible. Based on this analysis, it seems the coincidental timing of burning and snow cover extent is a linking factor in determining the importance of crop residue-related BC emissions and their impact on Arctic albedo.

This study confirmed the importance of springtime cropland burning in relation to the deposition on the Arctic snow. Based on the analysis of the transport time and the success percentage, it is clear that despite the low injection heights, potential BC emissions from cropland burning can be transported and deposited onto Arctic snow in the spring from at least 40°N. This study also identified that the cropland regions within European Russia contained the highest percentage of successful transport to the Arctic snow. Although this study makes no attempt to quantify emissions, these regions contain the highest wheat yields within Russia (yield data compiled by USDA Foreign Agricultural Service, Mark Lindeman pers.comm.), therefore they are likely to also contain the highest volumes of crop residues and larger BC emissions. A recent interest in expanding arable land through reclaiming Post-Soviet abandoned cropland (e.g., Schierhorn et al., 2014; Meyfroidt et al., 2016) and in particular, a large concentration of cropland in European Russia is located along the fertile Chernozem soil belt which stretches from the southern tip of Russia (43°N, 44°E) toward Moscow (55°N, 37°E)-a region with higher wheat yields, raises concerns for associated increase in BC deposition on Arctic snow. Although an expansion of cropped area does not necessarily lead to an increase in fire activity, it does give rise to an increased opportunity for burning crop residue in the regions of higher transport potential. Moreover, if this increase in cropland area expands further north toward 50°N and leads to additional fire activity then based on the results of the northern extent analysis, there could also be an increase in BC deposition from cropland burning emissions on the permanent sea ice.

CONCLUSION

Crop residue burning has been reported to constitute a considerable source of BC deposited in the Arctic. However, previous studies relied on highly inaccurate estimates in terms of the amount and timing of cropland burning emissions resulting from uncertainties in estimates of burned area, biomass loads, and emission factors. This study introduces a simple approach to assess the potential for BC deposition in the Arctic based on reanalysis data of observed meteorological conditions and confirmed cropland burning. In addition, we specifically assess the impact of BC deposition on snow when the impact on surface albedo from deposition is the highest with considerable consequences for snow melt and establishment. Although our approach does not allow for quantifying the amount of BC deposited on the snow surface, it provides the baseline estimate of the spatio-temporal patterns of BC transport resulting from confirmed cropland burning and the potential for BC deposition on the snow.

It is clear based on the results of this study that cropland burning has the potential to significantly impact the Arctic via BC deposition. We estimate that approximately 10% of the observed cropland burning in March, April and May (7% annual) has the potential to contribute to the BC deposition on the Arctic snow. Despite the low injection heights, this study has shown that potential BC emissions from at least 40°N can be deposited on the Arctic snow. Furthermore, during the spring, which is the most vulnerable period for sea ice melt, potential cropland burning emissions can reach areas beyond 80°N. Analysis of the successful transport pathways identified areas containing concentrated trajectories particularly over European and Central Russia. These clusters of trajectories may be influenced by persistent wind patterns over these areas. The magnitude of this impact, however, cannot be quantified well due to current inaccuracies surrounding cropland emission inventory calculations.

Complex chemical-transport model outputs should be applied with caution, particularly when considering impacts from cropland burning. Additional improvements are needed to accurately represent the spatial and temporal cropland emission fluxes. Future work should be focused on improving the deficiencies associated with current cropland burning emission inventories. Improvements to all components of emission inventories, including area burned, the precise timing of burning (at least to the date), biomass loading, and emission factors, are absolutely essential to deriving meaningful estimates of the amount of BC deposited on the snow. Future studies should also investigate the causes behind these concentrated pollution pathways to the Arctic, revealed in this study, with a focus on large-scale atmospheric patterns that can act to enhance atmospheric transport of pollutants from lower mid-latitudes.

AUTHOR CONTRIBUTIONS

JH was the primary developer of the low-level transport algorithm which was a key component of her doctoral

research. JH was responsible for data collection, analysis, and interpretation and was the primary author of the manuscript. TL was the primary author's doctoral advisor and participated in advisory input in both the research project and the manuscript preparation. TL also gave critical revision of the manuscript.

FUNDING

This research did not receive any specific grant from funding agencies in the public, commercial, or not-for-profit sectors.

ACKNOWLEDGMENTS

The authors would like to thank Dr. Louis Giglio (University of Maryland), Dr. Christopher Justice (University of Maryland), and Dr. Gregory McCarty (USDA ARS) for their useful technical discussions.

SUPPLEMENTARY MATERIAL

The Supplementary Material for this article can be found online at: https://www.frontiersin.org/articles/10.3389/feart.2017.00109/full#supplementary-material

REFERENCES

Akagi, S., Yokelson, R. J., Wiedinmyer, C., Alvarado, M., Reid, J., Karl, T., et al. (2011). Emission factors for open and domestic biomass burning for use in atmospheric models. *Atmos. Chem. Phys.* 11, 4039–4072. doi: 10.5194/acp-11-4039-2011

AMAP (2015). *AMAP Assessment 2015: Black Carbon and Ozone as Arctic Climate Forcers*. Oslo: Arctic Monitoring and Assessment Programme (AMAP).

Andreae, M. O., and Merlet, P. (2001). Emission of trace gases and aerosols from biomass burning. *Global Biogeochem. Cycles* 15, 955–966. doi: 10.1029/2000GB001382

Arnold, S., Law, K., Thomas, J., Starckweather, S., von Salzen, K., Stohl, A., et al. (2016). *Arctic air Pollution*. Elementa: Science of the Anthropocene.

Berrisford, P., Dee, D., Poli, P., Brugge, R., Fielding, K., Fuentes, M., et al. (2011). *The ERA-Interim Archive Version 2.0*. ERA Report Series 1, Shinfield Park; Reading: ECMWF. 13177.

Bond, T. C., Doherty, S. J., Fahey, D. W., Forster, P. M., Berntsen, T., DeAngelo, B. J., et al. (2013). Bounding the role of black carbon in the climate system: a scientific assessment. *J. Geophys. Res. Atmos.* 118, 5380–5552. doi: 10.1002/jgrd.50171

Cape, J. N., Coyle, M., and Dumitrean, P. (2012). The atmospheric lifetime of black carbon. *Atmos. Environ.* 59, 256–263. doi: 10.1016/j.atmosenv.2012.05.030

Chapin, F. S., Sturm, M., Serreze, M. C., McFadden, J. P., Key, J. R., Lloyd, A. H., et al. (2005). Role of land-surface changes in Arctic summer warming. *Science* 310, 657–660. doi: 10.1126/science.1117368

Cheng, M.-D. (2014). Geolocating Russian sources for Arctic black carbon. *Atmos. Environ.* 92, 398–410. doi: 10.1016/j.atmosenv.2014.04.031

Doherty, S. J., Steele, M., Rigor, I., and Warren, S. G. (2015). Interannual variations of light-absorbing particles in snow on Arctic sea ice. *J. Geophys. Res. Atmos.* 120, 11,391–11,400. doi: 10.1002/2015JD024018

Dou, T. F., and Xiao, C. D. (2016). An overview of black carbon deposition and its radiative forcing over the Arctic. *Adv. Clim. Change Res.* 7, 115–122. doi: 10.1016/j.accre.2016.10.003

Dozier, J. (1989). Spectral signature of alpine snow cover from the Landsat Thematic Mapper. *Remote Sens. Environ.* 28, 9–22. doi: 10.1016/0034-4257(89)90101-6

EPA (2016). *Methane and Black Carbon Impacts on the Arctic: Communicating the Science*. US Environmental Protection Agency. Available online at: https://19january2017snapshot.epa.gov/sites/production/files/2016-09/documents/arctic-methane-blackcarbon_communicating-the-science.pdf

Evangeliou, N., Balkanski, Y., Hao, W., Petkov, A., Silverstein, R. P., Corley, R., et al. (2016). Wildfires in northern Eurasia affect the budget of black carbon in the Arctic–a 12-year retrospective synopsis (2002–2013). *Atmos. Chem. Phys.* 16, 7587–7604. doi: 10.5194/acp-16-7587-2016

Friedl, M. A., Sulla-Menashe, D., Tan, B., Schneider, A., Ramankutty, N., Sibley, A., et al. (2010). MODIS Collection 5 global land cover: algorithm refinements and characterization of new datasets. *Remote Sens. Environ.* 114, 168–182. doi: 10.1016/j.rse.2009.08.016

Giglio, L., Descloitres, J., Justice, C. O., and Kaufman, Y. J. (2003). An enhanced contextual fire detection algorithm for MODIS. *Remote Sens. Environ.* 87, 273–282. doi: 10.1016/S0034-4257(03)00184-6

Giglio, L., Loboda, T., Roy, D. P., Quayle, B., and Justice, C. O. (2009). An active-fire based burned area mapping algorithm for the MODIS sensor. *Remote Sens. Environ.* 113, 408–420. doi: 10.1016/j.rse.2008.10.006

Giglio, L., Randerson, J. T., and van der Werf, G. R. (2013). Analysis of daily, monthly, and annual burned area using the fourth-generation global fire emissions database (GFED4). *J. Geophys. Res. Biogeosci.* 118, 317–328. doi: 10.1002/jgrg.20042

Groisman, P. Y., Sherstyukov, B. G., Razuvaev, V. N., Knight, R. W., Enloe, J. G., Stroumentova, N. S., et al. (2007). Potential forest fire danger over Northern Eurasia: changes during the 20th century. *Glob. Planet. Change* 56, 371–386. doi: 10.1016/j.gloplacha.2006.07.029

Hall, J. V., Loboda, T. V., Giglio, L., and McCarty, G. W. (2016). A MODIS-based burned area assessment for Russian croplands: mapping requirements and challenges. *Remote Sens. Environ.* 184, 506–521. doi: 10.1016/j.rse.2016.07.022

Hall, D., Salomonson, V., and Riggs, G. (2016). *MODIS/Terra Snow Cover Daily L3 Global 0.05 Deg CMG, Version 6*. Boulder, CO: National Snow and Ice Data Center.

Hao, W. M., Petkov, A., Nordgren, B. L., Corley, R. E., Silverstein, R. P., Urbanski, S. P., et al. (2016). Daily black carbon emissions from fires in northern Eurasia for 2002-2015. *Geosci. Model Dev.* 9:4461. doi: 10.5194/gmd-9-4461-2016

Hirdman, D., Sodemann, H., Eckhardt, S., Burkhart, J. F., Jefferson, A., Mefford, T., et al. (2010). Source identification of short-lived air pollutants in the Arctic using statistical analysis of measurement data and particle dispersion model output. *Atmos. Chem. Phys.* 10, 669–693. doi: 10.5194/acp-10-669-2010

Huang, L., Gong, S., Sharma, S., Lavoué, D., and Jia, C. (2010). A trajectory analysis of atmospheric transport of black carbon aerosols to Canadian high Arctic in winter and spring (1990–2005). *Atmos. Chem. Phys.* 10, 5065–5073. doi: 10.5194/acp-10-5065-2010

Ichoku, C., and Kaufman, Y. J. (2005). A method to derive smoke emission rates from MODIS fire radiative energy measurements. *IEEE Trans. Geosci. Remote Sens.* 43, 2636–2649. doi: 10.1109/TGRS.2005.857328

Jacobson, M. Z. (2001). Strong radiative heating due to the mixing state of black carbon in atmospheric aerosols. *Nature* 409, 695–697. doi: 10.1038/35055518

Kalnay, E., Kanamitsu, M., Kistler, R., Collins, W., Deaven, D., Gandin, L., et al. (1996). The NCEP/NCAR 40-year reanalysis project. *Bull. Am. Meteorol. Soc.* 77, 437–471. doi: 10.1175/1520-0477(1996)077<0437:TNYRP>2.0.CO;2

Klonecki, A., Hess, P., Emmons, L., Smith, L., Orlando, J., and Blake, D. (2003). Seasonal changes in the transport of pollutants into the Arctic troposphere-model study. *J. Geophys. Res. Atmos.* 108:8367. doi: 10.1029/2002JD002199

Koch, D., and Hansen, J. (2005). Distant origins of Arctic black carbon: a Goddard Institute for Space Studies ModelE experiment. *J. Geophys. Res. Atmos.* 110:D04204. doi: 10.1029/2004JD005296

Larkin, N. K., DeWinter, J. L., Strand, T. M., Brown, S. G., Brown, S. M., Raffuse, S. M., et al. (2012). *Identification of Necessary Conditions for Arctic Transport of Smoke from United States Fires*. JFSP Research Project Reports. Paper 93.

Law, K. S., and Stohl, A. (2007). Arctic air pollution: origins and impacts. *Science* 315, 1537–1540. doi: 10.1126/science.1137695

Lebedeva, M. G., Krymskaya, O. V., Lupo, A. R., Chendev, Y. G., Petin, A. N., and Solovyov, A. B. (2015). Trends in summer season climate for Eastern Europe and Southern Russia in the Early 21st Century. *Adv. Meteorol.* 2016:5035086. doi: 10.1155/2016/5035086

Liu, D., Quennehen, B., Darbyshire, E., Allan, J. D., Williams, P. I., Taylor, J. W., et al. (2015). The importance of Asia as a source of black carbon to the European Arctic during springtime 2013. *Atmos. Chem. Phys.* 15, 11537–11555. doi: 10.5194/acp-15-11537-2015

Martin, M. V., Logan, J. A., Kahn, R. A., Leung, F.-Y., Nelson, D. L., and Diner, D. J. (2010). Smoke injection heights from fires in North America: analysis of 5 years of satellite observations. *Atmos. Chem. Phys.* 10, 1491–1510. doi: 10.5194/acp-10-1491-2010

McCarty, J. L., Ellicott, E. A., Romanenkov, V., Rukhovitch, D., and Koroleva, P. (2012). Multi-year black carbon emissions from cropland burning in the Russian Federation. *Atmos. Environ.* 63, 223–238. doi: 10.1016/j.atmosenv.2012.08.053

Meyfroidt, P., Schierhorn, F., Prishchepov, A. V., Müller, D., and Kuemmerle, T. (2016). Drivers, constraints and trade-offs associated with recultivating abandoned cropland in Russia, Ukraine and Kazakhstan. *Glob. Environ. Change* 37, 1–15. doi: 10.1016/j.gloenvcha.2016.01.003

Monks, S., Arnold, S., Emmons, L., Law, K. S., Turquety, S., Duncan, B., et al. (2015). Multi-model study of chemical and physical controls on transport of anthropogenic and biomass burning pollution to the Arctic. *Atmos. Chem. Phys.* 15, 3575–3603. doi: 10.5194/acp-15-3575-2015

NOAA (2017). *Arctic Report Card*. Available online at: http://arctic.noaa.gov/Report-Card (Accessed Mar 12, 2017).

Qi, L., Li, Q., Li, Y., and He, C. (2017). Factors controlling black carbon distribution in the Arctic. *Atmos. Chem. Phys.* 17, 1037–1059. doi: 10.5194/acp-17-1037-2017

Quinn, P. K., Stohl, A., Arneth, A., Berntsen, T., Burkhart, J. F., Christensen, J., et al. (2011). *The Impact of Black Carbon on Arctic Climate*. AMAP Technical Report No. 4. Arctic Monitoring and Assessment Programme (AMAP), (Oslo).

Ramanathan, V., and Carmichael, G. (2008). Global and regional climate changes due to black carbon. *Nat. Geosci.* 1, 221 – 227. doi: 10.1038/ngeo156

Randerson, J. T., Chen, Y., van derWerf, G. R., Rogers, B. M., and Morton, D. C. (2012). Global burned area and biomass burning emissions from small fires. *J. Geophys. Res.* 117, G04012, doi: 10.1029/2012JG002128

Riggs, G. A., and Hall, D. K. (2015). *MODIS Snow Products Collection 6 User Guide.* Available online at: https://nsidc.org/sites/nsidc.org/files/files/MODIS-snow-user-guide-C6.pdf

Roy, D. P., Boschetti, L., Justice, C. O., and Ju, J. (2008). The collection 5 MODIS burned area product-Global evaluation by comparison with the MODIS active fire product. *Remote Sens. Environ.* 112, 3690–3707. doi: 10.1016/j.rse.2008.05.013

Satterwhite, M. B., Mitchell, H., Hemmer, T., and Leckie, J. D. (2003). "Field spectral signatures of snow, ice, and water," in *Proceedings of SPIE, the International Society for Optical Engineering* (Orlando, FL).

Schierhorn, F., Müller, D., Prishchepov, A. V., Faramarzi, M., and Balmann, A. (2014). The potential of Russia to increase its wheat production through cropland expansion and intensification. *Glob. Food Secur.* 3, 133–141. doi: 10.1016/j.gfs.2014.10.007

Schiffer, R., and Rossow, W. B. (1983). The International Satellite Cloud Climatology Project (ISCCP)-the first project of the World Climate Research Programme. *Am. Meteorol. Soc. Bull.* 64, 779–784.

Seiler, W., and Crutzen, P. J. (1980). Estimates of gross and net fluxes of carbon between the biosphere and the atmosphere from biomass burning. *Clim. Change* 2, 207–247. doi: 10.1007/BF00137988

Sharma, S., Ishizawa, M., Chan, D., Lavoué, D., Andrews, E., Eleftheriadis, K., et al. (2013). 16-year simulation of Arctic black carbon: transport, source contribution, and sensitivity analysis on deposition. *J. Geophys. Res. Atmos.* 118, 943–964. doi: 10.1029/2012JD017774

Shindell, D. T., Chin, M., Dentener, F., Doherty, R. M., Faluvegi, G., Fiore, A. M., et al. (2008). A multi-model assessment of pollution transport to the Arctic. *Atmos. Chem. Phys.* 8, 5353–5372. doi: 10.5194/acp-8-5353-2008

Soja, A. J., Fairlie, T. D., Westberg, M. D. J., and Pouliot, G. (2012). *Biomass burning plume injection height using CALIOP, MODIS and the NASA Langley Trajectory Model*. Available online at: https://www3.epa.gov/ttn/chief/conference/ei20/session7/asoja.pdf

Stein, A., Draxler, R., Rolph, G., Stunder, B., Cohen, M., and Ngan, F. (2015). NOAA's HYSPLIT atmospheric transport and dispersion modeling system. *Bull. Am. Meteorol. Soc.* 96, 2059–2077. doi: 10.1175/BAMS-D-14-00110.1

Stohl, A., Andrews, E., Burkhart, J. F., Forster, C., Herber, A., Hoch, S. W., et al. (2006). Pan-Arctic enhancements of light absorbing aerosol concentrations due to North American boreal forest fires during summer 2004. *J. Geophys. Res. Atmos.* 111:D22214. doi: 10.1029/2006JD007216

Stohl, A., Berg, T., Burkhart, J. F., Fjaeraa, A. M., Forster, C., Herber, A., et al. (2007). Arctic smoke - record high air pollution levels in the European Arctic due to agricultural fires in Eastern Europe in spring 2006. *Atmos. Chem. Phys.* 7, 511–534. doi: 10.5194/acp-7-511-2007

Treffeisen, R., Tunved, P., Ström, J., Herber, A., Bareiss, J., Helbig, A., et al. (2007). Arctic smoke–aerosol characteristics during a record smoke event in the European Arctic and its radiative impact. *Atmos. Chem. Phys.* 7, 3035–3053. doi: 10.5194/acp-7-3035-2007

USDA FAS (2016). *Foreign Agricultural Service. Russian Federation Grain and Feed Annual*. Gain Report number RS1617. Available online at: https://gain.fas.usda.gov/Recent%20GAIN%20Publications/Grain%20and%20Feed%20AnnualMoscowRussian%20Federation4-18-2016.pdf (Accessed Mar 11, 2017).

Warneke, C., Froyd, K. D., Brioude, J., Bahreini, R., Brock, C. A., Cozic, J., et al. (2010). An important contribution to springtime Arctic aerosol from biomass burning in Russia. *Geophys. Res. Lett.* 37:L01801. doi: 10.1029/2009GL041816

Wexler, H. (1953). "Radiation balance of the Earth as a factor in climatic change," in *Climatic Change*, ed H. Shapley (Cambridge, MA: Harvard University Press), 73–105.

Wiedinmyer, C., Akagi, S., Yokelson, R. J., Emmons, L., Al-Saadi, J., Orlando, J., et al. (2011). The Fire INventory from NCAR (FINN): a high resolution global model to estimate the emissions from open burning. *Geosci. Model Dev.* 4:625. doi: 10.5194/gmd-4-625-2011

Winiger, P., Andersson, A., Eckhardt, S., Stohl, A., Semiletov, I. P., Dudarev, O. V., et al. (2017). Siberian Arctic black carbon sources constrained by model and observation. *Proc. Natl. Acad. Sci. U.S.A.* 114, E1054–E1061. doi: 10.1073/pnas.1613401114

Conflict of Interest Statement: The authors declare that the research was conducted in the absence of any commercial or financial relationships that could be construed as a potential conflict of interest.

frontiers in Earth Science

ORIGINAL RESEARCH
published: 27 August 2018
doi: 10.3389/feart.2018.00126

Contribution of Saharan Dust to Ion Deposition Loads of High Alpine Snow Packs in Austria (1987–2017)

Marion Greilinger[1,2], Gerhard Schauer[3], Kathrin Baumann-Stanzer[3,4], Paul Skomorowski[3,4], Wolfgang Schöner[5] and Anne Kasper-Giebl[2]*

[1] Climate Monitoring and Cryosphere, Central Institution for Meteorology and Geodynamics, Vienna, Austria, [2] Environmental and Process Analytics, Institute of Chemical Technologies and Analytics, Vienna University of Technology, Vienna, Austria, [3] Sonnblick Observatory, Central Institution for Meteorology and Geodynamics, Salzburg, Austria, [4] Environmental Meteorology, Central Institution for Meteorology and Geodynamics, Vienna, Austria, [5] Institute of Geography and Regional Research, University of Graz, Graz, Austria

We investigate the influence of Saharan dust on the chemical composition and deposition loads of a 31-year long snow chemistry data set (1987–2017) of high alpine snow packs situated close to the Sonnblick Observatory, a global GAW (Global Atmospheric Watch) station, in the National Park Hohe Tauern in the Austrian Alps. Based on the snow pack of the winter accumulation period 2015/2016, when two Saharan dust events were visible by a reddish color of the snow, we define a pH > 5.6 together with a Ca^{2+} concentration > 10 μeq/l as thresholds to identify Saharan dust affected snow layers. This criterion is checked with an intercomparison with trajectories and on-line aerosol data determined at the Sonnblick Observatory. This check was extended to the accumulation periods 2014/2015 and 2016/2017 before the whole time series is investigated regarding the contribution of Saharan dust to ion deposition loads. Especially Mg^{2+}, Ca^{2+}, and H^+ depositions are strongly affected by Saharan dust input causing, as average values across the 30 years period, increased Mg^{2+} (25%) and Ca^{2+} (35%) contributions of affected snow layers, while the contribution to the snow water equivalent was only 11%. For H^+ Saharan dust affected snow layers show a much lower contribution (2%) while the contribution of other ions is well comparable to the deposition amount expected according to the snow water equivalent of affected snow layers. The pH range of Saharan dust affected snow layers covers 5.58–7.17, while the median value of all samples is 5.40. The long term trends of ion deposition are not affected by the deposition of Saharan dust.

Keywords: mineral dust, Saharan dust, snow chemistry, high alpine snow pack, deposition loads

OPEN ACCESS

Edited by:
Pavla Dagsson-Waldhauserova, Agricultural University of Iceland, Iceland

Reviewed by:
Silvia Becagli, Università degli Studi di Firenze, Italy
Dragana S. Đorđević, University of Belgrade, Serbia

****Correspondence:***
Marion Greilinger
marion.greilinger@zamg.ac.at

Specialty section:
This article was submitted to Cryospheric Sciences, a section of the journal Frontiers in Earth Science

Received: *07 March 2018*
Accepted: *10 August 2018*
Published: *27 August 2018*

Citation:
Greilinger M, Schauer G, Baumann-Stanzer K, Skomorowski P, Schöner W and Kasper-Giebl A (2018) Contribution of Saharan Dust to Ion Deposition Loads of High Alpine Snow Packs in Austria (1987–2017). Front. Earth Sci. 6:126. doi: 10.3389/feart.2018.00126

INTRODUCTION

Deserts serve as a major source for aerosols in the atmosphere with mineral dust as a main contributor to primary aerosol mass. Especially the Sahara, the largest desert in the world, contributes roughly half of the primarily emitted aerosol mass found in the atmosphere and is thus the world's largest source for Aeolian soil dust (Prospero, 1996; Goudie and Middleton, 2001 and references therein). Once in the atmosphere, desert dust can be transported over thousands of kilometers via synoptic wind patterns to regions far beyond (e.g., Prospero, 1996; Moulin et al., 1997). Online aerosol measurements conducted since 2013 at Austria's high alpine Sonnblick

Observatory, listed as a global station within the Global Atmospheric Watch Program of the World Meteorological Organization, suggest up to 30 days per year with the influence of mineral dust. Due to the predominant contribution of dust origination from the Sahara the term Saharan dust will be used within this paper. Transported dust can be removed from the atmosphere through wet and dry deposition processes.

If dust is deposited on mountain snow packs it causes several direct and indirect effects. Firstly, Saharan dust deposited onto snow surfaces decreases the albedo due to a darkening of the surface and consequently higher absorption of solar radiation, leading to an earlier removal of the snow cover or increased glacier melt-off (Goudie and Middleton, 2001; Field et al., 2010). This triggering of faster and earlier melt-off due to the dust deposition can potentially result in a lower total and less late-season water supply (Field et al., 2010) due to melt-off already during the season. This is especially important in areas where water supply is scarce. A more recent study of Gabbi et al. (2015) investigated the long-term effect of snow impurities, mainly Saharan dust and Black Carbon, on albedo and glacier mass balance and found that their presence lowered the albedo by 0.04–0.06, thereby increasing melt by 15–19% and reducing the mean annual mass balance.

Secondly, dust plays an important role in the control of global and regional biogeochemical cycles. These effects have been studied mostly in seawater or the Amazonas basin. For seawater especially P and Fe are supposed to be the main actors to estimate the contribution of atmospheric inputs stimulating the productivity of oceanic plankton, thus accelerating CO_2 uptake and stimulating N_2-fixation (Gruber and Sarmiento, 1997; Field et al., 2010; Schulz et al., 2012). For the Amazonas basin, Swap et al. (1992) and Rizzolo et al. (2017) showed that especially Fe^{3+}, Na^+, Ca^{2+}, K^+, and Mg^{2+} are the main constituents introduced via Saharan dust, acting as fertilizer or micronutrients essential for plant growth by offsetting the losses of nutrients due to leaching or weathering of the soil. Many other studies propose the significant influence of Saharan dust on microbiology, nutrient supply, acid neutralization and geochemistry in Europe as well. Avila et al. (1998) for example found that red rains, indicating Saharan dust influence, are important for biogeochemical consequences of a Holm oak forest in Catalonia, Spain, due to addition of nutrient elements such as K^+, Ca^{2+}, and Mg^{2+} and input adding to the neutralizing capacity of the soils in the catchment. The effect of Saharan dust on high alpine snow biogeochemistry is still poorly investigated although many studies propose that the ionic composition and deposition load of snow is of high biogeochemical interest because snow serves as interface where the water and nutrient cycle interact (De Angelis and Gaudichet, 1991; Kuhn, 2001). Marchetto et al. (1995) just showed that for alpine lakes in areas of low weathering rocks, such as silicate rocks also present at the site investigated in this study, lake chemistry, including acidity and alkalinity, is mainly determined by atmospheric deposition. Additionally it is well known that Saharan dust alters the chemical composition and neutralizing capacity of precipitation and, if deposited, also of snow packs and thus influences surface water chemistry (De Angelis and Gaudichet, 1991; Rogora et al., 2004). If the chemical composition of high alpine snow packs is investigated the main ions analyzed generally are Cl^-, SO_4^{2-}, NO_3^-, NH_4^+, Na^+, K^+, Mg^{2+}, Ca^{2+} as well as the pH and conductivity. Their origin can be assigned to different sources like anthropogenic sources, sea salt or mineral dust (Maupetit and Delmas, 1994). Greilinger et al. (2016) who analyzed the long-term series of snow chemistry data used in this study found three different clusters of ions representing different types of origin. Thereby one cluster representing mineral dust sources was found, positively correlated with Ca^{2+} and Mg^{2+} together with a negative correlation for H^+, representing the alkaline characteristics of mineral dust. Findings are comparable to results from Maupetit and Delmas (1994). It can be proposed that increased Ca^{2+} and Mg^{2+} concentrations change the chemical characteristics of the samples, especially the pH value.

Thirdly, Aeolian dust and as such also Saharan dust, is used by microorganisms to disperse and colonize new habitats. It is assumed, that microorganisms that are able to survive in the harsh conditions of the Sahara and the atmosphere during transport may also be able to colonize other sites with comparably challenging conditions such as the high Alps (Chuvochina et al., 2011) or the Himalaya (Zhang et al., 2008). It has been shown in a recent study of Weil et al. (2017) that those microbial dust passengers introduced to high alpine snow packs via Saharan dust can favor a rapid microbial contamination of sensitive habitats after snowmelt.

Due to the described effects of Saharan dust on mountain snow packs, the main purpose of this paper is to investigate the intensity and frequency of Saharan dust deposited in high alpine snow packs via a retrospective evaluation of a unique high alpine snow chemistry data set of 31 years (1987–2017) and to quantify the impact of these events on the deposition load.

According to Psenner (1999), who investigated the relevance of airborne dust like Saharan dust for the ecology of alpine lakes, an interdisciplinary research is necessary to elucidate the impact of dust on ecological issues. An estimation of the contribution of Saharan dust to the chemical variability of the ecosystems is not easy due to lack of quantitative studies in remote areas but cannot be neglected when dealing with acidification and recovery processes. Thus, our study provides relevant input for further investigations and conclusions, and indicates that the stochastic occurrence of Saharan dust deposition is on the long run a constant factor influencing the terrestrial and aquatic ecosystem of the Alpine region.

MEASUREMENTS AND METHODS

The study area, sampling, and measurement techniques as well as data quality issues are thoroughly described in Greilinger et al. (2016) and are only summarized shortly in this section.

Study Area

Snow profiles were sampled at the Goldbergkees (GOK), a remote glacier field, part of the Goldberggruppe at an elevation of more than 3,000 m.a.s.l. (**Figure 1**) close to the Sonnblick Observatory, listed as a global station within the Global

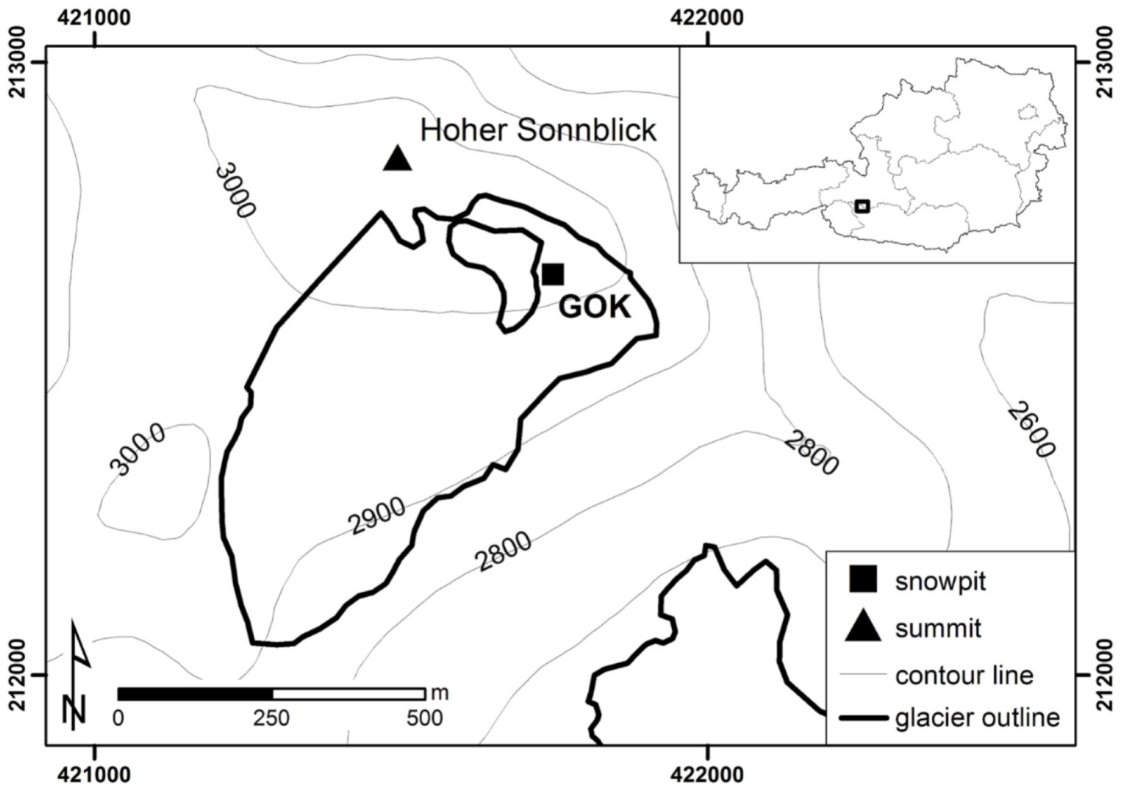

FIGURE 1 | Location of the Goldberggruppe in Austria, the sampling site Goldbergkees (GOK) on a glacier field in the Eastern Alps and of the mountain summit Hoher Sonnblick where the meteorological observatory is situated.

Atmospheric Watch Program of the World Meteorological Organization. The site is not exposed to any local anthropogenic influence.

Snow Sampling and Chemical Analysis

Snow samples representing the whole winter accumulation period are taken annually in a vertical resolution of 10 cm increments just prior to the start of significant snowmelt (usually at the end of April or the beginning of May). Just in 1997 the size of the increments was 40 cm. Note that the respective increments could either represent a portion of a single precipitation event or include mixed information of several events, depending on precipitation amount and settling of the snow cover. After digging a snow pit until the horizon when winter accumulation had started snow samples were taken with a stainless steel cylinder and stored in polyethylene bags. To avoid contamination of the samples gloves and a mask were used during sampling. Samples were taken to the lab frozen and were analyzed immediately after thawing. Analytical protocols changed slightly during the period of observation, but quality assurance was maintained by regular participation in the laboratory intercomparison of the World Data Center for Precipitation Chemistry (Global Atmosphere Watch). Conductivity and pH were determined electrochemically using a conductivity cell and a glass electrode, respectively. Anion (chloride, nitrate and sulfate) and monovalent cation (sodium, potassium, ammonium) concentrations were determined by suppressed ion chromatography. Bivalent cation (calcium, magnesium) concentrations were determined by atomic absorption spectroscopy until 1993, and only later by ion chromatography. Limits of detections (LODs) changed slightly during the years but were in the range of 0.01 and 0.015 mg/L for all ions and years, aside from sulfate and the time period until 1993, when a LOD of 0.029 mg/L was obtained. More details are given in Winiwarter et al. (1998) and Greilinger et al. (2016) including data quality control, outlier discussion and general presentation of the data.

Trajectory Analysis

In meteorology trajectories are defined as the paths of infinitesimally small particles of air. Such an air parcel, 'marked' at a certain point in space at a given time, can be traced forward or backward in time along its trajectory. In this study, air mass trajectories are calculated using the Flextra model (Stohl et al., 2001) based on meteorological data provided by ECMWF (European Centre for Medium Range Weather Forecast) with a horizontal resolution of 0.2°. The trajectories are starting from Sonnblick Observatory eight times per day (00UTC, 03UTC, 06UTC, 09UTC, 12UTC, 15UTC, 18UTC, and 21UTC) and trace the path of the air parcel backward in time for the previous 96 h, giving an indication where the major part of the air mass came from.

Aerosol Measurements

Aerosol sampling is performed via a heated (+20°C) whole air inlet designed according to GAW guidelines, with an upper size cut of 20 μm at a wind speed of 20 m/s. Details about the setup are given in Schauer et al. (2016). Episodes with a dominant influence of dust are continuously identified via the optical properties of the aerosol and the corresponding calculation of the wavelength dependence of the Single Scattering Albedo (SSA) according to Coen et al. (2003). Therefore a three-wavelength polar Nephelometer (Aurora 4000, Ecotech) was used for the determination of the light scattering coefficients at 450, 525, and 635 nm. Absorption coefficients were determined with an Aethalometer (AE33, Magee Scientific) at seven wavelengths, i.e., 370, 470, 525, 590, 660, 880, and 940 nm. A detailed description of the respective calculations can be found in Schauer et al. (2016). Based on this identification and on particulate matter (PM) concentrations a "dust index" is calculated on a routine base. A positive DI is reported when an influence of dust is identified for at least eight half hourly means during the day with a PM concentration above 5 $\mu g/m^3$. Mass concentrations of particulate matter are determined via a combination of nephelometry and β-attenuation (Sharp 5030, Thermo Scientific).

RESULTS

Several studies (e.g., Maupetit and Delmas, 1994; Greilinger et al., 2016) investigated the qualitative source assignments of high alpine snow packs using principal component analysis (PCA) and identified a factor related to Ca^{2+}, Mg^{2+} and the pH, being indicative for a marked contribution of Saharan dust. However, to get quantitative information on the contribution of Saharan dust to the respective ion composition or annual deposition loads the investigation of single snow layers is essential.

Identification of Saharan Dust Affected Snow in the Snowpack of the Winter Accumulation Period 2015/2016

Chemistry of the Snow Pack GOK2016

In the snowpack representing the winter accumulation period from September 2015 to April 2016 (=GOK2016), reddish colored snow layers where observed during sampling in about 120–160 cm depth (compare picture of the snow pack in **Figure 2**). Still, this depth has to be regarded as an approximate value and can be inaccurate by about 10–15 cm. This is because sampling is performed in an up to 2 m wide snow pit and the actual sampling of the 10 cm increments might be 0.5–1 m off the position where the depth, the snow morphology and also the color were determined. This "red snow," along the lines of "red rain" as used by Avila et al. (1998), is interpreted as an indicator of long-range transport of mineral dust, most likely originating from the Sahara. Although the color can vary from yellowish to brownish and up to now reddish, we stick to the term "red snow" throughout the paper.

To identify potential Saharan dust affected snow by chemical analysis, we build on a 2-step approach based on Rogora et al. (2004). They investigated a 15- to 20-year long time series of rain water chemistry data of Northwest Italy and grouped rain events in acid and alkaline events with a pH of 5.6 as the threshold, representing the pH of pure water equilibrated with atmospheric CO_2. Although a pH of 5.6 still represents acid conditions, the samples denoted as "alkaline" feature comparable high pH. Within this work we will use the same notation as Rogora et al. (2004) and denote "alkaline increments" to 10 cm sample increments featuring pH > 5.6. After the identification of the alkaline events, Rogora et al. (2004) characterized Saharan dust episodes, as a subgroup of the alkaline events, via a high Ca^{2+} and alkalinity content, but no strict values are given for this classification.

Using the pH > 5.6 threshold we identified five alkaline increments of 10 cm (**Table 1**). This is one more (350–360 cm) than visually identified as "red snow." These alkaline increments can be further distinguished via their chemical composition. Either an elevated Ca^{2+} concentration often accompanied by increased concentration of the other ions, representing a Saharan dust influence, or an increased NH_4^+ concentration most likely associated to anthropogenic sources in agriculture (Greilinger et al., 2016) was noted. Both, Ca^{2+} and NH_4^+ act as important neutralizing agents for the anions SO_4^{2-} and NO_3^- (Das et al., 2005). The chemical composition of all 10 cm increments is given in **Table 1** and **Figure 2** (right).

Ca^{2+} and Mg^{2+} concentrations of the increments 130–140 cm, 140–150 cm, and 350–360 cm were all above the 87th percentile. The 160–170 cm increment showed elevated concentrations as well, but concentrations of NH_4^+ and NO_3^- were much more pronounced than Ca^{2+} and are the highest observed for the whole snow pack. The pH was actually just slightly above the threshold of 5.6. The 150–160 cm increment showed markedly elevated concentrations of NH_4^+, NO_3^- and SO_4^{2-}, and just slightly elevated Ca^{2+} concentrations. Based on these results we can separate the alkaline increments in one fraction dominated by increased Ca^{2+} concentrations (increments from 130 to 140 cm, 140 to 150 cm, and 350 to 360 cm) and one fraction dominated by increased NH_4^+ concentrations (150–160 cm). As the 160–170 cm increment is featuring both characteristics highest concentrations for NH_4^+ and NO_3^-, but also elevated concentrations of Ca^{2+}, it cannot be clearly assigned to one of the two categories.

Taking 10 μeq/l as threshold (higher than the 85th percentile, close to the arithmetic mean of 8.9 μeq/l and below the concentrations of the six samples showing the upper and detached range of the frequency distribution) four 10 cm increments (130–140 cm, 140–150 cm, 160–170 cm, and 350–360 cm) can be classified as affected by Saharan dust in the 2015/2016 snow pack. This fits nicely to the classification of the alkaline increments given above as it does not include the one from 150 to 160 cm, dominated by increased NH_4^+ concentration. Furthermore the increment at the bottom of the snow pack (350–360 cm) is identified, although it was not visible as 'red snow.' For completeness we want to point out that two increments show Ca^{2+} concentrations higher than 10 μeq/l but a pH less than 5.6. Thus the combination of the pH criterion and the Ca^{2+} threshold is mandatory.

TABLE 1 | Ion concentrations, pH, conductivity, and ion sum of every single 10 cm increments of the snow pack from the accumulation period September 2015 to April 2016.

Snow depth (cm)	Ion concentration (μeq/l)									Σ ions (μeq/l)	pH	Conductivity (μS/cm)
	Na^+	NH_4^+	K^+	Mg^{2+}	Ca^{2+}	Cl^-	NO_3^-	SO_4^{2-}	H^+			
0–10	5.96	16.38	2.25	1.46	5.63	5.20	14.09	6.02	2.67	59.66	5.39	9.19
10–20	1.43	39.19	0.72	0.81	5.20	1.53	21.44	14.24	3.77	88.33	5.24	13.36
20–30	1.28	42.99	0.87	0.74	4.21	1.70	22.49	21.31	4.32	99.91	5.17	17.63
30–40	1.56	3.29	0.59	0.16	0.64	1.46	2.00	2.74	5.08	17.52	5.10	4.02
40–50	0.62	0.83	0.22	0.05	0.27	0.45	0.28	0.74	2.43	5.89	5.21	1.91
50–60	0.63	0.76	0.22	0.10	0.53	0.57	0.69	0.68	2.43	6.61	5.21	2.23
60–70	0.85	0.38	0.31	0.07	0.38	1.01	0.63	1.35	4.16	9.14	5.18	1.94
70–80	0.99	1.99	0.34	0.62	1.98	1.01	2.26	1.51	3.23	13.93	5.29	2.13
80–90	0.88	7.39	0.21	0.40	0.73	1.15	5.86	2.08	4.68	23.38	5.24	3.36
90–100	0.50	12.89	0.15	0.27	0.73	0.60	9.07	2.95	4.79	31.95	5.23	4.56
100–110	0.58	11.55	0.22	0.26	0.55	0.95	6.09	1.75	4.03	25.98	5.29	3.66
110–120	0.41	12.60	0.34	0.65	1.26	0.44	7.02	1.82	2.92	27.46	5.43	3.55
120–130	3.54	14.53	1.24	2.21	6.29	3.56	6.47	2.87	3.69	44.40	5.43	4.91
130–140	**16.89**	**22.94**	**2.92**	**13.40**	**171.51**	**19.64**	**28.23**	**33.70**	**0.07**	**309.30**	**7.17**	**28.80**
140–150	**2.77**	**17.11**	**0.56**	**3.44**	**40.87**	**3.32**	**14.01**	**6.43**	**0.32**	**88.83**	**6.49**	**8.38**
150–160	**1.82**	**29.59**	**0.38**	**1.15**	**5.17**	**1.91**	**19.40**	**5.00**	**1.86**	**66.28**	**5.73**	**6.27**
160–170	**5.20**	**47.98**	**1.10**	**3.90**	**24.42**	**3.72**	**41.33**	**16.67**	**2.05**	**146.37**	**5.74**	**13.02**
170–180	0.74	10.50	0.37	0.28	1.35	0.89	8.09	4.09	6.34	32.65	5.25	3.07
180–190	2.83	4.25	0.77	1.43	11.72	2.30	8.06	7.40	5.44	44.20	5.33	3.87
190–200	0.66	4.96	0.08	0.29	0.52	0.92	3.28	0.60	4.96	16.27	5.37	1.04
200–210	2.06	8.16	0.47	0.97	4.18	1.88	5.91	3.27	4.28	31.18	5.40	2.64
210–220	2.29	4.71	0.38	0.97	11.75	2.03	5.81	3.00	7.61	38.55	5.15	3.84
220–230	0.36	2.92	0.18	0.14	0.96	0.27	5.95	2.27	10.92	23.97	5.04	3.80
230–240	0.47	2.46	0.18	0.49	2.93	0.61	7.53	2.05	9.30	26.02	5.11	3.31
240–250	0.37	3.75	0.16	0.44	3.17	1.03	6.57	1.21	6.05	22.75	5.25	2.31
250–260	0.37	7.21	0.22	0.12	1.02	0.49	9.64	1.75	7.79	28.61	5.14	3.70
260–270	0.32	1.08	0.08	0.30	2.38	0.45	2.77	0.46	12.20	20.04	5.00	3.73
270–280	4.41	1.89	1.34	1.31	6.15	4.61	5.57	1.42	8.84	35.54	5.14	3.64
280–290	3.42	3.41	0.67	1.29	3.53	3.55	8.27	2.51	12.81	39.46	5.01	5.10
290–300	1.03	1.16	0.37	0.32	1.96	1.81	3.66	1.17	6.72	18.20	5.29	1.45
300–310	1.12	1.73	0.42	0.56	2.51	1.73	4.71	1.70	12.69	27.17	5.03	3.74
310–320	0.65	1.36	0.24	0.67	4.41	0.96	4.78	1.76	5.41	20.24	5.40	1.32
320–330	0.49	1.59	0.07	0.67	2.45	0.63	5.79	1.04	6.45	19.18	5.20	2.45
330–340	0.80	3.74	0.16	0.59	2.30	0.98	7.01	1.41	6.45	23.44	5.20	2.70
340–350	0.30	4.47	0.08	1.52	7.20	0.42	5.06	1.25	4.19	24.49	5.44	1.28
350–360	**0.35**	**2.75**	**0.08**	**1.90**	**11.57**	**0.49**	**3.89**	**2.09**	**0.70**	**23.82**	**6.22**	**1.12**
360–370	0.51	2.08	0.19	0.12	1.07	0.73	2.39	1.41	7.97	16.47	5.13	2.37
370–380	0.28	1.01	0.07	0.12	0.48	0.33	3.38	0.20	5.39	11.26	5.30	0.99
380–390	0.46	2.98	0.34	0.32	0.92	0.70	1.92	1.17	8.08	16.89	5.21	1.71
390–400	0.46	4.65	0.09	0.15	0.79	0.67	2.35	1.12	7.21	17.49	5.26	1.55
Min	0.28	0.38	0.07	0.05	0.27	0.27	0.28	0.20	0.07	5.89	5.00	0.99
1st quantile	0.47	1.97	0.18	0.27	0.89	0.61	3.36	1.24	3.58	18.03	5.17	2.08
2nd quantile	0.77	4.00	0.33	0.58	2.42	1.00	5.89	1.79	5.02	25.24	5.25	3.46
Mean	1.77	9.13	0.49	1.12	8.89	1.92	8.09	4.16	5.51	41.07	5.36	4.74
3rd quantile	1.88	11.81	0.57	1.19	5.31	1.89	8.14	3.07	7.31	38.78	5.39	4.16
Max	16.89	47.98	2.29	13.40	171.51	19.64	41.33	33.70	12.81	309.30	7.17	28.80

Bold values represent the alkaline increments using a pH > 5.6 for identification.

Comparison With Backward Trajectories and Aerosol Measurements

Based on the recording of precipitation events and snow height measurements the increments affected by Saharan dust can roughly be assigned to respective time periods. To confirm the influence of Saharan dust during these time periods backward trajectories and on-line aerosol measurements are used.

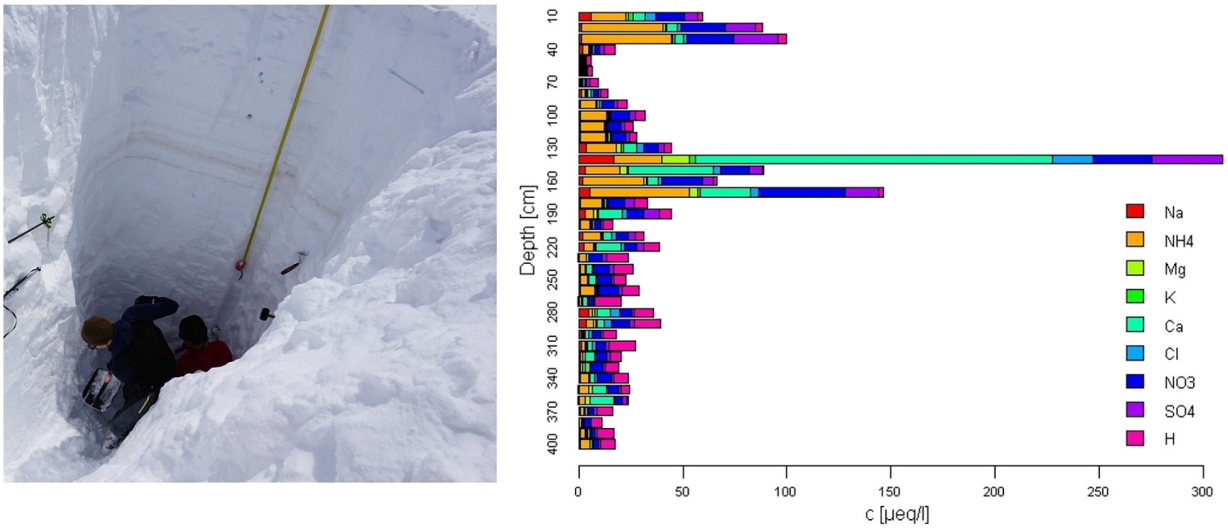

FIGURE 2 | (Left) Picture of the snow pack where the reddish Saharan dust snow layer in a depth of 120–140 cm is clearly visible. **(Right)** Chemical composition of every 10 cm increment of the whole snow pack showing Saharan dust layers from 120 to 180 cm with increased ion concentrations of especially Ca^{2+}.

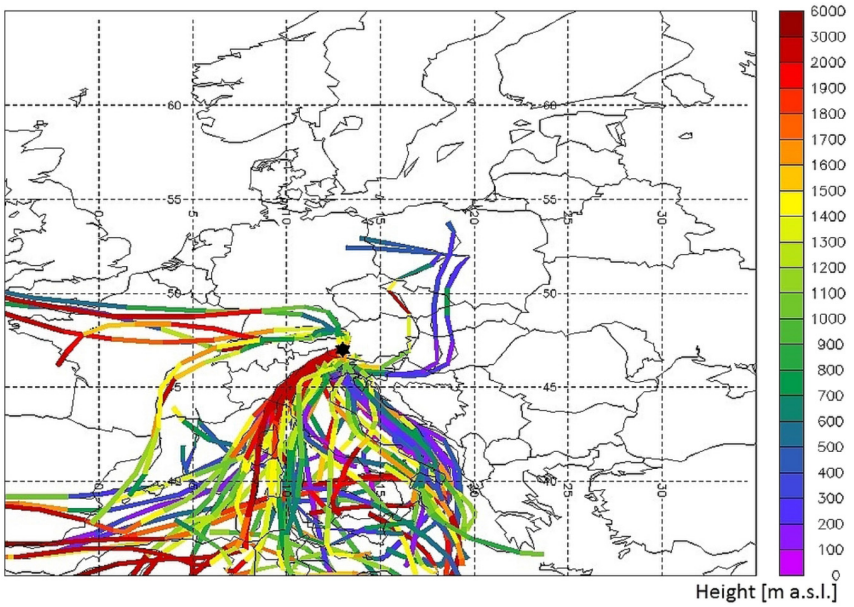

FIGURE 3 | Ninety-six hours backward trajectories starting from the Sonnblick Observatory every 3 h between 31 March 2016 00UTC and 8 April 2016 21UTC. Trajectories from the South reveal that Saharan dust occurrence at the sampling site during that time is very likely.

The 10 cm increments from 130 to 150 cm and 160 to 170 cm represent precipitation events occurring in spring and can be assigned to a strong Saharan dust event in April, which is documented by backward trajectories for the period from 31 March 2016 00UTC until 8 April 2016 21UTC given in **Figure 3**. The frame of the image includes only the coastal area of Egypt and Tunisia and not the Sahara as such because the high resolution meteorological data of the ECMWF (horizontal resolution of 0.2°) is not available further south. Backward trajectories running southward out of the frame and descending from high altitudes are highly likely to come from the Sahara. On-line aerosol measurements at Sonnblick Observatory indicate that this event can be separated in two episodes. The first episode lasts from 31 March until 3 April 2016 and the second one, which was three times stronger regarding the mass concentration of particulate matter starting at 4 April 2016. Due to wind drift accumulation and precipitation, causing a slight increase in snow height in-between the episodes (measured by an automatic ultrasonic sensor next to the sampling site and shown in **Supplementary Figure 1**) it is plausible that they are separated in the snow

TABLE 2 | Years and depth where visible red snow was recorded in handwritten protocols and photographs during sampling and associated snow sample increments featuring a pH > 5.6 and a Ca^{2+} concentration of >10 μeq/l.

	Year	Depth recorded in protocols (cm)	Depth of snow sample increments (cm)	Ca^{2+} > 10 μeq/l
1	1987	80–84	75–85	+
2	1987	130	115–125	+
3	1987	370	365–375	+
4	1991	106–109	100–110	+
5	1992		210–220	+
6	1993	Snow surface	–	
7	1994	27–32	20–30 and 30–40	+
8	1995	290–292	280–290	+
9	1995	351–351.5*	–	–
10	1996	9–10	10–20	+
11	1996	130–140	130–140	+
12	1996	220–230	210–220	+
13	1997	368–370**	–	–
14	1997	377–381**	–	–
15	1997	520–527	500–540	+
16	2000	234–240	230–240	+
17	2003	240–241	240–250	+
18	2007	200	210–220	+
19	2012	150	150–160	+
20	2014	95–100	90–100	+
21	2014	184–189	180–190	+
22	2016	120–130	130–140	+
23	2016	130–140	140–150	+

**Indicates that there is a note in the metadata that Saharan dust was not continuously present. **Indicates that in 1997 the height of the sampling increments was 40 cm, leading to a loss of information due to dilution. The pH of these layers was 5.48, hence they slightly missed the pH-criterion.*

cover by one 10 cm increment. The 350–360 cm increment, showing an increased pH and a slight increase in the ion sum and Ca^{2+} concentration, represent snow samples from autumn (November and possibly also December 2015), which were concentrated in this depth due to an almost stable snow cover height during this time. Backward trajectories as well as on-line aerosol measurements indicate an influence of Saharan dust, though much lower than in spring 2016, during several days in November and December 2015 (**Supplementary Figures 2–4**) and thus justify the chemical identification of this increment.

Concluding, reasonable agreement of the identification of Saharan dust episodes between backward trajectories, aerosol measurements and the snow pack was obtained. This allows to extend the presented approach to the entire data set to retrospectively identify Saharan dust affected samples of snow packs back until 1987.

Retrospective Identification of Saharan Dust Layers

For 12 years (1987, 1991–1997, 2000, 2003, 2014, and 2016) hand written records reveal the presence of visible red snow in the respective snow pack. Besides, photographs of the snow packs are available since 2004, except for 2015. They show red snow for the years 2007, 2012, 2014, and 2016. Thus in total 23 layers within 14 years feature visually present red snow (listed in **Table 2**). Their position within the snow pack is reported in the column named "depth recorded in protocols." The respective depth of affected increments identified via the pH and Ca^{2+} criterion is also reported in **Table 2** in the column "depth of snow sample increments." Thereby it is important to mention that the recorded snow depth need not correspond exactly to the sample increments of the same layer due to variations in the snow pit as described earlier. Additionally it is possible, that the Saharan dust layer (SDL) is split into two 10 cm sample increments or that it is much thinner than the sample increment, both leads to a dilution of the concentration in the affected layer.

Table 2 shows that 19 out of the 23 layers with red dust identified by visual inspection are identified using the pH > 5.6 and Ca^{2+} > 10 μeq/l thresholds. Reasons for this mismatch can be easily given. In 1995 it was recorded that the colored layer was not continuously present across the width of the snow pit. Hence it is not contradicting that Ca^{2+} concentrations were not markedly elevated. In 1997 sample increments were 40 cm instead of 10 cm, leading to a dilution and thus to a poorer sensitivity of the analytical approach. The respective increment showed a pH value of 5.48 which is only slightly lower than the used threshold of 5.6. In 1993 Saharan dust was visible on the snow surface but the respective increment only matched the Ca^{2+} criterion but, with a pH of 4.78, not the pH criterion. Maybe other influences on the surface (e.g., snow surface–air interactions) do play a role for the pH. Excluding those layers from the evaluation all recorded red dust layers could be verified by the chemical analysis.

The total data set covers 28 years of snow pack data (1987–2017, except 1988, 1989, and 1990 due to missing values for bivalent cations) and comprises 1,163 chemically analyzed 10 cm increments. Increments which were identified to feature Saharan dust input are here named as "SDLs," although they do not necessarily represent different stratigraphic layers or single events. Based on the chemical information we find 394 alkaline layers (equal to 34% of the whole data set) using the pH criterion only. For comparison, the mean pH of all samples is 5.44 with 75th percentile and 90th percentile values of 5.70 and 6.15, respectively. Including the Ca^{2+} criterion this number of layers decreases to 104 (equal to 9% of the whole data set or 26% of the alkaline layers) with pH values ranging from 5.58 to 7.17. As it was the case for the GOK2016 snow pack there are more sample increments chemically identified as SDLs than samples showing a visible appearance of red snow. More precisely we find five times more based on chemistry compared to the visual identification.

Some validation can be given for the accumulation periods 2014/2015 and 2016/2017, as back trajectories and on-line aerosol data are available for these years as well. In both years, no red snow was visible, but in case of the 2016/2017 period (GOK2017) one SDL was chemically identified in the lower part of the snow pack. Backward trajectories indicate the influence of Saharan dust in October 2016 and also two much weaker episodes in spring 2017 (compare **Supplementary Figures 5** and **6**). Complementary on-line aerosol measurements yielded a positive dust index during the respective time periods. Thus the SDL identified in the bottom part of the snow pack much likely represents the event in October 2016. The spring events in February and March 2017 are, using the present methods, not identified in the snow pack. Still sample increments which can be assigned to the relevant time period meet the pH criterion and show a Ca^{2+} concentration of 9.72 μeq/l, i.e., only slightly below the threshold of 10 μeq/l. Within the snow pack of the 2014/2015 accumulation period (GOK2015) no SDLs were chemically identified. Again backward trajectories and on-line aerosol data shows some influence during early winter at the end of November and beginning of December 2014 (**Supplementary Figure 7**), which is not reflected in the lowest part of the snow pack. This seems surprising, but snow height measurements revealed the absence of wet deposition during these events. During spring time the situation was similar to the conditions described for the GOK2017 and the GOK2016 snow pack. A Saharan dust influence occurred in March 2015 (backward trajectories given in **Supplementary Figure 8**) and the respective sample increments again meet the pH criterion, but were slightly below the 10 μeq/l Ca^{2+} threshold (Ca^{2+} concentration of 9.48 μeq/l). This intercomparison suggests that it is most likely that no overestimation of SDLs occurs when the criteria defined within this paper are used. Weak events might even be missed. Furthermore the influence of Saharan dust, and not just a general influence of mineral dust, is likely for all identified events.

In literature markedly higher Ca^{2+} values can be found to identify Saharan dust affected samples. Maupetit and Delmas (1994) report a value of 23.8 μeq/l for alkaline snow samples collected in the French Alps. A Ca^{2+} threshold of 20 μeq/l was also used by Schwikowski et al. (1999) to classify ice core data from an Alpine ice core (Colle Gnifetti). Of course these concentrations are strongly driven by the respective accumulation rates and thus can vary from site to site. Still we want to elucidate how sensitive the classification is to respective thresholds. If we would use a threshold of 20 μeq/l, the recovery in the chemical analysis of the visually identified reddish SDLs would decrease. Consequently the number of identified SDLs of the whole data set including all increments (not only the visually noticeable ones) decreases as shown in **Table 3**. Despite this decreasing trend the snow pack still experiences an impact of Saharan dust during more than half of the years when the 20 μeq/l criterion is used. Regarding only years with more than one identified layer (reflecting a repeated or longer lasting Saharan dust influence) more than two-thirds of the years are affected when the 10 μeq/l Ca^{2+} threshold is used. This number decreases to about one-third for the higher threshold. Obviously the level of the threshold influences the number of detected SDLs as well as years affected, but, as will be shown later, the respective deposition loads are affected much less.

TABLE 3 | Overview and seasonality of the number of Saharan dust layers (SDLs) using different Ca^{2+} thresholds of 28 years of snow pack data (1987–2017, missing data in 1988, 1989, and 1990).

	Ca^{2+} > 10 μeq/l	Ca^{2+} > 20 μeq/l
Total years investigated	28	28
Total amount of analyzed increments	1,163	1,163
Total amount of alkaline layers (pH > 5.6)	394	394
Years with minimum one SDL	26	16
Years without SDLs	2	12
Years with more than one SDL	19	8
SDLs via pH > 5.5 and Ca^{2+} threshold	104	45
SDLs in fall (September to November)	32	17
SDLs in winter (December to February)	48	19
SDLs in spring (March to April)	24	9

If the snowpack is subdivided into the different seasons of fall (September to November), winter (December to February) and spring (March and April) according to Greilinger et al. (2016), it seems as if the most Saharan dust events occur during winter (**Table 3**). This result seems surprising, since a clear fall and spring maximum can be found for Saharan dust in the atmosphere (Coen et al., 2003). Possible explanations are that potential events occurring in September might have been melted away or that they occurred without snowfall, remained airborne and were thus not deposited in or on the snow pack. Besides, during September rain is still very likely at the sampling site which might wash away already deposited Saharan dust on the snow or glacier surface or enables a deposition with rain due to rain water run-off. Events occurring in May, still accounting to the spring maximum given in Coen et al. (2003), were not captured in the snow pack analysis due to sampling end of April, latest beginning of May. Also the snow water equivalent is on average much higher for the winter period (mean over the period 1987–2017 of 663 mm) compared to fall or spring (mean over the period 1987–2017 of 491 mm and 447 mm, respectively). Thus, a Saharan dust deposition during snowfall is more likely

TABLE 4 | Mean relative ion composition of the mean overall annual depositions (MOAD) including all layers, as well as for SDLs and non-SDLs separately using the 10 μeq/l Ca^{2+} threshold.

	Cl^-	NO_3^-	SO_4^{2-}	Na^+	NH_4^+	K^+	Mg^{2+}	Ca^{2+}	H^+
All	8.5%	18.1%	13.9%	9.6%	16.5%	2.6%	2.7%	15.6%	12.9%
SDLs	7.2%	13.3%	11.0%	7.6%	12.7%	2.4%	4.1%	39.6%	2.1%
Non-SDLs	9.1%	18.7%	14.3%	10.3%	16.5%	2.8%	1.9%	11.9%	14.4%

TABLE 5 | Mean overall annual depositions (MOAD) in meq/m^2 and snow water equivalent (SWE) in mm of all years (1987–2017) and all layers, SDLs and non-SDLs as well as the absolute and relative contribution of the respective ions.

		MOAD (meq/m^2)	SWE (mm)	Cl^-	NO_3^-	SO_4^{2-}	Na^+	NH_4^+	K^+	Mg^{2+}	Ca^{2+}	H^+
	All	70.2	1579	6.0	12.7	9.8	6.7	11.6	1.8	1.6	10.9	9.0
Ca > 10 μeq/l	SDLs	10.0	172	0.7	1.3	1.1	0.8	1.3	0.2	0.4	3.9	0.2
		(14%)	(11%)	(11%)	(10%)	(11%)	(11%)	(12%)	(11%)	(25%)	(35%)	(2%)
	Non-SDLs	60.5	1420	5.5	11.3	8.6	6.2	10.0	1.7	1.2	7.2	8.7
		(86%)	(89%)	(89%)	(90%)	(89%)	(89%)	(88%)	(89%)	(75%)	(65%)	(98%)
Ca > 20 μeq/l	SDLs	8.7	125	0.5	1.0	0.9	0.5	0.9	0.1	0.3	4.4	0.1
		(11%)	(8%)	(7%)	(7%)	(8%)	(7%)	(8%)	(5%)	(16%)	(32%)	(1%)
	Non-SDLs	70.9	1508	6.3	13.0	10.9	6.8	11.0	1.8	1.6	9.3	10.3
		(89%)	(92%)	(93%)	(93%)	(92%)	(93%)	(92%)	(95%)	(84%)	(68%)	(99%)

in winter than in fall or spring. The increased number of SDLs in winter is also biased by single years (e.g., 1996 and 2014) where a huge number of layers were identified, all occurring in the winter period.

Influence of Saharan Dust Layers on the Relative Ion Composition

The mean relative ion composition was calculated for all layers together as well as for SDLs and non-SDLs separately. Results are presented in **Table 4**. Note that non-SDLs account for 89% of the snow water equivalent (**Table 5**) and hence also for the majority of the analyzed snow layers and the water deposited.

The relative ion composition of non-SDLs is almost identic to the ion composition if all layers are considered. The ratio between the relative contributions of most of the single ions within non-SDLs to those of the entire snow pack is slightly above 1 aside from Mg^{2+} and Ca^{2+} showing ratios of 0.7 and 0.8, respectively.

For SDLs, the relative ion composition is different to the ion composition of the entire snow pack. Mg^{2+} is slightly increased with a ratio between the relative contributions of SDLs to those of all layers of 1.4, whereas Ca^{2+} is much more increased with a ratio of 2.5. H^+ is markedly lower in SDLs with a ratio of only 0.1 between the relative contributions of non-SDLs to those of all layers. Contributions of all other ions are slightly decreased in SDLs, compared to the contributions if all layers are considered, with ratios between 0.7 and 0.9.

Influence of Saharan Dust Layers on Mean Annual Ion Deposition Loads

Table 5 lists the mean overall annual deposition (MOAD, sum of all ions analyzed) as well as the mean annual deposition loads of the respective ions and the snow water equivalent of the complete data set (1987–2017), calculated via averaging the respective annual values. The same was performed for the contribution of the SDLs and the non-SDLs, calculated as sum over all SDL or non-SDL layers of the respective years and averaging these annual values. In addition to the absolute values the relative contributions of SDLs and non-SDLs to the overall "MOAD," to the snow water equivalent and to the deposition loads of the single ions are listed as percentage values given in parenthesis. Note that the sums of SDL and non-SDL deposition loads need not match the overall annual loads. This is due to the fact that years without any SDL were not considered when splitting annual averages into SDL and non-SDL contributions. This approach was taken to base the averages of SDL and non-SDL contributions on the same data set, i.e., the same years. This accounts for the year to year variability, which has to be expected and which is discussed later.

For most of the single ions the contribution of SDLs and non-SDLs to the mean annual deposition load is similar to the respective contribution of the snow water equivalent, ranging between 10–12% and 88–90%, respectively. This indicates, that the concentrations of these ions is almost similar between SDLs and non-SDLs. Only Mg^{2+} and Ca^{2+} show much higher contributions of SDLs (25% and 35%, respectively), whereas H^+ shows a much lower contribution of only 2% compared to the snow water equivalent.

Interestingly, the contributions of the deposition loads of single ions but also of MOAD to the entire data set do not vary a lot when the Ca^{2+} threshold is increased from 10 to 20 μeq/l (**Table 5**). At first this seems surprising as the number of identified increments did go down by a factor of three when the threshold was increased. Still the deposition load is very much driven by the maximum concentrations which usually largely exceed 20 μeq/l. Thus annual deposition loads are not very much affected by the different thresholds.

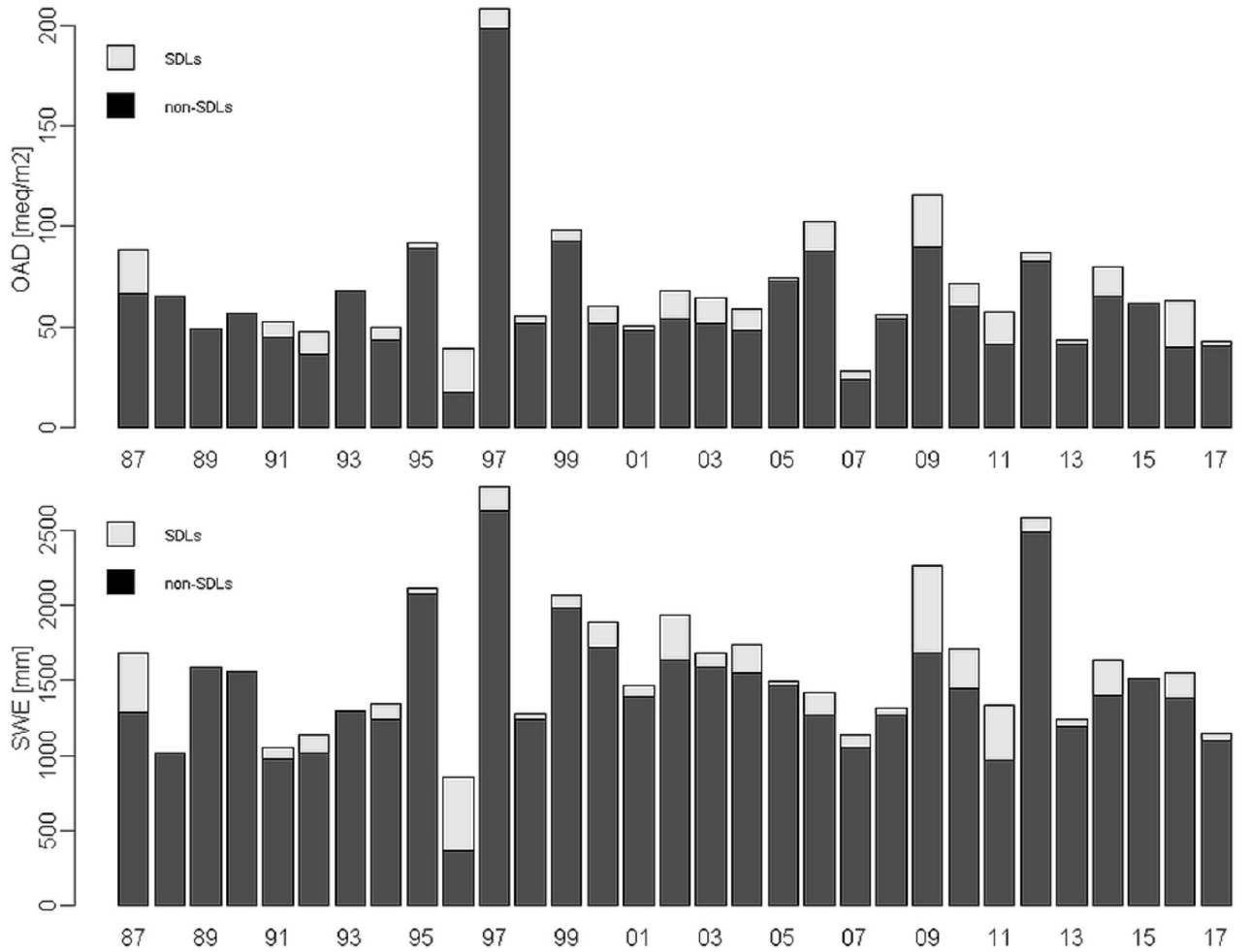

FIGURE 4 | Interannual variability of the overall annual deposition load including all ions (OAD) in meq/m^2 as well as of the snow water equivalent (SWE) in mm separated in the contribution of Saharan dust layers (SDLs) in gray and non-SDLs in black.

Interannual Variabilities of the Influence of Saharan Dust Layers on Ion Deposition

The interannual variability of the overall annual deposition load including all ions (OAD) as well as of the snow water equivalent is displayed in **Figure 4**.

The interannual variability of the OAD results for 9 of the 26 years with SD influence in a 13–19% contribution of SDLs whereas 2 years (1996 and 2016) show much higher contribution up to 55% and 36%, respectively (compare **Figure 4**). Likewise, also the annual depositions of the single ions show a high interannual variability with different trends. A detailed investigation of these annual trends, not quantifying the influence of deposited dust, can be found in Greilinger et al. (2016). Here results are exemplarily shown for Ca^{2+} and SO_4^{2-} in **Figure 5**. SO_4^{2-} depositions show a declining trend caused by decreasing emissions of sulfur dioxide (Greilinger et al., 2016). This trend is not altered if the deposition loads related to the deposition of SD would be deducted. Regarding the deposition of Ca^{2+} no significant time trend can be observed using the Mann-Kendall Test with a two-sided p-value below 5% for level of significance when the overall depositions are considered (Kendall's tau = 0.246 and 2-sided-p = 0.06). Also the contribution of SDLs to the annual Ca^{2+} deposition does not show any statistical trend (Kendall's tau = −0.119 and 2-sided-p = 0.38).

A boxplot shown in **Figure 6**, displaying the contribution of SDLs to the annual deposition of the single ions, reflects the interannual variability. The first box represents the interannual variability of the contribution of the SDLs to the annual snow water equivalent, showing a less than 10% for most of the years whereas outliers outside the upper whisker in the boxplot show 3 years where contributions were higher (1996, 2009, and 2011). In 1996 it was highest with 53%. Two years (1996 and 2006) were observed where all ions show a more than 25% contribution, for 1996 even more than 45%. For Ca^{2+} and Mg^{2+} more years were found with contributions of SDLs to the annual ion deposition load higher than 25%. For Ca^{2+} 16 years (1987, 1991, 1992,

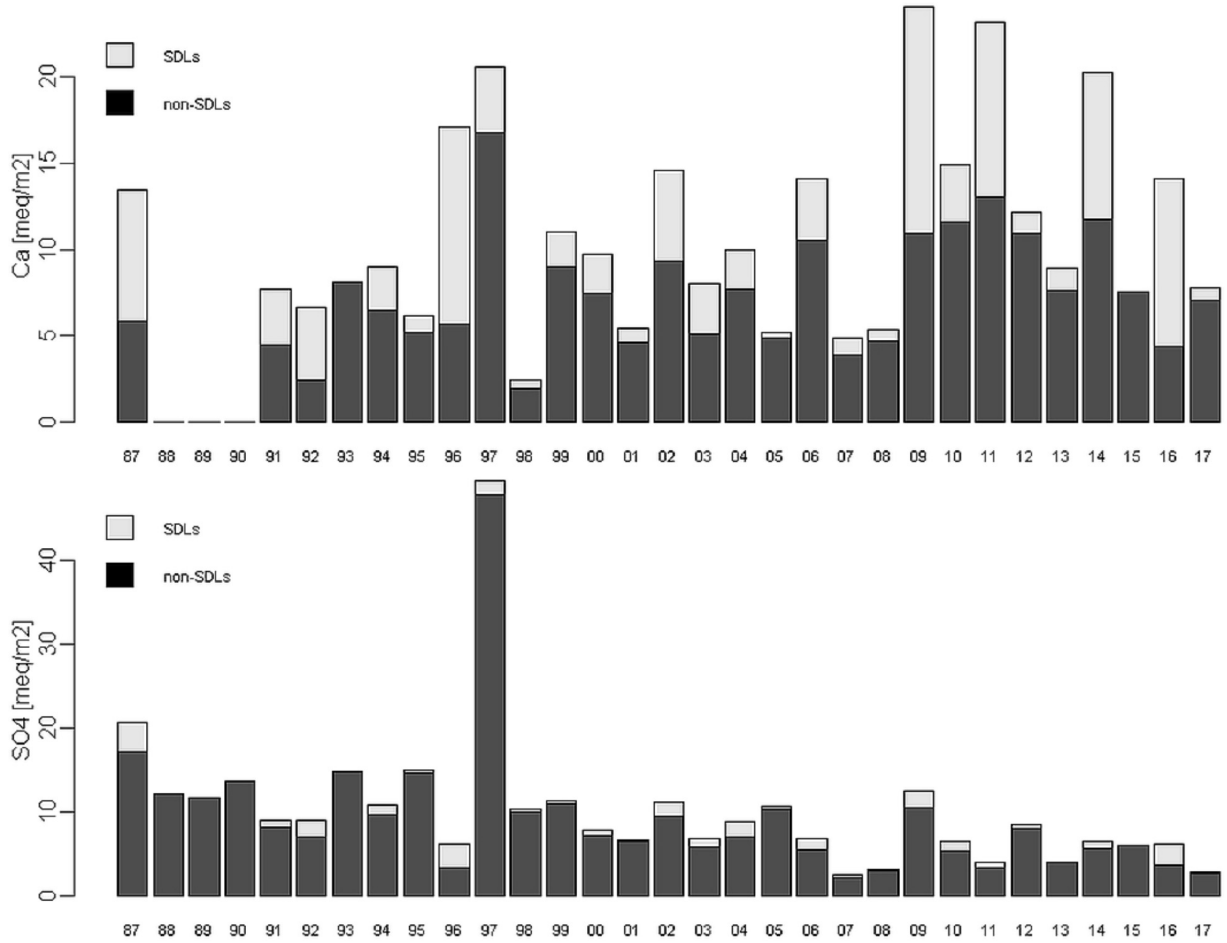

FIGURE 5 | Deposition of Ca^{2+} and SO_4^{2-} for all years of observation in meq/m^2 separated in the contribution of Saharan dust layers (SDLs) in gray and non-SDLs in black.

1994, 1996, 1998, 2000, 2002, 2003, 2004, 2006, 2007 2009, 2011, 2014, and 2016) where identified and five of these years (1987, 1992, 1996, 2009, and 2016) show contributions of more than 45%, in 1992, 1996, and 2016 even more than 60%. For Mg^{2+} 10 years (1987, 1991, 1996, 2001, 2002, 2003, 2007, 2011, 2014, and 2016) showed contributions above 25%, in 1987 and 2016 even more than 50%. Contributions for H^+ are always very low with maximum values of 5%. Contributions of single years (1996, 2004, 2009, and 2010) marked as outliers in **Figure 6** were higher with contributions of 33%, 18%, 14%, and 8%, respectively.

From these results we find 2 years, 1996 and 2016, which show remarkable high contributions of SDLs to the OAD as well as to the annual ion deposition. For both years red colored snow layers were already visually observed during sampling of the snow pack (**Table 2**) but the contribution of the SDLs to the annual snow water equivalent differ strongly with a contribution of 57% in 1996 but only 11% in 2016. This reveals, that in 1996 the contributions of SDLs to the annual ion deposition is high due to a high number of SDLs (12 layers) whereby the deposition load of these SDLs was not very high (Ca^{2+} concentrations between 15.0 and 42.7 μeq/l). In contrast to this, the high contributions of SDLs to the annual ion deposition in 2016 is associated to only three SDLs with very high Saharan dust input (Ca^{2+} concentrations of 24.4 μeq/l, 40.9 μeq/l, and 171.5 μeq/l).

The boxplot also underlines the main findings discussed before that the contribution of SDLs to the annual deposition loads is markedly different to the contribution of the snow water equivalent for Mg^{2+}, Ca^{2+}, and H^+ because these ions are most affected by Saharan dust. Regarding Cl^-, Na^+, and K^+, ions which are related to Saharan dust too but most likely have additional sources as well, the distributions are shifted to elevated contributions, but the differences to snow water equivalent are much less pronounced. The smallest influence can be seen for NO_3^-, SO_4^{2-}, and NH_4^+, but still 75th percentiles and whiskers reach up to markedly higher contributions of SDLs than can be expected due to the snow water equivalent of those layers.

DISCUSSION

In the following our results about the contribution of SDLs to the mean annual deposition loads are compared to those

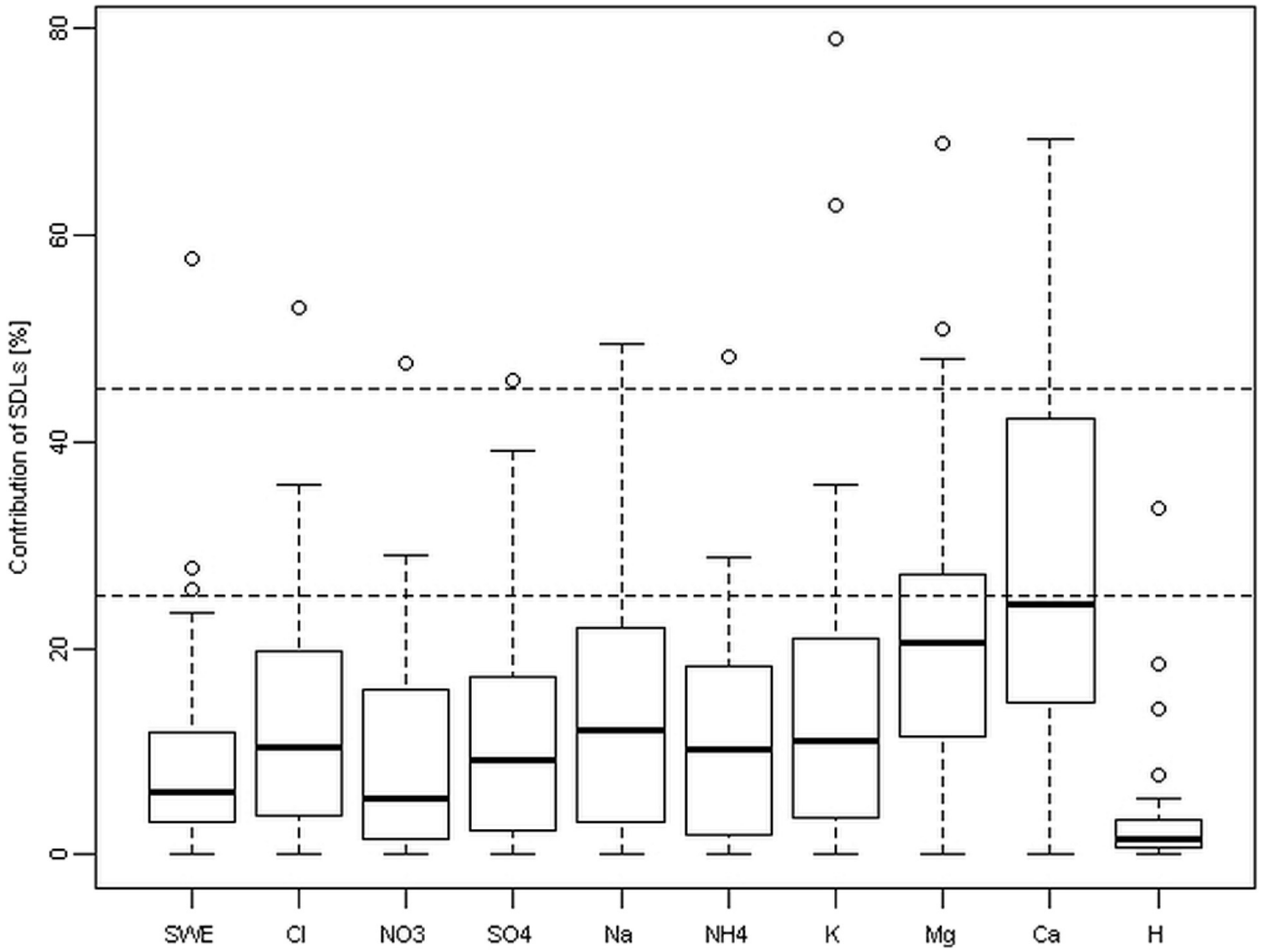

FIGURE 6 | Boxplot of the annual contributions of Saharan dust layers (SDLs) to the snow water equivalent (SWE) and the annual depositions of the single ions. The box represents the 25th and 75th percentile, the bold black line shows the median and whiskers extend to the most extreme data point which is no more than 1.5 times the interquartile range of the box. Dashed lines mark 25% and 45% contributions of SDLs.

of (Avila and Rodà, 1991), analyzing the dissolved nutrient amounts during red rains in Montseny Mountains, Spain from 1983 to 1988. They found that red rains are responsible for 46% Ca^{2+} input, between 20 and 25% for Na^+, K^+, Cl^-, and Mg^{2+} input and between 7 and 16% for SO_4^{2-}, NO_3^-, and NH_4^+ input featuring high interannual variability with coefficients of variations between 26 and 68% for the single ions. Still red rains contribute only 5% of the total annual precipitation for the study period, pointing to a higher relative influence of single events of red rains in Spain than in the present study. Rogora et al. (2004) report results on the impact of Saharan dust deposition on the long-term trends of atmospheric deposition in Italy from 1984 to 2002. They found that contribution of Saharan dust events to the annual precipitation amount was in average 10% whereas the mean contribution of the respective ions during these events where 43% Ca^{2+}, 20–24% of Mg^{2+}, Na^+, and Cl^- and 11–16% of NO_3^-, SO_4^{2-}, NH_4^+, and K^+, what is more similar to our results. Maupetit and Delmas (1994), investigating the snow chemistry of glaciers in the French Alps from 1989 to 1991, found alkaline samples to contribute 19% on average over all years, representing between 22 and 52% of the ionic load, with the highest amount for Ca^{2+}. Values of Maupetit and Delmas (1994) are highest, most likely due to the fact that they did not distinguish between alkaline samples originating from Saharan dust or from increased NH_4^+ concentrations, both acting as buffering agents. If no Ca^{2+} criterion would have been used in the present study the number of affected increments would have been more than threefold.

Regarding the nutrient input via Saharan dust the importance of Ca^{2+}, Mg^{2+}, and K^+ is mentioned in literature (e.g., Avila et al., 1998). Our data set shows that the input of Ca^{2+} and Mg^{2+} definitely is driven by long-range transport of mineral dust, while no marked effect becomes visible for K^+. In this case other sources, e.g., the more regional influence of combustion processes, are more important. The same is the case for Na^+, another ion, whose input could have been driven by mineral dust (e.g., Swap et al., 1992; Rizzolo et al., 2017).

Additionally to the influence of Saharan dust on ion deposition loads we suggest that Saharan dust in snow may

not only directly influence microbiology by acting as fertilizer and additional nutrient input to increase biomass but rather influences the metabolism, respiration, and productivity of microbes (Pulido-Villena et al., 2008; Reche et al., 2009; Schulz et al., 2012). In this respect, the changed acidity could be an important parameter as well. We found the pH to be distinctly different in SDLs compared to unaffected snow layers, providing distinctly different habitat conditions for microorganisms surviving within high alpine snow packs. Also the community diversity in high alpine snow is changed due to Saharan dust input (Zhang et al., 2008; Chuvochina et al., 2011). Due to the fact that Saharan dust introduces a variety of bacteria and microbial species to areas far away from their origin, it can be assumed that, especially in remote alpine snow, the accomplished input of Saharan dust simulate the natural habitat of those microbes so they can survive in very harsh and contrary conditions to their original habitat.

SUMMARY AND CONCLUSION

We investigated the intensity and frequency of Saharan dust deposited in high alpine snow retrospectively for a unique long-term data set of high alpine snow chemistry.

Based on a chemical criterion (pH $>$ 5.6 and Ca^{2+} concentration $>$ 10 μeq/l) we provide a robust method to identify SDLs within high alpine snow packs. Results for the use of a higher Ca^{2+} threshold (20 μeq/l) show, that it hardly affect the annual deposition loads whereas the number of identified layers goes down.

While contributions of SDLs and unaffected layers (10–12% and 88–89%, respectively) to the deposition load of Cl^-, NO_3^-, SO_4^{2-}, Na^+, NH_4^+, and K^+ is similar to the contribution of the snow water equivalent (11% and 86%, respectively), markedly elevated contributions of SDLs were observed for Mg^{2+} (25%) and Ca^{2+} (35%), while the impact of H^+ becomes negligible (2%). Also the relative ion composition in SDLs underlines the influence on Mg^{2+}, Ca^{2+}, and H^+.

Generally SO_4^{2-} depositions show a declining trend caused by decreasing emissions of sulfur dioxide but this trend is not altered if the deposition loads related to the deposition of Saharan dust would be deducted. Regarding the deposition of Ca^{2+} no significant time trend was observed at all.

Using the suggested Ca^{2+} threshold of 10 μeq/l, only 2 out of 28 investigated years without Saharan dust influence were observed. Two thirds of the affected years showed even more than one SDL. This is the case, although a 3-year comparison of the identified SDLs using backward trajectories and on-line aerosol measurements showed that we might miss weak events.

An estimation of the contribution of Saharan dust events to the chemical variability of the ecosystems is not easy due to lack of quantitative studies in remote areas but cannot be neglected. Our results provide relevant input not only on ion deposition loads. They can be used for further investigations and conclusions on the influence of Saharan dust on the albedo of snow and glacier surfaces, on the biogeochemistry of high alpine snow as well as on the microbiology of remote areas.

AUTHOR CONTRIBUTIONS

MG and AK-G conceived the study. MG processed the data and wrote the manuscript together with AK-G. GS performed and evaluated the aerosol sampling at the site and calculated the DI. KB-S and PS performed the backward trajectory analysis. WS was part of the team initiating the snow chemistry monitoring and ensuring ongoing sampling for most of the years. All co-authors commented on the results and on the manuscript content.

ACKNOWLEDGMENTS

The long-term monitoring was developed during the EUROTRAC-ALPTRAC Project and ongoing monitoring is financially supported by the BMLFUW. Thanks go to the members of the various sampling teams responsible for field work and colleagues conducting the chemical analysis during the nearly 31-year period. Furthermore, we would like to acknowledge the help from Claudia Flandorfer and Marcus Hirtl for WRFChem model simulations, Anton Neureiter for drawing the site map in GIS, Roland Koch for TAWES data and Daniela Kau for part of the analytical work regarding the GOK2016 data set. Aerosol measurements are carried out in cooperation with Umweltbundesamt. Finally we acknowledge the TU Wien University Library for financial support through its Open Access Funding Program.

SUPPLEMENTARY MATERIAL

The Supplementary Material for this article can be found online at: https://www.frontiersin.org/articles/10.3389/feart.2018.00126/full#supplementary-material

REFERENCES

Avila, A., Alarcón, M., and Queralt, I. (1998). The chemical composition of dust transported in red rains-its contribution to the biogeochemicl cycle of a holm oak forest in Catalonia (Spain). *Atmos. Environ.* 32, 179–191. doi: 10.1016/S1352-2310(97)00286-0

Avila, A., and Rodà, F. (1991). Red rains as major contributors of nutrients and alkalinity to terrestrial ecosystems at Montseny (NE Spain). *Orsis* 6, 215–229.

Chuvochina, M. S., Marie, D., Chevaillier, S., Petit, J.-R., Normand, P., Alekhina, I. A., et al. (2011). community variability of bacteria in alpine snow (mont blanc) containing saharan dust deposition and their snow colonisation potential. *Microbes Environ.* 26, 237–247. doi: 10.1264/jsme2.ME11116

Coen, M. C., Weingartner, E., Schaub, D., Hueglin, C., Corrigan, C., Schwikowski, M., et al. (2003). Saharan dust events at the Jungfraujoch: detection by wavelength dependence of the single scattering albedo and analysis of the events during the years 2001 and 2002. *Atmos. Chem. Phys. Discuss.* 3, 5547–5594. doi: 10.5194/acpd-3-5547-2003

Das, R., Das, S. N., and Misra, V. N. (2005). Chemical composition of rainwater and dustfall at Bhubaneswar in the east coast of India. *Atmos. Environ.* 39, 5908–5916. doi: 10.1016/j.atmosenv.2005.06.030

De Angelis, M., and Gaudichet, A. (1991). Saharan dust deposition over mont blanc (French Alps) during the last 30 years. *Tellus B* 43, 61–75. doi: 10.3402/tellusb.v43i1.15246

Field, J. P., Belnap, J., Breshears, D. D., Neff, J. C., Okin, G. S., Whicker, J. J., et al. (2010). The ecology of dust. *Front. Ecol. Environ.* 8, 423–430. doi: 10.1890/090050

Gabbi, J., Huss, M., Bauder, A., Cao, F., and Schwikowski, M. (2015). The impact of Saharan dust and black carbon on albedo and long-term mass balance of an Alpine glacier. *Cryosphere* 9, 1385–1400. doi: 10.5194/tc-9-1385-2015

Goudie, A. S., and Middleton, N. J. (2001). Saharan dust storms: nature and consequences. *Earth Sci. Rev.* 56, 179–204. doi: 10.1016/S0012-8252(01)00067-8

Greilinger, M., Schöner, W., Winiwarter, W., and Kasper-Giebl, A. (2016). Temporal changes of inorganic ion deposition in the seasonal snow cover for the Austrian Alps (1983–2014). *Atmos. Environ.* 132, 141–152. doi: 10.1016/j.atmosenv.2016.02.040

Grell, G. A., Peckham, S. E., Schmitz, R., McKeen, S. A., Frost, G., Skamarock, W. C., et al. (2005). Fully coupled "online" chemistry within the WRF model. *Atmos. Environ.* 39, 6957–6975. doi: 10.1016/j.atmosenv.2005.04.027

Gruber, N., and Sarmiento, J. L. (1997). Global patterns of marine nitrogen fixation and denitrification. *Glob. Biogeochem. Cycles* 11, 235–266. doi: 10.1029/97GB00077

Kuhn, M. (2001). The nutrient cycle through snow and ice, a review. *Aquat. Sci. Res. Boundaries* 63, 150–167. doi: 10.1007/PL00001348

Marchetto, A., Mosello, R., Psenner, R., Bendetta, G., Boggero, A., Tait, T., et al. (1995). Factors affecting water chemistry of alpine lakes. *Aquat. Sci.* 57, 81–89. doi: 10.1007/BF00878028

Maupetit, F., and Delmas, R. J. (1994). Snow chemistry of high altitude glaciers in the French Alps. *Tellus B Chem. Phys. Meteorol.* 46, 304–324. doi: 10.3402/tellusb.v46i4.15806

Moulin, C., Lambert, C. E., Dulac, F., and Dayan, U. (1997). Control of atmospheric export of dust from North Africa by the North Atlantic Oscillation. *Nature* 387, 691–694. doi: 10.1038/42679

Prospero, J. M. (1996). "Saharan dust transport over the North Atlantic Ocean and Mediterranean: an overview," in *Impact Desert Dust Mediterr*, eds S. Guerzoni and R. Chester (Alphen aan den Rijn: Kluwer Academic Publishers), 133–151. doi: 10.1007/978-94-017-3354-0_13

Psenner, R. (1999). Living in a dusty world: airborne dust as a key factor for alpine lakes. *Water Air Soil Pollut.* 112, 217–227. doi: 10.1023/A:1005082832499

Pulido-Villena, E., Wagener, T., and Guieu, C. (2008). Bacterial response to dust pulses in the western Mediterranean: implications for carbon cycling in the oligotrophic ocean: bacterial response to dust pulses. *Glob. Biogeochem. Cycles* 22:GB1020. doi: 10.1029/2007GB003091

Reche, I., Ortega-Retuerta, E., Romera, O., Villena, E. P., Baquero, R. M., and Casamayor, E. O. (2009). Effect of Saharan dust inputs on bacterial activity and community composition in Mediterranean lakes and reservoirs. *Limnol. Oceanogr.* 54, 869–879. doi: 10.4319/lo.2009.54.3.0869

Rizzolo, J. A., Barbosa, C. G. G., Borillo, G. C., Godoi, A. F. L., Souza, R. A. F., Andreoli, R. V., et al. (2017). Soluble iron nutrients in Saharan dust over the central Amazon rainforest. *Atmos. Chem. Phys.* 17, 2673–2687. doi: 10.5194/acp-17-2673-2017

Rogora, M., Mosello, R., and Marchetto, A. (2004). Long-term trends in the chemistry of atmospheric deposition in Northwestern Italy: the role of increasing Saharan dust deposition. *Tellus B Chem. Phys. Meteorol.* 56, 426–434. doi: 10.3402/tellusb.v56i5.16456

Schauer, G., Kasper-Giebl, A., and Močnik, G. (2016). Increased PM concentrations during a combined wildfire and Saharan dust event observed at high-altitude sonnblick observatory, Austria. *Aerosol Air Qual. Res.* 16, 542–554. doi: 10.4209/aaqr.2015.05.0337

Schulz, M., Prospero, J. M., Baker, A. R., Dentener, F., Ickes, L., Liss, P. S., et al. (2012). Atmospheric transport and deposition of mineral dust to the ocean: implications for research needs. *Environ. Sci. Technol.* 46, 10390–10404. doi: 10.1021/es300073u

Schwikowski, M., Döscher, A., Gäggeler, H. W., and Schotterer, U. (1999). Anthropogenic versus natural sources of atmospheric sulphate from an alpine ice core. *Tellus B Chem. Phys. Meteorol.* 51, 938–951. doi: 10.3402/tellusb.v51i5.16506

Stohl, A., Haimberger, L., Scheele, M. P., and Wernli, H. (2001). An intercomparison of results from three trajectory models. *Meteorol. Appl.* 8, 127–135. doi: 10.1017/S1350482701002018

Swap, R., Garstang, M., Greco, S., Talbot, R., and Kållberg, P. (1992). Saharan dust in the Amazon Basin. *Tellus B* 44, 133–149. doi: 10.1034/j.1600-0889.1992.t01-1-00005.x

Weil, T., De Filippo, C., Albanese, D., Donati, C., Pindo, M., Pavarini, L., et al. (2017). Legal immigrants: invasion of alien microbial communities during winter occurring desert dust storms. *Microbiome* 5:32. doi: 10.1186/s40168-017-0249-7

Winiwarter, W., Puxbaum, H., Schöner, W., Böhm, R., Werner, R., Vitovec, W., et al. (1998). Concentration of ionic compounds in the wintertime deposition: results and trends from the Austrian Alps over 11 years (1983–1993). *Atmos. Environ.* 32, 4031–4040. doi: 10.1016/S1352-2310(97)00252-5

Zhang, S., Hou, S., Wu, Y., and Qin, D. (2008). Bacteria in Himalayan glacial ice and its relationship to dust. *Biogeosci.* 5, 1741–1750. doi: 10.5194/bg-5-1741-2008

Conflict of Interest Statement: The authors declare that the research was conducted in the absence of any commercial or financial relationships that could be construed as a potential conflict of interest.

frontiers in Earth Science

ORIGINAL RESEARCH
published: 05 November 2018
doi: 10.3389/feart.2018.00187

Mineralogical and Chemical Records of Icelandic Dust Sources Upon Ny-Ålesund (Svalbard Islands)

Beatrice Moroni[1], Olafur Arnalds[2], Pavla Dagsson-Waldhauserová[2,3], Stefano Crocchianti[1], Riccardo Vivani[4] and David Cappelletti[1]*

[1] Department of Chemistry, Biology and Biotechnology, University of Perugia, Perugia, Italy, [2] Agricultural University of Iceland, Hvanneyri, Iceland, [3] Faculty of Environmental Sciences, Czech University of Life Sciences Prague, Prague, Czechia, [4] Department of Pharmaceutical Sciences, University of Perugia, Perugia, Italy

This work aims to identify the geochemical and mineralogical markers of Icelandic dust and to differentiate it from the dust of local origin deposited at the Ny-Ålesund station. We characterized representative sediment samples from Iceland and Svalbard and compared them to a set of aerosol samples collected in Ny-Ålesund to check the existence and type of the mineralogical markers. The sediment samples were analyzed by X-ray diffraction (XRD) to detect the mineralogical constrain of the geochemical markers. Both aerosol and sediment samples were examined by scanning electron microscopy coupled with EDS microanalysis (SEM-EDS) and image analysis to detect and to provide a morpho-chemical characterization of the mineralogical markers of dust provenance. Comparison between local and Icelandic sediments reveals the metal oxide particles as the most representative and distinguishing mineralogical/phase markers for Iceland dust sources. In particular, we have considered the magnetite-chromite and the magnetite-ülvospinel associations as marker facies of the tholeiitic magmatic series and the presence of volcanic glass as a further indicator of provenance from Iceland. The morphochemical characteristics of the metal oxide particles in the aerosol samples compared to those of the sediment samples have proved to be a powerful tool to separate Icelandic dust from other sources for dust. In particular, the small size, higher grain boundary complexity and lower Fe/Cr ratios suggest the influence of anthropogenic sources, well in accordance with the results of air mass backward trajectories which reveal a main contribution from industrialized areas in Eurasia. This study shows the reliability of the geochemical characterization of the metal oxide particles for the identification of the source regions of dust. In addition it provides an evidence that Icelandic dust can be transported long range to Svalbard confirming the importance of High Latitude Dust sources.

Keywords: atmospheric aerosol, Arctic region, loose sediment vs. aerosol samples, X-ray diffraction, scanning electron microscopy, mineral chemistry, metal oxide particles

OPEN ACCESS

Edited by:
Paolo Censi,
Università degli Studi di Palermo, Italy

Reviewed by:
Pierpaolo Zuddas,
Sorbonne Universités, France
Yigal - Erel,
Hebrew University of Jerusalem, Israel

****Correspondence:***
Beatrice Moroni
b.moroni@tiscali.it

Specialty section:
This article was submitted to Geochemistry, a section of the journal Frontiers in Earth Science

Received: *23 August 2018*
Accepted: *12 October 2018*
Published: *05 November 2018*

Citation:
Moroni B, Arnalds O, Dagsson-Waldhauserová P, Crocchianti S, Vivani R and Cappelletti D (2018) Mineralogical and Chemical Records of Icelandic Dust Sources Upon Ny-Ålesund (Svalbard Islands). Front. Earth Sci. 6:187. doi: 10.3389/feart.2018.00187

INTRODUCTION

The Arctic is experiencing a dramatic impact of the present climate change; an effect referred to as the 'Arctic amplification' (Serreze and Francis, 2006). The mechanisms of this phenomenon are not well established, but variations in the snow- and ice-covered areas, and the resulting albedo changes seem to play a primary role in the process (Screen and Simmonds, 2010; Serreze and Barry, 2011).

It has been suggested that mineral dust contributes to 'Arctic amplification' (Lambert et al., 2013). Light-absorbing particulate deposited on snow can reduce surface albedo and enhance the melting of snow and ice. Mineral dust can also affect the radiative forcing in the Arctic by scattering and absorbing solar and thermal radiation (direct effect), and by acting as condensation nuclei for ice and water droplets (indirect effect).

The primary identified High Latitude sources of dust reaching the Arctic are Alaska, Canada, Greenland, and Iceland (Bullard et al., 2016; Groot Zwaaftink et al., 2016; Meinander et al., 2016). Smaller high-latitude dust sources influencing the Arctic have been identified in Siberia, Kamchatka, and over the Svalbard Norwegian archipelago. The Svalbard dust sources comprise both natural sediments suspended from dry riverbeds and anthropogenic sources from coal mines, both activated at the end of the dry summer season (Dörnbrack et al., 2010).

Iceland, with its vast active dust emission areas, strong winds year round and high frequency of dust days is the most important and the best-studied high-latitude dust area in the Northern hemisphere (Arnalds et al., 2016; Bullard et al., 2016). Iceland is a volcanic province with intense eruptive activity generating fresh basaltic materials that are subjected to aeolian and glacial processes in extensive desert areas (Sigmarsson and Steinthórsson, 2007; Arnalds, 2010). Studies on global and regional air mass atmospheric circulation reveal a significant contribution from Iceland in the air masses reaching the Arctic (Groot Zwaaftink et al., 2016, 2017; Baddock et al., 2017; ; Kylling et al., 2018; **Figure 1**). Airborne measurements of Icelandic dust show a high proportion of submicron particles which are prone to travel long distances (Dagsson-Waldhauserova et al., 2014, 2016).

Despite these facts, studies assessing the mineralogical and the geochemical fingerprints of Icelandic dust are rare. Most of them focus on detritus matrices, both fresh and altered, collected in the proximity of the volcanic complexes (e.g., Baratoux et al., 2011). Other papers address the characterization of long-range transported volcanic ash emitted during the eruptions (e.g., Óladóttir et al., 2008). Volcanic ash, however, cannot be considered as dust since it is directly emitted in the atmosphere in few isolated events instead of being frequently uplifted from the surface.

This work aims to identify the geochemical and mineralogical markers of Icelandic dust and to differentiate it from the dust of local origin deposited at Ny-Ålesund (Svalbard). We have characterized representative sediment samples from Iceland and Svalbard and compared them to a set of aerosol samples collected in Ny-Ålesund in 2011 to check the existence and type of the mineralogical markers.

BACKGROUND, SAMPLES, AND METHODS

Geological Setting and Geomorphology

The Brøgger Peninsula

Ny-Ålesund is a Polar research town located on the Brøgger peninsula in Spitsbergen (**Figure 1**). The geology of the Brøgger peninsula (Dallmann, 2015) is characterized by a pile of thrust sheets of Permo-Carboniferous siliciclastic (sandstones and conglomerates) to carbonate (limestones and dolostones) rock formations with alternating shale levels. The thrust sheets overlie a pre-Devonian basement of low-grade metapelites (mica schists and phyllites) and marbles with minor gneissic units. In the Ny-Ålesund area, the stratigraphic sequence continues with Early Triassic dark shales overlain by a Palaeocenic succession of conglomerates, sandstones, and shales with exploitable coal seams.

Glacier retreat around the Kongsfjorden since the early-1900s has left behind large moraine fields. The loose sediments in the area of Ny-Ålesund consist of slope deposits, recent moraines, weathering material, and marine deposits. The deposits are of different extent and thickness and involve different bedrock types.

Iceland

Iceland is a volcanic island characterized by basaltic volcanic activity associated with about 30 active volcanic systems (Thordarson and Höskuldsson, 2008). Many of the most active systems are glaciated, such as the Katla, Grímsvötn, and Bárðarbunga systems. These lead to the formation of hyaloclastis by the interaction of magma and ice/water (e.g., Jakobsson and Gudmundsson, 2008), and rivers draining these glaciers are loaded with sediments made of poorly crystallized basaltic grains of tholeiitic and transitional alkaline composition (Jakobsson et al., 2008). The primary dust sources, reviewed by Arnalds et al. (2016) are often at glacial margins of the most active volcanoes, such as Dyngjusandur (Bárðarbunga volcanic system), Mýrdalssandur and Mælifellssandur (Katla volcanic system), and Skeiðarársandur (Grímsvötn volcanic system). These dust sources are capable of producing up to 1 M tons of basaltic dust in single storms under the most extreme conditions (Arnalds et al., 2014). Pyroxenes, plagioclases, and olivines usually dominate the mineralogy, however, often poorly crystallized and sometimes with "pure" volcanic glass (e.g., Jakobsson et al., 2008; Baratoux et al., 2011).

Loose Sediment Samples

Five samples from the low terraces near Ny-Ålesund, and three samples from "sandur planes" in Iceland are considered in this paper. These samples were chosen to represent a strictly local and a remote well-established dust sources, respectively. They do not, however, represent all the variety of the dust sources in the two regions.

The samples from Ny-Ålesund were collected on the outskirts of the research town in July 2015. Summer is the best period for sampling due to the best exposure and drier conditions

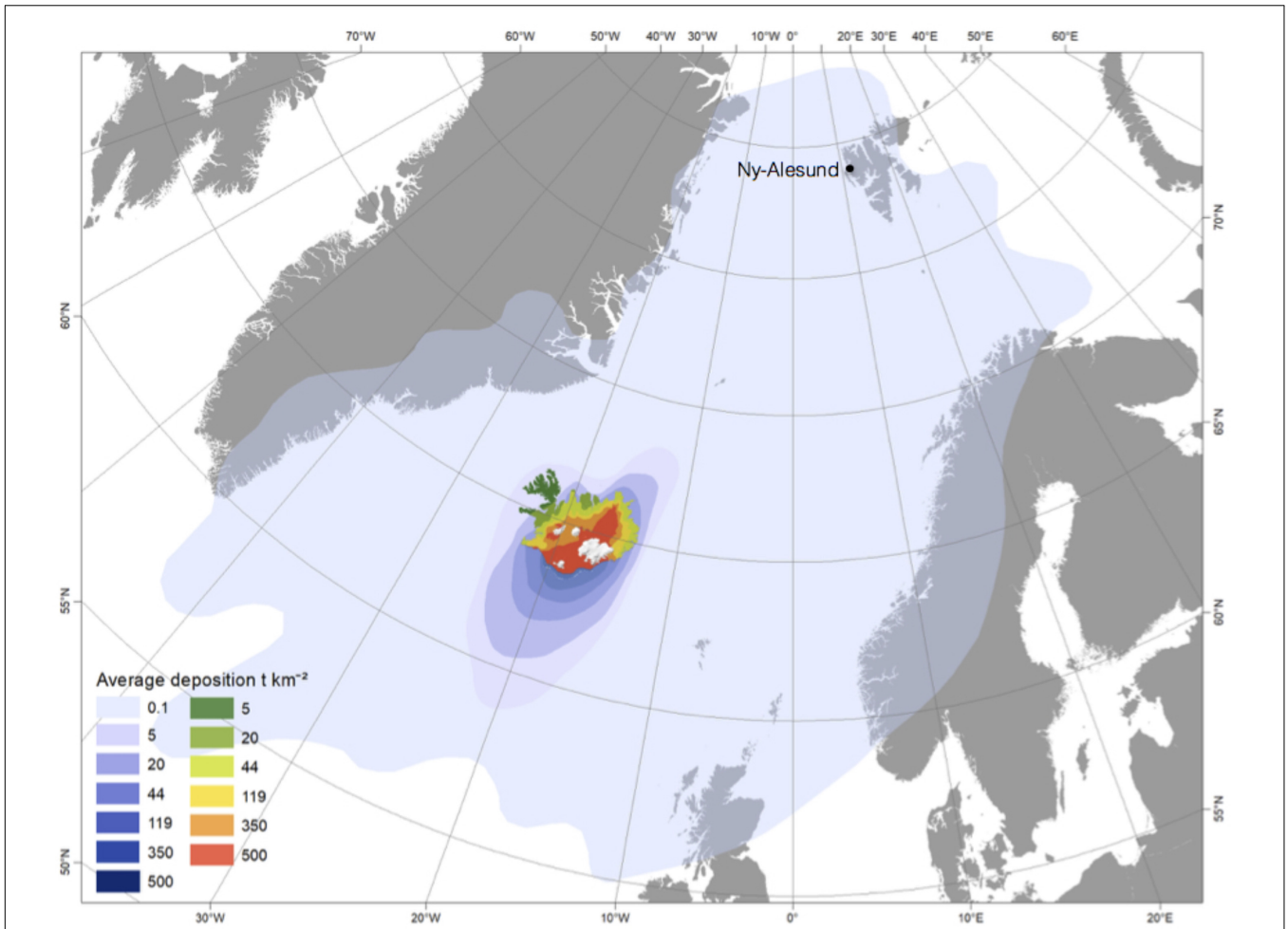

FIGURE 1 | Map of average distributions of dust and volcanic ash around Iceland with main dust sources in Iceland. The map is extended from the dust depostion map by Arnalds et al. (2014) including low dust deposition class from the calculations of Groot Zwaaftink et al. (2017).

of the ground surface after the strong drainage consequent to deglaciation. The samples are of different origin and nature as for the geological/stratigraphic features and the mechanisms of formation/deposition (**Table 1**).

The samples from Iceland were collected in three different sites in the southern and the north-eastern part of the island (**Table 1**). ICE1 refers to Mælifellssandur dust hot spot in South Iceland, a 50–60 km^2 unstable glaciofluvial highland plain at 550–650 m elevation. It was collected in 2013. ICE2 is a sample from Myrdalssandur, active 60 km^2 glacio-fluvial lowland plain under Katla volcano in South Iceland. ICE3 refers to Dyngjusandur in NE Iceland, the largest and most active of

TABLE 1 | Location of sediment sampling sites by Ny-Ålesund (NyA) and in Iceland (ICE).

Label	Latitude	Longitude	Elevation (asl)	Deposit Type
NyA 1	78° 55′ 27″ N	11° 53′ 46″ E	24 m	Short-transported weathering material (gelifluction deposit)
NyA 2	78° 54′ 36″ N	11° 59′ 50″ E	17 m	Short-transported slope deposit/ weathering material
NyA 3	78° 54′ 54″ N	12° 00′ 30″ E	1 m	Fluvial (braided river) deposit
NyA 4	78° 54′ 53″ N	11° 51′ 58″ E	38 m	Glaciofluvial/slope deposit
NyA 5	78° 55′ 10″ N	11° 50′ 13″ E	19 m	Fluvial (braided river) deposit
ICE 1[§]	63° 48′ 56″ N	19° 07′ 27″ W	650 m	Glaciofluvial dust hot-spot
ICE 2[§]	63° 32′ 18″ N	18° 42′ 19″ W	96 m	Glaciofluvial dust hot-spot
ICE 3[§]	64° 53′ 29″ N	16° 49′ 13″ W	756 m	Glaciofluvial dust hot-spot

[§]*All Icelandic samples are recently deposited fine glaciofluvial materials.*

the Icelandic dust sources, providing dust directly to the Arctic region (Dagsson-Waldhauserova et al., 2013). Dyngjusandur dust plumes extend several hundred km from the desert (Arnalds, 2010). The active aeolian sandsheet covered an area of 270 km^2 with up to 10 m thick sediments (Mountney and Russell, 2004), but new lava from the Holuhraun eruption in 2014–2015 covered about 85 km^2 of the surface. The sample was collected in 2016. Samples 1 and 2 originate from the Katla volcanic system, (transitional alkali basalt and poorly crystalline), sample 3 is from Dyngjusandur, dominated by the Bárðarbunga volcanic system (tholeiitic basalt and poorly crystalline, see Baratoux et al., 2011).

The sediments were dry sieved for grain size analysis using a stack of 11 sieves from 8 to 325 mesh (nominal sieve opening of 0.044, 0.088, 0.105, 0.297, 0.35, 0.50, 1.19, 1.41, 1.68, 2.00, and 2.38 mm). Results of the particle-size analysis revealed a variably sorted sandy granulometry for the Ny-Ålesund samples and a silty granulometry for the Iceland samples (**Figure 2**). Decreasing granulometry and increasing sorting generally follow the deposit type of the sediments from slope (low sorting) to fluvial (medium sorting) and glacio-fluvial (high sorting) sediment types.

After sieving the finest fraction of the sediment was splitted and passed over a shaking magnetic plate to retain the magnetic fraction. This latter operation was performed to obtain sediment enriched in the metal oxide particles.

Dust Emission and Air Mass Transport Activity

General Trend

The first estimates on dust emission production from Iceland range from 4 to 40 Mt per year of which about 7% can reach the high Arctic (>80 N, Arnalds et al., 2014; Groot Zwaaftink et al., 2017). Severe dust storms produce >300 000 t of dust, while the most severe wind erosion event reached aeolian transport of 11 t m^{-1}, about 1 million t of material transported during 24 h (Arnalds et al., 2013, 2014). Long-term dust frequency in Iceland based on synoptic weather codes resulted in 135 dust days per year in 1949–2011 with increasing trends in NE Iceland since 1990 (Dagsson-Waldhauserova et al., 2014).

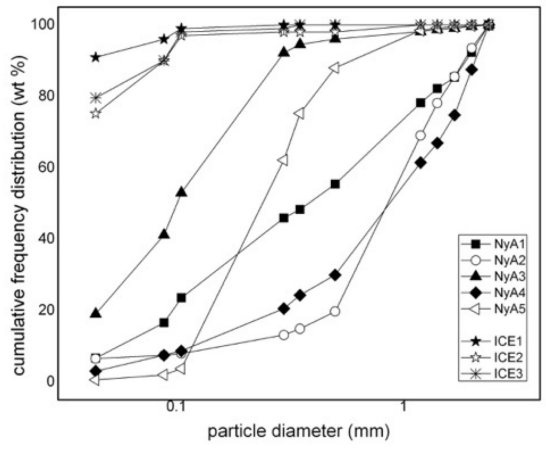

FIGURE 2 | Particle size distribution curves for the sediment samples from Ny-Alesund (NyA) and Iceland (ICE).

The Arctic dust events from the NE Iceland are typically warm, occurring during summer/autumn (May–September) under mild southwesterly winds, while the subarctic dust events from the S Iceland are mainly cold, occurring during winter/spring (March–May) and during strong northeasterly winds (Dagsson-Waldhauserova et al., 2014). About half of the dust events in S Iceland occurred in winter or at subzero temperatures. The main dust source for the NE Iceland is Dyngjusandur desert, while the most active dust sources in the S Iceland are Myrdalssandur, Landeyjarsandur, Hagavatn, and Maelifellssandur (Arnalds et al., 2016).

According to the established climatologies of the mean pressure distribution in the Arctic region (e.g., Liljequist, 1970), the trajectory climatology for Svalbard shows the North Atlantic and Eurasia as the main source regions of the air masses from winter to spring, and the Arctic region over Greenland, the North Atlantics (including Iceland) and the area surrounding Svalbard in the following period (Eneroth et al., 2003).

Phenomenologies in 2011

Long-term frequency of dust days in Iceland shows that the year 2011 was below average in dust days compared to the period 1949–2011 (Dagsson-Waldhauserova et al., 2014). Meteorological records of dust emission in 2011 report 21 dust days in NE Iceland and 69 dust days in the south of the island. In the northeast of Iceland, dust days occurred mainly in spring and summer with a peak in June and July. In southern Iceland, instead, the dust days mostly occurred in spring with highest numbers in April and May. That is in good accordance with the general trend obtained in the South Iceland (Prospero et al., 2012; Dagsson-Waldhauserova et al., 2014; Bullard et al., 2016). Duration of the dust events was quite different in the two sectors, namely in NE Iceland, a total of 11 out of 21 events lasted not about 3 h of the day whereas in S Iceland, a significant part of the dust events (28 out of 69 dust days) lasted more than half a day.

Results of back-trajectory (BT) analysis identify 23 days in 2011 characterized by air mass circulation passing over Iceland before reaching Ny-Ålesund. Six days were in winter (January and March), eight in spring (April), five in late summer (August to September), and four in winter (November). The winter air tracks affected the NW side of Iceland for up to 6 h during the day. The spring tracks passed over the S of Iceland and lasted 6 to 24 h while those in summer lapped the NW and SE coasts of the island for less than half a day and autumn tracks involved different sectors over the island and different time spans (6–24 h) over the day.

Combined evaluation of the dust emission and the BT data sets revealed April as the most favorable period for Icelandic dust advection over Svalbard due to the convergence between maximum frequency of dust events and maximum probability of air mass circulation over Iceland.

Aerosol Samples

Aerosol samples were collected at the Grüvebadet site, an Italian research facility located 800 m SW from the Ny-Ålesund

village. The station has been active since 2009 and is devoted to the study of the physical and chemical properties of the Arctic aerosol (Cappelletti et al., 2016). The site is equipped with a set of sampling devices (i.e., PM_{10} low and medium-volume samplers, four-stage and 12-stage impactors with daily and four-day resolution) operating with various filter media.

Aerosol samples were collected in the second half of April 2011. In particular, air mass BT analysis revealed an air mass circulation from North America passing over Iceland on both April 18 and 26, and circulation from the Arctic/Atlantic ocean with some part from Greenland and Iceland arriving in Svalbard on April 22 and 29 (**Figure 3**). Looking to the BT patterns, the contribution from Iceland to the dust load is expected to be high on April 26 when a channeled air flow originating in the Arctic ocean crossed the North American continent at high altitude before experiencing a steep descending motion over Iceland up to the Svalbard archipelago. On the other hand, the dust contribution from Iceland is expected to be low on April 18 for the presence of an atmospheric circulation from the Siberian coasts on that day. A mix of Greenland and Iceland contributions is expected to occur on April 22 and 29 when two distinct air mass circulations had passed at low height upon Greenland and Iceland before converging over Svalbard.

The desert Dyngjusandur in the NE Iceland was actively producing dust at the end of April 2011 (**Table 2**) and was responsible for the significant dust load observed in that period. The SYNOP codes from the weather station in Grimsstadir reported dust codes on April 30, but there was a gap in observations for the previous weeks. There is only one aerosol station in NE Iceland, which is located in Akureyri and provides PM_{10} concentrations. Although Akureyri is not located in the center of the pathways of dust storms from Dyngjusandur, it has captured episodes of increased PM_{10} on 14, 24, 26, and 27 April. BT analysis from Svalbard suggested that air parcels passing over NE Iceland on April 14, 24 and 26 reached Ny-Ålesund on April 18, 26, and 29, respectively. The BTs from Svalbard on April 22 passed South Iceland on April 18/19 when no dust was observed in Iceland. Dust was also detected at altitude 2–3 km above NE Iceland by CALIPSO on April 24/25 2011, shortly after the backward trajectory was passing Iceland. These are strong indications that Icelandic dust could have been transported to Svalbard during these periods.

The aerosol samples were collected 2 m above ground level using a DEKATI 4-stage (>10, 10–2.5, 2.5–1, <1 μm ranges) medium volume impactor (flow rate 29 L min^{-1}) operating with polycarbonate membranes (stages 1 to 3; Ø = 25 mm) and Teflon filters (stage 4; Ø = 47 mm). A progressive increase of the temperature characterized the synoptic conditions during sampling, relative humidity and pressure mean levels due to the orographically channeled wind. Sporadic to persistent cloud decks were also recorded at a different height above the ground level related to local orography and the persistent temperature inversion in the lower troposphere. A list of the samples with relevant features and corresponding environmental conditions is reported in **Table 3**.

X-Ray Powder Diffraction Spectroscopy

The phase composition of the sediment samples was investigated by X-ray powder diffraction (XRD) using a PANalytical X'Pert Pro diffractometer, with the Ni-filtered CuKα radiation (40 kV, 40 mA). The goniometer operated in Bragg-Brentano geometry and was equipped with an X'Celerator fast detector. Samples were grinded in an agate mortar and carefully sideloaded onto a zero-background sample holder. Data were collected in the 3 – 120° 2theta range using a 0.017° step scan and 100 s counting time.

Qualitative phase analysis was performed using the ICDD PDF2 database under the X'Pert Highscore software. The weight fraction of the amorphous component of the Icelandic samples was determined by an indirect method using a Rietveld refinement procedure: a weighed amount of fully crystalline internal standard (in this case silicon, about 10% w/w) was

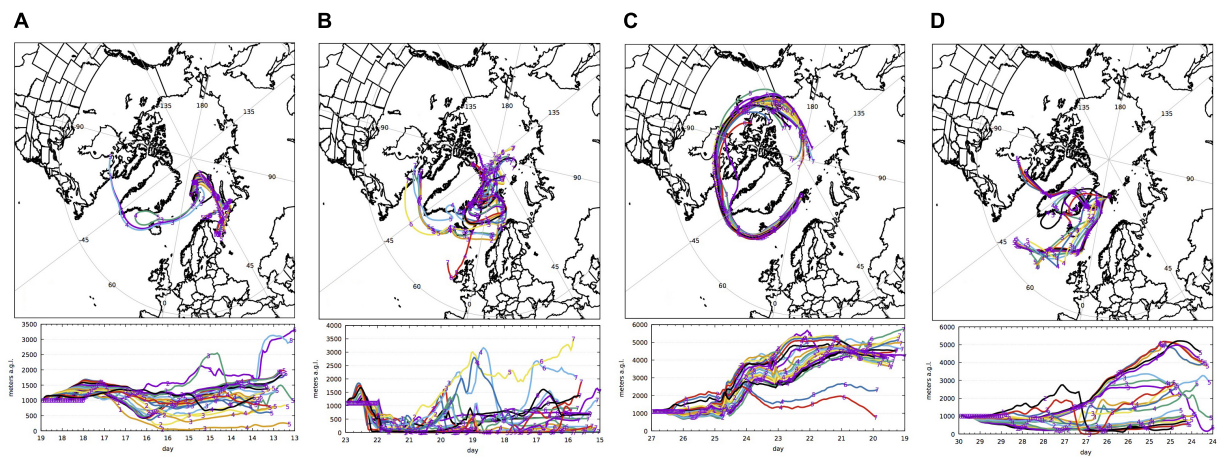

FIGURE 3 | Plots of 120 h back trajectories of April 18 **(A)**, 22 **(B)**, 26 **(C)**, and 29 **(D)**, 2011 ending at 1000 m a.g.l. (April 18 and 29) and at 1100 m a.g.l. (April 22 and 26) upon Ny-Ålesund.

TABLE 2 | Dates of dust days in Iceland and corresponding PM_{10} concentrations at Akureyri and dust load in Ny-Ålesund.

Date Svalbard sample	Trajectory passing Iceland	Increased PM_{10} Akureyri	PM_{10} hourly mean (μgm^{-3})	Ny-Ålesund daily PM_{10} (μgm^{-3})
18 April	14 April	YES	>40	3.77
22 April	18–19 April	NO	<10	5.65
26 April	24 April	YES	>70	10.74
29 April	26 April	YES	>100	n.d.
29 April	27 April morning	NO	>20	
29 April	27 April day	YES	>40	

TABLE 3 | Characteristics (time and duration) and environmental conditions of aerosol sampling.

Date	Time/duration (UTC)	T (°C)	RH (%)	WS (m/s)	WD	Visibility
18 April	15.20 / 4h	−9.0	52	5.0	NW	Clear sky
22 April	20.30 / 3h	−5.2	63	2.2	NW	Clear sky
26 April	16.30 / 4h	−0.4	60	0.6	NW	Clear sky
29 April	15.50 / 4h	−1.2	99	1.6	SE	Cloudy

added to the samples, and a quantitative phase analysis, with the Rietveld method, was performed. The procedure involved the refinement of scale factors, background, profile parameters, and if required, also a careful refinement of unit cell parameters, when little misfits between literature and experimental data were detected.

The refinement of scale factors per each crystalline phase allowed to determine the weight fractions of phases, referred to the crystalline fraction of samples. The knowledge of the added weight fraction of internal standard allowed to calculate the weight fractions referred to the whole sample, using the following equation:

$$x_{i,c} = x_i \frac{x_{s,w}}{x_s} \left(\frac{1}{1 - x_{s,w}} \right)$$

where $x_{i,c}$ is the recalculated actual weight fraction of phase i, x_i, and x_s are the refined weight fractions of phase i and the internal standard, respectively, and $x_{s,w}$ is the actual added weight of the internal standard. The weight fraction, x_a, of the amorphous component was then calculated following the method by Gualtieri et al. (2006):

$$x_a = 1 - \sum_i x_{i,c}$$

The patterns used for Rietveld refinements were collected in the 4 – 80° 2theta range using a 0.033° step scan and 3000 s counting time. Rietveld refienements were carried out using the GSAS software (Larson and von Dreele, 2001).

Scanning Electron Microscopy

Individual particle analyses were performed by scanning electron microscopy coupled with energy-dispersive X-ray microanalysis (SEM-EDS). The aerosol samples were prepared by cutting single portions (∼10 mm × 10 mm) from the central part of the polycarbonate sampling filters and mounting them on to SEM aluminum stubs using double-sided carbon tape. The loose sediment samples were prepared by mounting a small aliquot of the magnetically separated sediment directly onto the double-sided carbon tape. Both sample types were finally coated with a 100–150 Å carbon film to provide electrical conductivity and prevent charge build-up during the exposure to the electron beam.

Scanning electron microscopy imaging was performed using a ZEISS Supra 25 microscope equipped with a field emission gun and a GEMINI column employed at a variable voltage (0.5–15 kV) and magnification (500 to 350 000 ×) to distinguish particle types and textural details. The instrument is also equipped with an X-ray dispersive spectrometer (QUANTAX EDS microanalysis system coupled with ESPRIT software for data treatment). EDS spectra (spot size 5, working distance 8.5 mm) were collected for 90 s and the elemental composition obtained after standardless matrix correction provided by the ESPRIT software. Values lower than 0.1 wt% (SEM detection limit) were omitted.

Manually selected particles in the digitalized images underwent image analysis (IA) using the software Image Tool 3.0[1] and a set of morphological parameters for each particle grain was obtained. In particular, we consider the Feret diameter (FD) and the shape factor (SF). According to Russ (1995), the FD is the diameter of a circle having the same area as the object:

$$\mathrm{FD} = \sqrt{\frac{4\mathrm{A}}{\pi}}$$

while the SF is defined as the reciprocal of the roundness:

$$\mathrm{SF} = \frac{\mathrm{P}^2}{4\pi\mathrm{A}}$$

A and P are the area and the perimeter of the geometrical projection of a particle within the image. FD and SF, thus, provide a measurement of the mean grain size and the border complexity of grains, respectively. The analytical precision, obtained from triplicate measurements of selected particles at

[1] http://compdent.uthscsa.edu/dig/

different magnification (5000, 10000, and 20000×), is better than 2% for FD and better than 5% for the SF.

RESULTS AND DISCUSSION

Mineral Chemistry and Phase Composition of the Loose Sediment Samples

The five samples from Ny-Ålesund (hereafter NyA) contain the following mineral phases: dolomite, calcite, quartz, albite, and the sheet silicates vermiculite, muscovite, and clinochlore. NyA1 and NyA5 contain all the above phases in comparable amounts except for calcite, which is practically absent in NyA1. NyA2 is mainly composed of quartz with less albite, clinochlore, muscovite, and vermiculite and negligible calcite and dolomite amounts. NyA3 contains a minimal amount of calcite while NyA4 is dominated by quartz, calcite, and dolomite with only a small amount of muscovite and less clinochlore, albite and vermiculite. A rough estimate of the phase amounts in the samples based on the relative intensities of reflections is reported in **Table 4**.

The sheet silicates show two distinct patterns of composition related to the amounts of the ferromagnesian and the alkali elements with respect to the Al amounts (**Figure 4**). The first pattern, corresponding to the higher Mg/Al and Fe/Al ratios, can be ascribed to trioctahedral micas (biotite and phlogopite) and mica-like minerals (trioctahedral chlorites and Mg-vermiculite) these latter being enriched in Fe and depleted in Mg in respect to the reference minerals. This pattern is in good accordance with the mineralogy and the paragenesis of the underlying rocks (Dallmann, 2015). The second pattern, corresponding to the lower Mg/Al and Fe/Al ratios, can be ascribed to dioctahedral mica (muscovite) and mica-like minerals (mixed-layer illite-smectite). This pattern is characterized by a positive correlation between Fe and alkali amounts which suggests higher amounts of Fe^{3+} in respect to the Fe^{2+} amounts (a typical feature of illite/smectite minerals). Illite-smectite is one of the most common clay minerals in sedimentary rocks and a prime component in many soils as a weathering product of basic rocks.

SEM-EDS investigations revealed the presence of monazite, zircon, apatite, baryte, iron sulfate, Fe, Ti, Cu, and Zn ores as accessory phases (**Figures 5**, **6**). All these phases are well within the geological context. In particular monazite and zircon, two heavy minerals somewhat stable against meteoric and intrastratal solutions, are compatible with metapelitic schist basement rocks involved in prolonged fluvial transport (Hodson and Ferguson, 1999). The same occurs for the metal (Fe, Ti, Cu, and Zn) ores whereas apatite documents the raising of a submerged marine shelf area and the development of the coastal terrace after deglaciation (Cook and Kiaerner, 2008; Ottesen et al., 2010). Baryte and iron sulfate are related to the coal formations in which they can originate by syngenetic processes and by pyrite oxidation, respectively (Michelsen and Khorasani, 1991).

The XRD patterns of the three Icelandic samples (hereafter ICE) show the presence of plagioclase, pyroxene and a small amount of magnetite spinel over a bell-shaped background due to the remarkable presence of an amorphous phase. The Rietveld refinements provided the following weight fractions of the amorphous phase: 81% (ICE1), 87% (ICE2), and 79% (ICE3). The plagioclase has a labradorite-andesine composition; the pyroxene is an augite whereas magnetite shows a variable composition within the magnetite-ülvospinel series (**Figures 7a–d**). Results of SEM-EDS investigations also revealed the presence of abundant Fe-Cr-Ni-bearing hyaloclastic fragments (**Figures 7e,f**). These results are comparable to the findings for Mælifellssandur discussed by Dagsson-Waldhauserova et al. (2014), but Baratoux et al. (2011) separated their Dyngjusandur samples into pyroxene, plagioclase, olivine, and volcanic glass as the significant four phases.

Aerosol vs. Sediment Samples

The aerosol samples show a more varied and complex composition for the five main particle types, namely, silicates, metal oxides, carbonates, sulfates, and chlorides.

The silicates consist of quartz, feldspar, and sheet minerals. The sheet minerals show a range of composition from dioctahedral to trioctahedral micas and mica-like minerals (muscovite, mixed-layer illite-smectite, biotite, and chlorites; **Figure 8**). A large part of the sheet minerals in the aerosol samples of April 18 and 29 are dioctahedral while the sheet minerals of April 22 and 26 tend to the trioctahedral type. The composition of the sheet minerals is within the range of variation of the NyA samples.

TABLE 4 | Raw estimation of phase amounts in the samples, based on the relative intensities of XRD reflections.

Sample\mineral	NyA1	NyA2	NyA3	NyA4	NyA5	ICE1	ICE2	ICE3
Dolomite	+ +	−	+	+ +	+++			
Calcite	+	−	+	+ +	++			
Quartz	+ +++	+++ + +	+ ++	+++	+ +++			
Vermiculite	+ ++	+++	+ +	−	+ + +			
Muscovite	+ +	+++ +	+ ++++	+	+ +			
Clinochlore	+	++	+ +	−	+			
Albite	+ +	++	+ ++	+	+ +			
Plagioclase						+ ++	++	+ ++
Pyroxene						+ ++	+++	+ ++
Magnetite						+ ++	+++	−

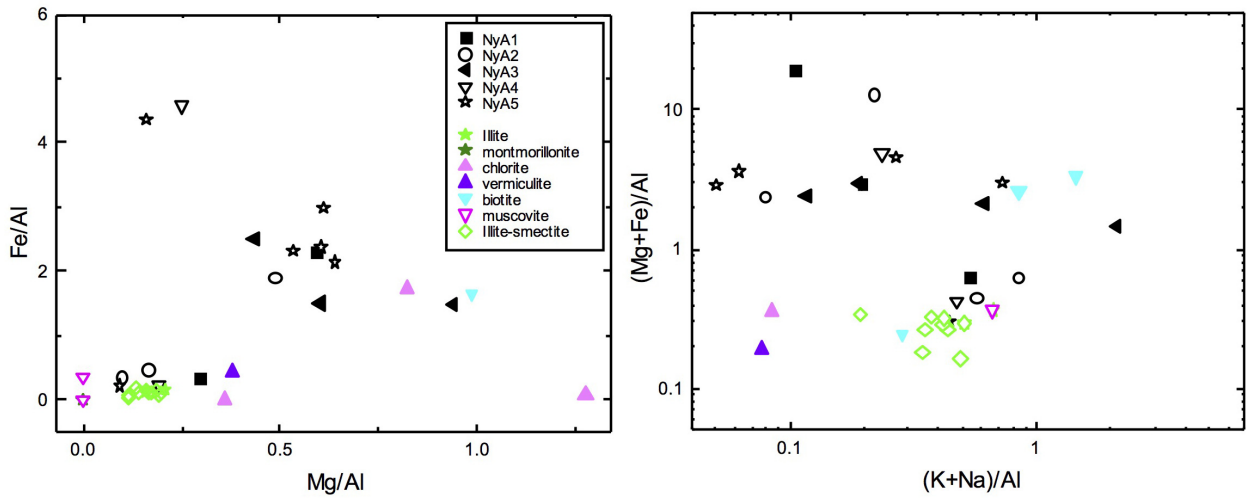

FIGURE 4 | Chemical composition by SEM-EDS microanalysis of the sheet minerals in the loose sediment samples from Ny-Ålesund (NyA). Analyses of reference sheet minerals (Srodon et al., 1986; Deer et al., 1992; http://www.webmineral.com) are reported for comparison.

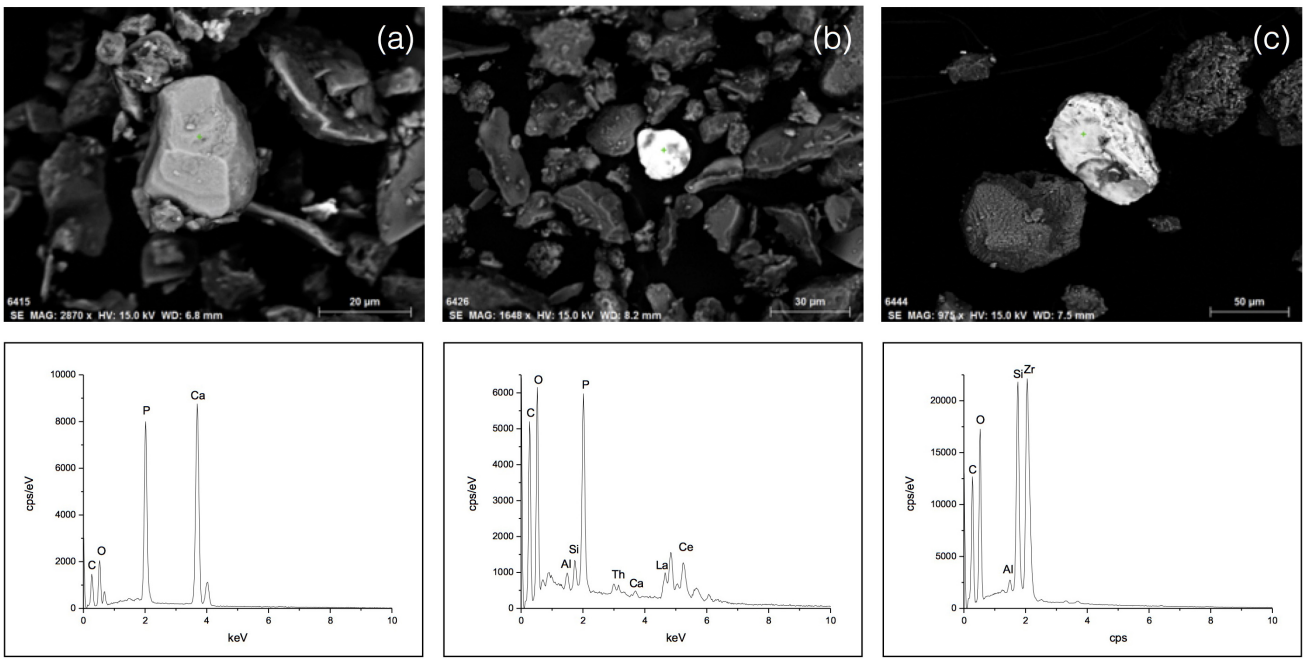

FIGURE 5 | Scanning electron microscopy micrographs and EDS spectra of **(a)** apatite, **(b)** monazite, and **(c)** zircon grains in NyA sediments. The green crosses mark the spot analysis.

The metal oxide particles are mainly composed of Fe, Ti, Fe-Cr, Fe-Ti, and Fe-Cr-Ti along with oxygen. The Fe-Cr particles are typically smooth and angular in shape though variable in size and contain trace amounts of Si, Al, and Ca (**Figures 9a,b**, **10**). They are very similar to the glass particles found in the volcanic sands from Iceland (**Figures 7e,f**). S and alkali elements (Na, Mg and K; **Figures 9c,d**) are frequently found in these particles, likely the result of internal mixing with sulfate nanoparticles. The Fe-Ti particles are micrometric to sub-micrometric particles frequently wrapped by internally mixed sulfates and chlorides (**Figures 9e,f**, **10**). In the ternary diagram of **Figure 11** the composition of the metal oxides fits the ranges for magnetite-ülvospinel ($Fe^{2+}Fe^{3+}{}_2O_4$-$Fe^{2+}{}_2TiO_4$) and magnetite-chromite ($Fe^{2+}Fe^{3+}{}_2O_4$-$Fe^{2+}Cr_2O_4$) spinels, or is compatible with ilmenite ($FeTiO_3$) and rutile (TiO_2). While the spinel facies is typical of the Icelandic sediments, ilmenite and rutile are found in the sediments from Ny-Ålesund. The Fe and the Fe-Cr-Ti particles are mostly submicron in size and show a

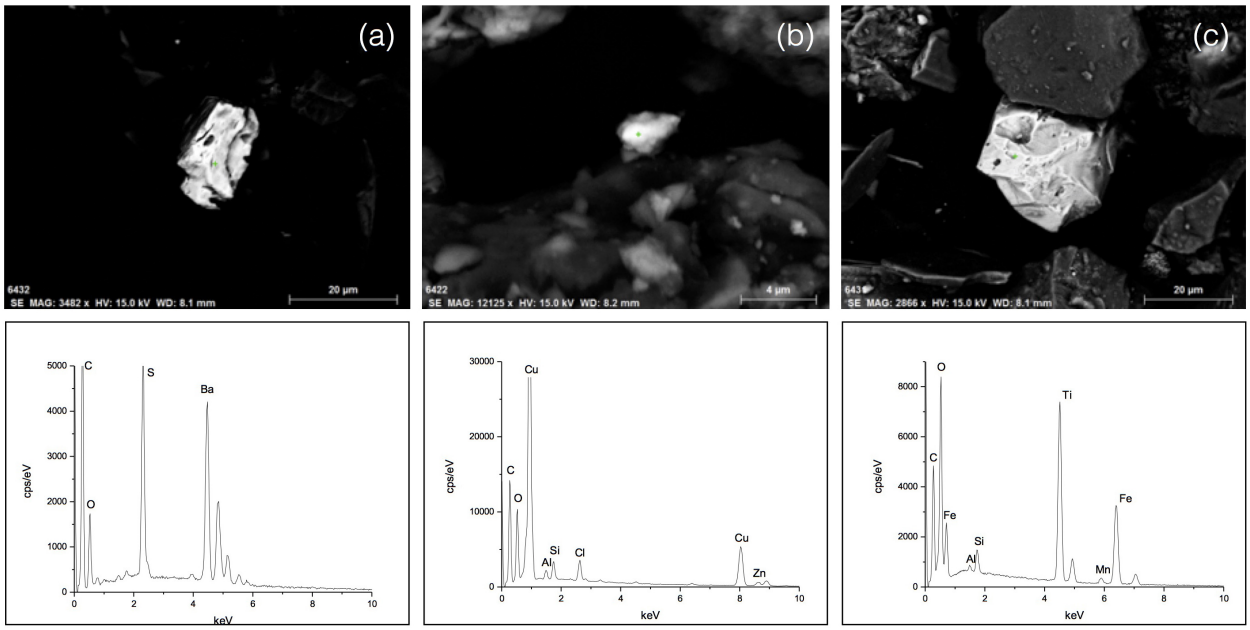

FIGURE 6 | Scanning electron microscopy micrographs and EDS spectra of **(a)** baryte, **(b)** Cu-Zn ore, and **(c)** Fe-Ti oxide grains in NyA sediments. The green crosses mark the spot analysis.

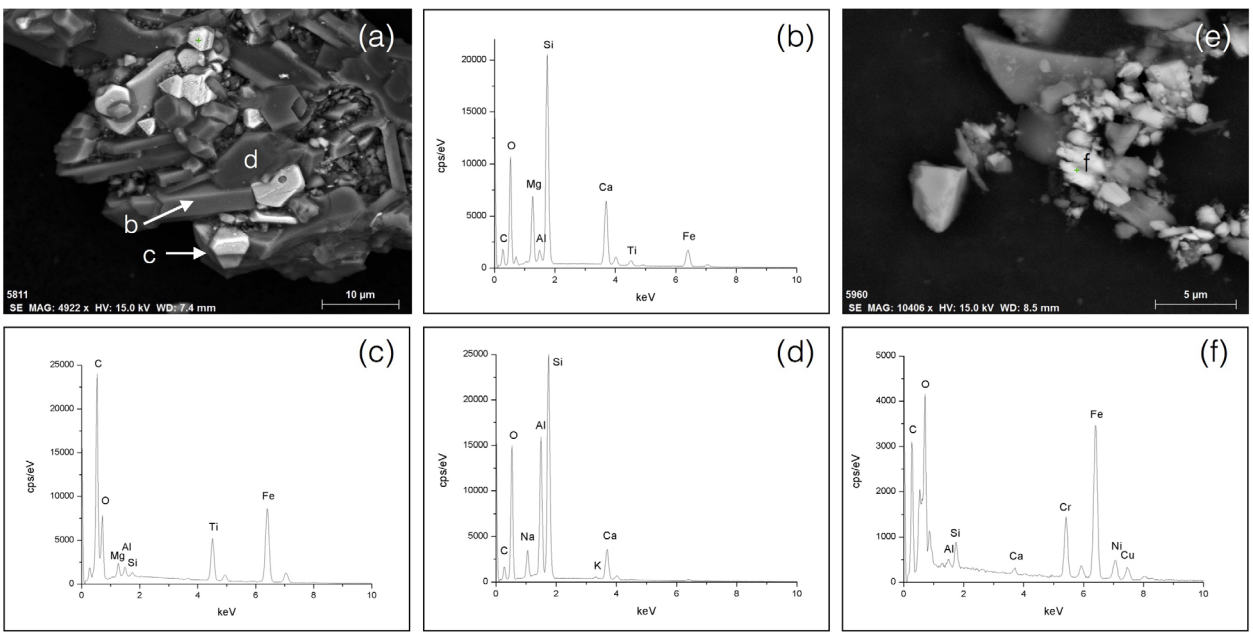

FIGURE 7 | Scanning electron microscopy micrographs and EDS spectra of representative phases of ICE sediments: **(a)** rock fragment containing augite clinopyroxene **(b)**, magnetite-ülvospinel **(c)** and andesine-labradorite plagioclase **(d)**; **(e,f)** Fe-Cr-Ni-bearing hyaloclastic fragments. The green crosses mark the spot analysis.

wide range of variation in shape while the Ti particles are typically submicrometric and roundish in shape (**Figure 10**).

Amongst the other particle types, the carbonates are represented by calcite and dolomite while the sulfates and chlorides consist of gypsum, alkali sulfate, and sodium chloride. These minerals are fine (mean diameter < 2.5 μm) to coarse grained (mean diameter > 2.5 μm), the carbonates do generally exhibit a rounded shape while the sulfates and chlorides are generally idiomorphic. The carbonates are very similar in size and shape to those found in the NyA sediments.

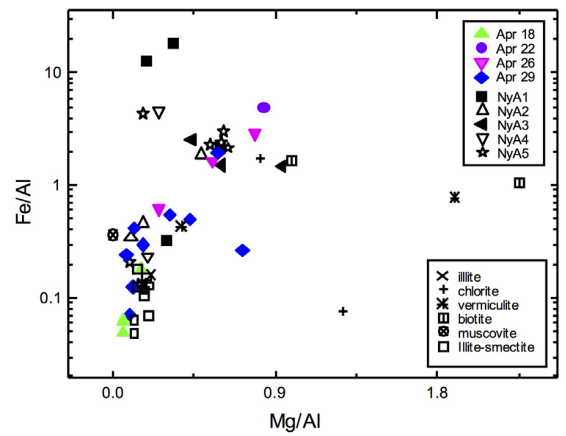

FIGURE 8 | Chemical composition by SEM-EDS microanalysis of the sheet minerals in the aerosol samples compared to the composition of NyA sediments and reference minerals.

Dust Sources

The dust sources under consideration are, indeed, very different. Iceland is characterized by volcanic desert terrains dominated by aeolian processes while Svalbard islands host a core metamorphic basement and a sedimentary cover subjected to glacial and alluvial fan transport and deposition. The mineralogical association and particle size distribution of the sediments reflect such a different origin. In particular, augite clinopyroxene, plagioclase, magnetite, and volcanic glass fragments are distinguishing phases of the Icelandic sediments while the mineralogical associations quartz-muscovite-chlorite-albite and calcite-dolomite are characteristic features of the low-grade metamorphic complexes and the sedimentary terrains in Svalbard. The Icelandic materials are well sorted by the intense action of the wind; the poor sorting of the sediments from Ny-Ålesund reflects the influence of glacial to alluvial transport on the origin and evolution of the sediments. It is clear that the Icelandic facies is very typical as a member of the tholeiitic magmatic series whereas the mineralogical association found at Ny-Ålesund has not the same diagnostic value because the constituent minerals are all somewhat common in many geological contexts and, thus, they cannot be univocally associated with the local metamorphic origins. The nature of the sheet minerals cannot be employed, at least at this level, to make any distinction between the source regions for the lack of diagnostic/significant amounts of the sheet minerals in the Icelandic aeolian sediments and soils in general (Arnalds, 2015).

When considering the aerosols in respect to the loose sediment samples the metal oxide particles turn out to be a main marker of the Icelandic terrains. In particular, the presence of metal bearing glass particles points to a provenance from a volcanic instead of a plutonic tholeiitic complex (e.g., the Skaergaard ultramafic plutonic complex in Greenland; McBirney, 1996). This fact opens up the possibility to discriminate the contributions from Iceland and Greenland when both sites are potential source regions of dust. That is the case of the aerosol samples collected on April 22 and April 29 for which BT analysis revealed a possible contribution from both eastern Greenland and Iceland.

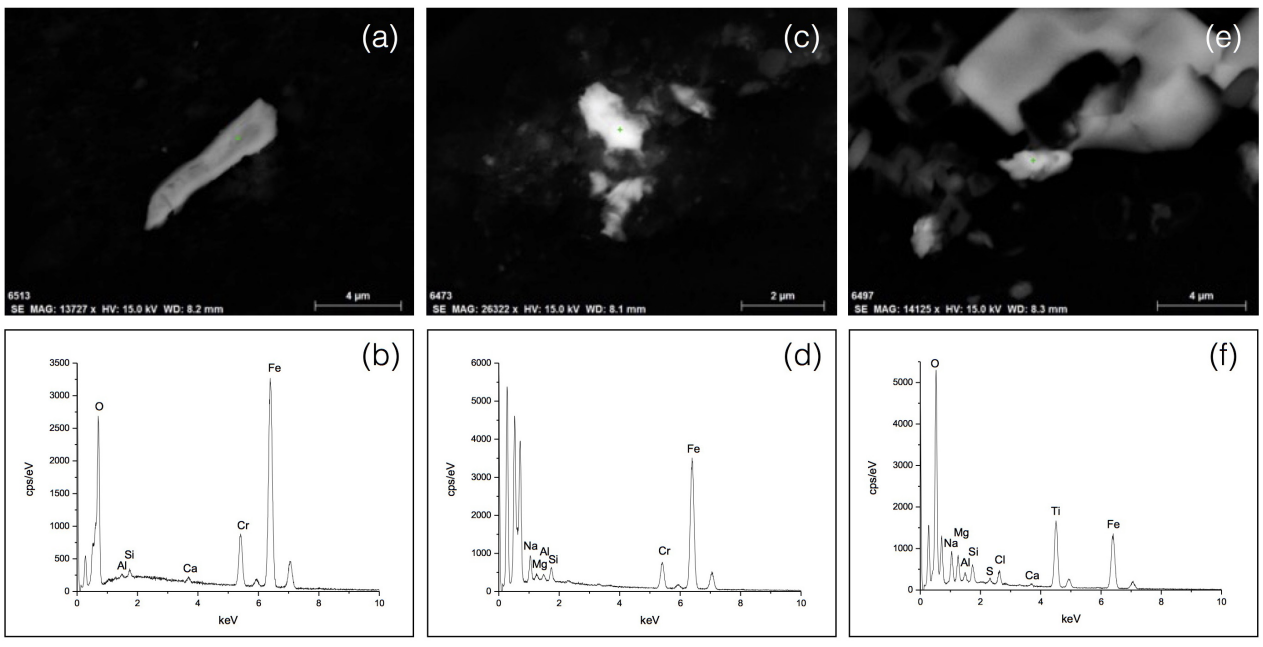

FIGURE 9 | Scanning electron microscopy micrographs and EDS spectra of **(a,b)** a Fe-Cr bearing hyaloclastic fragment, **(c,d)** a Fe-Cr bearing fragment internally mixed with alkaline sulfate, and **(e,f)** aTi-Fe bearing metal oxide particle externally mixed with alkaline sulfate, sodium chloride and silicate minerals. The green crosses mark the spot analysis.

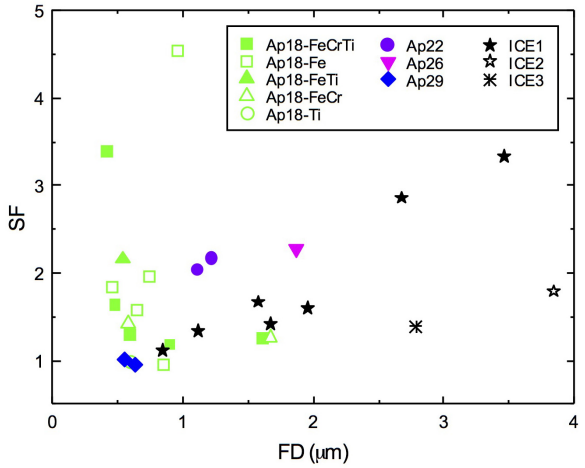

FIGURE 10 | Plot of the Feret diameter (FD) vs. the shape factor (SF) of aerosol and sediment samples.

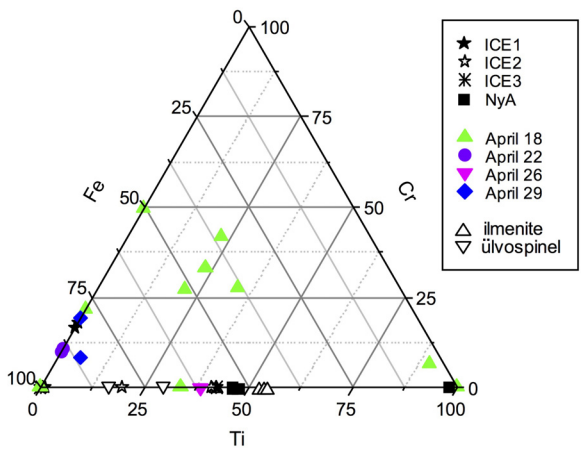

FIGURE 11 | Ternary diagram Ti-Cr-Fe of the chemical composition of the metal oxide particles in the aerosol samples. Data from SEM-EDS microanalysis. The composition of NyA and ICE sediments and of reference mineral are also reported for comparison. The composition of rutile fits the right corner of the triangle.

The glass phase and its relative abundance in the dust can indicate a provenance from different localities in Iceland. In particular, the glass enrichment in our samples suggests that the dust may have been raised in the air from formations of volcanic sands remarkably enriched in hyaloclastites such as the Dyngjusandur deposits in Northeast Central Iceland (Baratoux et al., 2011).

The chemical composition of the metal oxide particles is a further discriminative parameter of the provenance of dust. In fact, the metal oxide particles of April 22, 26 and, partly, of April 29 are very similar to the metal oxide ICE particles whereas the sample of April 18 has a more variable composition due to the presence of distinct Fe-Ti-Cr-bearing particles and aggregates. In this latter case, in particular, the lower Fe and higher Cr relative amounts along with the small size and higher grain boundary complexity in respect to the other particles suggest some influence of anthropogenic sources (e.g., Liu et al., 2018). Such a distinction can be ascribed to the variability of the source region of dust as is the case of the sample of April 18 for which the results of the BT analysis revealed a provenance from the Siberian coasts and only a minor contribution from Iceland. This further supports the reliability of the geochemical characterization of the metal oxide particles for the identification of the source regions of dust.

The glass particles are generally quite large, elongated and irregular shaped. The same results were found in samples from suspended Icelandic dust (Dagsson-Waldhauserova et al., 2014, 2015). This suggests a possible influence of the shape in favoring the uplift of the hyaloclastic volcanic sands due to local baric fields. Other phases in the loose Icelandic sediments, such as plagioclase and augite, show a similar shape. Thus, it is also important to consider the shape, specific weight and the size of the particle types. The specific weight, ρ_s, of the glass particles is extremely variable depending on porosity and weathering (Wolff-Boenisch et al., 2004; Franzson et al., 2010). The variable shape and density along with the much higher abundance of glass compared to the other phases in the Icelandic dust (Dagsson-Waldhauserova et al., 2014) can explain the presence and the abundance of the glass phase in the aerosol samples.

The size of the glass particles can be related to the dust plume formation and wind motion. According to Dagsson-Waldhauserova et al. (2014), dust plumes originating in Iceland show two maxima of the particle number concentration in the size range 0.3–0.337 μm and 1.5–5 μm in diameter during the dust peaks. The aerosol sample of April 26, which contains dust emitted during a storm in Iceland, reflects this condition with the relatively larger grain size of the particles (**Figures 9e**, **10**) in respect to the other samples.

The small dust particles are easily transported by the air masses after uplifting from ground level and are prone to remain suspended due to their small size before deposition on the ground. This is the case of the aerosol sample of April 29 which contains a minimal number of metal oxide particles despite its likely derivation from a dust storm in Iceland. In a previous paper (Moroni et al., 2015) we have shown the remarkable presence on that day of metal oxide particles a few hundred meters from the ground giving rise to a layered aerosol structure

TABLE 5 | Dust load estimates for April 2011.

Date	PM_{10} (μgm^{-3})	Average 7 + 7 days (μgm^{-3})	Average 15 + 15 days (μgm^{-3})	Moving perc50 (μgm^{-3})
14	2.1	neg.	neg.	neg.
15	2.6	neg.	neg.	neg.
22	5.7	1.6	1.6	1.8
23	4.4	0.4	0.3	0.6
25	3.7	neg.	neg.	neg.
26	10.7	6.5	6.7	6.9
27	3.2	neg.	neg.	neg.
30	2.4	neg.	neg.	neg.

due to local convective conditions. It is, thus, likely that the aerosol particles, once approaching the receptor, be entrapped in the lower troposphere and reach the ground at a variable rate depending on the local synopsis.

Dust Load Estimates

Having established the existence and the recognizability of the Icelandic dust contribution in the aerosol a further step can be to establish the extent of this contribution. Although the quantification of the Icelandic dust contribution is beyond the scope of this paper we have estimated the Icelandic dust load from the PM_{10} using the following approach.

For the days identified as belonging to Icelandic dust episodes, the daily net Icelandic dust load has been obtained by subtracting the background value to the PM_{10} value recorded on that day. To calculate the background concentration during the days affected by Icelandic contributions, two different statistical indicators have been used, i.e., the average value of a time series and the moving percentile 50. The average value has been calculated from the PM_{10} values registered 7 (and 15) days before and 7 (and 15) days after the intrusion (excluding dust days). The moving percentile 50 has been calculated for the PM_{10} concentrations registered during 15 days before and 15 days after the dust day (excluding dust days).

We have performed these calculations on the 2011 dust days for which the PM_{10} concentrations are available. The dust load values obtained (**Table 5**) are negative in all the samples except for those of April 22, 23, and 26. The dust load values of these samples obtained using different procedures of calculation are quite similar though very different from one sample to the other. Such a disparity confirms our previous observations on the different extent of the Icelandic contribution in different days.

Compared to the PM_{10} mass concentration registered from April to September 2011 the extent of the Icelandic mass contribution results about 2% of the total mass, and turns to about 7% in April. This means that the Icelandic contribution to the aerosol at Ny-Ålesund, though small to moderate in the long term, cannot be neglected especially during spring.

CONCLUSION

In this paper, we have evaluated the possibility of identifying the provenance of aerosols reaching the Arctic region at Ny-Ålesund based on the phase composition and the mineral chemistry of dust compared to reference sediment samples.

Comparison between local and Icelandic sediments reveals the metal oxide glass particles as the most representative and distinguishing mineralogical/phase markers for Iceland dust sources. In particular, we have considered the magnetite-chromite and the magnetite-ulvospinel associations as marker facies of the tholeiitic magmatic series and the presence of volcanic glass as a further indicator of provenance from Iceland rather than from tholeiitic plutonic districts such as Skaergaard, Greenland. However, the question remains about the actual origin of tholeiitic aerosols from Greenland both due to the lack of useful comparison samples and due to the lack of information on the presence of exposed soil/rock surfaces free from snow during spring (late April). The results of this preliminary study confirm that metal oxide particles are useful markers of sources and geographic provenance, provided that geochemical/morphochemical database of representative particle populations from different sources/source areas, both local/regional and long-range, is available.

This study provides an evidence that significant amounts of Icelandic dust can be transported long range to Svalbard showing the importance and the impact of High Latitude Dust sources.

AUTHOR CONTRIBUTIONS

BM was responsible for NyA samples and data collection, granulometric analysis, SEM-EDS microanalysis, and general interpretation of the results; she conceived the paper and was the primary author of the manuscript. PD-W provided the ICE samples, PD-W and OA described the geological setting and geomorphology of Iceland and discussed the results in the light of previous experience on the ground. SC performed air mass back trajectory analysis and discussed the results with BM. RV provided XRD analyses and Rietveld refinement. DC gave a critical revision of the manuscript.

FUNDING

OA and PD-W was funded by the Icelandic Research Fund (Rannis) Grant No. 152248-051 and supported by Vinir Vatnajokuls. DC, BM, and SC was funded by the project SIDDARTA (CUP project id: I52F17001230001).

REFERENCES

Arnalds, O. (2010). Dust sources and deposition of aeolian materials in Iceland. *Icel. Agric. Sci.* 23, 3–21.

Arnalds, O. (2015). *The Soils of Iceland. World Soils Book Series*. Dordrecht: Springer.

Arnalds, O., Dagsson-Waldhauserova, P., and Olafsson, H. (2016). The Icelandic volcanic aeolian environment: processes and impacts—a review. *Aeolian Res.* 20, 176–195. doi: 10.1016/j.aeolia.2016.01.004

Arnalds, O., Olafsson, H., and Dagsson-Waldhauserova, P. (2014). Quantification of iron-rich volcanogenic dust emissions and deposition over ocean from Icelandic dust sources. *Biogeoscience* 11, 6623–6632. doi: 10.5194/bg-11-6623-2014

Arnalds, O., Thorarinsdottir, E. F., Thorsson, J., Dagsson-Waldhauserova, P., and Agustsdottir, A. M. (2013). An extreme wind erosion event of the fresh Eyjafjallajokull 2010 volcanic ash. *Nat. Sci. Rep.* 3:1257. doi: 10.1038/srep01257

Baddock, M. C., Mockford, T., Bullard, J. E., and Thorsteinsson, T. (2017). Pathways of high-latitude dust in the North Atlantic. *Earth Planet. Sci. Lett.* 459, 170–182. doi: 10.1016/j.epsl.2016.11.034

Baratoux, D., Mangold, N., Arnalds, O., Bardintzeff, J.-M., Platevoet, B., Grégorie, M., et al. (2011). volcanic sands of Iceland – diverse origins of aeolian sand deposits revealed at Dyngjusandur and Lambahraun. *Earth Surf. Proc. Land.* 36, 1789–1808. doi: 10.1002/esp.2201

Bullard, J. E., Baddock, M., Bradwell, T., Crusius, J., Darlington, E., Gaiero, D., et al. (2016). High-latitude dust in the earth system. *Rev. Geophys.* 54, 447–485. doi: 10.1002/2016RG000518

Cappelletti, D., Azzolini, R., Langone, L., Ventura, S., Viola, A., Aliani, S., et al. (2016). Environmental changes in the Arctic: an Italian perspective. *Rend. Lincei.* 27, 1–6. doi: 10.1007/s12210-016-0555-1

Cook, N., and Kiaerner, T. (2008). "Mineralogy and paragenesis of selected base metal deposits," in *Proceedings 33rd International Geological Congress (2008), Session AAA-11 Metallogeny of the Arctic Region*, Oslo.

Dagsson-Waldhauserova, P., Arnalds, O., and Olafsson, H. (2013). Long-term frequency and characteristics of dust storm events in Northeast Iceland (1949-2011). *Atmos. Environ.* 77, 117–127. doi: 10.1016/j.atmosenv.2013.04.075

Dagsson-Waldhauserova, P., Arnalds, O., Olafsson, H., Hladil, J., Skala, R., Navratil, T., et al. (2015). Snow-dust storm a case study from Iceland, March 7th 2013. *Aeolian Res.* 16, 69–74. doi: 10.1016/j.aeolia.2014.11.001

Dagsson-Waldhauserova, P., Arnalds, O., Olafsson, H., Skrabalova, L., Sigurdardottir, G. M., and Branis, M., et al. (2014). Physical properties of suspended dust during moist and low wind conditions in Iceland. *Icel. Agric. Sci.* 27, 25–39.

Dagsson-Waldhauserova, P., Magnusdottir, A. Ö., Olafsson, H., and Arnalds, O. (2016). The spatial variation of dust particulate matter concentrations during two Icelandic dust storms in 2015. *Atmosphere* 7:77. doi: 10.3390/atmos7060077

Dallmann, W. K. (2015). *Geoscience Atlas of Svalbard*. Report Series No. 148. TromsØ: The Norsk Polarinstitutt.

Deer, W. A., Howie, R. A., and Zussman, J. (1992). *An Introduction to the Rock-Forming Minerals*. London: Longman Group UK.

Dörnbrack, A., Stachlewska, I. S., Ritter, C., and Neuber, R. (2010), Aerosol distribution around Svalbard during intense easterly winds. *Atmos. Chem. Phys.* 10, 1473–1490. doi: 10.5194/acpd-9-16441-12009

Eneroth, K., Kjellström, E., and Holmén, K. (2003). A trajectory climatology for Svalbard: investigating how atmospheric flow patterns influence observed tracer concentrations. *Phys. Chem. Earth* 28, 1191–1203. doi: 10.1016/j.pce.2003.08.051

Franzson, H., Guðfinnsson, G. H., Helgadóttir, H. M., and Frolova, J. (2010). "Porosity, density and chemical composition relationships in altered Icelandic hyaloclastites", in *Water-Rock Interaction*, eds P. Birkle and I. S. Torres-Alvarado (London: Taylor & Francis Group), 199–202.

Groot Zwaaftink, C. D., Arnalds, O., Dagsson-Waldhauserova, P., Eckhardt, S., Prospero, J. M., and Stohl, A. (2017). Temporal and spatial variability of Icelandic dust emission and atmospheric transport. *Atmos. Chem. Phys.* 17, 10865–10878. doi: 10.5194/acp-17-10865-2017

Groot Zwaaftink, C. D., Grythe, H., Skov, H., and Stohl, A. (2016). Substantial contribution of northern high-latitude sources to mineral dust in the Arctic. *J. Geophys. Res. Atmos.* 121, 13,678–13,697. doi: 10.1002/2016JD025482

Gualtieri, M. L., Prudenziati, M., and Gualtieri, A. F. (2006). Quantitative determination of the amorphous phase in plasma sprayed alumina coatings using the rietveld method. *Surf. Coat. Technol.* 201, 2984–2989. doi: 10.1016/j.surfcoat.2006.06.009

Hodson, A. J., and Ferguson, R. I. (1999). Fluvial suspended sediment transport from cold and warm-based glaciers in Svalbard. *Earth Surf. Proc. Land.* 24, 957–974. doi: 10.1002/(SICI)1096-9837(199910)24:11<957::AID-ESP19>3.0.CO;2-J

Jakobsson, S. P., and Gudmundsson, M. T. (2008). Subglacial and intraglacial volcanic formations in Iceland. *Jökull* 58, 179–196.

Jakobsson, S., Jónasson, K., and Sigurðsson, I. (2008). The three igneous rocks in Iceland: a review. *Jökull* 58, 117–138.

Kylling, A., Groot Zwaaftink, C. D., and Stohl, A. (2018). Mineral dust instantaneous radiative forcing in the Arctic. *Geophys. Res. Lett.* 45, 4290–4298. doi: 10.1029/2018GL077346

Lambert, F., Kug, J.-S., Park, R. J., Mahowald, N., Winckler, G., and Abe-Ouchi, A., et al. (2013). The role of mineral-dust aerosols in polar temperature amplification. *Nat. Clim. Chang.* 3, 487–491. doi: 10.1038/nclimate1785

Larson, C., and von Dreele, R. B. (2001). *Generalized Crystal Structure Analysis System*. Los Alamos, NM: Los Alamos National Laboratory.

Liljequist, G. H. (1970). *Klimatologi. Generalstabens Litografiska Anstalt*. Stockholm: Ulfstrand.

Liu, H., Yan, Y., Chang, H., Chen, H., Liang, L., Liu, X., et al. (2018). Magnetic signatures of natural and anthropogenic sources of urban dust aerosol. *Atmos. Chem. Phys. Discuss*. doi: 10.5194/acp-2018-452

McBirney, A. R. (1996). "The skaergaard intrusion", in *Layered Intrusions*, ed. R. G. Cawthorn (Amsterdam: Elsevier Science), 147–180. doi: 10.1016/S0167-2894(96)80007-8

Meinander, O., Dagsson-Waldhauserova, P., and Arnalds, O. (2016). Icelandic volcanic dust can have a significant influence on the cryosphere in Greenland and elsewhere. *Polar Res.* 35:31313. doi: 10.3402/polar.v35.31313

Michelsen, J. K., and Khorasani, G. K. (1991). A regional study of coals from Svalbard: organic facies, maturity and thermal history. *B Soc. Géol. Fr.* 162, 385–397.

Moroni, B., Becagli, S., Bolzacchini, E., Busetto, M., Cappelletti, D., Crocchianti, S., et al. (2015). Vertical profiles and chemical properties of aerosol particles upon Ny-Ålesund (Svalbard Islands). *Adv. Meteorol.* 2015:292081. doi: 10.1155/2015/292081

Mountney, N. P., and Russell, A. J. (2004). Sedimentology of cold climate Aeolian sand sheet deposits in the Askja region of northeast Iceland. *Sediment. Geol.* 166, 223–244. doi: 10.1016/j.sedgeo.2003.12.007

Óladóttir, B. A., Sigmarsson, O., Larsen, G., and Thordarson, T. (2008). Katla volcano, Iceland: magma composition, dynamics and eruption frequency as recorded by Holocene tephra layers. *Bull. Volcanol.* 70, 475–493. doi: 10.1007/s00445-007-0150-5

Ottesen, R. T., Bogen, J., Finne, T. E., Andersson, M., Dallmann, W. K., and Eggen, O. A., et al. (2010). *Geochemical Atlas of Norway, Part 2: Geochemical Atlas of Spitsbergen. Chemical Composition of Overbank Sediments*. Trondheim: Geological Survey of Norway.

Prospero, J. P., Bullard, J. E., and Hodgkins, R. (2012). High latitude dust over the North Atlantic: inputs from Icelandic proglacial dust storms. *Science* 335, 1078–1082. doi: 10.1126/science.1217447

Russ, J. C. (1995). *The Image Processing Handbook*. New York, NY: CRC Press.

Screen, J. A., and Simmonds, I. (2010). The central role of diminishing sea ice in recent Arctic temperature amplification. *Nature* 464, 1334–1337. doi: 10.1038/nature09051

Serreze, M. C., and Barry, R. G. (2011). Processes and impacts of Arctic amplification: a research synthesis. *Glob. Planet. Chang.* 77, 85–96. doi: 10.1016/j.gloplacha.2011.03.004

Serreze, M. C., and Francis, J. A. (2006). The arctic amplification debate. *Clim. Chang.* 76, 241–264. doi: 10.1007/s10584-005-9017-y

Sigmarsson, O., and Steinthórsson, S. (2007). Origin of Icelandic basalts: a review of their petrology and geochemistry. *J. Geodyn.* 43, 87–100. doi: 10.1016/j.jog.2006.09.016

Srodon, J., Morgan, D. J., Eslinger, E. V., Eberl, D. D., and Karlinger, M. R. (1986). Chemistry of illite/smectite and end-member illite. *Clays Clay Miner.* 34, 368–378. doi: 10.1346/CCMN.1986.0340403

Thordarson, T., and Höskuldsson, A. (2008). Postglacial volcanism in Iceland. *Jökull* 58, 197–228.

Wolff-Boenisch, D., Gislason, S. R., Oelkers, E. H., and Putnis C. V. (2004). The dissolution rates of natural glasses as a function of their composition at pH 4 and 10., and temperatures fron 25 to 74°C. *Geochim. Cosmochim. Acta* 68, 4843–4858. doi: 10.1016/j.gca.2004.05.027

Conflict of Interest Statement: The authors declare that the research was conducted in the absence of any commercial or financial relationships that could be construed as a potential conflict of interest.

frontiers in Earth Science

ORIGINAL RESEARCH
published: 08 November 2018
doi: 10.3389/feart.2018.00190

Characterizing Atmospheric Transport Pathways to Antarctica and the Remote Southern Ocean Using Radon-222

Scott D. Chambers[1], Susanne Preunkert[2], Rolf Weller[3], Sang-Bum Hong[4], Ruhi S. Humphries[5,6], Laura Tositti[7], Hélène Angot[8], Michel Legrand[2], Alastair G. Williams[1], Alan D. Griffiths[1], Jagoda Crawford[1], Jack Simmons[6], Taejin J. Choi[4], Paul B. Krummel[5], Suzie Molloy[5], Zoë Loh[5], Ian Galbally[5], Stephen Wilson[6], Olivier Magand[2], Francesca Sprovieri[9], Nicola Pirrone[9] and Aurélien Dommergue[2]*

[1] Environmental Research, ANSTO, Sydney, NSW, Australia, [2] CNRS, IRD, IGE, University Grenoble Alpes, Grenoble, France, [3] Alfred Wegener Institute for Polar and Marine Research, Bremerhaven, Germany, [4] Korea Polar Research Institute, Incheon, South Korea, [5] Climate Science Centre, CSIRO Oceans and Atmosphere, Aspendale, VIC, Australia, [6] Centre for Atmospheric Chemistry, University of Wollongong, Wollongong, NSW, Australia, [7] Environmental Chemistry and Radioactivity Lab, University of Bologna, Bologna, Italy, [8] Institute for Data, Systems and Society, Massachusetts Institute of Technology, Cambridge, MA, United States, [9] CNR-Institute of Atmospheric Pollution Research, Monterotondo, Italy

OPEN ACCESS

Edited by:
Pavla Dagsson-Waldhauserova, Agricultural University of Iceland, Iceland

Reviewed by:
Stephen Schery, New Mexico Institute of Mining and Technology, United States
Bijoy Vengasseril Thampi, Science Systems and Applications, United States

***Correspondence:**
Scott D. Chambers
szc@ansto.gov.au

Specialty section:
This article was submitted to Atmospheric Science, a section of the journal Frontiers in Earth Science

Received: *02 July 2018*
Accepted: *16 October 2018*
Published: *08 November 2018*

Citation:
Chambers SD, Preunkert S, Weller R, Hong S-B, Humphries RS, Tositti L, Angot H, Legrand M, Williams AG, Griffiths AD, Crawford J, Simmons J, Choi TJ, Krummel PB, Molloy S, Loh Z, Galbally I, Wilson S, Magand O, Sprovieri F, Pirrone N and Dommergue A (2018) Characterizing Atmospheric Transport Pathways to Antarctica and the Remote Southern Ocean Using Radon-222. Front. Earth Sci. 6:190. doi: 10.3389/feart.2018.00190

We discuss remote terrestrial influences on boundary layer air over the Southern Ocean and Antarctica, and the mechanisms by which they arise, using atmospheric radon observations as a proxy. Our primary motivation was to enhance the scientific community's ability to understand and quantify the potential effects of pollution, nutrient or pollen transport from distant land masses to these remote, sparsely instrumented regions. Seasonal radon characteristics are discussed at 6 stations (Macquarie Island, King Sejong, Neumayer, Dumont d'Urville, Jang Bogo and Dome Concordia) using 1–4 years of continuous observations. Context is provided for differences observed between these sites by Southern Ocean radon transects between 45 and 67°S made by the Research Vessel *Investigator*. Synoptic transport of continental air within the marine boundary layer (MBL) dominated radon seasonal cycles in the mid-Southern Ocean site (Macquarie Island). MBL synoptic transport, tropospheric injection, and Antarctic outflow all contributed to the seasonal cycle at the sub-Antarctic site (King Sejong). Tropospheric subsidence and injection events delivered terrestrially influenced air to the Southern Ocean MBL in the vicinity of the circumpolar trough (or "Polar Front"). Katabatic outflow events from Antarctica were observed to modify trace gas and aerosol characteristics of the MBL 100–200 km off the coast. Radon seasonal cycles at coastal Antarctic sites were dominated by a combination of local radon sources in summer and subsidence of terrestrially influenced tropospheric air, whereas those on the Antarctic Plateau were primarily controlled by tropospheric subsidence. Separate characterization of long-term marine and katabatic flow air masses at Dumont d'Urville revealed monthly mean differences in summer of up to 5 ppbv in ozone and 0.3 ng m^{-3} in gaseous

elemental mercury. These differences were largely attributed to chemical processes on the Antarctic Plateau. A comparison of our observations with some Antarctic radon simulations by global climate models over the past two decades indicated that: (i) some models overestimate synoptic transport to Antarctica in the MBL, (ii) the seasonality of the Antarctic ice sheet needs to be better represented in models, (iii) coastal Antarctic radon sources need to be taken into account, and (iv) the underestimation of radon in subsiding tropospheric air needs to be investigated.

Keywords: radon, Southern Ocean, Antarctica, atmospheric transport, MBL, troposphere, ozone, mercury

INTRODUCTION

The Southern Hemisphere is currently home to only around 10% of the global population, and non-Antarctic land masses cover less than 14% of its surface. These factors, combined with the vast extent of the Southern Ocean and efficient wet deposition removal within the circumpolar trough, have so far ensured that Antarctica has remained one of the most pristine places on earth. However, the presence of artificial radioactivity following weapons testing (Koide et al., 1979), the Antarctic ozone hole (Solomon, 1999), and ice core trace gas analyses (Etheridge et al., 1996), constitute some of the irrefutable evidence that anthropogenic influences have impacted this region for many decades. Still, the relatively pristine Antarctic atmosphere provides a rare opportunity to explore an approximation of pre-industrial conditions, and its seasonal meteorological extremes also provide unique opportunities to explore a range of surface and atmospheric chemical processes (Crawford et al., 2001; Davis et al., 2001; Eisele et al., 2008; Jones et al., 2008; Preunkert et al., 2008; Slusher et al., 2010; Angot et al., 2016c; Legrand et al., 2016).

The crucial role Antarctica plays in global atmospheric and oceanic circulation is well established, as is the importance of the expansive Southern Ocean to global climate, atmospheric composition, and marine life everywhere (Bromwich et al., 1993; Nicol et al., 2000; Gille, 2002; Manno et al., 2007; Sandrini et al., 2007; Stavert et al., 2018). Recent investigations have also shown that Antarctica's ice sheets, which provide a valuable window through which to view the past (Jouzel et al., 2007; Brook and Buizert, 2018), and hold around 70% of the world's fresh water (Fox et al., 1994), are particularly susceptible to the influences of climate change (Turner et al., 2006; DeConto and Pollard, 2016; Rintoul et al., 2018). Consequently, methods to improve the understanding of transport pathways of terrestrially influenced air masses (potentially containing pollutants, nutrients, pollen, etc.) to these remote and changing regions is of multidisciplinary interest (e.g., Jickells et al., 2005).

While some pollutants and trace atmospheric constituents found in Antarctic and sub-Antarctic regions are generated locally (via shipping, research bases, wildlife, volcanic activity and photochemical processes; Jones et al., 2008; Shirsat and Graf, 2009; Graf et al., 2010; Bargagli, 2016), the balance of these species are attributable to remote sources, primarily of terrestrial origin. Remotely sourced trace gasses and aerosols travel to Antarctica and the remote Southern Ocean by one of two pathways (Polian et al., 1986; Krinner et al., 2010; Chambers et al., 2014, 2017): directly, as a result of synoptic transport within the marine boundary layer (MBL), or indirectly, as a result of subsiding or intruding tropospheric air that has experienced recent continental influences (e.g., through deep convection or frontal uplift; e.g., Belikov et al., 2013).

While some terrestrial emissions travel great distances to reach Antarctica (e.g., from the Northern Hemisphere; Mahowald et al., 1999; Li et al., 2008), the majority of such material is typically of Southern Hemispheric origin (e.g., Albani et al., 2012), traveling over timescales and pathways that can be elucidated by measurements of the radioactive terrestrial tracer Radon-222 (radon). Having a short half-life (3.82 days) and an almost exclusively terrestrial source function, this noble gas provides an unambiguous means of characterizing the degree of recent terrestrial influence on air masses. In recent decades improvements in radon measurement technology have enabled routine detection down to concentrations of 5 – 40 mBq m^{-3} (e.g., Whittlestone and Zahorowski, 1998; Levin et al., 2002; Chambers et al., 2014, 2016; Williams and Chambers, 2016; Chambers and Sheppard, 2017). With detectors of this kind it is possible to track the movement of terrestrially influenced air masses over oceans (or in the troposphere) for up to 3 weeks.

Over the past four decades there has been a gradually expanding international network of continuous atmospheric radon monitors throughout Antarctica and the Southern Ocean. The resulting datasets have been highly valuable for "baseline" (hemispheric background) studies (e.g., Brunke et al., 2004; Zahorowski et al., 2013; Chambers et al., 2016), transport and mixing studies (Tositti et al., 2002; Pereira et al., 2006; Weller et al., 2014; Chambers et al., 2014, 2017), and as a tool for the evaluation of numerical model performance (e.g., Dentener et al., 1999; Law et al., 2010; van Noije et al., 2014; Locatelli et al., 2015).

Furthermore, an experimental meteorological technique was recently developed by Chambers et al. (2017) by which Antarctic air masses could be broadly separated into oceanic, coastal or katabatic fetch categories. Since many Antarctic research bases are in coastal locations, and free-tropospheric, Antarctic Plateau, coastal, and marine air masses have quite distinct properties, the ability to interpret atmospheric observations relies heavily on an ability to reliably identify air mass fetch. While simulated back trajectories have often been employed in this regard (e.g., Markle et al., 2012; Angot et al., 2016b), a dearth of supporting observations, the complex topography, and highly stable atmospheric conditions, pose significant sources of

simulation error in this region. Combining high quality radon observations (a proxy for terrestrial influence) with experimental fetch analyses techniques, stands to add yet another dimension to interpretations of Antarctic atmospheric observations.

The main aims of this study are: to summarize a collection of long-term radon observations in Antarctica and the remote southern ocean (some of which are still ongoing), to introduce Southern Ocean radon observations from the mobile platform RV *Investigator*, and to demonstrate the insight provided by such observations to transport processes in these remote regions (with particular emphasis on the circumpolar trough and Antarctic coast). As brief examples of the potential value to be added to Antarctic atmospheric research by the datasets and techniques described in this study, we also show some selected results from investigations of aerosols (cloud condensation nuclei), carbon dioxide, ozone and gaseous elemental mercury (GEM, Hg^0). More detailed investigation of these species is beyond the scope of this study and will be the subject of future investigations.

MATERIALS AND METHODS

Radon: A Proxy for Recent Terrestrial Influence on an Air Mass

Radon-222 (radon) is a gaseous decay product of Uranium-238. Its immediate parent, Radium-226, is ubiquitous in soils and rocks. Radon is a noble gas, poorly soluble, and radioactive ($t_{0.5}$ = 3.82 days), so it does not accumulate in the atmosphere on greater than synoptic timescales. Its average source function from unfrozen terrestrial surfaces is relatively well constrained (0.7 – 1.2 atoms cm^{-2} s^{-1}, Zhang et al., 2011; 1.0–1.25 atoms cm^{-2} s^{-1}, Griffiths et al., 2010; 0.4–1.0 atoms cm^{-2} s^{-1}, Karstens et al., 2015), and 2–3 orders of magnitude greater than that from the open ocean (Schery and Huang, 2004). Furthermore, on regional scales radon's terrestrial source function is not significantly affected by human activity. This combination of physical characteristics enables air masses that have been in contact with terrestrial surfaces to be tracked over the ocean, or within the troposphere, for 2–3 weeks. Consequently, radon observations constitute a convenient, economical, and unambiguous indicator of recent terrestrial influence on air masses. Since the majority of anthropogenic gaseous and aerosol pollutants are also of terrestrial origin, high-quality radon observations serve as a proxy for the 'pollution potential' of air masses in remote regions.

The radon concentration of air masses that have been in long-term equilibrium with the Southern Ocean is typically 30–50 mBq m^{-3} (e.g., Zahorowski et al., 2013; Chambers et al., 2016; Crawford et al., 2018). Consequently, key requirements of radon detectors deployed in such remote locations are: a detection limit of $\leq$50 mBq m^{-3}, stable absolute calibrations, and low maintenance.

Radon campaigns of varying duration and temporal resolution were conducted in and around Antarctica between 1960 and 1990 (see reviews by Polian et al., 1986; Ui et al., 1998; Chambers et al., 2014). In recent decades, however, the availability of continuous, long-term, high-quality radon observations at Southern Ocean and Antarctic stations has been slowly improving (e.g., Tositti et al., 2002; Pereira et al., 2004; Brunke et al., 2004; Zahorowski et al., 2013; Chambers et al., 2014, 2017; Weller et al., 2014). Detection methods have included electrostatic deposition (Pereira and da Silva, 1989; Ui et al., 1998; Tositti et al., 2002), static single-filter detectors (Levin et al., 2002), and two-filter detectors (Chambers et al., 2014). Stations presently contributing to the Southern Ocean network of radon detectors include: Cape Grim (CG), Baring Head (BH), Cape Point (CP), Macquarie Island (MI), Jang Bogo (JBS), King Sejong (KSG), and Neumayer (NM) (**Figure 1**).

Sites and Equipment

This article summarizes radon and auxiliary observations (e.g., meteorology, trace gasses and aerosols) from four of the long-term ongoing monitoring stations in the Southern Ocean network (MI, KSG, NM, and JBS), as well as Dumont d'Urville (DDU), Dome Concordia (DC), and selected observations from the Research Vessel *Investigator* (**Table 1**). Brief mention is also made of previously published observations from Mawson Base (Chambers et al., 2014). All reported times are local station times. For RV *Investigator* and MI observations the standard Southern Hemisphere seasonal convention has been adopted. For the Antarctic bases "summer" refers to the period November through February, "winter" the period April through September; March and October are considered transitional months.

The RV *Investigator's* radon detector was installed in September 2014 in the Aerosol Sampling Laboratory at the bow of the vessel, immediately below the sampling mast on the foredeck. Sample air is drawn at 65–75 L min^{-1} from a goose-neck inlet at 15 m above the foredeck (around 20–22 m above sea level, a.s.l.) through 25 mm HDPE agricultural pipe. A coarse aerosol filter, dehumidifier and water trap are installed upstream of the detector, to protect the detector's primary filter and internal components. Calibrations are performed on either a campaign or quasi-monthly basis by injecting radon from a PYLON Radon-222 source (20.62 $\pm$ 4% kBq ^{226}Ra, delivering 2.598 Bq min^{-1} ^{222}Rn)[1] for 6 h at a flow rate of $\sim$100 cc min^{-1}, and the instrumental background is checked either on a campaign basis or every 3 months. Details of other atmospheric observations aboard the RV *Investigator* are given in Protat et al. (2016).

Macquarie Island is small (34 × 5 km), and is situated roughly midway between Australia and Antarctica (**Figure 1**). Radon and meteorological observations are made at the "Clean Air Laboratory" on an isthmus at the northern end of the island ($\sim$54.5°S; **Figure 1**, inset 2). The MI radon detector was installed in March 2011, but technical problems delayed the start of the sampling program until March 2013. Sample air is drawn at $\sim$45 L m^{-1} from an inlet $\sim$5 m above ground level (a.g.l.) on a 10 m mast. The detector is calibrated monthly using a similar source to the RV *Investigator* (19.58 $\pm$ 4% kBq ^{226}Ra) injecting for 6 h at a flow rate of $\sim$170 cc min^{-1}. Instrumental background checks are performed quarterly by stopping the internal and external flow loop blowers for 24 h. Further information about MI observations can be found in Brechtel et al. (1998) and Stavert et al. (2018).

[1] https://pylonelectronics-radon.com/

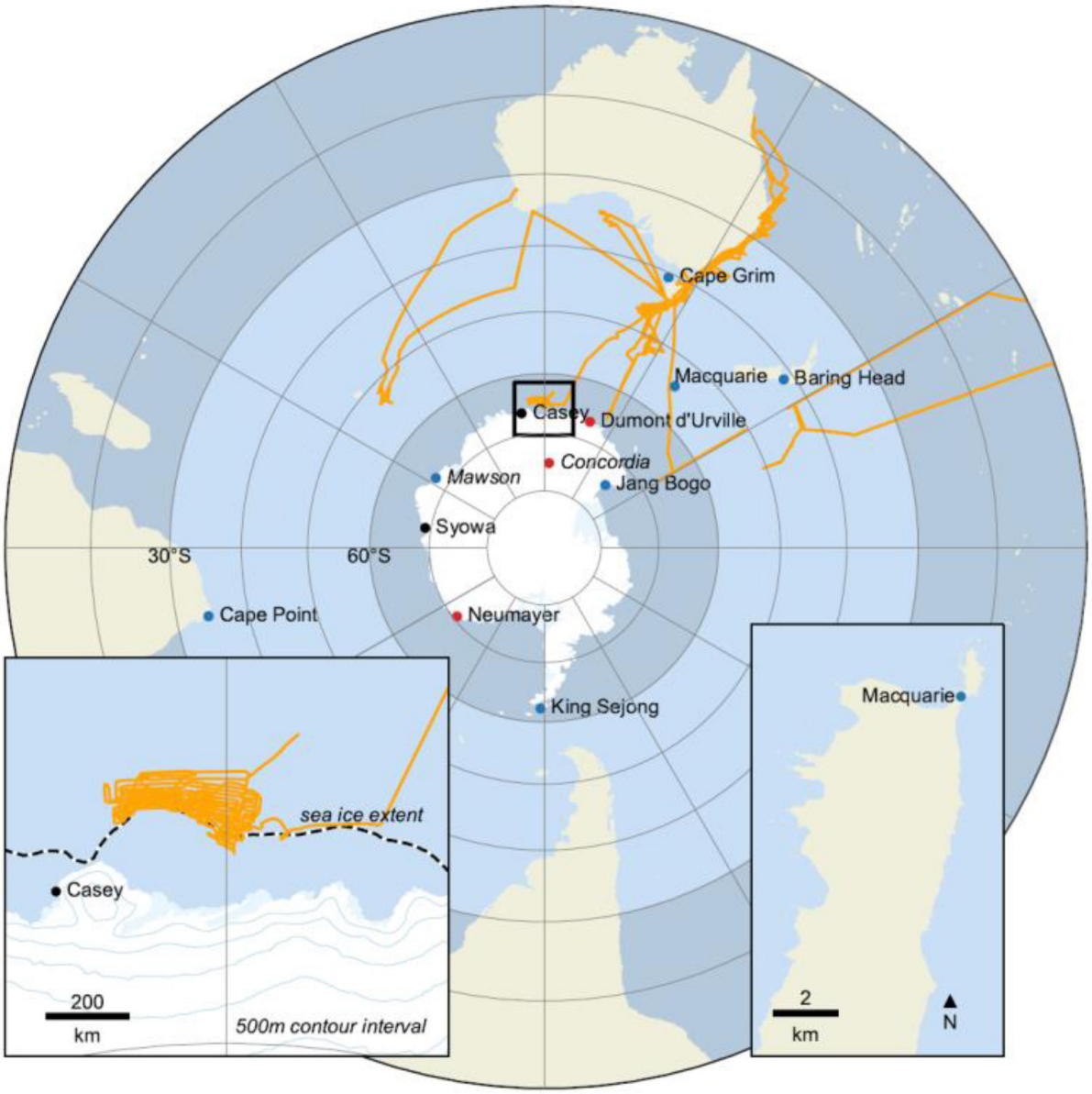

FIGURE 1 | Southern Ocean radon detector network: two-filter detectors (blue), single-filter detectors (red). RV Investigator cruise track (January 2015 to June 2017) shown in orange. Inset 1 shows RV Investigator maneuvers for sea floor mapping (January–February 2017), and includes the February 2017 sea ice extent based on the 20% concentration contour from passive microwave satellite data (Peng et al., 2013; Meier et al., 2017). Ice sheet elevation contours are from ETOPO1 (Amante and Eakins, 2009). Inset 2 shows location of Macquarie Island monitoring station with coastline data from Natural Earth and, for the Macquarie Island inset, the Australian Antarctic Division (2005).

A similar protocol is followed for the two-filter detectors at KSG and JBS. For details the reader is referred to existing publications (Chambers et al., 2014, 2017). Further details about the regions surrounding KSG and JBS are given in Evangelista and Pereira (2002) and Tositti et al. (2002).

Radon observations at NM, DDU, and DC were all made using single-filter ("by progeny") Heidelberg Radon Monitors (HRM, Levin et al., 2002). The current system providing 3-hourly radon observations at Neumayer Station has been in place since 1995. Specific details about the site as well as the setup and operation of the Neumayer HRM and other observations are provided in Weller et al. (2014). Specifically regarding the NM radon sampling inlet, ambient air is first sucked through 3 m of 200 mm electro-polished stainless steel at 8.8 m s^{-1}, then through 2.8 m of 50 mm electro-polished stainless steel tube at 2 m s^{-1}, and finally through ~50 cm of 6 mm stainless steel tube at 21 m s^{-1}.

At DDU the HRM was setup in laboratory "Labo 3" (e.g., Preunkert et al., 2012) in which other long-term atmospheric

TABLE 1 | Sites, detection method, time periods, and responsible organizations for observations discussed in this study.

Station/Platform	Period of observations	Radon detector, responsible organizations and lower limit of detection
RV Investigator (ongoing)	January-2015 to June-2017	700L two-filter detector; Australian Marine National Facility, CSIRO, ANSTO; LLD 40 mBq m^{-3}
Macquarie Island (ongoing)	March-2013 to December-2016	700L two-filter detector; Australian Antarctic Division (AAD), CSIRO, ANSTO; LLD 40 mBq m^{-3}
King Sejong (ongoing)	February-2013 to December-2016	1500L two-filter detector; Korea Polar Research Institute (KOPRI), ANSTO; LLD 25 mBq m^{-3}
Jang Bogo (ongoing)	January-2016 to December-2017	1200L two-filter detector; KOPRI, ANSTO; LLD 30 mBq m^{-3}
Neumayer (ongoing)	January-2010 to December-2011	Static single-filter detector; Alfred Wegener Institute for Polar and Marine Research, University of Heidelberg (Institut für Umweltphysik); LLD 20 mBq m^{-3}
Dumont d'Urville (terminated)	January-2006 to December-2008	Static single-filter detector; University Grenoble Alpes (CNRS), University of Heidelberg (Institut für Umweltphysik); LLD 60 mBq m^{-3}
Dome Concordia (terminated)	January-2010 to March-2011	Static single-filter detector; University Grenoble Alpes (CNRS), University of Heidelberg (Institut für Umweltphysik); LLD 60 mBq m^{-3}
Mawson (terminated)	January-1999 to August-2000	1500L two-filter detector; Australian Antarctic Division (AAD), ANSTO; LLD ∼50 mBq m^{-3}

measurements such as ozone (Legrand et al., 2009, 2016), sulfur species (Preunkert et al., 2008), gaseous elemental mercury (GEM, 2012–2015; Angot et al., 2016c; Sprovieri et al., 2016), other aerosols and reactive gasses are also conducted. The radon measurement resolution was hourly and sampling was more direct than at NM, simply through ∼4 m of 6 mm diameter Teflon tubing from 2 m a.g.l. In all other respects the HRM and its operation were as for NM. The DC HRM was situated in the main building of the station. The device was also set to sample hourly, through ∼4 m of 6 mm diameter Teflon tubing, but at a height of 17 m a.g.l., and run in parallel to long-term measurements of aerosols, SO_2 (Legrand et al., 2017a,b) and ozone (Legrand et al., 2009, 2016) as well as GEM (Angot et al., 2016b). In all other respects, the HRM instrument and operation were as for NM.

Specifically regarding the two-filter detectors, both the 700 and 1500 L models have a response time of ∼45 min (which can be corrected for in post-processing; Griffiths et al., 2016), and their response to even very low radon concentrations (<100 mBq m^{-3}) is linear. Their lower limits of detection (LLD; i.e., the concentration at which the detector's counting error reaches 30%) are ∼25 mBq m^{-3} and ∼40 mBq m^{-3}, for the 1500 and 700 L models, respectively. Their measurement error is typically 12–14% for concentrations of 100 mBq m^{-3} (Chambers et al., 2014; Schmithüsen et al., 2017). This uncertainty is contributed to by the counting error, the coefficient of variability of monthly calibrations, and the calibration source uncertainty. The counting error's contribution reduces with increasing radon concentration and, when sampling from a consistent fetch, the detector's measurement error reduces as $\sim N^{-1/2}$ for N samples. For the purposes of this study the half-hourly raw counts from each detector were integrated to hourly values before calibration to activity concentrations (mBq m^{-3}), thereby reducing the counting error by a factor of $\sqrt{2}$.

The two-filter method detects radon by zinc sulfide alpha scintillation, which does not distinguish between alpha particles of different energies, so a ∼5 min delay volume is incorporated within every detector's inlet line to allow the short-lived radon isotope (^{220}Rn, thoron, $t_{0.5}$ = 56 s) to decay to less than 0.5% of its ambient values before sample air enters the detector. Radon concentrations provided by some "direct" methods (e.g., two-filter detectors or electrostatic deposition detectors; Pereira and da Silva, 1989; Wada et al., 2010; Grossi et al., 2012) are not adversely influenced by high ambient humidity or changing aerosol loading conditions, proximity to local sources, atmospheric stability or fetch conditions. In a possible exception to this however, under low humidity conditions (i.e., 0–20%; common during Antarctic winters when cold ambient air is brought to detector temperature), the two-filter method can theoretically report concentrations up to 10% below ambient values due to a reduction in diffusivity, and consequent lower filtration efficiency, of the unattached progeny formed inside the detector (Griffiths et al., 2016). However, this effect is counteracted by reduced losses in the delay tank of the detector, and no significant evidence of a reduced detector sensitivity to radon concentrations was found based on 2 years of monthly calibrations of the Antarctic two-filter detectors over relative humidity values between 5 and 45%.

Specifically regarding the HRMs (single filter detectors), a correction factor of 1.11 has been applied to observations from all three sites to better harmonize their radon concentrations with the two-filter detector observations (as recommended by Schmithüsen et al., 2017). The radon disequilibrium correction discussed by Schmithüsen et al. (2017) is not required for the NM or DC observations due to the lack of significant local radon sources. Similarly, under oceanic fetch conditions at DDU no disequilibrium correction is required. For DDU observations under other fetch conditions a disequilibrium factor of 0.85–0.9 would be applicable to radon contributions from local fetch regions. However, since the relative contributions of local and remote radon sources to DDU observations under other fetch conditions are uncertain, no disequilibrium factor was applied to results presented. Although a large fraction of the hourly DDU and DC radon observations were below the LLD reported in

Table 1, the uncertainty of monthly mean/median values, and diurnal composites by season, reduces as $\sim N^{-1/2}$ for N hourly samples. Finally, as noted by Levin et al. (2017), "tube loss" of ambient radon progeny can reduce HRM radon estimates, particularly under very low ambient radon concentrations as is typical of the Antarctic atmosphere. We were unable to accurately characterize the magnitude of this influence on the NM, DDU and DC radon observations, but it is believed to have contributed in part to reported mean radon concentrations 10–15 mBq m^{-3} lower than those of the two-filter detectors under similar fetch conditions.

RESULTS

The Southern Ocean in Cross-Section

During the initial 2.5 years that radon was measured aboard the RV *Investigator* the vessel completed five full crossings of the Southern Ocean between the latitudes 45°S and 67°S, including a month of maneuvres near the Antarctic coast to the east of Casey Station for sea floor mapping (**Figure 1**). Since all transects were conducted in months between January and April they are representative of warmer conditions for this region. To demonstrate the utility of radon as a tracer of recent terrestrial influence, and provide a late-summer cross-section "snapshot" of potentially polluted air masses within the Southern Ocean's MBL, we prepared a composite of mean radon concentrations within 0.2° latitude bins (**Figure 2A**). This figure constitutes a significant improvement to transects reported by Polian et al. (1986) at 2–3 degree resolution, or the daily ship-based measurements reported by Taguchi et al. (2013), and provides context for measurements at the fixed sites discussed in the following sections.

Between 49–51°S and 62–64°S average radon concentrations were close to 50 mBq m^{-3}, indicative of minimal terrestrial influence within the past 2–3 weeks (i.e., marine "baseline" values, with radon in equilibrium with the Southern Ocean surface; Crawford et al., 2018 and references therein). By comparison, near the middle of this composite transect (i.e., 53–56°S) an enhancement of 30–40 mBq m^{-3} above baseline conditions was observed. Some previous studies have hypothesized that enhanced radon in the mid-Southern Ocean is entirely attributable to a wind-speed induced increase in the oceanic radon flux (e.g., Schery and Huang, 2004; Zahorowski et al., 2013). However, more recent evidence from an initial comparative baseline analyses of Cape Grim (Tasmania) and Macquarie Island air masses (Williams et al., 2017), suggests this radon enhancement is largely attributable to vestigial terrestrial influences on mid-Southern Ocean air masses. A detailed evaluation of this hypothesis will be the subject of a separate investigation. Notable similarities between **Figure 2A** and earlier transects reported by Polian et al. (1986) include higher concentrations around 60°S and at the Antarctic coast, with a local minimum in concentration around 63–64°S.

Several examples of isolated radon excursions from otherwise background conditions are evident in **Figure 2A** (e.g., at 46.5, 52.5, and 56.5°S). Back trajectories (HYSPLIT v4.0, Draxler and Rolph, 2003; using GDAS wind fields) indicated that contributing events were attributable to low-level (MBL) synoptic transport from Australia or New Zealand (e.g., **Figure 3**).

The corresponding Southern Ocean CO_2 transect (**Figure 2B**) shows enhancements associated with each of the three synoptic transport events identified in the radon record. Of equal interest, however, is the structure evident in the composite CO_2 transect that is not associated with recent terrestrial influence (e.g., Stavert et al., 2018). This demonstrates the utility of high-quality shipborne radon observations in helping to isolate CO_2 contributions arising from oceanic processes, terrestrial influences in excess of 3-weeks old or shipping exhaust.

A broad region of enhancement in both radon and CO_2 is evident between 59 and 61°S. Back trajectories corresponding to the largest of these events (not shown) were not associated with synoptic MBL transport events, but were found to have recently descended from above the MBL. A mechanism for such transport events, postulated by Humphries et al. (2016), is terrestrially influenced free tropospheric air subsiding or intruding into the MBL in the vicinity of the circumpolar trough ("Polar Front"). This may provide further insight to high particle concentration events observed previously in the region (e.g., Humphries et al., 2015, 2016). Decay-correcting the observed radon concentrations based on modeled tropospheric transport times may provide a means of constraining the magnitude of the original terrestrial influence on the tropospheric air mass.

The last pronounced feature of **Figure 2A** is a "ramping" of radon concentration between 64 and 67°S (over ∼350 km). This increasing terrestrial influence on MBL air masses approaching the Antarctic coast in summer-autumn is attributable to two separate influences: a local Antarctic radon contribution from coastal exposed rocks (Evangelista and Pereira, 2002; Taguchi et al., 2013; Burton-Johnson et al., 2016; Chambers et al., 2017), and a remote terrestrial contribution within the outflow of tropospheric air masses that are descending over the Antarctic continent (Polian et al., 1986; Chambers et al., 2014, 2017). The fact that there is a step increase in CO_2 within this same zone indicates that the outflow of subsiding tropospheric air is a large contributing factor, as the CO_2 increase likely represents air that has not been in recent contact with the oceanic CO_2 sink (Stavert et al., 2018). The ramping of radon concentrations may be partially a result of radioactive decay, indicating that the net northward movement of these outflowing air masses is quite slow (as expected of the strong easterly flow south of the circumpolar trough).

Seasonality of Terrestrial Influence in the Mid-Southern Ocean

Despite the isolation of MI (2000 km from mainland Australia, 1500 km from Tasmania, 1000 km from New Zealand), high radon concentrations (1500–3000 mBq m^{-3}) were observed on average 4 times a year. Based on the conditions necessary to measure a significant ($\geq$200 mBq m^{-3}) local influence, i.e., a wind sector of 180–270° (**Figure 1**, inset 2) and wind

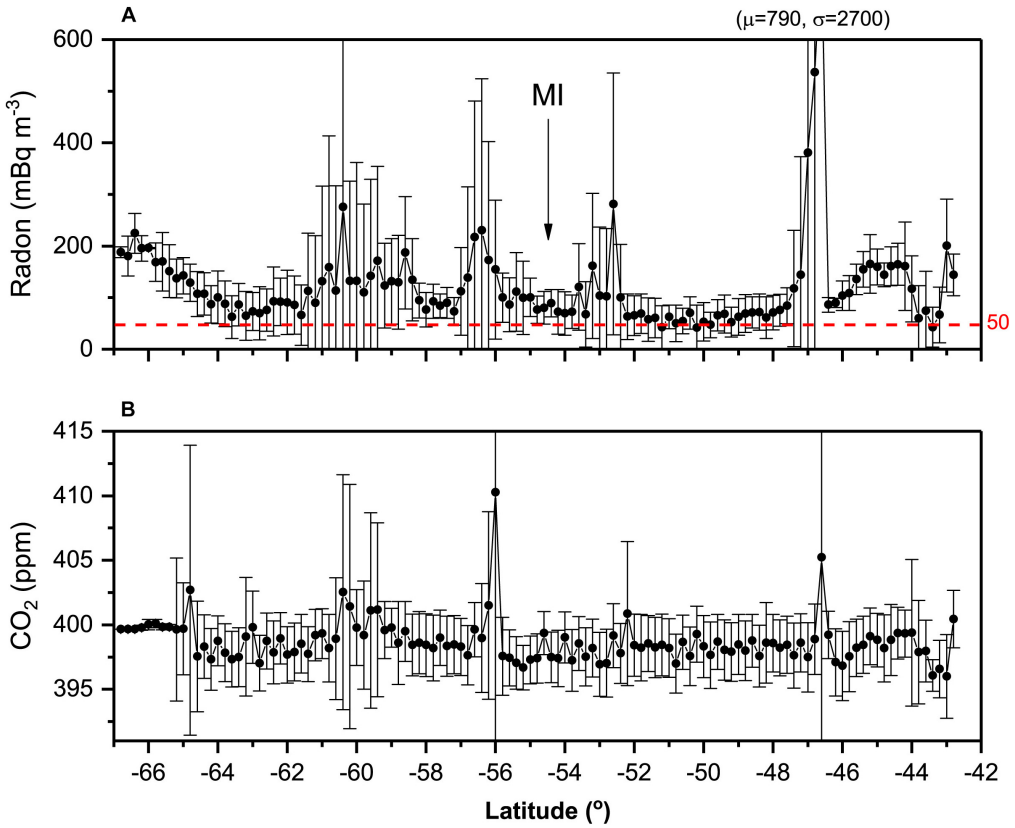

FIGURE 2 | 5-track composite of **(A)** radon, and **(B)** carbon dioxide, concentrations (0.2° latitude bin means) between 45 and 67°S of Southern Ocean MBL. Whiskers represent ± 1σ. Approximate location of Macquarie Island is marked.

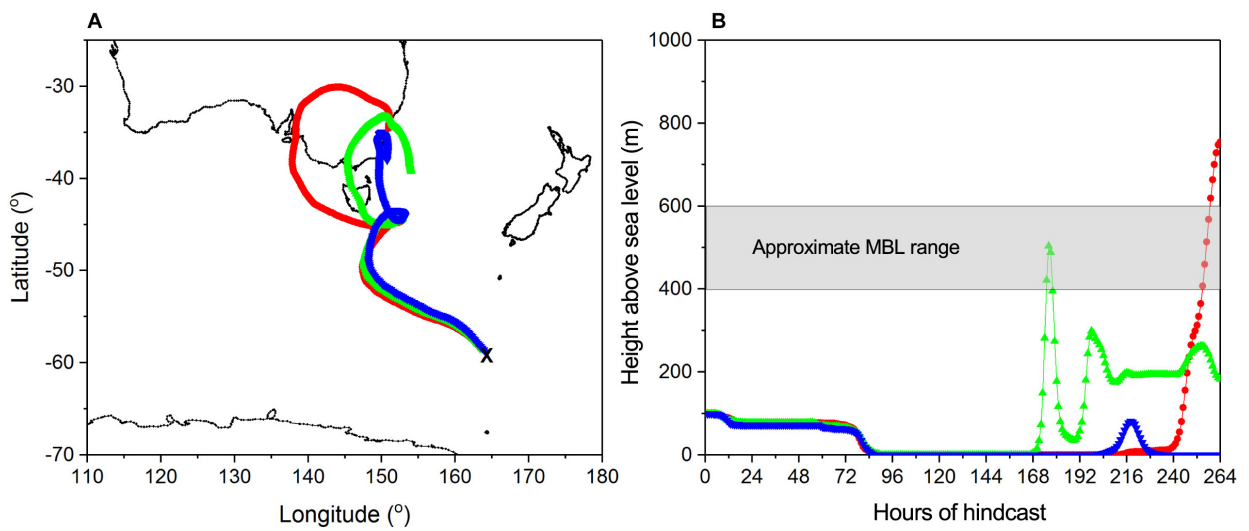

FIGURE 3 | Back trajectories, **(A)** x-y and **(B)** x-z projections, associated with a mid-Southern Ocean radon enhancement event originating from south eastern Australia observed by the RV *Investigator*. Typical height range of the mid-Southern Ocean marine boundary layer inversion indicated.

speeds < 10 m s^{-1}, less than 0.5% of events > 200 mBq m^{-3} in **Figure 4A** could be attributed to local island influences. When compared to radon in air masses leaving mainland Australia (50th – 75th percentile events 2000–4000 mBq m^{-3}; Zahorowski et al., 2013), this indicates that it is possible for terrestrially influenced air masses

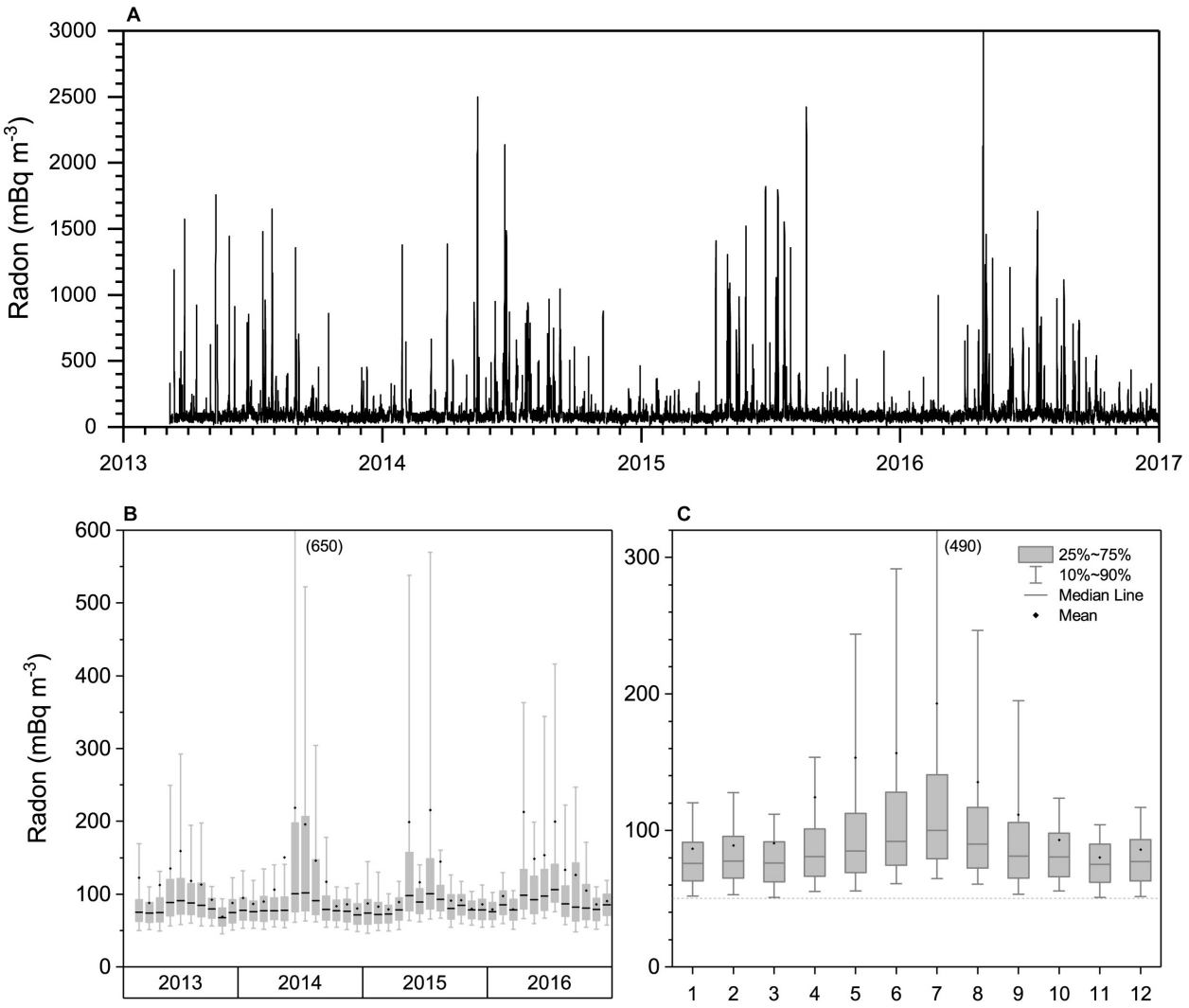

FIGURE 4 | (A) Hourly, and **(B,C)** monthly distributions of radon concentrations at Macquarie Island based on a 4-year (2013–2016) composite of hourly observations. Refer to key for distribution box-plot details.

to travel far into the Southern Ocean without substantial dilution.

Monthly means and distributions of radon (**Figures 4B,C**) indicated a pronounced seasonal cycle characterized by a winter maximum and summer minimum. This cycle is thought to be largely attributable to the seasonal migration (north in winter, south in summer) of the surface divergence zone between the Hadley and Ferrel Cells (the "Subtropical ridge"), the average position of which is ∼30°S (see Figure 5 of Doering and Saey, 2014; Williams et al., 2017). Back trajectories calculated by Williams et al. (2017) indicated that even the seasonal cycle in the 10th percentile values is caused by vestigial continental influences.

To investigate possible wind speed influences on mid-Southern Ocean radon concentrations we calculated monthly wind speed distributions (not shown). The seasonal cycle, characterized by a broad March–October maximum (monthly median wind speeds of 10.3–11.3 m s^{-1}) and November–February minimum (monthly median wind speeds 8.8–10.3 m s^{-1}), had a low amplitude and did not match well with the seasonal radon cycle. Clearly, the seasonality of wind speed at this site is not the dominant influence on the seasonality in MBL radon concentrations.

Mean summer-autumn radon in the RV *Investigator* data at 54.5°S (**Figure 2A**) was 90–100 mBq m^{-3}. This agrees well with the January–April monthly mean MI radon concentrations (**Figure 4A**). Agreement of mean concentrations within ∼10 mBq m^{-3} (i.e., ∼10%) between independently calibrated two-filter detectors provides confidence in comparisons drawn between other two-filter detectors in the Southern Ocean Network. Further confidence in the absolute radon concentrations reported by the RV *Investigator* is given by the estimate of 50 mBq m^{-3} for MBL air masses in the 49–51°S region of the Southern

Ocean, as also reported by the independently operated 5000 L radon detector (LLD < 10 mBq m^{-3}) at Cape Grim Station, Tasmania (Williams et al., 2017; Crawford et al., 2018).

It has already been demonstrated (**Figure 2A**) that minimum MBL radon concentrations in summer-autumn are higher toward the middle of the Southern Ocean than around 49 or 63°S. In addition, **Figure 4C** demonstrates that the magnitude of this enhanced terrestrial influence in the Southern Ocean varies seasonally, and is largest in winter.

Approaching the Antarctic Coast

In late summer 2017 (20-January to 25-February) the RV *Investigator* conducted a sea floor mapping exercise 200 – 400 km east of Casey Station, between about 50 and 150 km off the Antarctic coast (**Figure 1**, inset 1). Periods of considerable variability in trace atmospheric constituents and cloud condensation nuclei (CCN; TSI CPC Model 3776, size range > 3nm) were observed during this voyage. We investigate here whether they could be attributed to similar processes as the free-tropospheric particle events observed near the circumpolar trough ("Polar Front") by Humphries et al. (2015, 2016).

This far offshore, little diurnal variability in MBL depth or radon concentration was expected given the ocean's heat capacity, and the fact that the open ocean is a weak radon source without a diurnal cycle (Schery and Huang, 2004; Zahorowski et al., 2013), respectively. Over the course of the 37-day mission, however, amplitudes of the radon diurnal cycle varied from 0 to 50 mBq m^{-3} (**Table 2**). The amplitudes reported in **Table 2** were calculated as the difference between 5-h means centered on the daily maximum and minimum hourly values.

On some days the diurnal cycle was characterized by a daytime maximum and on others a nocturnal maximum (**Table 2**; **Figure 5A**). While the magnitudes of these diurnal cycles are 2–3 orders of magnitude lower than typically found at inland terrestrial sites (e.g., Chambers et al., 2015), the absolute accuracy of the two-filter detectors (<12% on a 1-h count for Rn > 100 mBq m^{-3}; see Sites and Equipment), nevertheless provides confidence in the observed differences discussed below. Specifically, the uncertainty on each diurnal cycle amplitude (DU) is twice the uncertainty of the daily maximum or minimum estimate ($\frac{12\%}{\sqrt{5}} = 5.4\%$); i.e., DU = 2(5.4%) = 10.8% ≈ 14 mBq m^{-3}. While this level of uncertainty can't guarantee clear distinction between type 2 and 3 events in **Table 2**, it is sufficient to distinguish type 1 and type 4 events, and each of these events from either type 2 or 3.

Type 1 days were characterized by daytime radon around 140 mBq m^{-3} (**Figure 5A**), wind directions from the southeast (**Figure 5B**; along the local coastline, **Figure 1** inset 1), relatively consistent wind speeds (**Figure 5C**), and no pronounced diurnal cycle in CCN (**Figure 5D**). In this case the radon diurnal cycle amplitude (Rn_{AMP} = 25 mBq m^{-3}) is likely attributable to changes in the coastal radon source function related to the diurnal freeze-thaw cycle, and this coastal air mixing to the local MBL (e.g., Bromwich et al., 1993). The January mean daily maximum and minimum coastal temperatures at Casey were +2.3 and −2.5°C, respectively.

TABLE 2 | Daily summary of MBL radon concentration characteristics observed from the RV *Investigator* between 20-January and 25-February 2017.

Type	Diurnal radon amplitude (RnAMP)	# days	Description
1	8 – 50 mBq m^{-3}	18	Daytime maximum
2	0 – 4 mBq m^{-3}	9	No significant cycle
3	7 – 12 mBq m^{-3}	5	Nocturnal maximum (weak katabatic outflow)
4	30 – 50 mBq m^{-3}	5	Nocturnal maximum (strong katabatic outflow)

Type 2 days had no consistent radon diurnal cycle and wind directions that changed from southerly to south-easterly, consistent with the passage of cyclonic synoptic systems. On overcast summer days coastal air temperatures typically peaked between −2 to 0°C, leading to less of a change in the coastal radon source function. Indeed, diurnal mean radon on these days was similar to the nocturnal concentrations for Type 1 days. The diurnal course of CCN on Type 2 days seemed to closely correspond to diurnal changes in wind speed and direction (oceanic fetch is more recent for south easterly air masses), indicating that salt spray was likely a dominant component of these aerosols.

Type 4 days were characterized by Rn_{AMP} = 46 mBq m^{-3}, with a late morning minimum (**Figure 5A**). Until shortly after midnight the wind direction was roughly parallel to the coast and wind speeds were decreasing. From 0100 to 0200 h wind direction swung round to the south and southwest, almost perpendicular to the local coastline, and wind speeds increased by ∼3 m s^{-1}. During this period, CCN increased to values higher than observed under the windiest conditions of Type 2 days, indicating that their origin is unlikely to relate to sea spray. Type 3 days shared many characteristics with Type 4 days, but to a lesser degree (reduced morning radon minimum, smaller and delayed morning peak in CCN).

In **Figure 6** we investigate Type 4 days in more detail. Radon variability in the offshore flow (0400–1100 h) was lower than for periods of alongshore flow (**Figure 6A**). Air masses associated with offshore flow were also drier (**Figure 6B**). Ozone concentrations from 0400 to 1100 h were higher and less variable, and an increase was observed in all supersaturation ranges (0.25 – 1.05%) of CCN. The combination of timing, wind direction and air mass humidity suggest these morning events on Type 4 days are associated with katabatic outflow from the Antarctic mainland.

Since air within Antarctic katabatic flow events originates in the free-troposphere (Nylen et al., 2004), and crosses the coast at right angles (rather than traveling along or obliquely to it), there is a reduced opportunity for fetch across exposed rock, thereby reducing the average radon enhancement above "background" levels (30–50 mBq m^{-3}) during outflow events.

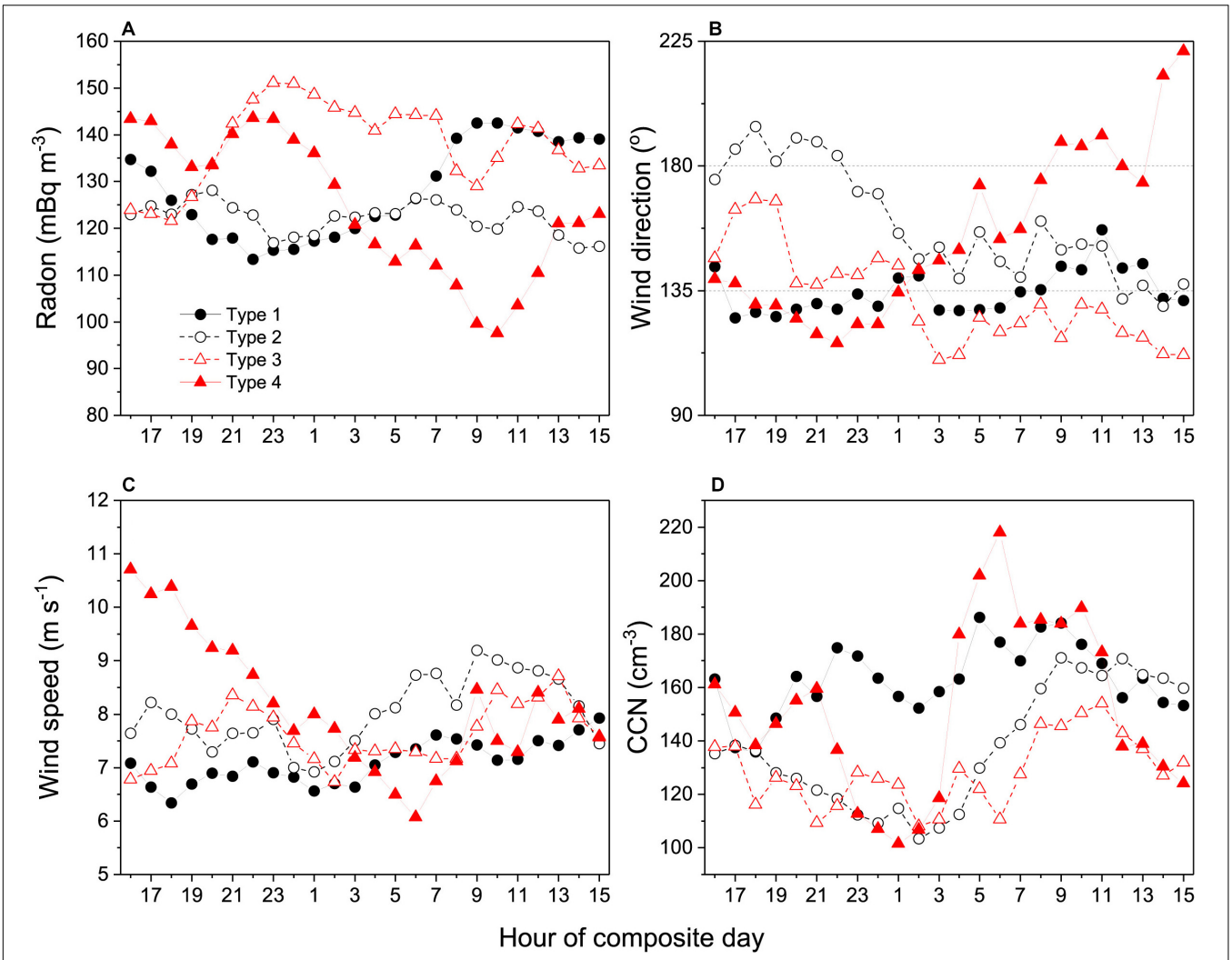

FIGURE 5 | Diurnal composite **(A)** radon (means), **(B)** wind direction (medians), **(C)** wind speed (means), and **(D)** CCN (means across all supersaturation ranges; see **Figure 6D**), as observed from the RV *Investigator* for each day type described in **Table 2**. Time axis shifted to focus on the nocturnal period.

Having originated from the free-troposphere, these air masses also start out considerably drier than MBL air masses, and with higher ozone content. With their origin in mind, the observed increase in CCN of these recently tropospheric air masses is likely attributable to sulfate influences in the free-troposphere (Humphries et al., 2016; Obryk et al., 2018). In these regions the sulfate could be of anthropogenic, marine or volcanic origin (Graf et al., 2010). Related to these observations, Jaenickle et al. (1992) also reported an increase of CCN in subsiding tropospheric air at Neumayer station. As expected, back trajectories (not shown) confirmed that the free-tropospheric contributions to MBL air between 0400 and 1100 h on the outflow days of this study did not derive from the same tropospheric injection processes as those described by Humphries et al. (2016).

Five strong katabatic events in 37 days (**Table 2**), a relative frequency of ∼14%, is very similar to the 12% event frequency of pronounced katabatic flow in summer at Jang Bogo station reported by Chambers et al. (2017). The timing of the peak outflow was delayed by about 3 h compared to that of coastal events reported by Chambers et al. (2017), but this can be attributed to travel time based on the vessel's distance from shore and the observed mean wind speeds of 8–9 m s^{-1}.

The relatively weak contrasts in radon and humidity between katabatic outflow and MBL air masses shown in **Figures 6A–C** compared to the results of Chambers et al. (2017) and Section "Continental Antarctica" below indicate that considerable mixing (or ocean-atmosphere exchange) of the outflow air mass has occurred in transit to the RV *Investigator*. While this mixing prevents the reliable characterisation of tropospheric air in the outflow events in the way that can be achieved at coastal Antarctic sites (see Continental Antarctica), our findings clearly demonstrate that shipborne aerosol and trace gas measurements near the Antarctic coast should separately treat katabatic outflow days, or consider diurnal sampling windows, since the characteristics of recently tropospheric

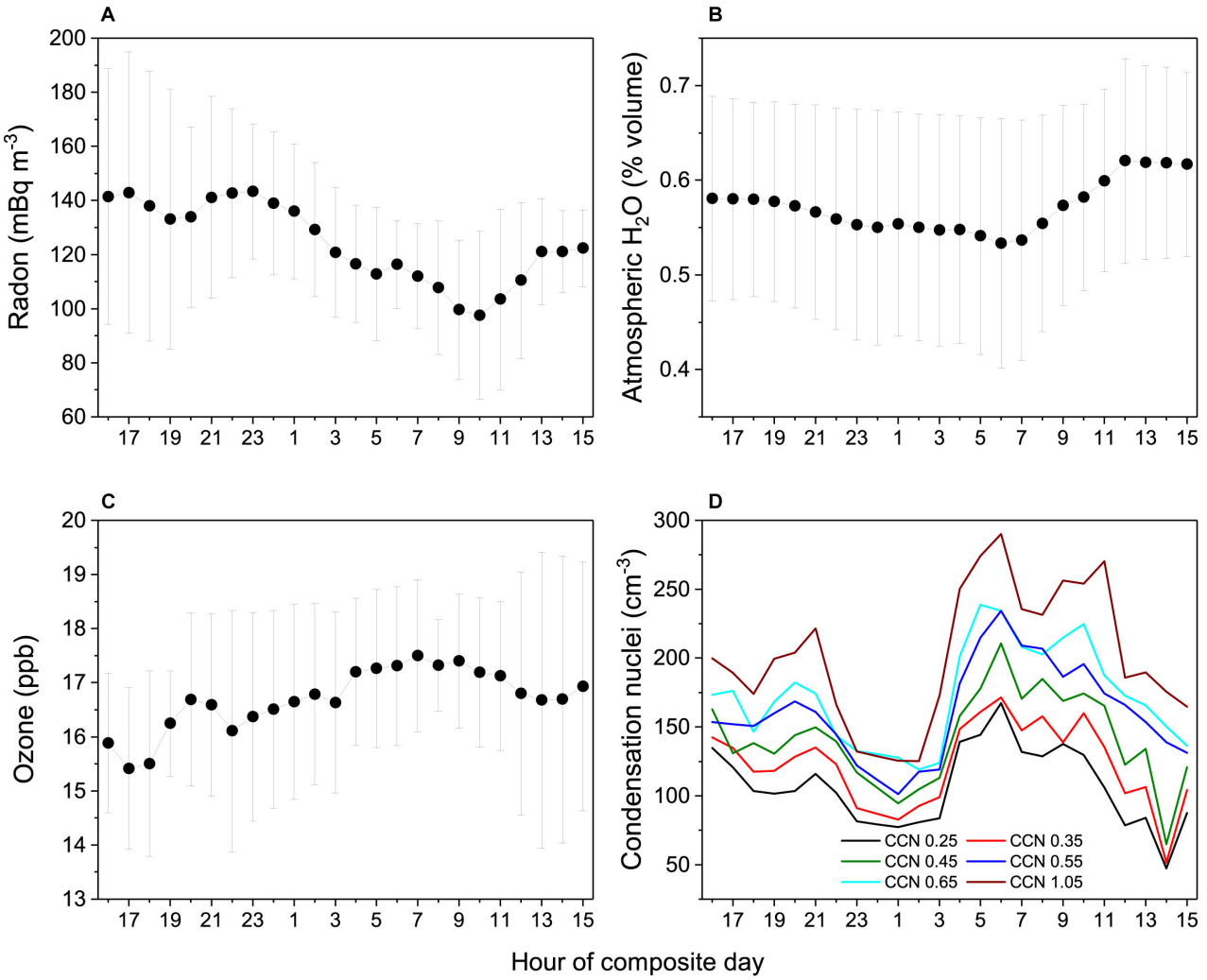

FIGURE 6 | Diurnal composites of **(A)** radon, **(B)** % volume of water, **(C)** ozone, and **(D)** CCN (cm^{-3}) within supersaturation ranges 0.25 – 1.05%, based on 5 days of katabatic outflow conditions. Whiskers represent hourly ± 1σ for the 5 days composite.

outflow air masses (i.e., potentially containing remote terrestrial influences) will not be representative of local conditions and may temporarily modify local ocean-atmosphere exchange processes.

Continental Antarctica

Coastal Sub-Antarctic (King Sejong Station: 62.2°S)

King Sejong Station is among the northernmost of the Antarctic bases (**Figure 1**), being about 500 km further north than most of the Antarctic coastline. Since the station is well removed from the topographic influences of the East Antarctic ice sheet, which reaches elevations above 4000 m a.s.l., of the Antarctic bases in this study KSG is best suited for year-round characterisation of marine baseline air masses of the remote Southern Ocean. In addition, the tip of the Antarctic Peninsula is also closer than any other part of continental Antarctica to another Southern Hemisphere continent (South America), so it also provides unique opportunities to observe the influence of recent direct transport of natural and anthropogenic terrestrial emissions to the frozen continent (e.g., Pereira, 1990; Pereira et al., 2004; Chambers et al., 2014).

Peak KSG radon concentrations (1500–2000 mBq m^{-3}; **Figure 7A**) were lower than at MI, despite KSG being closer to South America than MI is to Australia. This is attributable to the combination of limited land fetch across South America (Pereira, 1990; Chambers et al., 2014), and high soil moistures in southern Chile.

Summer median KSG radon concentrations were 50–55 mBq m^{-3} (**Figures 7B,C**), similar to the minimum 0.2° latitude bin mean values reported for this zone by the RV *Investigator* (**Figure 2A**), but lower than the corresponding MI values (75–80 mBq m^{-3}; **Figure 4C**). This difference provides further independent confirmation of the small mid-Southern Ocean radon enhancement observed in the RV *Investigator* composite transect (**Figure 2A**). It should be noted here that, due to the

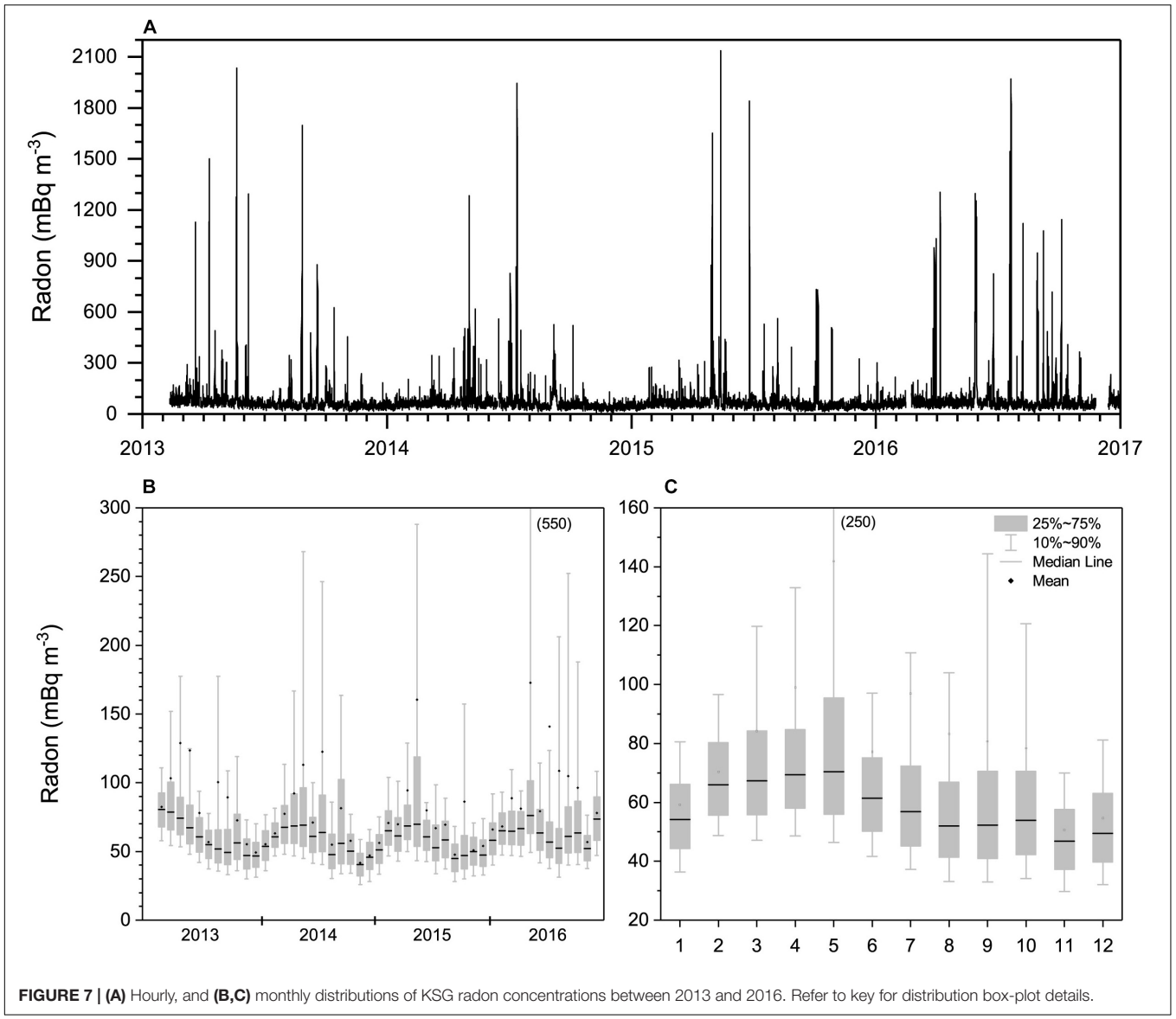

FIGURE 7 | (A) Hourly, and **(B,C)** monthly distributions of KSG radon concentrations between 2013 and 2016. Refer to key for distribution box-plot details.

station's location (see Chambers et al., 2014), many KSG air masses with extensive oceanic fetch have to traverse at least ∼2 km of King George Island before reaching the site. Based on typical radon fluxes, mixing depths and wind speeds reported in Chambers et al. (2014), this terrestrial influence could enhance oceanic fetch radon concentrations by 5–10 mBq m^{-3}.

The KSG radon seasonal cycle (**Figures 7B,C**) was quite distinct from that at MI. While minimum values were observed at both sites between November and January, peak values at KSG were bimodal, occurring in March-May and September–October. The latitude of KSG is close to the mean location of the circumpolar trough (convergence zone between the Ferrel and Polar Cells). Consequently, the seasonal migration of the circumpolar trough results in KSG switching between the influence of mid-latitude westerlies and Polar easterlies. In the non-summer months the synoptic cyclone track within the circumpolar trough is well located to bring air masses from the tip of South America to the station (Pereira et al., 2006 and references therein; Chambers et al., 2014).

Coastal Antarctica

Dumont d'Urville (66.7°S)

Two of the RV *Investigator* transects summarized in Section "The Southern Ocean in Cross-Section" approached the Antarctic coast near Dumont d'Urville (**Figure 1**). Inland from DDU the elevation reaches 2000 m a.s.l. within 200 km, before continuing up to >4000 m a.s.l. at the highest point of the Antarctic Plateau. Consequently, DDU is ideally situated to separately characterize long-term Southern Oceanic MBL air masses, as well as tropospheric air that has recently subsided over the Antarctic Plateau and comes down as katabatic flow events.

Peak DDU radon concentrations (180 – 275 mBq m^{-3}; **Figure 8**) were an order of magnitude less than MI or KSG values,

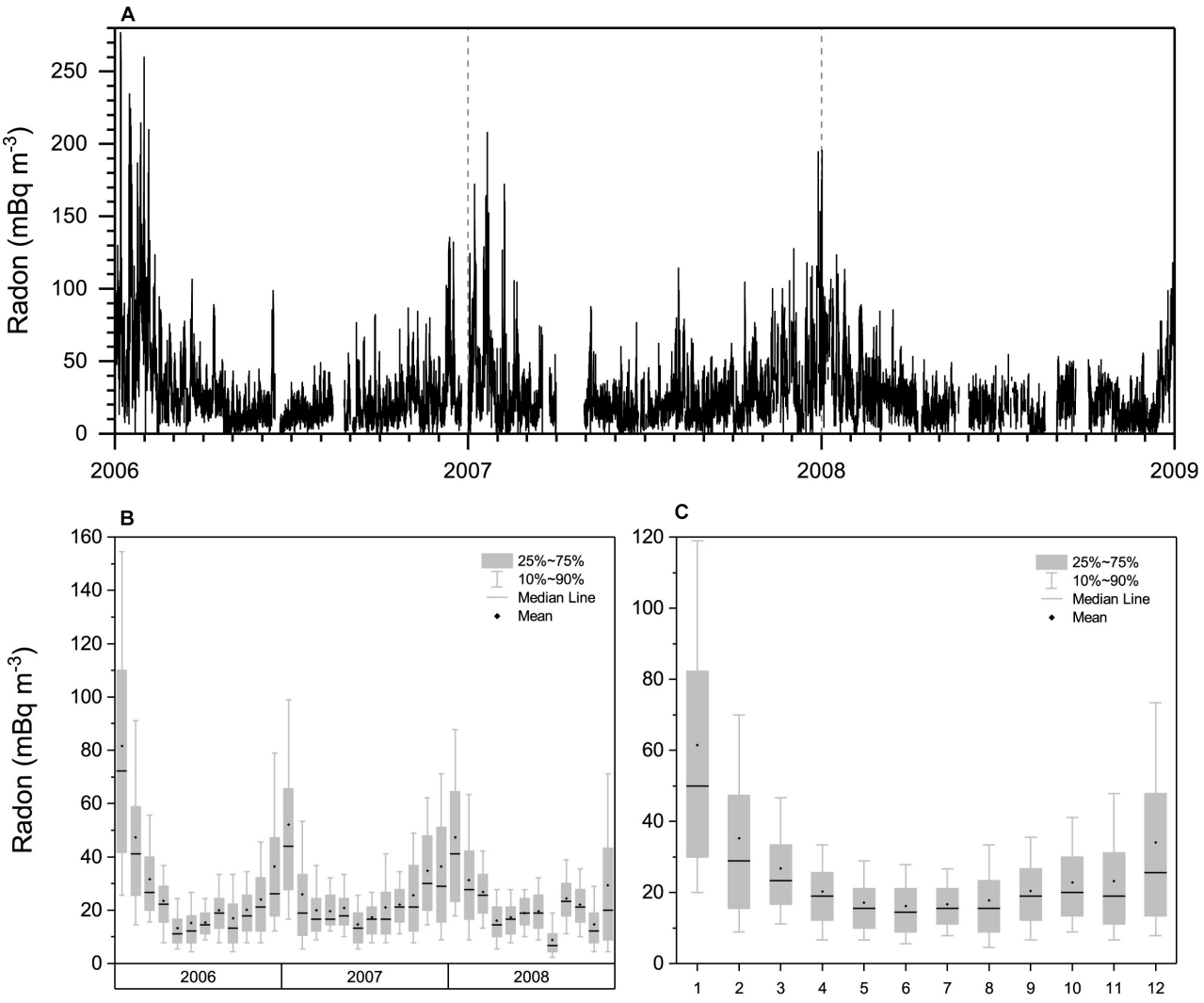

FIGURE 8 | (A) Hourly, and **(B,C)** monthly distributions of DDU radon concentrations between 2006 and 2009. Refer to key for distribution box-plot details.

presumably because the nearest upwind non-frozen terrestrial fetch is 2500 – 3000 km away. However, the seasonal DDU radon cycle reported here (18 – 61 mBq m^{-3}, based on monthly means), was also less than that reported by Polian et al. (1986) for DDU (25 – 65 mBq m^{-3}), and less than the seasonal cycle at Mawson (67.5°S) (30 – 130 mBq m^{-3}; Chambers et al., 2014). Furthermore, Ui et al. (1998) reported spring-summer daily mean radon concentrations at the coastal station of Syowa (69°S) between 150 and 270 mBq m^{-3}. Potential factors contributing to this discrepancy have been discussed in Section "Sites and Equipment."

Similar to MI, the seasonal DDU radon cycle was unimodal, although peak concentrations occurred in mid-summer (**Figure 8**). Three factors are thought to have contributed to the summer increase in DDU radon concentrations: (i) the southward shift of the circumpolar trough permits passing cyclonic weather systems to bring air containing vestigial terrestrial influences from deeper within the Southern Ocean MBL directly to DDU; (ii) a greater amount of exposed rock and shallow coastal water at this time gives rise to an increased local radon flux from land and ocean; and (iii) tropospheric air descending over Antarctica in summer typically has experienced more recent terrestrial influence than corresponding winter air masses.

To further investigate these possible influences we employed a recently developed technique to separate air masses of different fetch at coastal East Antarctic sites (see Section 3.5 of Chambers et al., 2017). Here, the multi-year dataset was analyzed in 24-h blocks (defined from 1400 h to 1300 h the following day), each of which were assigned a category of "katabatic," "local" or "oceanic" based on the mean 2-week high-pass filtered absolute humidity within an 8-h window (0000–0700 h) typically associated with katabatic flow. Days with the lowest 20% absolute humidity over this 8-h window are most likely to have experienced katabatic flow events. Days with the highest 20% absolute humidity over this 8-h window have experienced

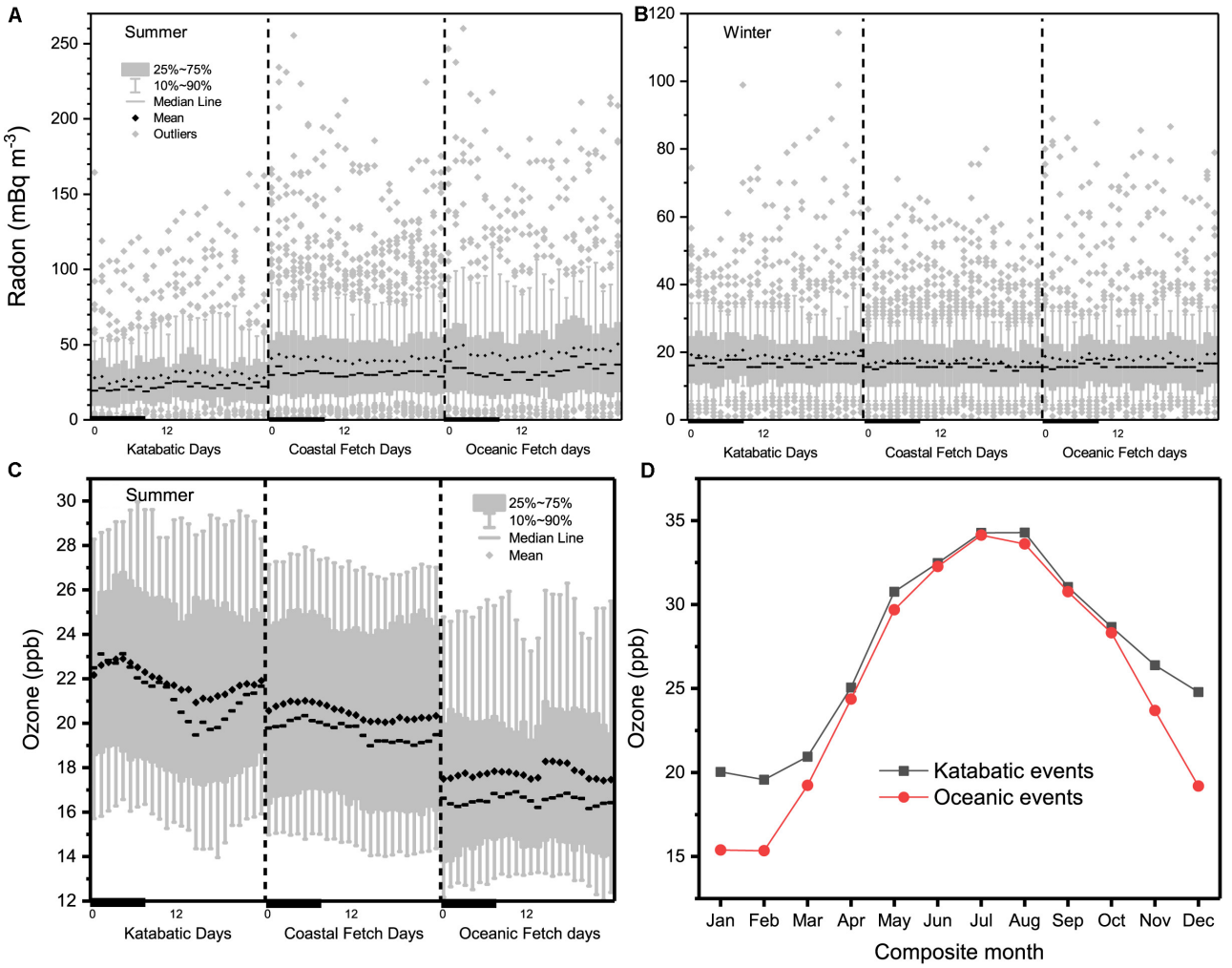

FIGURE 9 | Diurnal composite **(A,B)** radon, and **(C)** ozone distributions, for days containing periods of katabatic, coastal and oceanic fetch at DDU, based on absolute humidity in the window 0000–0700 h (see text and plot key for details); **(D)** comparison of monthly mean ozone in katabatic and MBL air masses, at DDU based on observations from 2006 and 2008.

the most consistent oceanic fetch (i.e., arrived at the site most directly from the ocean). All remaining days (60% of the observations) were placed in the "coastal fetch" category (**Figures 9A,B**). Since the technique relies upon a measure of absolute humidity to assess fetch categories, as opposed to wind speed and direction or other meteorological quantities, it is capable of distinguishing between downslope flow that is truly katabatic, and downslope flow that has been synoptically forced.

While results are presented here as full diurnal composites (0000 – 2300 h), the fetch analysis described above only strictly applies to the 0000–0700 h diurnal window, which has been marked with a bold line on each plot. Across the edges of the 24-h compositing window (i.e., between and close to the hours 1300–1400 h), discontinuities can arise due to edge effects of the compositing process (e.g., **Figure 9C**). Wind direction for oceanic fetch within the 8-h window was 110–120° and changed to 140–150° under katabatic conditions.

The highest mean DDU radon concentrations in summer (45–50 mBq m^{-3}) occurred under oceanic fetch conditions (**Figure 7A**, RHS), consistent with expected radon concentrations for air in equilibrium with the Southern Ocean surface (30–50 mBq m^{-3}; Zahorowski et al., 2013; Chambers et al., 2016). Outlier values of 90 – 265 mBq m^{-3} for these events indicate that oceanic air masses occasionally exhibit a vestigial terrestrial influence, likely attributable to long-range synoptic transport within the MBL (though possibly also related to subsidence near the circumpolar trough, see The Southern Ocean in Cross-Section).

On summer days, when coastal fetch prevailed in the 0000–0700 h diurnal window, mean radon concentrations were slightly lower (40–45 mBq m^{-3}; **Figure 9A**, center), despite median values for oceanic and coastal events being almost identical. The reduced skewness of coastal events (90th percentile concentrations of 75–90 mBq m^{-3} compared with

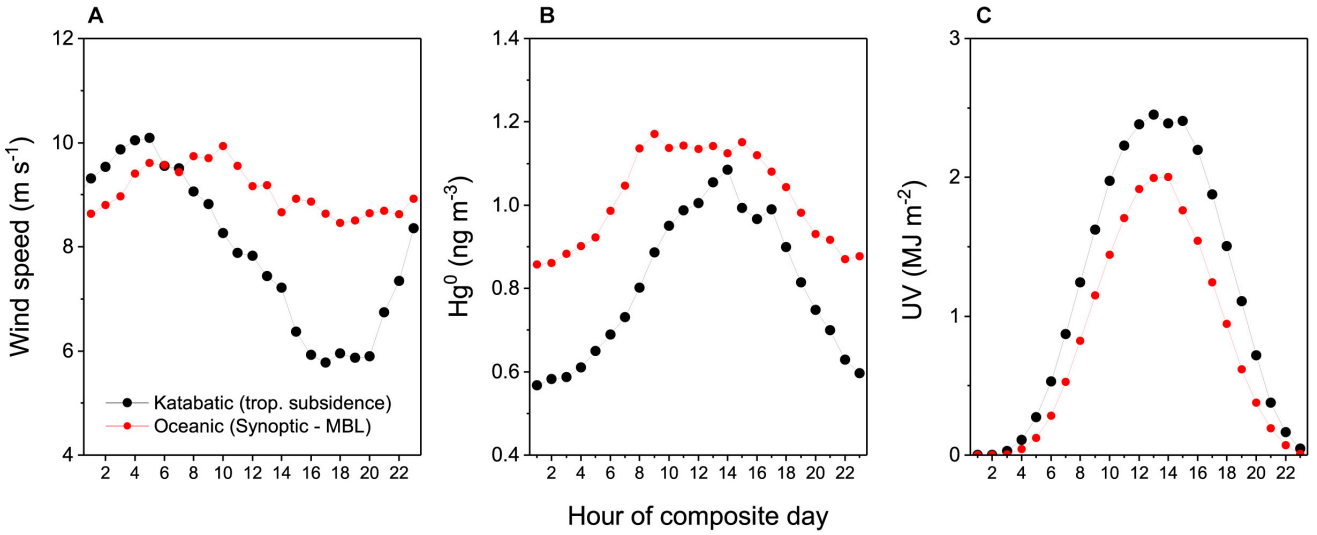

FIGURE 10 | Diurnal composite **(A)** wind speed, **(B)** gaseous elemental mercury, and **(C)** ultraviolet radiation, at DDU (January-2012 to May-2015).

95–100 mBq m^{-3} for oceanic events), is consistent with coastal events receiving low radon contributions from small, local coastal sources as discussed by Evangelista and Pereira (2002) and Chambers et al. (2014, 2017).

The lowest mean DDU radon concentrations in summer (24–29 mBq m^{-3}) were associated with katabatic drainage events (from the free-troposphere/Antarctic Plateau). Unlike boundary layer air masses, free-tropospheric air masses have had an opportunity to be removed from all radon sources (terrestrial or oceanic) for a period of time, enabling them to achieve radon concentrations below even the 30–50 mBq m^{-3} associated with clean marine air. However, 10% of katabatic flow events (the marked outliers in **Figure 9A**, LHS) had radon concentrations between 55 and 165 mBq m^{-3}, suggesting terrestrial influence within the past 2–3 weeks (ignoring dilution within the troposphere). Vertical profiles near DDU reported by Polian et al. (1986) also indicated an increase in radon concentrations from ∼15 mBq m^{-3} near the surface to ∼80 mBq m^{-3} between 2000 and 3000 m a.s.l., which is near the elevation of genesis for katabatic flow.

In summer there is ∼600 m of partially-exposed (∼50%) rock and soil to the south (inland) of DDU station (Preunkert et al., 2012). At speeds typical of katabatic flow (6–12 m s^{-1}, gusting to 23 m s^{-1}), even assuming a large radon flux (20 mBq m^{-2} s^{-1}), and shallow mixing depths for these wind speeds (∼100 m), it is very unlikely that this fetch could contribute more than 10–15 mBq m^{-3} to the observed concentrations in the katabatic flow. Consequently, the bulk of the signal must arise from terrestrial influences within the tropospheric air.

Contrary to the summer results, the highest mean DDU radon concentrations in winter (**Figure 9B**) were in the katabatic flow events (18–21 mBq m^{-3}; 27% lower than corresponding summer events). Peak concentrations of the winter katabatic events were 35–80 mBq m^{-3}, indicating a summer-winter reduction in terrestrial influence on tropospheric air over DDU of almost a factor of two. Median winter radon concentrations of coastal and oceanic events were the same (∼16 mBq m^{-3}), although mean values of the events coming most directly from the ocean were around 10% higher. The lower concentrations for coastal events are likely attributable to a greater air mass fetch time over ice, from which no radon is emitted, rather than open ocean, as previously mentioned by Weller et al. (2014) for radon observations at Neumayer Station. Based on baseline radon concentrations of 30–50 mBq m^{-3}, and the 3.8-day radon half-life, winter "oceanic" DDU air masses have likely spent 4–6 days traveling over ice.

To demonstrate the ability of this technique to separately characterize dominant fetch regions of coastal Antarctic air masses, we briefly investigate some other DDU trace atmospheric constituents. **Figure 9C** compares diurnal composite summer ozone concentrations for katabatic, coastal fetch, and oceanic fetch days. Within the 8-h analysis window mean summer ozone concentrations were highest in katabatic flow (from the Antarctic Plateau) and lowest under oceanic fetch conditions.

The diurnal cycle of ozone at DDU was largest for days that experienced morning katabatic flow events (**Figure 9C**). The amplitude of this cycle was 2 (3) ppb based on hourly means (medians). These days typically experienced high radiation levels (e.g., **Figure 10C**) and lower mean wind speeds when averaged over the entire diurnal cycle. The ozone cycle was characterized by a mid-afternoon minimum and an early morning maximum at the time of peak katabatic flow, as evident in **Figure 10A** (black filled circles). Conversely, no consistent diurnal cycle was evident under oceanic fetch conditions (excluding the edge effect of the diurnal compositing procedure in the early afternoon). On coastal fetch days the amplitude of the diurnal ozone cycle was smaller, with the morning peak occurring a few hours later (**Figure 9C**, middle). Based on back trajectory fetch analyses Legrand et al. (2016) also found that ozone concentrations of air masses arriving at DDU in summer from the Antarctic interior

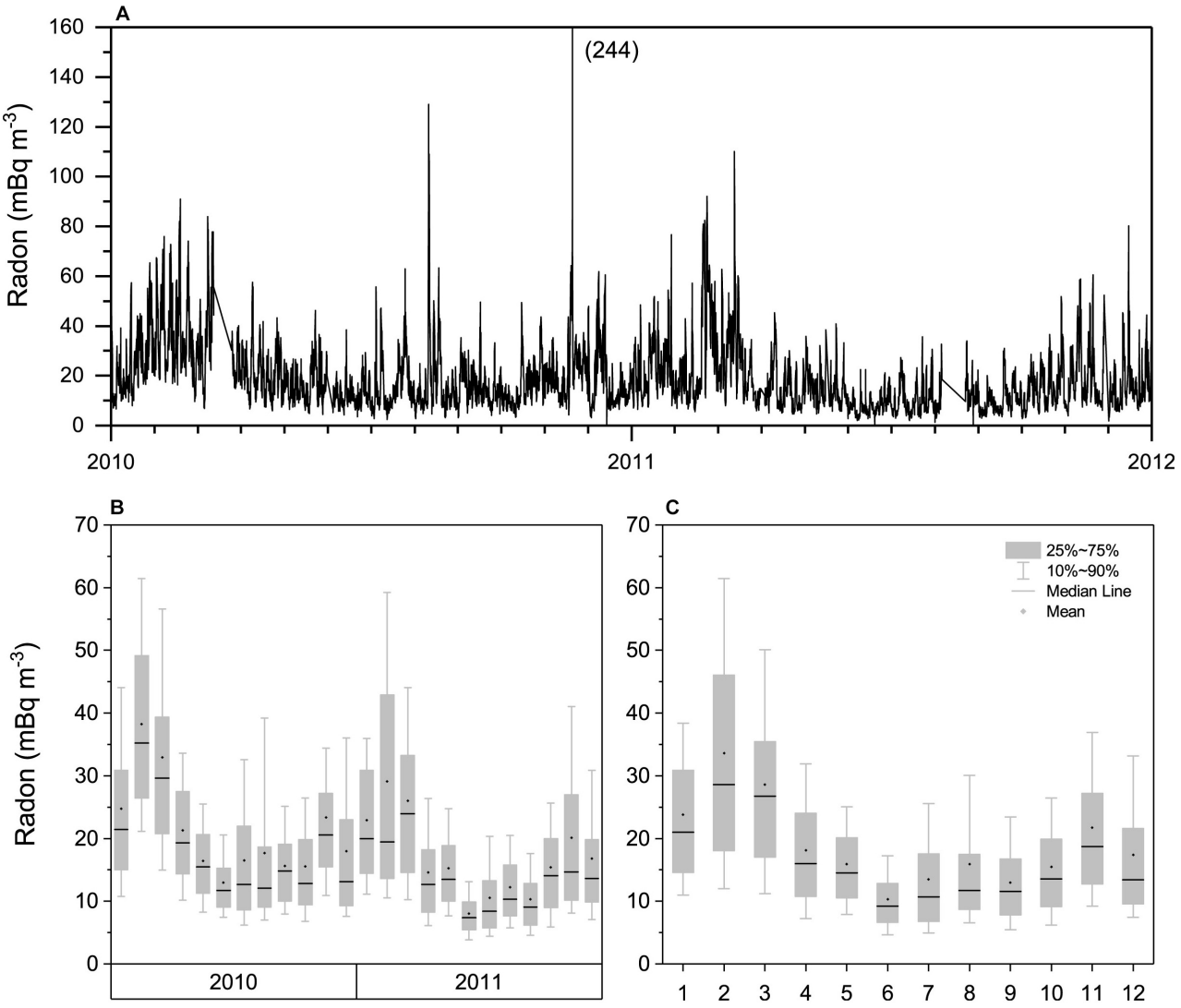

FIGURE 11 | (A) Three-hourly, and **(B,C)** monthly distributions of NM radon concentrations for 2010 and 2011. Refer to key for distribution box-plot details.

were higher than those of oceanic air masses, in some cases by up to 10 ppbv.

We calculated the daily mean ozone concentrations each month (using only observations within the 8-h analysis window) for katabatic flow and oceanic fetch events and prepared a 3-year composite (**Figure 9D**). In the summer months (November–February) we found that air descending from the Antarctic Plateau in katabatic flow events had monthly mean ozone concentrations around 5 ppb higher than oceanic air masses. The difference was much lower for the remainder of the year, but the tropospheric concentrations were always higher than those of oceanic air masses.

We processed a separate set of GEM observations at DDU (January-2012 to May-2015) in the same way to separate katabatic flow and oceanic fetch events (**Figure 10**). Mindful of possible temperature or UV-related GEM production in the coastal Antarctic environment (Angot et al., 2016c; Bargagli, 2016), we looked at the difference between summer mercury concentrations of katabatic flow and oceanic fetch events when UV levels were lowest (2300–0300 h; **Figure 10C**). We found that the katabatic flow was depleted around 0.3 ng m^{-3} in GEM compared to long-term oceanic air masses. This difference is of the same sign, but larger in magnitude, than that initially reported by Angot et al. (2016b) based on a back trajectory method of katabatic flow event identification. Based on estimated values of GEM in the Antarctic free troposphere of 0.9–1.0 ng m^{-3} [see Antarctic Plateau (Dome Concordia: 75°S, 3,233 m a.s.l.); and Song et al., 2018], the recently free-tropospheric katabatic flow events must have incorporated a large amount of air from the Antarctic Plateau where nocturnal GEM concentrations in summer are relatively depleted [Antarctic Plateau (Dome Concordia: 75°S, 3,233m a.s.l.); and Angot et al., 2016c].

The higher GEM concentrations in oceanic air at DDU are consistent with a combination of natural (including oceanic,

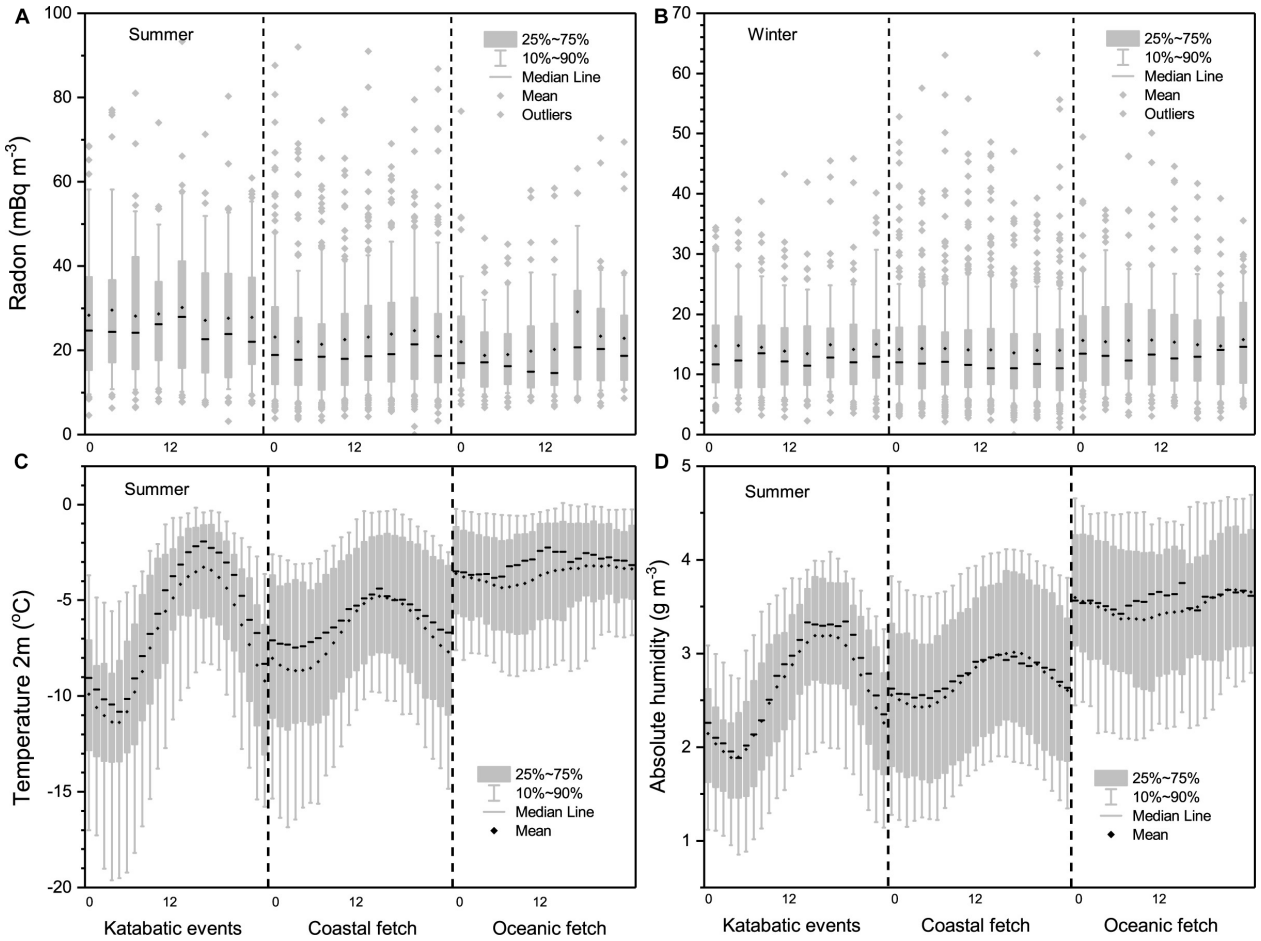

FIGURE 12 | (A,B) Comparison of summer and winter diurnal composite radon distributions for katabatic, coastal and oceanic fetch, and **(C,D)** diurnal composite summer temperature and absolute humidity values for katabatic, coastal and oceanic fetch at NM in 2010 and 2011. Refer to key for distribution box-plot details.

especially in summer and fall) and anthropogenic sources of this long-lived (∼1 year residence time; Bargagli, 2016) gas. However, our estimated summertime oceanic GEM concentrations at DDU of ∼0.86 ng m^{-3} were slightly lower than summer concentrations reported at Troll Station (235 km inland of the Antarctic coast; 0.9 – 1.1 ng m^{-3}), or at Italian Antarctic Station, Terra Nova Bay (74°41′S; 164°07′E) (0.9 ± 0.3 ng m^{-3}) (Sprovieri et al., 2002, 2010; Dommergue et al., 2010), or Amsterdam Island (∼1.0 ng m^{-3}) (Angot et al., 2014; Slemr et al., 2015; Sprovieri et al., 2016), consistent with observations at Cape Grim (Tasmania) and Singleton (NSW) (Slemr et al., 2015; Howard et al., 2017), but higher than reported by Kuss et al. (2011) for the southern Atlantic Ocean (0.72 ng m^{-3}).

Neumayer (70.6°S)

Neumayer differs from most coastal Antarctic stations in that, instead of being built on rock, the station sits on the Ekström Ice Shelf, away from potential local sources of radon. Peak 3-hourly radon concentrations at Neumayer (110 – 155 mBq m^{-3}; **Figure 11A**) were lower even than observed at DDU. While tempting to attribute these events to transport from South America, Weller et al. (2014) found little evidence for this. Rather, trajectory analyses often traced the origins of these events to the Antarctic interior. Ui et al. (1998) also reported high radon at Syowa station associated with southerly winds (from the Antarctic interior) and lower wind speeds (characteristic of anticyclonic conditions), but attributed this – we believe incorrectly – to unidentified local sources.

As for KSG the NM seasonal radon cycle was bimodal, but with peak concentrations in February and November, and a pronounced mid-winter minimum (**Figures 11B,C**). Related to these observations, a strong seasonal cycle in CCN at NM has also been reported by Weller et al. (2011), characterized by a winter minimum and broad bi-modal maximum between September and April, peaking in March. Interestingly, the seasonal cycle of CCN at South Pole (considered to be attributable to largescale atmospheric transport processes in the free-troposphere; Samson et al., 1990), shares many features with the NM radon record (**Figure 11C**); including winter minimum, spring increase, reduced values in December and peak values in February through March.

Mean radon during katabatic outflow (27–30 mBq m^{-3}) was higher than for oceanic fetch (20–22 mBq m^{-3}) (**Figure 12A**), indicating more remote terrestrial influence in the Antarctic troposphere over NM than in the MBL air masses. Evidence of the katabatic nature of the events bringing the most recently tropospheric air to NM is given in the temperature and humidity plots of **Figures 12C,D**. Temperature and absolute humidity are extremely low for summer conditions during the suspected katabatic flow events, consistent with air originating in the free troposphere and passing over the Antarctic Plateau. Thus, most of the high radon events at NM are attributable to the subsidence of tropospheric air that has experienced recent (<3-week) terrestrial influence.

In contrast to DDU, coastal air masses at NM have a lower mean radon concentration than the katabatic events. This is likely attributable to a smaller amount of exposed rock in the vicinity of NM (Weller et al., 2014). Also in contrast to DDU, oceanic air masses at NM have a lower mean radon concentration than those of katabatic air masses. This is attributable to a combination of more sea ice near NM (Weller et al., 2014; Legrand et al., 2016), and a reduced opportunity for significant recent terrestrial fetch for NM air masses.

The most extreme cases of recent terrestrial influence in the troposphere over Neumayer (55 – 90 mBq m^{-3}) were considerably less than observed over DDU (55 – 170 mBq m^{-3}). By contrast, the modeling studies of Li et al. (2008) and Albani et al. (2012) indicated a greater terrestrial influence in the free troposphere over NM than DDU. Clearly, further investigation is warranted of simulated terrestrial influence in Antarctica and the remote Southern Ocean (see also Discussion).

Outlier radon concentrations (45 – 90 mBq m^{-3}) on days dominated by coastal fetch conditions indicate that coastal exposed-rock radon sources ("local" as in Antarctic, but remote from the station) can also influence observations at this site, but far less than at DDU. For days dominated by coastal fetch conditions a weak diurnal cycle (amplitude < 5 mBq m^{-3}) was evident, but this was not significant given the variability of observations. No consistent radon diurnal cycle was observed on days that experienced morning katabatic flow events or predominantly oceanic fetch conditions (**Figure 12A**).

In summer, when sea ice extent is minimized, median radon concentrations for the most direct oceanic fetch conditions at coastal Antarctic sites should approximate the value for air masses in equilibrium with the Southern Ocean (i.e., 30–50 mBq m^{-3}). At KSG, accounting for local fetch over King George Island [see Coastal Sub-Antarctic (King Sejong Station: 62.2°S)], median oceanic fetch radon concentrations in summer were 45–50 mBq m^{-3}.

At DDU (**Figure 7A**) and NM (**Figure 10A**) median summer oceanic radon concentrations were 30–33 and 19–21 mBq m^{-3}, respectively. The difference in median oceanic fetch radon concentrations between DDU and NM is believed to be largely attributable to sea ice in the vicinity of NM, some of which can still be present in summer. The 5–10 mBq m^{-3} difference between radon concentrations of oceanic air masses at DDU and those typical of the deep Southern Ocean MBL, on the other hand, might be attributable to tube loss of the sampled radon progeny (Levin et al., 2017). Given the short sample tube lengths at DDU, NM, and DC (see Sites and Equipment), this effect would not usually be significant, however, tube losses increase for radon concentrations < 1 Bq m^{-3}, and at low ambient aerosol concentrations (when there can be a large unattached fraction of radon progeny; Levin et al., 2017). While tube loss effects at these sites have not yet been investigated, the possibility of a small (∼10–15 mBq m^{-3}), possibly concentration-dependent, underestimation of radon concentrations by the HRMs in these extreme environments should be taken into consideration when interpreting reported free-tropospheric terrestrial influences (see also Sites and Equipment).

In winter there was little evidence of significant vestigial terrestrial influence in the free troposphere over NM (**Figure 12B**; LHS). Most of the larger winter radon events appeared to originate from coastal fetch events, including four events between 100 and 135 mBq m^{-3} that were not shown on **Figure 12B** to prevent compressing the scale of the plot. Mean radon for all winter air masses was well below the 30–50 mBq m^{-3} expected for oceanic air, which Weller et al. (2014) attributed to the extensive ice coverage in the region cutting off even the oceanic radon flux. Further evidence in support of this claim is that the mean concentration of radon in air masses coming most directly from the ocean in winter are slightly (∼8%) larger than air that has meandered around the Antarctic coastal regions.

Coastal/Interior (Jang Bogo, Terra Nova Bay: 75°S)

Jang Bogo (Chambers et al., 2017; and this study) and nearby Mario Zucchelli (Tositti et al., 2002), stations in Terra Nova Bay, are unique among all long-term Antarctic radon monitoring stations in their seasonal radon characteristics for two reasons: the amount of observed radon, and its source regions. Peak radon concentrations at these bases (3000 – 5500 mBq m^{-3}; e.g., **Figure 13A**) are higher than observed at any other Antarctic Base, in some cases by more than an order of magnitude. Furthermore, as described by Tositti et al. (2002) and Chambers et al. (2017), the majority of this radon is from local Antarctic sources.

North and south of Terra Nova Bay, along the foothills of the Transantarctic Mountains, there is a substantial amount of exposed rock from which the mean summer radon flux has been estimated to be 0.09 – 0.11 atoms cm^{-2} s^{-1} (Chambers et al., 2017). The height and extent of the Transantarctic Mountains usually results in air masses approaching Terra Nova Bay from either the north or south, regardless of their longer-term fetch characteristics (e.g., katabatic outflow from the Ross Ice Shelf, barrier winds, and recent oceanic air masses – all from the south to southwest; or weaker anti-cyclonic flows from the north to northeast) (Markle et al., 2012; Coggins et al., 2014). As demonstrated by Markle et al. (2012) and Sinclair et al. (2013), even the freshest oceanic air masses are briefly redirected northward by the Transantarctic Mountains en route to Terra Nova Bay after moving from the Southern Pacific Ocean over the Ross Ice Shelf.

The combination of exposed rock fetch (100s of km in either direction), and relatively shallow mixing depths, frequently results in JBS radon concentrations of 1500–3000 mBq m^{-3} (Chambers et al., 2017). Additional radon sources, sometimes

responsible for radon peaks > 4000 mBq m^{-3}, include the active volcanos Mt Erebus and Mt Melbourne, along with their fumaroles (Polian and Lambert, 1979; Tositti et al., 2002).

The JBS seasonal radon cycle was not very consistent or pronounced in either mean or median values (**Figures 13B,C**). The most consistent features included a January maximum and October minimum. The seasonal cycle in 10th percentile values, on the other hand, was more consistent. This cycle was characterized by a February-April peak, consistent values throughout the winter months, and an October minimum.

Using the same 0000 – 0700 h diurnal analysis window as applied to observations at the other coastal Antarctic sites, 12% of summer days experienced pronounced katabatic flow events, and 18% of summer days experienced air mass fetch fairly directly from the ocean. The remaining 70% of summer days were classified as coastal fetch events (see Chambers et al., 2017, Section 3.5 for details).

As summarized in Figure 16 of Chambers et al. (2017), for brevity not repeated here, wind speeds of the summer oceanic fetch events were quite consistent, diurnal temperature amplitudes were low, and air masses made their final approach to the site from the southwest. Mean radon concentrations of these oceanic events were around 400 mBq m^{-3}, an order of magnitude above typical marine baseline radon concentrations, due to the interaction of these air masses with the Transantarctic Mountains south of the station (Markle et al., 2012; Chambers et al., 2017). The modal summer radon concentration reported by Tositti et al. (2002) in this region was also 400 mBq m^{-3}; with *very* few concentrations recorded below 200 mBq m^{-3}.

By comparison, summer coastal fetch events had more variable wind speeds, typically approached from the north to northwest, and had radon concentrations around 900 mBq m^{-3}, consistent with a longer fetch (∼330 km) along the foothills of the Transantarctic Mountains north of the site. In the case of summer katabatic flow events, at the time of peak katabatic wind speed (0200–0500 h) the composite mean radon concentration achieved a peak value of around 1000 mBq m^{-3}. While a large contribution to this observed radon concentration from the local foothills of the Transantarctic Mountains can't be ruled out (or accurately quantified), the katabatic flow is perpendicular to the mountain flanks so the air mass' time over exposed ground is minimized (3–5 h as opposed to 1–3 days when coming from the north or south). Consequently, it is possible that 25–50% of the observed 900 – 1000 mBq m^{-3} of radon in katabatic flow events could derive from subsiding tropospheric air. This would mean that the troposphere over this part of Antarctica contained air of more recent terrestrial influence than that over DDU.

Antarctic Plateau (Dome Concordia: 75°S, 3,233 m a.s.l.)

Peak radon concentrations observed at the inland Dome Concordia Station (65–95 mBq m^{-3}; **Figure 14A**), were the smallest of all Antarctic monitoring stations, and were restricted almost entirely to the summer months. The DC seasonal radon cycle (**Figure 14B**) was characterized by a February–March maximum, a September–October minimum, and relatively consistent concentrations between May and August; very similar to the 10th percentile seasonal cycle at JBS.

Unfortunately, no reliable humidity observations were available at the station for the 2010–2011 radon observation period. However, since subsidence events are usually strongest under anti-cyclonic conditions (clear-sky, light gradient winds), which usually also give rise to the greatest diurnal temperature variability at the surface, we approximated air mass type for these observations using surface temperature measurements.

We defined the diurnal temperature amplitude as the difference between 3-h means of the 2 m air temperature centered on the maximum and minimum observed hourly temperatures. We then calculated the diurnal amplitude of temperature for every day of the dataset and ranked these values for each season. Given that DC is cloud-free 75% of the time (Lawrence et al., 2004), we decided to categorize days with diurnal temperature amplitudes in the largest 33% as "anti-cyclonic," those with the lowest 33% amplitudes as "strong advection," and the remaining days were categorized as "weak advection." Diurnal composite temperature plots for each of these 3 categories in summer are shown in **Figure 15A**.

The highest mean DC radon concentrations in summer occurred on anti-cyclonic days (strongest subsidence; **Figure 15B**, LHS). Conversely, the lowest mean radon concentrations were observed on days when flow had been synoptically forced over the Antarctic interior ("strong advection" days). Almost all of the outlier events of magnitude 55 – 95 mBq m^{-3} were attributable to conditions during which the strongest tropospheric subsidence was thought to be occurring (anti-cyclonic conditions). It is notable that the radon concentrations observed for tropospheric subsidence events at DC compare well to those for "katabatic" conditions at both DDU and NM (22 – 33 mBq m^{-3}), peaking at 55 – 90 mBq m^{-3}.

We used the same fetch categorisation method to briefly examine the DC ozone record in summer and winter (**Figures 15C,D**). Median summer ozone for anti-cyclonic conditions (**Figure 15C**, LHS) was ∼21 ppbv, whereas corresponding winter values were 33 ppbv (**Figure 15D**, LHS). This is consistent with Legrand et al. (2009, 2016), who reported a seasonal cycle of ozone at DC characterized by a February minimum (∼21 ppbv) and July maximum (∼34 ppbv).

Anti-cyclonic days, in both summer and winter, were the only conditions under which consistent diurnal cycles of mean hourly ozone concentration were observed at DC. In summer the diurnal cycle was characterized by an early afternoon minimum. Legrand et al. (2016) demonstrate that daytime ozone minima on warm summer days at DC are attributable to increased boundary layer depths. In winter the diurnal cycle was characterized by a small noon maximum. In contrast to the case of summer the cause of this diurnal cycle in winter remains, however, basically unexplained.

In summer, the median ozone concentrations were 3 ppbv higher under strong advection conditions, when air masses were being synoptically forced over the Antarctic Plateau, than observed under subsidence conditions. Legrand et al. (2009, 2016) also report increased ozone concentrations at DC in summer when air is being advected to the site from other regions

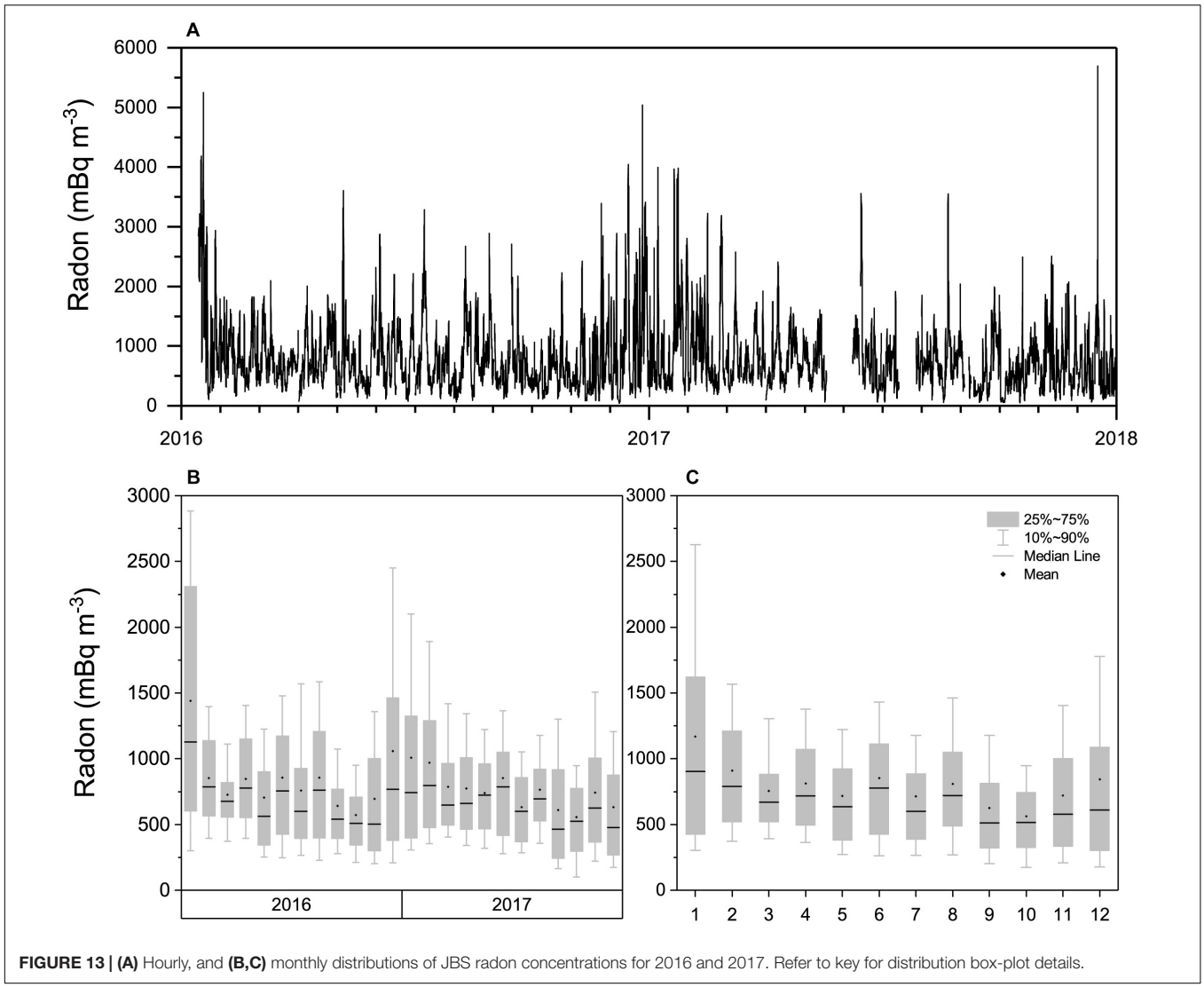

FIGURE 13 | (A) Hourly, and **(B,C)** monthly distributions of JBS radon concentrations for 2016 and 2017. Refer to key for distribution box-plot details.

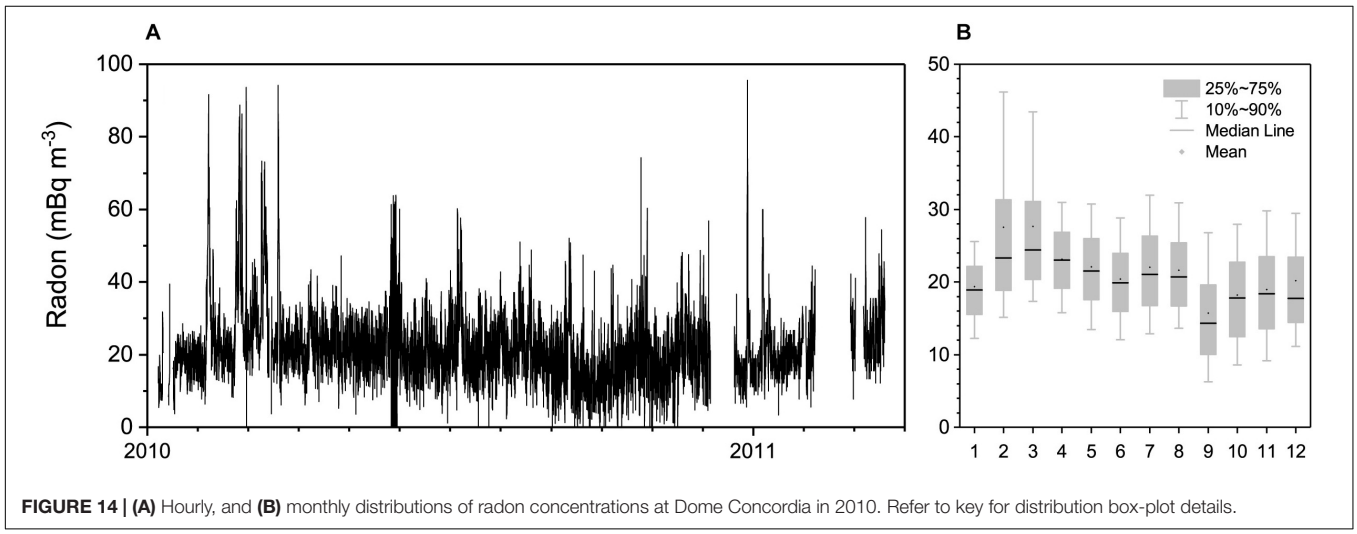

FIGURE 14 | (A) Hourly, and **(B)** monthly distributions of radon concentrations at Dome Concordia in 2010. Refer to key for distribution box-plot details.

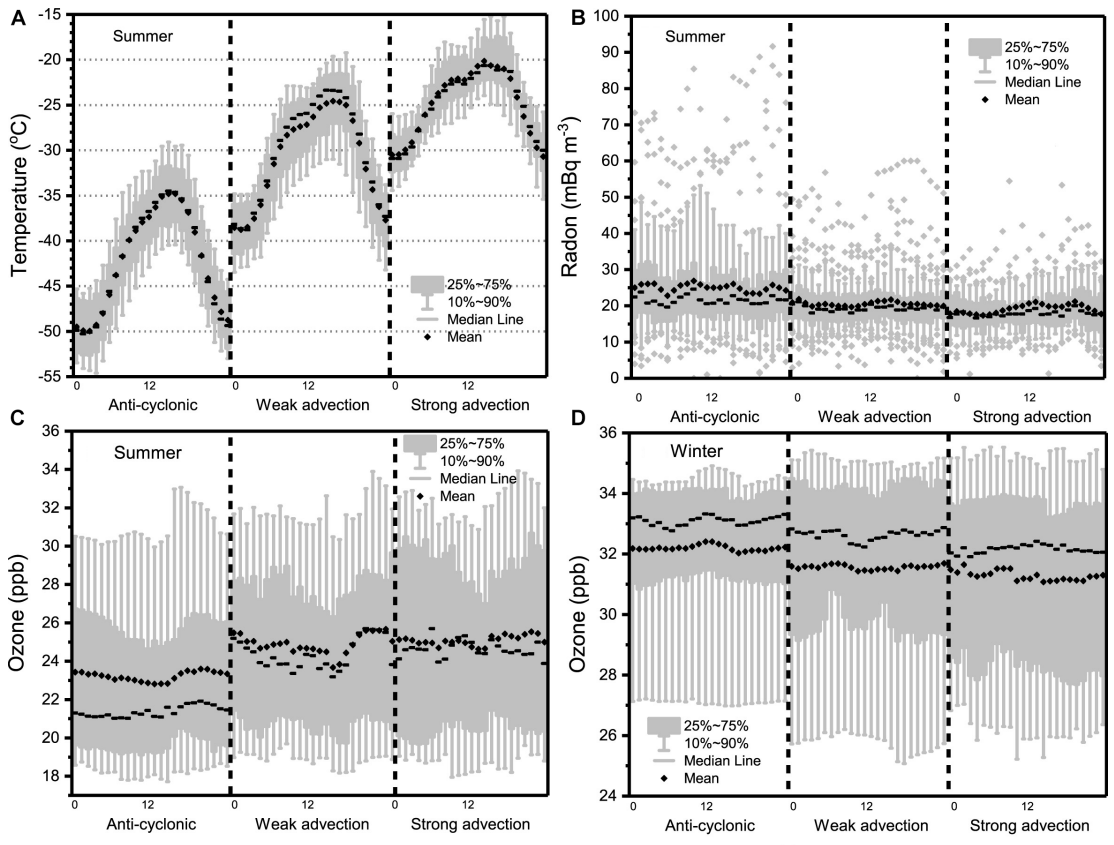

FIGURE 15 | (A,B) Summer diurnal composite distributions of hourly temperature and radon at DC for the three fetch classes, and **(C,D)** summer-winter comparison of diurnal composite distributions of ozone at DC for the three fetch classes in 2010.

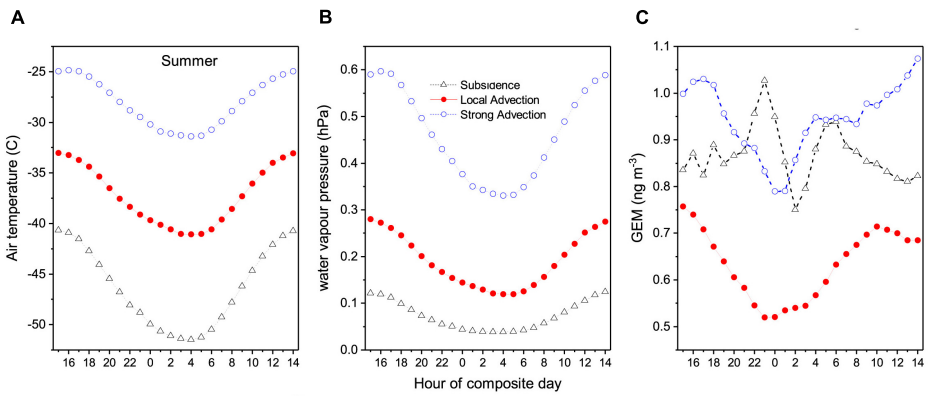

FIGURE 16 | (A–C) Diurnal composite temperature, water vapor pressure, and GEM in summer for the three fetch categories in 2012–2013.

of the plateau. In winter, however, median ozone concentrations associated with strong air mass advection across the Antarctic Plateau were 1 ppbv lower than those observed under subsidence conditions.

In 2012–2013, when humidity measurements were available at DC, we separated daily air mass fetch conditions into tropospheric subsidence, local advection and strong advection (most recently oceanic) categories to investigate the source of the katabatic GEM depletion events observed at DDU (see **Figure 10**). In summer (**Figure 16**) we observed that air masses associated with direct tropospheric subsidence had 0000–0700 h mean GEM concentrations of 0.89 ± σ0.5 ng m^{-3}, and those of air masses arriving most directly from the coast were 0.88 ± σ0.4 ng m^{-3}. However, air masses that had been

meandering locally about the Antarctic Plateau had average concentrations of 0.56 ± σ0.25 ng m^{-3}, consistent with a strong summertime GEM sink on the Antarctic Plateau (Angot et al., 2016a,c; Wang et al., 2016) highlighting that the summertime removal mechanism of GEM is probably caused by other chemical processes than the springtime atmospheric mercury depletion events occurred in other polar areas. The higher variability of GEM concentrations in subsiding tropospheric air is likely attributable to changing levels of terrestrial influence, but radon observations were not available at DC in 2012–2013 to investigate this further.

DISCUSSION

Measurement Uncertainties and Historical Observations

Since this investigation sought to compare radon observations from numerous Southern Ocean/Antarctic sites made by independent instruments and measurement techniques, ideally a detector inter-comparison study should have been conducted first, in order to harmonize the results. However, since the datasets were collated retrospectively, this was not possible. As has been demonstrated by previous studies of this nature (Collé et al., 1996a,b; Schmithüsen et al., 2017), the value of instrument inter-comparisons should not be understated, rigorous calibration checks, particularly those performed "blind" with an independent referee, can shed considerable light upon expected or assumed performance.

As an example, Collé et al. (1996a,b) report on a 2-week inter-comparison of radon detectors performed in Bermuda (October 1991) including four participating laboratories, during which time ambient air was "spiked" 14 times with a Radon-222 sample of undisclosed activity. The measurement techniques compared included intermittent and continuous two-filter detectors, cryogenic separation using charcoal, and intermittent Radon-222 progeny collection on filters with equilibrium ratio assumptions. As noted by Collé et al. (1996b), both two-filter techniques "were in excellent agreement with the NIST [^{222}Rn] additions." In general, however, the continuous two-filter observations were overly smoothed by the detector's 90-min time constant, changing particulate concentrations within the detector added considerably to the detector's counting uncertainty, concentrations were initially overestimated by ∼10% (reduced to an overestimation of 2.7% only after a retrospective instrumental background correction), and there was considerable variability in concentrations at very low ambient radon levels, thought to be attributable to problems with instrumental background characterization.

The dual-flow-loop two-filter radon detectors employed in this study are based on the one originally tested in the Collé et al. (1996b) study, however, there have been considerable improvements to their design and performance in the 26 years since the Collé et al. (1996b) inter-comparison campaign. The original ANSTO two-filter radon detector design was superseded in the late 1990s by a completely new design involving the introduction of an innovation known as a "dual flow-loop" (Whittlestone and Zahorowski, 1998). Considerable additional improvements have been made since that time, as detailed in Chambers et al. (2014), Williams and Chambers (2016), Griffiths et al. (2016), and other articles. Williams and Chambers (2016), in particular, provide a detailed description of the progression of changes as realized for ANSTO two-filter detectors at the Cape Grim Baseline Air Pollution Station in Tasmania.

Briefly, key improvements to the two-filter detection systems in recent decades include: (i) the introduction of a second, high flow rate "internal" recirculation loop past the detection head, removing the need for a particle generator within the detector's delay chamber to reduce plate-out losses of the newly formed radon progeny to the tank walls; together with a change of the main filter within the instrument sensing head from a coarse membrane filter to a 20 micron stainless steel mesh filter (enabled by the consequent change from predominantly particle-attached to unattached radon progeny within the tank), this has resulted in substantial increases in performance, consistency and reliability; (ii) a reduction in the instrument response time from 90 to 45 min; (iii) computer automation, which has enabled the performance of regular 3-monthly instrumental background checks and monthly system calibrations; and (iv) development of a response-time correction algorithm (Griffiths et al., 2016).

The lack of a formal evaluation of the performance of contemporary dual-flow-loop two-filter radon detectors is regrettable given the considerable discrepancy between Southern Ocean MBL radon concentrations reported at Cape Grim (e.g., Crawford et al., 2018) and in this study, and those reported in earlier Antarctic and sub-Antarctic studies, including that of Polian et al. (1986). Contemporary two-filter detector estimates of radon concentrations of air masses in long-term (≥3-week) equilibrium with the Southern Ocean based on observations at Cape Grim (Crawford et al., 2018), King Sejong Station, and aboard the RV *Investigator*, yield values typically between 40 and 50 mBq m^{-3}. Furthermore, median summertime radon concentrations of oceanic air masses at Dumont d'Urville station measured by the single-filter method are around 30 mBq m^{-3} (*prior* to accounting for known tube-loss effects). Median Southern Ocean MBL radon concentrations reported by Polian et al. (1986), on the other hand, were around 15 mBq m^{-3}. In order to determine which of these results is most representative, we sought to independently estimate MBL radon concentrations for the Southern Ocean region.

Assuming a uniformly mixed MBL, the radon concentration of oceanic air masses that have not been subjected to terrestrial influence in the past 3 weeks (Rn_{MBL}) can be estimated as follows:

$$Rn_{MBL} = \frac{F_{Rn\ Oc}}{(w_e + h\lambda)} \quad (1)$$

where F_{Rn_Oc} is the oceanic radon flux (mBq m^{-2} s^{-1}), w_e is the entrainment velocity (m s^{-1}) across the MBL inversion, h is the depth of the MBL (m) and λ is the radon decay constant (2.0982 × 10^{-6} s^{-1}). Average MBL depths near the northern extremity of the Southern Ocean (40–45°S) have been estimated to be around 900 – 1000 m (Zahorowski et al., 2013). Near the southern extremity (60–65°S) MBL depths

have been estimated to be typically in the range 440 – 610 m (Chambers et al., 2014). Typical entrainment velocities for the Southern Ocean are of order 0.003–0.004 m s^{-1} (Zahorowski et al., 2013 and references therein). The seasonal variability of oceanic radon flux reported by Zahorowski et al. (2013) was in the range 0.19–0.34 mBq m^{-2} s^{-1}, and other literature reviewed by Zahorowski et al. (2013) considered 0.24 mBq m^{-2} s^{-1} to be a generally representative oceanic radon flux.

Based on an entrainment velocity of 0.0035 m s^{-1} and an oceanic radon flux of 0.24 mBq m^{-2} s^{-1}, for h = 1000 m, Equation (1) predicts Rn_{MBL} = 42.9 mBq m^{-3}, whereas for h = 600 m, Rn_{MBL} = 50.4 mBq m^{-3}. These estimates are in very good agreement with the Southern Ocean MBL radon concentrations reported in this study. Furthermore, with the notable exception of air masses recently mixed down from the free-troposphere or stratosphere that have been removed from all radon sources for a period of time, these findings indicate that the Southern Ocean MBL radon concentrations reported by Polian et al. (1986) are too low. The close agreement at very low ambient radon concentrations between independently calibrated two-filter radon detectors at Cape Grim (5000L model), aboard the RV *Investigator* (700L model), and at King Sejong station (1500L model), also provides confidence in contemporary methods to characterize the instrumental background compared to the two-filter detector that was employed in the Collé et al. (1996b) inter-comparison.

Comparison With Global Climate Model Simulations

A unique combination of physical properties (i.e., its source and sink terms, reactivity and half-life), makes radon an ideal tool to provide unambiguous information about terrestrial influence and transport mechanisms to remote Southern Ocean regions and Antarctica. Given the comparatively low land fraction of the Southern Hemisphere, it should provide an ideal "testing ground" for the performance of transport and mixing/convection parameterisations of global climate models (GCMs). Investigating spatial and temporal differences between observed and simulated radon concentrations throughout the Southern Hemisphere can provide significant insight to the behavior of GCMs.

A number of studies have successfully simulated synoptic radon transport in the MBL (sometimes called "radonic storms") deep into the Southern Ocean (e.g., Balkanski and Jacob, 1990; Dentener et al., 1999). However, attempts by GCMs to reproduce the seasonal behavior of radon in coastal Antarctic regions have been far less successful (e.g., Heimann et al., 1990; Genthon and Armengaud, 1995; Taguchi et al., 2002; Josse et al., 2004; Zhang et al., 2008, 2011), which Josse et al. (2004) partly attributed to the paucity of reliable observational data. A summary of simulated radon seasonal cycles at Dumont d'Urville is presented in **Figure 17**.

The models of Genthon and Armengaud (1995), Taguchi et al. (2002), Josse et al. (2004), and Zhang et al. (2008) all produced a Dumont d'Urville radon seasonal cycle with a strong winter maximum and summer minimum. The phase of this seasonal cycle is completely opposite that of our observations at DDU (**Figure 8C**), but is similar to that observed at Macquarie Island (**Figure 4C**). With the exception of Heimann et al. (1990) and Zhang et al. (2011), similarities of the simulated seasonal cycle at DDU with MI observations indicate that these models are overestimating radon contributions at DDU that result from synoptic transport within the MBL. The complete failure to predict higher radon concentrations between November and February by these models is most likely mainly attributable to the fact that coastal radon sources in summer in Antarctica are not accounted for (see **Figures 8C**, **9A,B**). Lastly, part of the higher observed radon concentration at DDU in January-February, and the sustained higher concentration into March, is likely attributable to the subsidence of tropospheric air containing vestigial terrestrial influence within the past 3 weeks. The models of Genthon and Armengaud (1995), Taguchi et al. (2002), Josse et al. (2004), and Zhang et al. (2008) all appear to have missed this contribution.

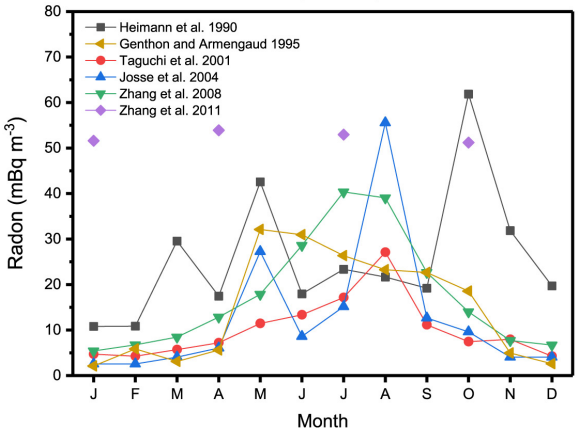

FIGURE 17 | Monthly mean simulated radon concentrations at Dumont d'Urville for various years (see references for details).

By comparison, Zhang et al. (2011) predict higher radon concentrations year round at DDU than the other models, and also at Mawson (not shown). However, the magnitude of these values compares reasonably well with oceanic radon concentrations in the lower parts of Southern Ocean observed by the RV *Investigator* (55–70 mBq m^{-3}; **Figure 2A**), and median radon concentrations reported at KSG (50–70 mBq m^{-3}). This similarity indicates that the Schery and Huang (2004) oceanic radon flux parameterisation used by Zhang et al. (2011) provides representative oceanic MBL radon values in that region of the Southern Ocean. The overestimation of radon concentrations in the winter months compared to observations at DDU and NM is likely due to a combination of (i) a slight underestimation of the observed radon concentrations by the HRMs at DDU and NM (see Sections "Sites and Equipment" and "Coastal Antarctica"), and (ii) an underestimation in the model of how much of the oceanic radon source function is "turned off" by the extensive winter ice sheet.

The amplitude of the seasonal radon cycle predicted by the Zhang et al. (2011) model (∼4 mBq m^{-3} at Dumont d'Urville, ∼15 mBq m^{-3} at Mawson) was, however, very low compared to observed values. The majority of this difference is likely attributable to a lack of consideration given to local Antarctic radon sources in the model (Evangelista and Pereira, 2002; Burton-Johnson et al., 2016; Chambers et al., 2017). Uniquely among the models compared here, the Zhang et al. (2011) seasonality predicts an autumn maximum concentration at Dumont d'Urville and a summer maximum at Mawson. Given that no account was made in these simulations for coastal Antarctic radon sources, this shift in phase of the radon seasonal cycle compared to the other models may indicate a more accurate representation of either the amount of continental air that is being injected to the mid-latitude troposphere, or the rate at which this air is subsequently traveling poleward.

CONCLUSION

We have discussed remote terrestrial influences on the boundary layer air masses over the Southern Ocean and Antarctica, as well as the mechanisms by which they arise, using continuous atmospheric radon (^{222}Rn) measurements as a proxy. A composite of 5 Southern Ocean transects by the RV *Investigator* were used to provide a late-summer cross-sectional 'snapshot' of terrestrial influence in the marine boundary layer. These voyages provided considerable insight to tropospheric subsidence events occurring in the vicinity of the circumpolar trough, and the characteristics of outflow events that extend 100s of kilometers from the Antarctic continent.

The radon seasonal cycle at Macquarie Island, in the mid-Southern Ocean, was characterized by a summer minimum, winter maximum, and mean amplitude of ∼100 mBq m^{-3}. Radon excursions beyond the 50 mBq m^{-3} marine background value were attributable to synoptic transport of continental air within the MBL. At King Sejong, in the sub-Antarctic, the radon seasonal cycle was bimodal with peaks in autumn and spring. Here radon excursions above background levels were contributed to by a combination of synoptic transport from South America, local radon sources, and subsidence of terrestrially influenced tropospheric air. Radon seasonal cycles at Dumont d'Urville and Neumayer Stations were dominated by local sources and tropospheric subsidence events, while that at Jang Bogo was primarily driven by local emissions. At Dome Concordia, far removed from coastal sources at 3,233 m a.s.l. on the Antarctic Plateau, the radon seasonal cycle was dominated by tropospheric subsidence events.

Separation of long-term marine and katabatic flow air masses was performed using a technique involving absolute humidity observations recently developed by Chambers et al. (2017). At Dumont d'Urville, this technique revealed monthly mean differences in ozone concentrations of around 5 ppbv in summer and 1 ppbv in winter. Averaged over a whole summer, concentrations of GEM were 0.03 ng m^{-3} lower in air masses that had recently subsided and traveled to the station from the Antarctic Plateau than in air masses of recent marine origin.

A comparison of our observations with simulated Antarctic radon seasonal cycles indicated that: (i) some models overestimate synoptic transport to Antarctica in the MBL, (ii) seasonality of the Antarctic ice sheet needs to be better represented, (iii) coastal Antarctic radon sources need to be taken into account, and (iv) the underestimation of radon in subsiding tropospheric air needs to be investigated.

The main purpose of this study was to bring together, and demonstrate the value of, seasonal high-sensitivity, high temporal resolution atmospheric radon observations from a number of contrasting locations in a growing network of Southern Ocean and Antarctic radon monitoring sites. By clearly demonstrating the cross-disciplinary benefits of an unambiguous indicator of terrestrial influence (or 'potential pollution') on MBL air masses throughout the Southern Ocean and coastal Antarctic regions, we hope to promote awareness, and encourage greater use of these datasets throughout the environmental research community. To assist with the interpretation of ongoing measurement programs, and continually improve the predictive ability of global models, every effort should be made to continue radon monitoring at existing stations, with a view to eventually making atmospheric radon observations a standard research measurement tool. However, given the low concentrations of radon typically present in remote Southern Ocean and Antarctic environments, and the range of measurement techniques and capabilities of contemporary detectors, further research in this field would greatly benefit from a detector inter-comparison campaign that specifically targeted concentrations approaching instrument detection limits.

DATA AVAILABILITY STATEMENT

All source data of figures within this manuscript has been made available at the following location: 10.13140/RG.2.2.19918.92485 (https://www.researchgate.net/publication/327434026_Radon_concentrations_in_the_Southern_Ocean_and_Antarctic_regions). Regarding the RV Investigator in particular, meteorological data used was collected on the Marine National Facility (MNF) RV Investigator voyage IN2017_V01. The dataset in2017_v01uwy5min_csv.zip downloaded on 29-May-2018 was collected on voyage IN2017_v01 on the RV Investigator granted by the Marine National Facility. It is made available under a Creative Commons Attribution 4.0 International License; the data was processed by V. Dirita (CSIRO O&A). Data from the RV Investigator is available through the Earth Sciences section of the CSIRO Data Access Portal (https://data.csiro.au/dap/browse). Mercury data reported in this paper are available at https://gmos.aeris-data.fr/ (GMOS-FR Aeris database project) as well as within the central database of the GMOS global network at http://sdi.iia.cnr.it/geoint/publicpage/GMOS upon request. Radon measurements from the Air Chemistry Observatory at Neumayer Station are available from http://www.awi.de/en/go/air_chemistry_observatory). Meteorological observations from the Dome Concordia Automatic Weather Station (AWS 8989) of University of Wisconsin- Madison are available from ftp://amrc.ssec.wisc.edu/pub/aws/.

AUTHOR CONTRIBUTIONS

SC, S-BH, and AW planned the study. SC installed the two-filter radon detectors and calibrated their observations, processed and interpreted meteorological and trace gas data from each site (provided calibrated and quality checked by co-authors), and drafted the initial manuscript. As well as roles played by many co-authors collecting data at field sites featured in this study, all co-authors actively contributed to revising and refining the interpretation of results presented. Additional contributions were as follows: SP and ML were responsible for meteorological, ozone and single-filter radon data from Dumont d'Urville and Dome Concordia. RW was responsible for meteorological and single-filter radon data from Neumayer. S-BH, TC, and LT provided meteorological data, and assisted with the collection of radon data, from King Sejong and Jang Bogo. RH, JS, SW, PK, SM, ZL, and IG were responsible for measurements of meteorology, carbon dioxide, ozone and condensation nuclei on the RV *Investigator* and at Macquarie Island. HA, OM, FS, NP, and AD were responsible for meteorology and GEM observations at Dumont d'Urville and Dome Concordia. AG and JC assisted with back trajectory calculation and figure production.

FUNDING

This research was partly supported by KOPRI research grants (PE18010) and The Australia Korea Foundation (AKF2014Grant00102). Atmospheric Hg measurements were supported by the FP7 (2010–2015) Global Mercury Observation System (GMOS) project. This work contributed to the EU-FP7 project Global Mercury Observation System (GMOS, www.gmos.eu) and has been supported by a grant from Labex OSUG@2020 (Investissements d'avenir – ANR10 LABX56). Logistical and financial support was provided by the French Polar Institute IPEV (Program 1028, GMOstral and Program 1011) and a grant from the U.S. National Science Foundation (NSF, PLR#1142145). The Automatic Weather Station Project, which supplied the meteorological parameters for Dome Concordia, is run by Charles R. Stearns at the University of Wisconsin-Madison and is funded by the National Science Foundation of the United States of America.

ACKNOWLEDGMENTS

We thank over-wintering staff at all contributing Antarctic stations, and crew of the RV *Investigator*, for their part in maintaining the radon, meteorological and other equipment from which data has been gathered for this study. In particular we wish to thank Ot Sisoutham and Sylvester Werczynski, of ANSTO, for their support of the radon measurement program. Field logistic supplies for the Rn measurements at DDU and DC were provided by Institut Polaire Français-Paul Emile Victor (IPEV) within program 414. We thank Météo France, who provided meteorological data for DDU, and Charles R. Stearns for the Automatic Weather Station Project that provided meteorological parameters for Dome Concordia. We thank LEFE/IMAGO programs CLAPA and GABLS4, IPEV CALVA program 1013 (PI: Christophe Genthon), and Observatoire des Sciences de l'Univers de Grenoble (GLACIOCLIM observatory) for providing meteorological data for 2012–2013 in Concordia station. We gratefully acknowledge the Air Resources Laboratory (ARL) for provision of the HYSPLIT transport and dispersion model on READY website (https://ready.arl.noaa.gov/HYSPLIT_traj.php) used in this publication. Last but not least, we would also like to thank the reviewers for their insightful and constructive feedback, which has helped improving the clarity and utility of the final manuscript.

REFERENCES

Albani, S., Mahowald, N. M., Delmonte, B., Maggi, V., and Winckler, G. (2012). Comparing modeled and observed changes in mineral dust transport and deposition to Antarctica between the Last Glacial Maximum and current climates. *Clim. Dyn.* 38, 1731–1755. doi: 10.1007/s00382-011-1139-5

Amante, C., and Eakins, B. W. (2009). *ETOPO1 1 Arc-Minute Global Relief Model: Procedures, Data Sources and Analysis. NOAA Technical Memorandum NESDIS NGDC*-24. Silver Spring, MD: NOAA. doi: 10.7289/V5C8276M

Angot, H., Barret, M., Magand, O., Ramonet, M., and Dommergue, A. (2014). A 2-year record of atmospheric mercury species at a background Southern Hemisphere station on Amsterdam Island. *Atmos. Chem. Phys.* 14, 11461–11473. doi: 10.5194/acp-14-11461-2014

Angot, H., Dastoor, A., de Simone, F., Dastoor, A., De Simone, F., Gårdfeldt, K., et al. (2016a). Chemical cycling and deposition of atmospheric mercury in polar regions: review of recent measurements and comparison with models. *Atmos. Chem. Phys.* 16, 10735–10763. doi: 10.5194/acp-16-10735-2016

Angot, H., Dion, I., Vogel, N., Legrand, M., Magand, O., and Dommergue, A. (2016b). Multi-year record of atmospheric mercury at Dumont d'Urville, East Antarctic coast: continental outflow and oceanic influences. *Atmos. Chem. Phys.* 16, 8265–8279. doi: 10.5194/acp-16-8265-2016

Angot, H., Magand, O., Helmig, D., Ricaud, P., Quennehen, B., Gallée, H., et al. (2016c). New insights into the atmospheric mercury cycling in central Antarctica and implications on a continental scale. *Atmos. Chem. Phys.* 16, 8249–8264. doi: 10.5194/acp-16-8249-2016

Australian Antarctic Division (2005). *Macquarie Island and Adjacent Islands 1:50000 Coastline GIS Dataset*. Available at: https://data.gov.au/dataset/e4c01f74-de78-4233-80f4-444dfdc7380b

Balkanski, Y. J., and Jacob, D. J. (1990). Transport of continental air to the Subantarctic Indian Ocean. *Tellus* 42B, 62–75. doi: 10.3402/tellusb.v42i1.15192

Bargagli, R. (2016). Atmospheric chemistry of mercury in Antarctica and the role of cryptogams to assess deposition patterns in coastal ice-free areas. *Chemosphere* 163, 202–208. doi: 10.1016/j.chemosphere.2016.08.007

Belikov, D. A., Maksyutov, S., Krol, M., Fraser, A., Rigby, M., Bian, H., et al. (2013). Off-line algorithm for calculation of vertical tracer transport in the troposphere due to deep convection. *Atmos. Chem. Phys.* 13, 1093–1114. doi: 10.5194/acp-13-1093-2013

Brechtel, F. J., Kreidenweis, S. M., and Swan, H. B. (1998). Air mass characteristics, aerosol particle number concentrations, and number size distributions at Macquarie Island during the First Aerosol Characterisation Experiment (ACE 1). *J. Geophys. Res.* 103, 16351–16367. doi: 10.1029/97JD03014

Bromwich, D. H., Parish, T. R., Pellegrini, A., Stearns, C. R., and Weidner, G. A. (1993). Spatial and temporal characteristics of the intense katabatic winds at Terra Nova Bay, Antarctica. *Antarct. Res. Ser.* 61, 47–68. doi: 10.1029/AR061p0047

Brook, E. J., and Buizert, C. (2018). Antarctic and global climate history viewed from ice cores. *Nature* 558, 200–208. doi: 10.1038/s41586-018-0172-5

Brunke, E.-G., Labuschagne, C., Parker, B., Scheel, H. E., and Whittlestone, S. (2004). Baseline air mass selection at Cape Point, South Africa: application of ^{222}Rn and other filter criteria to CO_2. *Atmos. Environ.* 38, 5693–5702. doi: 10.1016/j.atmosenv.2004.04.024

Burton-Johnson, A., Black, M., Fretwell, P. T., and Kaluza-Gilbert, J. (2016). An automated methodology for differentiating rock from snow, clouds and sea in Antarctica from Landsat 8 imagery: a new rock outcrop map and area estimation for the entire Antarctic continent. *Cryosphere* 10, 1665–1677. doi: 10.5194/tc-10-1665-2016

Chambers, S., and Sheppard, S. C. (2017). Letter to the editor. *J. Environ. Radioact.* 172, 261–263. doi: 10.1016/j.jenvrad.2017.04.013

Chambers, S. D., Choi, T., Park, S. J., Williams, A. G., Hong, S.-B., Tositti, L., et al. (2017). Investigating local and remote terrestrial influence on air masses at contrasting Antarctic sites using Radon-222 and back trajectories. *J. Geophys. Res. Atmos.* 122, 13525–13544. doi: 10.1002/2017JD026833

Chambers, S. D., Hong, S.-B., Williams, A. G., Crawford, J., Griffiths, A. D., and Park, S.-J. (2014). Characterising terrestrial influences on Antarctic air masses using Radon-222 measurements at King George Island. *Atmos. Chem. Phys.* 14, 9903–9916. doi: 10.5194/acp-14-9903-2014

Chambers, S. D., Williams, A. G., Conen, F., Griffiths, A., Reimann, S., Steinbacher, M., et al. (2016). Towards a universal "baseline" characterisation of air masses for high- and low-altitude observing stations using radon-222. *Aerosol Air Qual. Res.* 16, 885–899. doi: 10.4209/aaqr.2015.06.0391

Chambers, S. D., Williams, A. G., Crawford, J., and Griffiths, A. D. (2015). On the use of radon for quantifying the effects of atmospheric stability on urban emissions. *Atmos. Chem. Phys.* 15, 1175–1190. doi: 10.5194/acp-15-1175-2015

Coggins, J. H. J., McDonald, A. J., and Jolly, B. (2014). Synoptic climatology of the Ross ice shelf and Ross Sea region of Antarctica: k-means clustering and validation. *Int. J. Climatol.* 34, 2330–2348. doi: 10.1002/joc.3842

Collé, R., Unterweger, M. P., Hodge, P. A., and Hutchison, J. M. (1996a). An international marine-atmospheric 222Rn measurement intercomparison in Bermuda Part I: NIST calibration and methodology for standardized sample additions. *J. Res. Natl. Inst. Stand. Technol.* 101, 1–19.

Collé, R., Unterweger, M. P., and Hutchison, J. M. (1996b). An international marine-atmospheric 222Rn measurement intercomparison in Bermuda Part II: results for the participating laboratories. *J. Res. Natl. Inst. Stand. Technol.* 101, 21–46.

Crawford, J., Chambers, S. D., Cohen, D. D., and Williams, A. G. (2018). Baseline characterisation of source contributions to daily-integrated PM2.5 observations at Cape Grim using Radon-222. *Environ. Pollut.* 243, 37–48. doi: 10.1016/j.envpol.2018.08.043

Crawford, J. H., Davis, D. D., Chen, G., Buhr, M., Oltmans, S., Weller, R., et al. (2001). Evidence for photochemical production of ozone at the South Pole surface. *Geophys. Res. Lett.* 28, 3641–3644. doi: 10.1029/2001GL013055

Davis, D., Nowak, J. B., Chen, G., Buhr, M., Arimoto, R., Hogan, A., et al. (2001). Unexpected high levels of NO observed at South Pole. *Geophys. Res. Lett.* 28, 3625–3628. doi: 10.1029/2000GL012584

DeConto, R. M., and Pollard, D. (2016). Contribution of Antarctica to past and future sea-level rise. *Nature* 531, 591–597. doi: 10.1038/nature17145

Dentener, F., Feichter, J., and Jeuken, A. (1999). Simulation of the transport of Rn222 using on-line and off-line global models at different horizontal resolutions: a detailed comparison with measurements. *Tellus* 51B, 573–602. doi: 10.3402/tellusb.v51i3.16440

Doering, C., and Saey, P. (2014). Hadley cell influence on 7Be activity concentrations at Australian mainland IMS radionuclide particulate stations. *J. Environ. Radioact.* 127, 88–94. doi: 10.1016/j.jenvrad.2013.10.011

Dommergue, A., Sprovieri, F., Pirrone, N., Ebinghaus, R., Brooks, S., Courteaud, J., et al. (2010). Overview of mercury measurements in the Antarctic troposphere. *Atmos. Chem. Phys.* 10, 3309–3319. doi: 10.5194/acp-10-3309-2010

Draxler, R. R., and Rolph, G. D. (2003). *Hybrid Single-Particle Lagrangian Integrated Trajectory (HYSPLIT), Model*. Available at: http://www.arl.noaa.gov/ready/hysplit4.html [accessed September 2016].

Eisele, F., Davis, D. D., Helmig, D., Oltmans, S. J., Neff, W., Huey, G., et al. (2008). Antarctic tropospheric chemistry investigation (ANTCI) 2003 overview. *Atmos. Environ.* 42, 2749–2761. doi: 10.1016/j.atmosenv.2007.04.013

Etheridge, D. M., Steele, L. P., Langenfelds, R. L., Francey, R. J., Barnola, J.-M., and Morgan, V. I. (1996). Natural and anthropogenic changes in atmospheric CO2 over the last 1000 years from air in Antarctic ice and firn. *JGR Atmos.* 101, 4115–4128. doi: 10.1029/95JD03410

Evangelista, H., and Pereira, E. B. (2002). Radon flux at king George island, Antarctic peninsula. *J. Environ. Radioact.* 61, 283–304. doi: 10.1016/S0265-931X(01)00137-0

Fox, A. J., Paul, A., and Cooper, R. (1994). Measured properties of the Antarctic Ice Sheet derived from the SCAR Antarctic Digital Database. *Polar Res.* 30, 201–206. doi: 10.1017/S0032247400024268

Genthon, C., and Armengaud, A. (1995). Radon 222 as a comparative tracer of transport and mixing in two general circulation models of the atmosphere. *J. Geophys. Res.* 100, 2849–2866. doi: 10.1029/94JD02846

Gille, S. T. (2002). Warming of the Southern Ocean since the 1950s. *Science* 295, 1275–1277. doi: 10.1126/science.1065863

Graf, H.-F., Shirsat, S. V., Oppenheimer, C., Jarvis, M. J., Podzun, R., and Jacob, D. (2010). Continental scale Antarctic deposition of sulphur and black carbon from anthropogenic and volcanic sources. *Atmos. Chem. Phys.* 10, 2457–2465. doi: 10.5194/acp-10-2457-2010

Griffiths, A. D., Chambers, S. D., Williams, A. G., and Werczynski, S. R. (2016). Increasing the accuracy and temporal resolution of two-filter radon–222 measurements by correcting for the instrument response. *Atmos. Meas. Tech.* 9, 2689–2707. doi: 10.5194/amt-9-2689-2016

Griffiths, A. D., Zahorowski, W., Element, A., and Werczynski, S. (2010). A map of radon flux at the Australian land surface. *Atmos. Chem. Phys.* 10, 8969–8982. doi: 10.5194/acp-10-8969-2010

Grossi, C., Arnold, D., Adame, A. J., ópez-Coto, I. L., Bolívar, J. P., de la Morena, B. A., et al. (2012). Atmospheric 222Rn concentration and source term at El Arenosillo 100 m meteorological tower in southwest Spain. *Radiat. Meas.* 47, 149–162. doi: 10.1016/j.radmeas.2011.11.006

Heimann, M., Monfray, P., and Polian, G. (1990). Modeling the long-range transport of 222Rn to subantarctic and Antarctic areas. *Tellus* 42B, 83–99. doi: 10.3402/tellusb.v42i1.15194

Howard, D., Nelson, P. F., Edwards, G. C., Morrison, A. L., Fisher, J. A., Ward, J., et al. (2017). Atmospheric mercury in the Southern Hemisphere tropics: seasonal and diurnal variations and influence of inter-hemispheric transport. *Atmos. Chem. Phys.* 17, 11623–11636. doi: 10.5194/acp-17-11623-2017

Humphries, R. S., Klekociuk, A. R., Schofield, R., Keywood, M., Ward, J., and Wilson, S. R. (2016). Unexpectedly high ultrafine aerosol concentrations above East Antarctic sea ice. *Atmos. Chem. Phys.* 16, 2185–2206. doi: 10.5194/acp-16-2185-2016

Humphries, R. S., Schofield, R., Keywood, M. D., Ward, J., Pierce, J. R., Gionfriddo, C. M., et al. (2015). Boundary layer new particle formation over East Antarctic sea ice – possible Hg-driven nucleation? *Atmos. Chem. Phys.* 15, 13339–13364. doi: 10.5194/acp-15-13339-2015

Jaenickle, R., Dreiling, V., Lehmann, E., Koutsenoguii, P. K., and Stingl, J. (1992). Condensation nuclei at the German Antarctic Station "Georg von Neumayer". *Tellus* 44B, 311–317.

Jickells, T. D., An, Z. S., Andersen, K. K., Baker, A. R., Bergametti, G., Brooks, N., et al. (2005). Global iron connections between desert dust, ocean biogeochemistry, and climate. *Science* 308, 67–71. doi: 10.1126/science.1105959

Jones, A. E., Wolff, E. W., Salmon, R. A., Bauguitte, S. J.-B., Roscoe, H. K., Anderson, P. S., et al. (2008). Chemistry of the Antarctic boundary layer and the interface with snow: an overview of the CHABLIS campaign. *Atmos. Chem. Phys.* 8, 3789–3803. doi: 10.5194/acp-8-3789-2008

Josse, B., Simon, P., and Peuch, V.-H. (2004). Radon global simulations with the multiscale chemistry and transport model MOCAGE. *Tellus B* 56, 339–356. doi: 10.1111/j.1600-0889.2004.00112.x

Jouzel, J., Masson-Delmotte, V., Cattani, O., Dreyfus, G., Falourd, S., Hoffmann, G., et al. (2007). Orbital and millennial Antarctic climate variability over the past 800,000 years. *Science* 317, 793–796. doi: 10.1126/science.1141038

Karstens, U., Schwingshackl, C., Schmithüsen, D., and Levin, I. (2015). A process-based 222Radon flux map for Europe and its comparison to long-term observations. *Atmos. Chem. Phys.* 15, 12845–12865. doi: 10.5194/acp-15-12845-2015

Koide, M., Michel, R., Goldberg, E. D., Herron, M. M., and Langway, C. C. Jr. (1979). Depositional history of artificial radionuclides in the Ross Ice shelf,

Antarctica. *Earth Planet. Sci. Lett.* 44, 205–223. doi: 10.1016/0012-821X(79)90169-9

Krinner, G., Petit, J.-R., and Delmonte, B. (2010). Altitude of atmospheric tracer transport towards Antarctica in present and glacial climate. *Quat. Sci. Rev.* 29, 274–284. doi: 10.1016/j.quascirev.2009.06.020

Kuss, J., Zülicke, C., Pohl, C., and Schneider, B. (2011). Atlantic mercury emission determined from continuous analysis of the elemental mercury sea-air concentration difference within transects between 50N and 50S. *Glob. Biogeochem. Cycles* 25:GB3021. doi: 10.1029/2010GB003998

Law, R. M., Steele, L. P., Krummel, P. B., and Zahorowski, W. (2010). Synoptic variations in atmospheric CO2 at Cape Grim: a model intercomparison. *Tellus* 62B, 810–820. doi: 10.1111/j.1600-0889.2010.00470.x

Lawrence, J. S., Ashley, M. C., Tokovinin, A., and Travouillon, T. (2004). Exceptional astronomical seeing conditions above Dome C in Antarctica. *Nature* 431, 278–281. doi: 10.1038/nature02929

Legrand, M., Preunkert, S., Jourdain, B., Gallée, H., Goutail, F., Weller, R., et al. (2009). Year round record of surface ozone at coastal (Dumont d'Urville) and inland (Concordia) sites in East Antarctica. *J. Geophys. Res.* 114:D20306. doi: 10.1029/2008JD011667

Legrand, M., Preunkert, S., Savarino, J., Frey, M. M., Kukui, A., Helmig, D., et al. (2016). Inter-annual variability of surface ozone at coastal (Dumont d'Urville, 2004-014) and inland (Concordia, 2007-2014) sites in East Antarctica. *Atmos. Chem. Phys.* 16, 8053–8069. doi: 10.5194/acp-16-8053-2016

Legrand, M., Preunkert, S., Weller, R., Zipf, L., Elsasser, C., Merchel, S., et al. (2017a). Year-round record of bulk and size-segregated aerosol composition in central Antarctica (Concordia site) – Part 2: biogenic sulfur (sulfate and methanesulfonate) aerosol. *Atmos. Chem. Phys.* 17, 14055–14073. doi: 10.5194/acp-17-14055-2017

Legrand, M., Preunkert, S., Wolff, E., Weller, R., Jourdain, B., and Wagenbach, D. (2017b). Year-round records of bulk and size- segregated aerosol composition in central Antarctica (Concordia site) – Part 1: fractionation of sea-salt particles. *Atmos. Chem. Phys.* 17, 14039–14054. doi: 10.5194/acp-17-14039-2017

Levin, I., Born, M., Cuntz, M., Langendörfer, U., Mantsch, S., Naegler, T., et al. (2002). Observations of atmospheric variability and soil exhalation rate of Radon-222 at a Russian forest site: technical approach and deployment for boundary layer studies. *Tellus B* 54, 462–475. doi: 10.1034/j.1600-0889.2002.01346.x

Levin, I., Schmithüsen, D., and Vermeulen, A. (2017). Assessment of 222Radon progeny loss in long tubing based on static filter measurements in the laboratory and in the field. *Atmos. Meas. Tech.* 10, 1313–1321. doi: 10.5194/amt-10-1313-2017

Li, F., Ginoux, P., and Ramaswamy, V. (2008). Distribution, transport, and deposition of mineral dust in the Southern Ocean and Antarctica: contribution of major sources. *J. Geophys. Res.* 113:D10207. doi: 10.1029/2007JD009190

Locatelli, R., Bousquet, P., Hourdin, F., Saunois, M., Cozic, A., Couvreux, F., et al. (2015). Atmospheric transport and chemistry of trace gases in LMDz5B: evaluation and implications for inverse modelling. *Geosci. Model Dev.* 8, 129–150. doi: 10.5194/gmd-8-129-2015

Mahowald, N., Kohfeld, K., Hansson, M., Balkanski, Y., Harrison, S. P., Prentice, I. C., et al. (1999). Dust sources and deposition during the last glacial maximum and current climate: a comparison of model results with paleodata from ice cores and marine sediments. *J. Geophys. Res.* 104, 15895–15916. doi: 10.1029/1999JD900084

Manno, C., Sandrini, S., Tositti, L., and Accornero, A. (2007). First stages of degradation of *Limacina helicina* shells observed above the aragonite chemical lysocline in Terra Nova Bay (Antarctica). *Antarct. Sci.* 19, 395–407. doi: 10.1016/j.jmarsys.2006.11.002

Markle, B. R., Bertler, N. A. N., Sinclair, K. E., and Sneed, S. B. (2012). Synoptic variability in the Ross Sea region, Antarctica, as seen from back-trajectory modeling and ice core analysis. *J. Geophys. Res.* 117:D02113. doi: 10.1029/2011JD016437

Meier, W., Fetterer, F., Duerr, R., Stroeve, J., Savoie, M., and Mallory, S. (2017). *NOAA/NSIDC Climate Data Record of Passive Microwave Sea Ice Concentration, Version 3. February 2017 Mean Ice Concentration*. Boulder, CO: NSIDC.

Nicol, S., Pauly, T., Bindoff, N. L., Wright, S., Thiele, D., Hosie, G. W., et al. (2000). Ocean circulation off east Antarctica affects ecosystem structure and sea-ice extent. *Nature* 406, 504–507. doi: 10.1038/35020053

Nylen, T. H., Fountain, A. G., and Doran, P. T. (2004). Climatology of katabatic winds in the McMurdo dry valleys, southern Victoria Land, Antarctica. *J. Geophys. Res.* 109:D03114. doi: 10.1029/2003JD003937

Obryk, M. K., Fountain, A. G., Doran, P. T., Lyons, W. B., and Eastman, R. (2018). Drivers of solar radiation variability in the McMurdo Dry Valleys, Antarctica. *Nat. Sci. Rep.* 8:5002. doi: 10.1038/s41598-018-23390-7

Peng, G., Meier, W., Scott, D., and Savoie, M. (2013). A long-term and reproducible passive microwave sea ice concentration data record for climate studies and monitoring. *Earth Syst. Sci. Data* 5, 311–318. doi: 10.5194/essd-5-311-2013

Pereira, E. B. (1990). Radon-222 time series measurements in the Antarctic Peninsula [1986– 1987]. *Tellus* 42, 39–45. doi: 10.3402/tellusb.v42i1.15190

Pereira, E. B., and da Silva, H. E. (1989). Atmospheric radon measurements by electrostatic precipitation. *Nucl. Instrum. Methods* A280, 503–505. doi: 10.1016/0168-9002(89)90960-1

Pereira, E. B., Evangelista, H., Pereira, K. C. D., Cavalcanti, I. F. A., and Setzer, A. W. (2006). Apportionment of black carbon in the South Shetland Islands, Antarctic Peninsula. *J. Geophys. Res.* 111:D03303. doi: 10.1029/2005JD006086

Pereira, K. C. D., Evangelista, H., Pereira, E. B., Simões, C. J., Johnson, E., and Melo, R. L. (2004). Transport of crustal microparticles from Chilean Patagonia to the Antarctic Peninsula by SEM-EDS analysis. *Tellus Ser. B* 56, 262–275. doi: 10.3402/tellusb.v56i3.16428

Polian, G., and Lambert, G. (1979). Radon daughters and sulfur output from Erebus volcano, Antarctica. *J. Volcanol. Geothermal Res.* 6, 125–137. doi: 10.1016/0377-0273(79)90050-7

Polian, G., Lambert, G., Ardouin, B., and Jegou, A. (1986). Long-range transport of continental radon in subantarctic and Antarctic areas. *Tellus B* 38, 178–189. doi: 10.3402/tellusb.v38i3-4.15126

Preunkert, S., Ancellet, G., Legrand, M., Kukui, A., Kerbrat, M., Sarda-Estève, R., et al. (2012). Oxidant Production over Antarctic Land and its Export (OPALE) project: an overview of the 2010-2011 summer campaign. *J. Geophys. Res.* 117:D06308. doi: 10.1029/2011JD017145

Preunkert, S., Jourdain, B., Legrand, M., Udisti, R., Becagli, S., and Cerri, O. (2008). Seasonality of sulfur species (sulfate, methanesulfonate and dimethyl sulfur) in Antarctica: inland versus coastal regions. *J. Geophys. Res.* 113:D15302. doi: 10.1029/2008JD009937

Protat, A., Schulz, E., Rikus, L., Sun, Z., Xiao, Y., and Keywood, M. (2016). Shipborne observations of the radiative effect of Southern Ocean clouds. *JGR Atmos.* 122, 318–328. doi: 10.1002/2016JD026061

Rintoul, S. R., Chown, S. L., DeConto, R. M., England, M. H., Fricker, H. A., Masson-Delmotte, V., et al. (2018). Choosing the future of Antarctica. *Nature* 558, 233–241. doi: 10.1038/s41586-018-0173-4

Samson, J. A., Barnard, S. C., Obremski, J. S., Riley, D. C., Black, J. J., and Hogan, A. W. (1990). On the systematic variation in surface aerosol concentration at South Pole. *Atmos. Res.* 25, 385–396. doi: 10.1016/0169-8095(90)90023-6

Sandrini, S., Ait-Ameur, N., Rivaro, P., Massolo, S., Touratier, F., Tositti, L., et al. (2007). Anthropogenic carbon distribution in the Ross Sea, Antarctica. *J. Mar. Syst.* 68, 91–102. doi: 10.1017/S0954102007000405

Schery, S. D., and Huang, S. (2004). An estimate of the global distribution of radon emissions from the ocean. *Geophys. Res. Lett.* 31:L19104. doi: 10.1029/2004GL021051

Schmithüsen, D., Chambers, S. D., Fischer, B., Gilge, S., Hatakka, J., Kazan, V., et al. (2017). A European-wide 222Rn and 222Rn progeny comparison study. *Atmos. Meas. Tech.* 10, 1299–1312. doi: 10.5194/amt-10-1299-2017

Shirsat, S. V., and Graf, H. F. (2009). An emission inventory of sulfur from anthropogenic sources in Antarctica. *Atmos. Chem. Phys.* 9, 3397–3408. doi: 10.5194/acp-9-3397-2009

Sinclair, K. E., Bertler, N. A. N., Trompetter, W. J., and Baisden, W. T. (2013). Seasonality of airmass pathways to coastal Antarctica: ramifications for interpreting high-resolution ice core records. *J. Clim.* 26, 2065–2076. doi: 10.1175/JCLI-D-12-00167.1

Slemr, F., Angot, H., Dommergue, A., Magand, O., Barret, M., Weigelt, A., et al. (2015). Comparison of mercury concentrations measured at several sites in the Southern Hemisphere. *Atmos. Chem. Phys.* 15, 3125–3133. doi: 10.5194/acp-15-3125-2015

Slusher, D. L., Neff, W. D., Kim, S., Huey, L. G., Wang, Y., Zeng, T., et al. (2010). Atmospheric chemistry results from the ANTCI 2005 Antarctic plateau airborne study. *JGR Atmos.* 115:D07304. doi: 10.1029/2009JD012605

Solomon, S. (1999). Stratospheric ozone depletion: a review of concepts and history. *Rev. Geophys.* 37, 275–316. doi: 10.1029/1999RG900008

Song, S., Angot, H., Selin, N. E., Gallée, H., Sprovieri, F., Pirrone, N., et al. (2018). Understanding mercury oxidation and air-snow exchange on the East Antarctic Plateau: a modeling study. *Atmos. Chem. Phys. Discuss.* doi: 10.5194/acp-2018-436 [Epub ahead of print].

Sprovieri, F., Pirrone, N., Bencardino, M., D'Amore, F., Carbone, F., Cinnirella, S., et al. (2016). Atmospheric Mercury Concentrations observed at ground-based monitoring sites globally distributed in the framework of the GMOS network. *Atmos. Chem. Phys.* 16, 1–21. doi: 10.5194/acp-16-11915-2016

Sprovieri, F., Pirrone, N., Ebinghaus, R., Kock, H., and Dommergue A. (2010). A review of worldwide atmospheric mercury measurements. *Atmos. Chem. Phys.* 10, 8245–8265. doi: 10.1016/j.scitotenv.2014.10.112

Sprovieri, F., Pirrone, N., Hedgecock, I. M., Landis, M. S., and Stevens, R. K. (2002). Intensive atmospheric mercury measurements at Terra Nova Bay in Antarctica during November and December 2000. *J. Geophys. Res.* 107, 4722–4729. doi: 10.1029/2002JD002057

Stavert, A. R., Law, R. M., van der Schoot, M., Langenfelds, R. L., Spencer, D. A., Krummel, P. B., et al. (2018). The Macquarie Island [LoFlo2G] high-precision continuous atmospheric carbon dioxide record. *Atmos. Meas. Tech.* doi: 10.5194/amt-2018-300 [Epub ahead of print].

Taguchi, S., Iida, T., and Moriizumi, J. (2002). Evaluation of the atmospheric transport model NIRE-CTM-96 by using measured radon-222 concentrations. *Tellus* 54B, 250–268. doi: 10.1034/j.1600-0889.2002.01364.x

Taguchi, S., Tasaka, S., Matsubara, M., Osada, K., Yokoi, T., and Yamanouchi, T. (2013). Air-sea gas transfer rate for the Southern Ocean inferred from 222Rn concentrations in maritime air and a global atmospheric transport model. *J. Geophys. Res. Atmos.* 118, 7606–7616. doi: 10.1002/jgrd.50594

Tositti, L., Pereira, E. B., Sandrini, S., Capra, D., Tubertini, O., and Bettoli, M. G. (2002). Assessment of summer trends of tropospheric radon isotopes in a coastal Antarctic Station (Terra Nova Bay). *Int. J. Environ. Anal. Chem.* 82, 259–274. doi: 10.1080/03067310290027767

Turner, J., Lachlan-Cope, T. A., Colwell, S., Marshall, G. J., and Connolley, W. M. (2006). Significant warming of the Antarctic winter troposphere. *Science* 311, 1914–1917. doi: 10.1126/science.1121652

Ui, H., Tasaka, S., Hayashi, M., Osada, K., and Iwasaka, Y. (1998). Preliminary results from radon observations at Syowa Station, Antarctica, during 1996. *Polar Meteorol. Glaciol.* 12, 112–123.

van Noije, T. P. C., Le Sager, P., Segers, A. J., van Velthoven, P. F. J., Krol, M. C., Hazeleger, W., et al. (2014). Simulation of tropospheric chemistry and aerosols with the climate model EC-Earth. *Geosci. Model Dev.* 7, 2435–2475. doi: 10.5194/gmd-7-2435-2014

Wada, A., Murayama, S., Kondo, H., Matsueda, H., Sawa, Y., and Tsuboi, K. (2010). Development of a compact and sensitive electrostatic Radon-222 measuring system for use in atmospheric observation. *J. Meteorol. Soc. Jpn.* 88, 123–134. doi: 10.2151/jmsj.2010-202

Wang, J., Zhang, L., and Xie, Z. (2016). Total gaseous mercury along a transect from coastal to central Antarctic: spatial and diurnal variations. *J. Hazard. Mater.* 317, 362–372. doi: 10.1016/j.jhazmat.2016.05.068

Weller, R., Levin, I., Schmithüsen, D., Nachbar, M., Asseng, J., and Wagenbach, D. (2014). On the variability of atmospheric 222Rn activity concentrations measured at Neumayer, coastal Antarctica. *Atmos. Chem. Phys.* 14, 3843–3853. doi: 10.5194/acp-14-3843-2014

Weller, R., Wagenbach, D., Legrand, M., Elsässer, C., Tian-Kunze, X., and König-Langlo, G. (2011). Continuous 25-yr aerosol records at coastal Antarctica – I: inter-annual variability of ionic compounds and links to climate indices. *Tellus B* 63, 901–919. doi: 10.1111/j.1600-0889.2011.00542.x

Whittlestone, S., and Zahorowski, W. (1998). Baseline radon detectors for shipboard use: development and deployment in the First Aerosol Characterization Experiment (ACE 1). *J. Geophys. Res.* 103, 16743–16751. doi: 10.1029/98JD00687

Williams, A. G., and Chambers, S. D. (2016). *A History of Radon Measurements at Cape Grim. Baseline Atmospheric Program (Australia) History and Recollections*. Melbourne: Bureau of Meteorology, 131–146.

Williams, A. G., Chambers, S. D., and Griffiths, A. D. (2017). "Seasonal variations in 'deep baseline' radon over the Southern Ocean. Atmospheric composition & chemistry observations & modelling conference incorporating the cape grim annual science meeting 2017 [oral], 8-10 November 2017, Murramarang, NSW," in *Bureau of Meteorology and CSIRO Oceans and Atmosphere*, eds N. Derek and P. B. Krummel (Melbourne: Climate Science Centre), 10.

Zahorowski, W., Griffiths, A. D., Chambers, S. D., Williams, A. G., Law, R. M., Crawford, J., et al. (2013). Constraining annual and seasonal radon-222 flux density from the Southern Ocean using radon-222 concentrations in the boundary layer at Cape Grim. *Tellus B* 65:19622. doi: 10.13402/tellusb.v19665i19620.19622

Zhang, K., Feichter, J., Kazil, J., Wan, H., Zhuo, W., Griffiths, A. D., et al. (2011). Radon activity in the lower troposphere and its impact on ionization rate: a global estimate using different radon emissions. *Atmos. Chem. Phys.* 11, 7817–7838. doi: 10.5194/acp-11-7817-2011

Zhang, K., Wan, H., Zhang, M., and Wang, B. (2008). Evaluation of the atmospheric transport in a GCM using radon measurements: sensitivity to cumulus convection parameterization. *Atmos. Chem. Phys.* 8, 2811–2832. doi: 10.5194/acp-8-2811-2008

Conflict of Interest Statement: The authors declare that the research was conducted in the absence of any commercial or financial relationships that could be construed as a potential conflict of interest.

frontiers in Earth Science

ORIGINAL RESEARCH
published: 03 December 2018
doi: 10.3389/feart.2018.00207

Aerosol Concentrations in Relationship to Local Atmospheric Conditions on James Ross Island, Antarctica

Jan Kavan[1], Pavla Dagsson-Waldhauserova[2,3], Jean Baptiste Renard[4], Kamil Láska[1] and Klára Ambrožová[1]*

[1] Department of Geography, Faculty of Science, Masaryk University, Brno, Czechia, [2] Faculty of Agricultural and Environmental Sciences, Agricultural University of Iceland, Reykjavik, Iceland, [3] Faculty of Environmental Sciences, Czech University of Life Sciences Prague, Prague, Czechia, [4] Laboratoire de Physique et Chimie de l'Environnement et de l'Espace, CNRS, Orléans, France

Several important ice-free areas (e.g., Seymour Island, Cape Lamb on Vega Island, Terrapin Hill) are located in the Eastern Antarctic Peninsula region. The largest of these ice-free areas can be found on the Ulu Peninsula, James Ross Island, where this study was undertaken. The Ulu Peninsula covers an area of 312 km^2, and has been found to be an important active High Latitude Dust source. In this study, aerosol concentrations and local wind properties are described together with their linkages and typical synoptic situations. The highest aerosol concentrations of 57 $\mu g\ m^{-3}$ for PM_{10} were detected during high wind speed events that exceeded 10 m s^{-1}, which is also a threshold level for activating local mineral material sources. Surface deposition of dust particles can have significant environmental impacts such as changes in properties of atmosphere or enhanced snow melting.

Keywords: aerosol, surface wind, Antarctica, high latitude dust sources, atmospheric conditions, Antarctic Peninsula

OPEN ACCESS

Edited by:
Gert-Jan Steeneveld, Wageningen University & Research, Netherlands

Reviewed by:
Lucas Alados-Arboledas, Universidad de Granada, Spain
Yoav Yosef Yair, Interdisciplinary Center Herzliya, Israel

****Correspondence:***
Jan Kavan
jan.kavan.cb@gmail.com

Specialty section:
This article was submitted to Atmospheric Science, a section of the journal Frontiers in Earth Science

Received: *30 July 2018*
Accepted: *30 October 2018*
Published: *03 December 2018*

Citation:
Kavan J, Dagsson-Waldhauserova P, Renard JB, Láska K and Ambrožová K (2018) Aerosol Concentrations in Relationship to Local Atmospheric Conditions on James Ross Island, Antarctica. Front. Earth Sci. 6:207. doi: 10.3389/feart.2018.00207

INTRODUCTION

Antarctica is the largest polar desert in the world, of which approximately 2% of its surface area is ice-free and contains active High Latitude Dust sources (HLD, Bullard et al., 2016). It is the coldest, windiest (maximum speed of 90 m s^{-1}) and driest continent, with annual precipitation reaching approximately 300 mm in the coastal areas (King and Turner, 1997; van Lipzig et al., 2004). However, mean annual precipitation is greatly reduced at the dust sources in Antarctica, ranging between 3–50 mm per year (Fountain et al., 2009). One of the most important ice-free landscape shaping processes, apart fluvial activities, is aeolian transport. Aeolian processes acting in high latitudes develop a specific range of surface landforms, such as ripples or small-scale dunes. However, these landforms are spatially restricted to areas with low surface moisture contents and an absence of vegetation cover (Bullard et al., 2016). These conditions enable the mineral material to be uplifted by wind and transported for long distances. Consequently, in periglacial environments where glaciers have recently receded and left large amounts of unsorted

Abbreviations: AOT, Aerosol Optical Thickness; HLD, high latitude dust sources; JGM, Johann Gregor Mendel Station; JRI, James Ross Island; LOAC, light optical aerosol counter; PM, particulate matter.

mineral material, wind erosion processes frequently occur (Ballantyne, 2002). Wiggs et al. (2004) identified surface moisture content as the second most important critical variable influencing aeolian transport apart wind velocity.

High wind velocities are usually required to trigger wind transportation processes of large particles and grains. Antarctica is more prone to wind erosion than other areas, as a result of its prevailing strong katabatic winds (Nylen et al., 2004; Bullard et al., 2016). However, the development of large aeolian landforms in periglacial environments is limited by the presence of permafrost. The thickness of the active layer ranges between 50 and 150 cm in the Antarctic islands and maritime East Antarctica, and 15 to 50 cm in the Antarctic interior (Bockheim, 1995). As a result, there is only a limited amount of surface material available for aeolian processes. Weathering (predominantly freeze-thaw processes) plays a crucial role in preparing the surface for further exogenic processes; however, the right combination of rock temperature and moisture can cause salt, insolation, hydration, or chemical weathering to be dominant (Elliot, 2003). Hedding et al. (2015) observed the evolution of aeolian landforms (megaripples) on Marion Island, and suggested that aeolian processes are also actively modifying solifluction landforms. Ripples with a height of several decimeters were found in several localities, with the annual (horizontal) aeolian sediment flux estimated at 0.36–3.85 kg cm^{-2} $year^{-1}$ (Hedding et al., 2015). Aeolian deposition also plays a vital role as an input vector of material to the surface of glaciers. Fortner et al. (2011) identified aeolian trace elements on the surface of Taylor Glacier as well as in its glaciofluvial system. Concentrations of these elements are often an important variable for the development of organisms in lakes and rivers. A similar study was undertaken by Šabacká et al. (2012) in Taylor Valley resulting in the identification of foehn winds as a main factor controlling the input of mineral and biotic material to the valley ecosystem. For example, Bristow et al. (2010) identified dunes in Victoria Valley that were composed mainly from coarse sand. In contrast, Arctic aeolian material sources are limited to areas located close to glaciers or floodplains, where material is freely available and is not covered by vegetation (Ballantyne, 2002), with the exception of Iceland where volcanic material input can be independent of wind speed (Dagsson-Waldhauserova et al., 2014). Bullard and Austin (2011) studied dust generation from glaciofluvial sediments in a proglacial flood plain in West Greenland. They found that wind speeds of 6 m s^{-1} only moved the finest sediment fractions during the summer. Furthermore, Prospero et al. (2012) identified proglacial systems as the main source of material for major dust storms from a 6-year record in Iceland.

As Antarctica is almost entirely ice covered, most of the previous studies undertaken are geographically constrained to sparse ice-free areas, such as the McMurdo Dry Valleys (e.g., Lancaster, 2002; Fortner et al., 2011; Šabacká et al., 2012) and locations in the Antarctic Peninsula (e.g., Asmi et al., 2018). The best-known local dust sources are located in West Antarctica, with the McMurdo Dry Valleys being the largest ice-free area (approximately 4,800 km^2) with documented frequent dust suspension (Lancaster, 2002; Ayling and McGowan, 2006; Atkins and Dunbar, 2009; Bullard et al., 2016). Bory et al. (2010) suggested that there are dust sources in the ice-free areas of East Antarctica based on dust samples collected in snow pits on Berkner Island. Coastal ice-free areas have also been identified as active dust sources around the Maitri Station, Larsemann Hills, and Neumayer Station in East Antarctica (Weller et al., 2008; Chaubey et al., 2011; Budhavant et al., 2015), as well as in the Antarctic Peninsula region (Artaxo and Rabello, 1992; Kavan et al., 2017; Asmi et al., 2018). Alternately, aeolian material can be resuspended from the surface of glaciers where sediments that were previously incorporated into the ice re-emerge at the surface as a result of ablation (Atkins and Dunbar, 2009). Long-range transport of dust from other HLD sources, such as South America (Patagonia), New Zealand, and deserts in Australia and Africa, contribute to the dust depositions in Antarctica (Neff and Bertler, 2015; Bullard et al., 2016; Asmi et al., 2018). The main non-Antarctic dust sources for the Antarctic Peninsula region are in Patagonia - Tierra del Fuego, Provinces of Chubut (e.g., Lago Colhué Huapi), and Santa Cruz (Bullard et al., 2016). Patagonian dust sources consist of fine dust material and are extremely active, with >120 dust days per year since 2012 (Gassó and Torres, 2018, unpublished). Patagonian dust was found in ice cores and snow samples in the Antarctic Peninsula and in East Antarctica, showing the possibility of long-range transport of dust to Antarctica (Basile et al., 1997; Pereira et al., 2004; McConnell et al., 2007; Bory et al., 2010; Delmonte et al., 2017). There is a lack of research investigating long-range transport of Patagonian dust to the Antarctic as a result of sparse direct measurements of aerosols in Antarctica. However, during the measurement period of this study (January-March 2018) several dust storms occurred in Patagonia (SYNOP data from the local weather stations and MODIS satellite images obtained from Santiago Gassó, NASA).

High latitude dust sources produce at least 5% of the global dust budget (100 mil tons per year), where, for instance, dust emissions from Iceland range between 31–40 mil tons per year (Arnalds et al., 2014; Bullard et al., 2016). Measured dust deposition rates reported from the HLD sources seem to reach higher values than those from the global deserts (Hugenholtz and Wolfe, 2010; Arnalds et al., 2013; Bullard, 2013). The most extreme wind erosion event recorded on Earth was measured in Iceland in 2010 when aeolian transport of 11 t m^{-1} occurred during one 23-h storm (Arnalds et al., 2013). Deposition rates of >33,000 g m^{-2} $year^{-1}$ were recorded in Canada, while rates >100 gm^{-2} $year^{-1}$ were reported from New Zealand, Iceland, and Patagonia (Bullard, 2013; Bullard et al., 2016). Deposition rates measured in Greenland and McMurdo Dry Valleys are lower than other HLD sources with rates of <8 g m^{-2} $year^{-1}$ (Lancaster, 2002; Bullard, 2013). Atkins and Dunbar (2009) measured dust fluxes of 7.8–24.5 g m^{-2} $year^{-1}$ while Chewings et al. (2014) reported fluxes of 0.2–55 g m^{-2} $year^{-1}$ in the McMurdo Dry Valleys, West Antarctica.

Direct aerosol measurements in Antarctica are sparse although Particulate Matter (PM) properties provide crucial information on the impact of particles on the climate in Antarctica. For the coastal areas in East Antarctica, the main identified particles were sea salt, sulfate, and crustal components. The mass concentrations of PM_{10} (particles with a diameter of

<10 μm) and $PM_{2.5}$ (particles with a diameter of <2.5 μm) were 5.1 and 4.3 μg m^{-3}, respectively in the Larsemann Hills during summer (Budhavant et al., 2015), and 8.3 and 6.03 μ gm^{-3} at the Maitri station (Chaubey et al., 2011). PM_{10} concentrations from McMurdo station during two summers in 1995–1997 were 3.4 and 4.1 μg m^{-3} on average (Mazzera et al., 2001). Mean PM_{10} and $PM_{2.5}$ concentrations of 4.4 μg m^{-3} and 2.4 μ gm^{-3}, respectively were measured in the Antarctic Peninsula during the late 1980s (Artaxo and Rabello, 1992). Seasonal variations in aerosol loadings showed increased concentrations in January and a decrease in February and March in Terra Nova Bay, West Antarctica in 2000–2001 (Truzzi et al., 2005). PM_{10} concentrations of 2.1–5 μg m^{-3} on average were reported from the Antarctic Peninsula, with higher concentration in summer (October to March) in 2013–2015 (Asmi et al., 2018). Asmi et al. (2018) emphasized that the concentrations of sea salt and soil particles nearly doubled on average in summer when winds were high.

The main purpose of this study was to identify summer aerosols and the physical properties of PM in the north-eastern sector of the Antarctic Peninsula. The objectives were to provide mass and number concentrations of PM with a diameter of 0.2–100 μm, typology of measured aerosols, sources of measured aerosols, and compare PM concentrations with Aerosol Optical Thickness (AOT). Comparison of local wind properties with PM and AOT should identify typical synoptic situations, where aerosol concentrations are particularly high and important. This study aims to provide more evidence to suggest that Antarctica's ice-free desert surfaces are active HLD sources providing natural air pollution.

MATERIALS AND METHODS

Study Site

James Ross Island (JRI) is situated in the Weddell Sea region on the eastern side of the Antarctic Peninsula. It constitutes one of the largest ice-free areas in Antarctica (BAS, 2005) which covers an area of 552 km^2, representing 1.2% of the total ice-free area of the continent. More than half of the ice-free surfaces on JRI (312 km^2; 12.5% of JRI) are located on the Ulu Peninsula (Kavan et al., 2017), in close proximity to the Johann Gregor Mendel (JGM) Station, where the presented LOAC measurements were undertaken (**Figure 1**). This ice-free area represents one of the largest Antarctic oases after the McMurdo Dry Valleys (4900 km^2) and Bunger Oasis (450 km^2), exceeding the size of both Schirmacher Oasis (34 km^2) and the Larsemann Hills (40 km^2). Large bare surface areas produce dust during frequent dust storms (Kavan et al., 2017). The JGM Station, located on the northern shore of JRI, is exposed to prevailing S-NW winds (Zvěřina et al., 2014) which cross active bare surfaces approximately 15 km away from the station. The surface predominantly constitutes unconsolidated fine sediments in the lower parts of the terrain, and bare rock on top of the volcanic mesas which reach an elevation of approximately 300–400 m a.s.l. An important source of aeolian material is derived from the braid plains of the Bohemian Stream (<100 m from JGM) and the adjacent Algal Stream, which serve as redistribution areas of fluvial and aeolian material (Kavan et al., 2017; Kavan and Nývlt, 2018).

The climate of JRI is affected by the regional-scale atmospheric circulation formed by the Antarctic Peninsula Mountains, which provide an effective barrier to westerly winds associated with cyclonic systems centered in the circumpolar trough (King et al., 2003). The mean annual air temperatures (2006–2015) in the northern part of JRI ranged from −7.0°C at the Johann Gregor Mendel Station (JGM) to less than −8.0°C in higher elevated areas (375 m a.s.l. on Bibby Hill) (Ambrožová and Láska, 2016; Hrbáček et al., 2018). The meteorological observations from Johnson Mesa (320 m a.s.l.) in the period 2008–2010 showed that the wind directions are mainly between southern and western sectors (Zvěřina et al., 2014). These directions correspond to the position and orography of the Antarctic Peninsula, which strongly affects the airflow along the eastern side of the peninsula, before approaching the northern coast of JRI. The summer and winter wind directions are slightly different, but they remain in the S-NW sector (Bohuslavová et al., 2018).

Wind Speed and Direction

Wind speed and direction were measured at 2 m above the ground using the USA-1 sonic anemometer (METEK GmbH, Germany) connected with the internal data system. The wind components were sampled at a frequency of 10 Hz and stored as 5-min averaged values. The mast with the USA-1 anemometer was placed 10 m southeast from the meteorological tower at the JGM Station. The temporal variability of the horizontal wind components was analyzed and visualized with the Grapher 13 software for 16 directional sectors of a wind rose.

Aerosol Optical Thickness

Aerosol Optical Thickness and water vapor measurements were obtained with the hand-held Microtops II sun photometer (referred to here as Sun photometer) manufactured by the Solar Light Inc., United States. It provides direct information on irradiance components in five spectral wave bands (340, 380, 500, 870, and 936 nm), giving automatically AOT and water vapor information. The field of view of each of the optical channels is 2.5° and the sun target assembly allows up to 0.1° pointing resolution. The Sun photometer calculates the AOT value at each wavelength based on the channel's signal, its extra-terrestrial constant, atmospheric pressure, altitude, time, and location (Morys et al., 2001). Before the field campaign the instrument was calibrated in the laboratory of the Solar Light Company, Inc. Further information on the Microtops Sun photometer can be found in Morys et al. (2001). To avoid cloudiness influence, AOT measurements were conducted on cloud-free days with a cloud cover $<30\%$ or when the clouds were located $>2.5°$ from the Sun disk. The instrument was set to carry out 32 rapid scan samples within one measurement, from which the average AOT was calculated and archive to the logger memory. During each measurement session, the Sun photometer was used to take a sequence of five measurements within 1 min. When possible, measurements were carried out

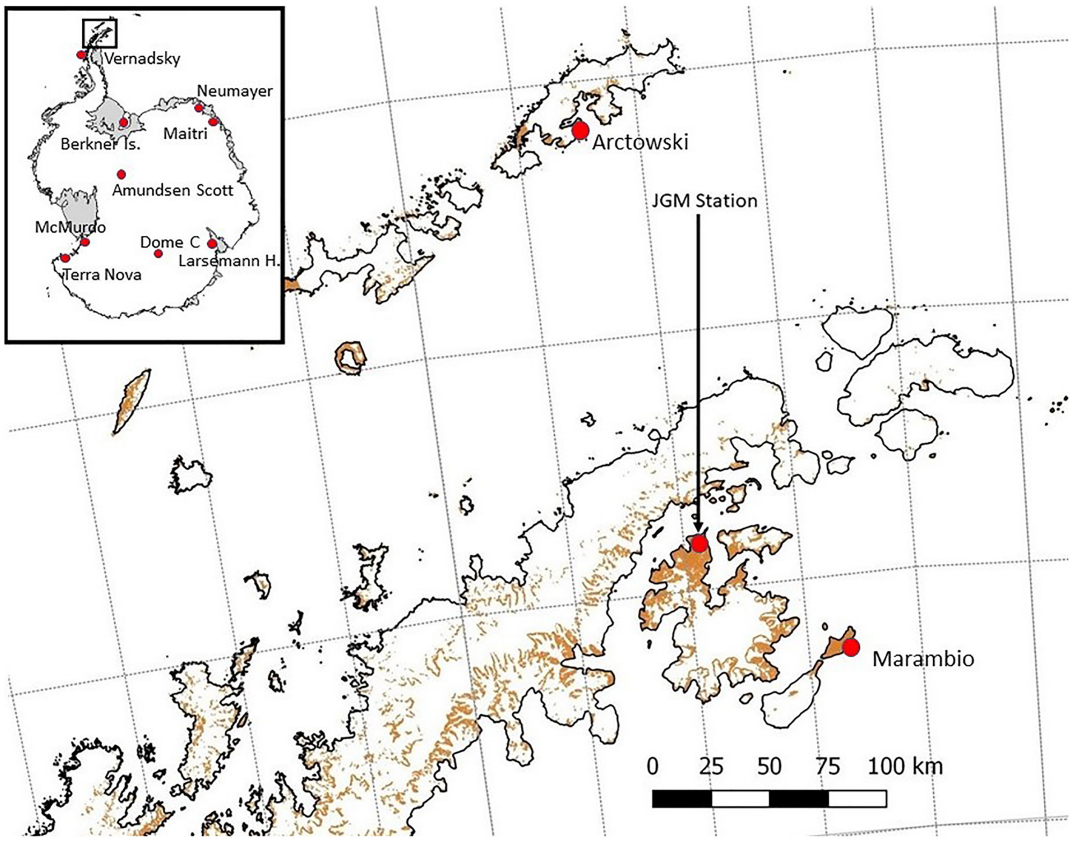

FIGURE 1 | Study site location (JGM Station) and other Antarctic sites used in the text, ice free areas in brown.

between 11:00 and 13:00 UTC when solar zenith angles were $<60°$, in order to eliminate the effect of optical distortions by the atmosphere.

LOAC – Light Optical Aerosol Counter

The LOAC (Light Optical Aerosols Counter) is a light aerosol counter which is well adapted to detect dust particles, and provides size distributions as well as the main typologies of particles present The LOAC instrument uses a novel optical design to retrieve the particle number, mass concentration, size, and the typology of the particles in ambient air (Renard et al., 2016a,b). The particles get injected through an optical chamber by a pumping system and cross a laser beam, where two detectors record the scattered light. The first detector analyses the small scattering angles in the 10–15° range, where the light is scattered by irregular grains by diffraction, and is not dependent on the refractive index or the porosity (Lurton et al., 2014). A direct correlation is therefore established between the intensity of the light scattered and the optical diameter of the particles. The LOAC provides the concentration of particles for 19 size classes in the 0.2–100 μm range. The instrument was calibrated using latex and glass beads, as well as with irregular grains to better represent the solid particles that can be found in the ambient air. The second detector collects data at scattering angles that range between 50°–70°, recording scattered light that is very sensitive to the refractive index and the porosity of the particles. By combining the data from the two detectors, a "speciation index" that is representative of the ability of the particles to absorb light can be produced. Laboratory measurements were performed with reference samples, water droplets, sand, carbonaceous particles, and black carbon, to establish the speciation index of the particles. Subsequently, the speciation index retrieved is compared to these reference indices to provide the identification of the nature of the observed particles (transparent for the liquid droplets, semi-transparent for mineral/dust particles, strongly absorbent for carbonaceous and strongly porous particles). A good correlation was found between the LOAC measurements (counting and typology), other counting instruments, and satellite instruments, in particular during dust events (Renard et al., 2018).

The LOAC was operated directly in the ambient air. To take into consideration any possible changes in the electronic offset, mainly as a result of temperature variations, an automatic check was performed every 10 min. If an offset had evolved, an internal re-calibration of the instrument was undertaken.

The aerosols were collected with an omnidirectional collecting device and were subsequently injected in to the optical chamber though a vertical inlet measuring several cm in length to ensure that the collected particles will not fall out of suspension inside the instrument before crossing the laser beam. The sampling

efficiency for large particles is near to 100% when the wind speed is lower than approximately 20 m s^{-1}.

The uncertainty for the total aerosol concentration measurements is ±20% for concentration values greater than 1 particle per cm^3 (for a 10-min integration time). In contrast, the uncertainty increases to approximately 60% for concentration values less than 10-2 particle per cm^3. Finally, the precision in size calibration is ±0.025 μm for particles smaller than 0.6 μm, 5% for particles in the 0.7–2 μm range, and 10% for particles larger than 2 μm.

In this study, the LOAC was operated from 17 January 2018 to 21 March 2018. During this period, the LOAC encountered some strong electromagnetic perturbations; however, the data was kept where the perturbations were low so that the detection of particles was not altered by more than a few μm. The data was collected every 10 s and integrated over 5 min to reduce the dispersion of the measurements in case of low concentrations (data were integrated in a 5-min period together with the wind speed and direction data). The LOAC was temporally installed on the meteorological platform next to JGM station at the height of 3.5 m above the ground. During the study period, the power supply experienced several blackouts as a result of the electromagnetic interference created by other electric instruments in the vicinity. Therefore, post processing of the measured data resulted in an approximate data coverage of 60% the study period (compare with **Figure 2**).

Horizontal Aeolian Sediment Sampling

A passive horizontal aeolian sediment sampler (PHASS), based on the marble dust collector concept originally developed by Ganor (1975), was installed approximately 500 m from the LOAC site (to avoid interference with the station service activities). The PHASS was located on the ground surface to collect transported aeolian material during three periods in the 2018 summer season. The material was collected, filtered through a 3 μm filtration paper, and dried directly in the JGM Station laboratory. The dried material was weighed with the instrument precision of 0.0001 g, and the horizontal deposition was calculated.

RESULTS

Aerosol Concentrations During the Study Period

Mean (median) mass concentrations of the PM_{10} were 6.4 ± 1.4 (3.9 ± 1) μg m^{-3}, while the $PM_{2.5}$ was 3.1 ± 1 (2.3 ± 0.9) μg m^{-3} for the whole measurement period in January-March 2018. The median values are representative of the mass concertation outside the dust episodes. These results are similar to those recorded for the Larsemann Hills (Budhavant et al., 2015); however, they are lower than reported from the Maitri station (Chaubey et al., 2011). Mean values from JRI are higher than those from McMurdo station in 1995–1997 (Mazzera et al., 2001), the Antarctic Peninsula in late 1980s (Artaxo and Rabello, 1992), as well as from Marambio station in the Antarctic Peninsula in 2013–2015 (Asmi et al., 2018). A mean PM_{10} value of 6.4 μg m^{-3} from the Antarctic Peninsula is also comparable to two stations in Norway (annual mean of 7.5 μg m^{-3}), but higher than the annual mean of 4.4 μg m^{-3} in Sevettijarvi, Finland (Putaud et al., 2010). The mean $PM_{2.5}$ value in Antarctica is, however, lower than stations in Northern Europe.

The mean particle number concentrations were low, while the submicron particles were typically ten to hundred times lower during the clean conditions than during dust pollution events. Over 15 high-dust episodes, particles greater than 10 μm (PM_{10} > 20 μg m^{-3}) were detected (**Figure 3**), with concentrations similar to moderate Saharan dust events above the Mediterranean Sea (Renard et al., 2018). However, in contrast to the Mediterranean Sea region, the concentrations of submicron particles did not significantly increase during the dust events in Antarctica.

In the present study, we will focus on strong dust event recorded by LOAC in the 31 January – 2 February 2018, 14–16 March 2018 and the 18 March 2018. The dust events were characterized by strong concentration enhancements of particles larger than 10 μm (up to a thousand times greater than the background values). The LOAC typology indicates that the particles are indeed dust, with mean optical absorbing properties between "semi-transparent" and "absorbent," typical of dark

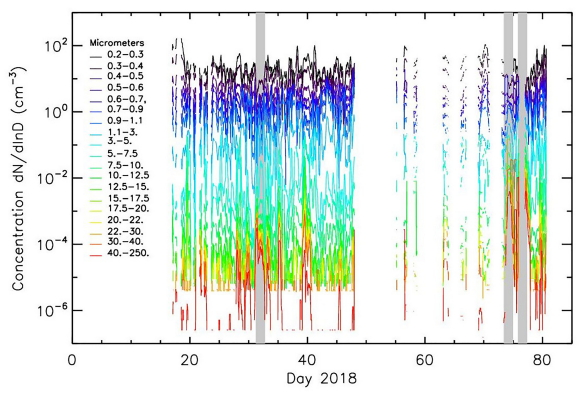

FIGURE 2 | Evolution of the LOAC concentrations for the 19 size classes; the three events are indicated by gray zones.

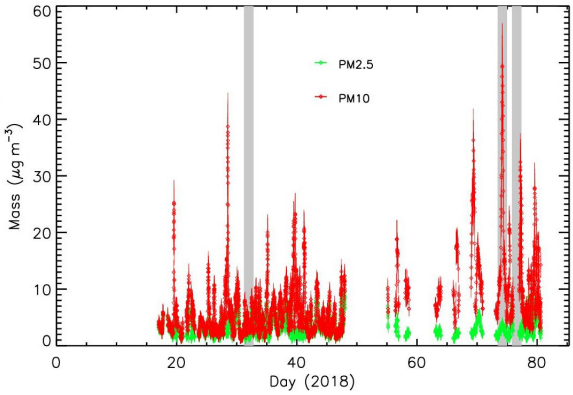

FIGURE 3 | Evolution of the $PM_{2.5}$ and PM_{10} masses; the three events are indicated by gray zones.

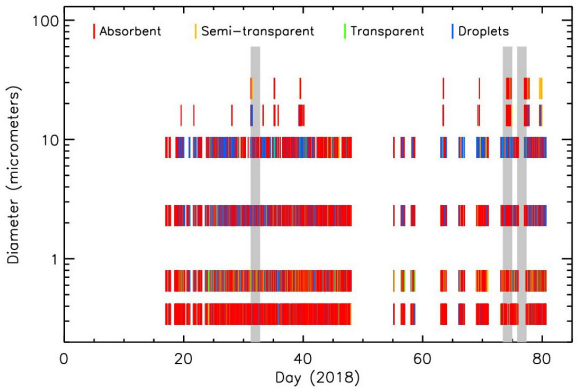

FIGURE 4 | The LOAC typology measurements; the three events are indicated by gray zones.

mineral. Nevertheless, some liquid particles are present, with average concentrations in the order of 10–20% for sizes below 20 μm (**Figure 4**).

Non-dust background conditions in the Antarctic Peninsula can be described by excluding selected dust events from the mean (median) mass concentrations of the whole measurement period. Mean (median) mass concentrations of the PM10 for non-dusty background conditions would decrease to 6.0 ± 1.3 (3.8 ± 1) μg m^{-3} while the $PM_{2.5}$ concentrations would increase to 3.2 ± 1 (2.4 ± 0.9) μg m^{-3} for the period January-March 2018. There are small differences in the median values between the whole measurement period and the same period excluding the dust events, showing the importance of using medians for interpretation of aerosol data. The small increase in the $PM_{2.5}$ background concentrations points to the different origin of the smaller particles in Antarctica than in the desert sources.

Near Surface Wind Conditions During the Summer 2018 Season

The average wind speed during the summer 2018 season was 5.2 m s^{-1}. However, on 31 January and 1 February, 17 February (day 48), 25 February (day 55), 16 March (day 74), 18 and 19 March (day 76 and 77), the daily mean wind speed exceeded 15 m s^{-1} with a maximum value of 18.7 m s^{-1} on 19 March.

The main wind directions were south-south-western and western, which occurred for 21 and 14% of the summer season, respectively. The most frequent wind directions came from southerly to westerly directions (64% of the season), and these winds were also the strongest with the wind speeds >10 m s^{-1}. The east-north-eastern and north-eastern winds were observed during 12% of the season, with wind speeds of <10 m s^{-1}. Wind speed and direction during the study period are shown in **Figures 5**, **6**.

Relationship Between Wind Properties and Aerosol Concentrations

Comparison of wind speed and aerosol concentration in different particle size classes shows a strong relationship during the

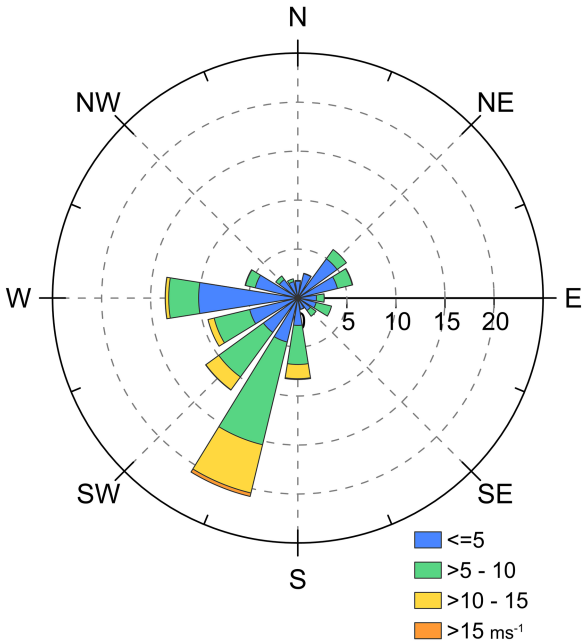

FIGURE 5 | Wind rose indicating average wind speed and direction during the period from 26 January to 21 March 2018.

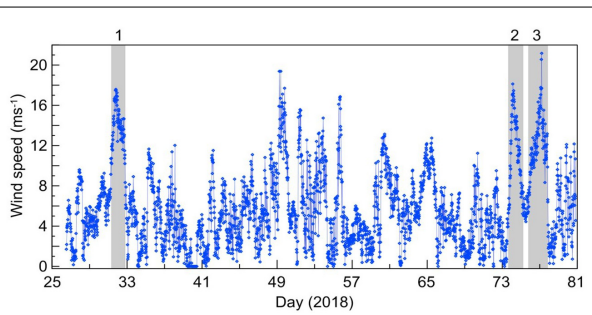

FIGURE 6 | Wind speed during the study period with highlighted maximum wind speed events described more in detail.

study period. Concentration of aerosol particles >5 μm shows a positive correlation with wind speed above the wind speed threshold of approximately 10 m s^{-1}. This correlation increases in strength with the increasing size of the particles. The table of correlation coefficients for individual classes (**Table 1**) shows that during high wind speed events (over 10 m s^{-1}) the larger particles (larger than 5 μm) from local sources are uplifted and transported. These high wind speed events occurred during 7.8% of the study period.

Particles that range in size from 10–20 μm were rarely detected during the low wind speed episodes (wind speed <10 m s^{-1}), suggesting that local material undergoes aeolian transport in short repeating periods. Approximately 83% of particles in the 10–20 μm size range were detected while wind speeds exceeded 10 m s^{-1}.

TABLE 1 | Correlation coefficients of wind speed and aerosol concentration in individual particle size classes for wind speed >10 m s^{-1} ($p < 0.02$ in bold) for the whole study period and three major dust events.

Whole study period						
Particle size classes (μm)	0.2–0.5	0.5–0.9	0.9–5	5–12.5	12.5–20	20–100
Correlation coefficient	−0.13	−0.11	0.09	**0.24**	**0.32**	**0.17**
Event 1						
Particle size classes (μm)	0.2–0.5	0.5–0.9	0.9–5	5–12.5	12.5–20	20–100
Correlation coefficient	0.03	0.01	−0.04	**−0.18**	**−0.15**	**−0.29**
Event 2						
Particle size classes (μm)	0.2–0.5	0.5–0.9	0.9–5	5–12.5	12.5–20	20–100
Correlation coefficient	−0.17	−0.15	**0.39**	**0.71**	**0.44**	**0.22**
Event 3						
Particle size classes (μm)	0.2–0.5	0.5–0.9	0.9–5	5–12.5	12.5–20	20–100
Correlation coefficient	−0.17	−0.09	−0.04	0.08	**0.17**	**0.82**

Synoptic Situation During Major Dust Events

Three major dust events were detected by the LOAC during high wind speed events (**Figure 7** for wind speed and direction). The wind speed was >8 m s^{-1} for the following events:

1st event: 31 Jan 0600 – 1 Feb 1930 UTC.
2nd event: 14 Mar 1100 – 16 Mar 1200 UTC.
3rd event: 16 Mar 1300 – 18 Mar 2000 UTC.

The synoptic situation for the three case studies was described according to hourly 850-hPa level geopotential height data from the MERRA-2 reanalysis (Global Modeling and Assimilation Office, 2015). On 31 January, a deepening cyclone was moving from the southern Atlantic Ocean toward South Orkney Islands. The 850-hPa wind was predominantly south-eastern, and it strengthened up to 14 m s^{-1} before midnight as a result of an increasing pressure gradient. Wind speeds near to the surface were even stronger (>15 m s^{-1}) and mainly coming from the south-south-west. The pressure field on 15 March was influenced by a cyclone approaching JRI from the South Shetland Islands, and continuing toward the central Weddell Sea, while still deepening. Consequently, the 850-hPa wind over JRI was the strongest in the morning, and as it weakened, it gradually changed from north-eastern to north-western. The wind near the surface exceeded 15 m s^{-1} less frequently than observed on 31 January, and despite the wind direction being predominantly south-south-western, it was variable. On 18 March, a low-pressure trough moved eastward in the Drake Passage, to the north of JRI. This situation resulted in the wind changing direction from the southwest to the west over JRI, which was accompanied by a wind speed increase that reached 19 m s^{-1}. During this even, the near surface wind was almost entirely south-western and above 10 m s^{-1}.

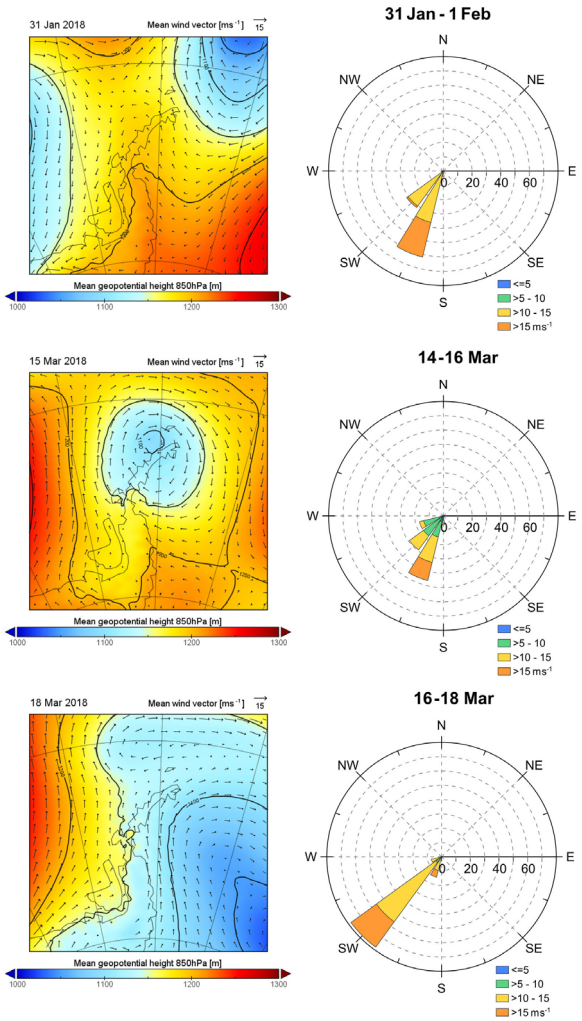

FIGURE 7 | Synoptic situation over the Antarctic Peninsula, wind roses for all three major dust events.

Major Dust Events in Detail

The three major dust events were analyzed in detail to identify relationship between wind speed and aerosol concentrations. An example of the influence that abrupt changes in wind direction has is illustrated on the 29 January 2018.

The two events that occurred in March show a good correlation, with a clear positive relationship; however, Event 1 (31 January – 1 February) does not correlate with the other two. The relationships between wind speed and aerosol concentration are shown on an example of an integrated particle class (5–12.5 μm) in **Figure 8**. Event 1 had significantly lower (approximately one order of magnitude) aerosol concentrations than both Events 2 and 3, probably as a result of higher ground surface moisture contents in the beginning of the summer season blocking the uplift of larger particles. The volumetric soil water

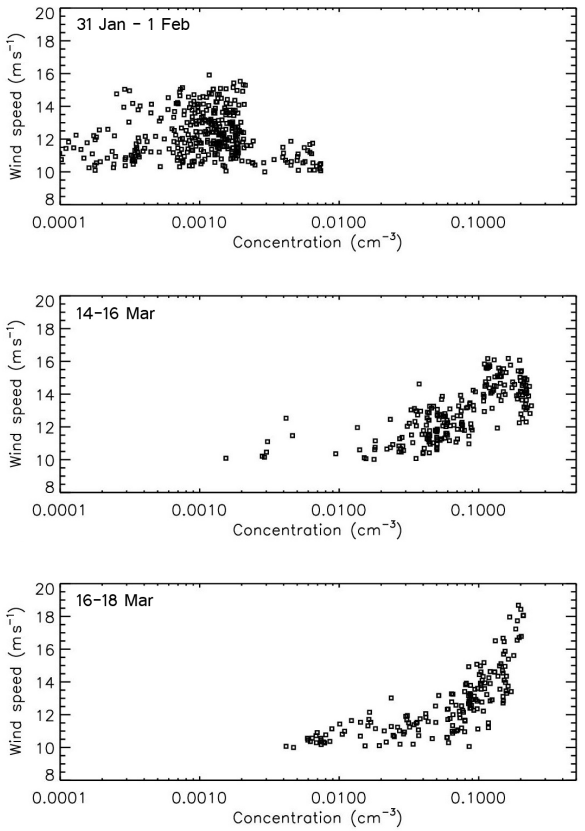

FIGURE 8 | Particle size class 5–12.5 μm aerosol concentration and wind speed relationship for the three major dust Events.

content at a depth of 5 cm during the first Event reached 31%, whereas it only reached 22% during Events 2 and 3. The influence of ground surface moisture content is well illustrated when comparing Events 1 and 2, as both events experienced approximately the same wind speed and similar wind directions, resulted in concentrations up to 0.25 n cm^{-3}. This influence can also explain why there is no significant correlation between aerosol concentration and wind speed, as is shown in **Table 1**. Significant and linear correlation was found during Event 3 at the end of the summer season.

Event 1 shows an unusual pattern in aerosol concentration. Contrary to the other two events, there is no clear correlation between wind speed and aerosol concentration of larger particle size classes. A detailed look at the dynamics of the event 1 (**Figure 9**) shows a rapid increase in aerosol concentration of larger particles (>5 μm) during the beginning of the high wind speed event, with peak concentrations occurring around 10:00 UTC when the wind speed was approximately 10 m s^{-1}. However, during the wind speed maximum (approximately 16 m s^{-1}) at 16:00–23:00 UTC, the concentrations were comparatively low. An interesting feature is the relatively high concentration of particle size class 5–12.5 μm at the end of the event, that may be associated with the change in wind direction.

A period of increased $PM_{2.5}$ concentrations (>4.2 μg m^{-3}) occurred at the JGM Station between 5 and 8 February 2018. $PM_{2.5}$ concentrations contributed with high proportions to PM_{10} during this period. HYSPLIT backward trajectory analyses (**Figure 10**) shows air parcels arriving to JGM Station from the Patagonian Desert areas, where several weather stations had reported the SYNOP codes for dust observations from 5 February to 7 February 2018. There are unfortunately no clear satellite images showing dust plumes for this period as, for example, on 12 February 2018. We have not obtained aerosol samples for the chemical analyses to confirm that the dust could have been transported from the Patagonian dust sources to Antarctica. The Patagonian dust sources were, however, very active in producing dust from mid-January to the end of March 2018.

The Event 2 (**Figure 11**) (14 March - 16 March 2018) has a well-defined peak period for both wind speed and aerosol concentration on 15 March from approximately 00:00 to 08:00 UTC. The maximum wind speed exceeded 16 m s^{-1} and aerosol concentrations in the size class 5–12.5 μm reached 0.23 n cm^{-3}. Timing of peak concentrations of larger (but even smaller) particles relatively well correspond with the period of highest wind speed even though the concentration peak was delayed behind the wind speed maximum of several hours.

Directly after the second event, another high wind speed episode (Event 3) occurred from 16 March to 18 March 2018 (**Figure 12**). This event is characterized by the highest wind speed recorded during the study period – 18.7 m s^{-1}. The available aerosol concentration measurement corresponds well to the observed wind speeds (correlation coefficient for particles 12.5–20 μm and wind speed is 0.69), even though a middle section of the event is missing the LOAC measurements. The best fit of aerosol concentrations and wind speed is found again for the particles larger than 5 μm. Aerosol concentrations in size class 5–12.5 μm reaches 0.21 n cm^{-3} during the peak wind speed.

Wind direction and aerosol concentrations were also associated as shown for example on 29 January 2018 (**Figure 13**). The day was not particularly windy, with an average wind speed of 4.1 m s^{-1} and a maximum wind speed of 6.0 m s^{-1}. The most pronounced change in wind conditions was the switch from a southern wind to a western wind at around 12:00 UTC, which lasted until 21:00 UTC. This was accompanied by a gradual increase in aerosol concentration, especially in the case of larger particles (typically >5 μm). The positive correlation between wind direction and aerosol concentration is significant ($p > 0.01$) for particles larger than 7.5 μm ($p > 0.02$ for particles 5–7.5 μm).

AOT

Mean AOT during the study period ranged between 0.48 at 380 nm and 0.55 at 870 nm with an average mean AOT value of 0.50. Mean AOT for 500 nm (**Figure 14A**) showed remarkable day to day variations with a peak on 6 February (1.941) and a mean value of 0.51 ± 0.53; showing no obvious trend during the summer. However, a strong positive correlation was found between water vapor and mean AOT for 500 nm when water the vapor column was >0.8 cm (correlation coefficient 0.82; statistically significant at the significance level of 0.01). When

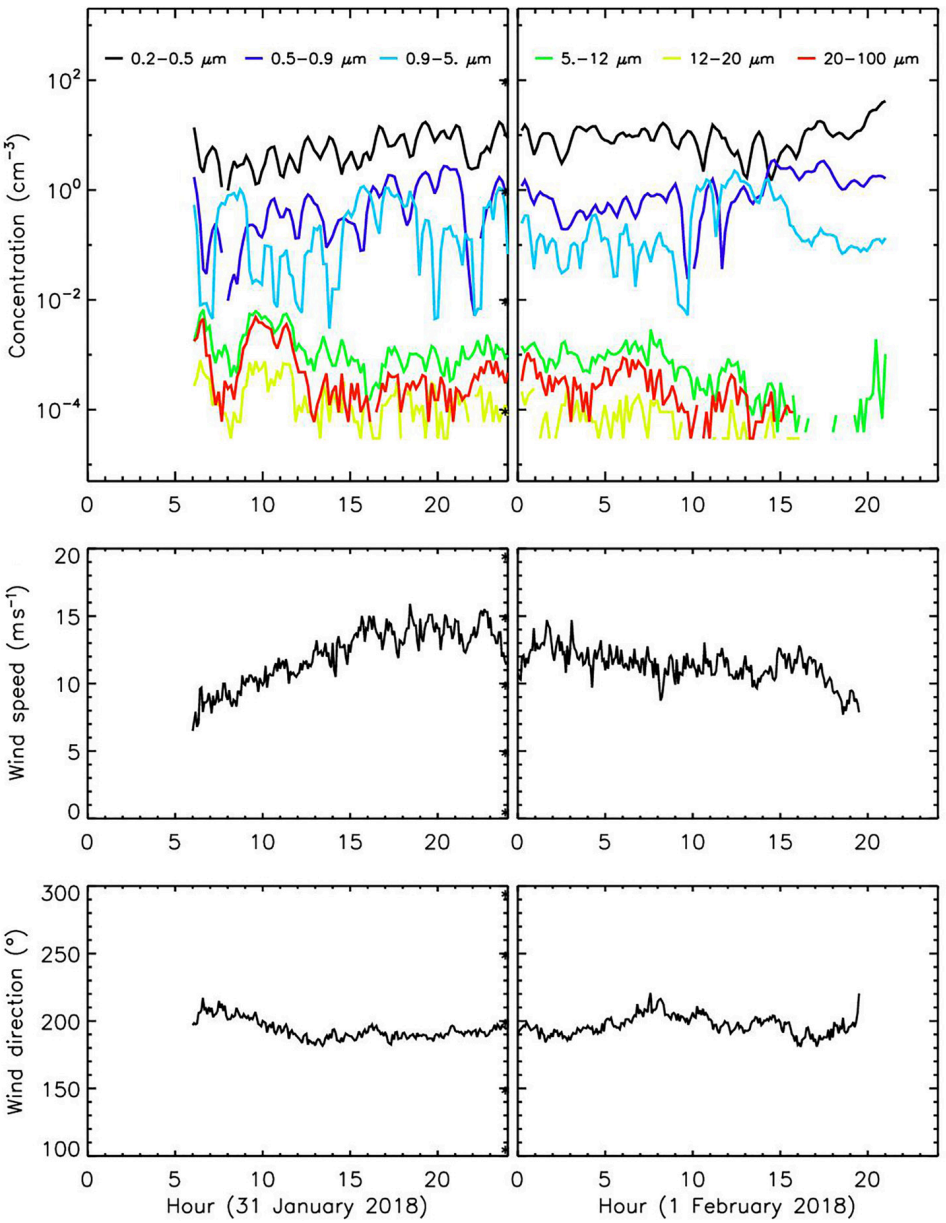

FIGURE 9 | Event 1 – wind conditions and aerosol concentration.

the AOT for 500 nm were filtered to contain only measurements with the water vapor column ≤0.8 cm (**Figure 14B**), the mean AOT for 500 nm was 0.14 ± 0.14, with values only exceeding 0.300 on 15 January and 18 March. For 15 January, no wind or aerosol concentration data were available; however, on 18 March, the highest wind speed of the whole summer season was recorded, and increased PM10 concentrations were captured by the LOAC.

Horizontal Aeolian Sediment Transport

A total of 11 days sampling from 23 January to 3 February 2018 resulted in 36.4 g m^{-2} of material. A total of 138.3 g m^{-2} was collected during the second period from 3 February to 25 February 2018, and 62.9 g m^{-2} from 25 February to 10 March 2018. In total 237.6 g m^{-2} was collected in the passive sediment sampler, makes an average of 4.95 g m^{-2} d^{-1}. However, according to personal observation, most of the material was trapped during the high wind speed events. Installation during the whole year (February 2017 – January 2018) revealed an approximate sediment deposition rate of 1471 g m^{-2} $year^{-1}$.

DISCUSSION AND CONCLUSION

It is challenging to obtain quality aerosol data (mass and number concentrations, typology of particles) from remote areas and/or

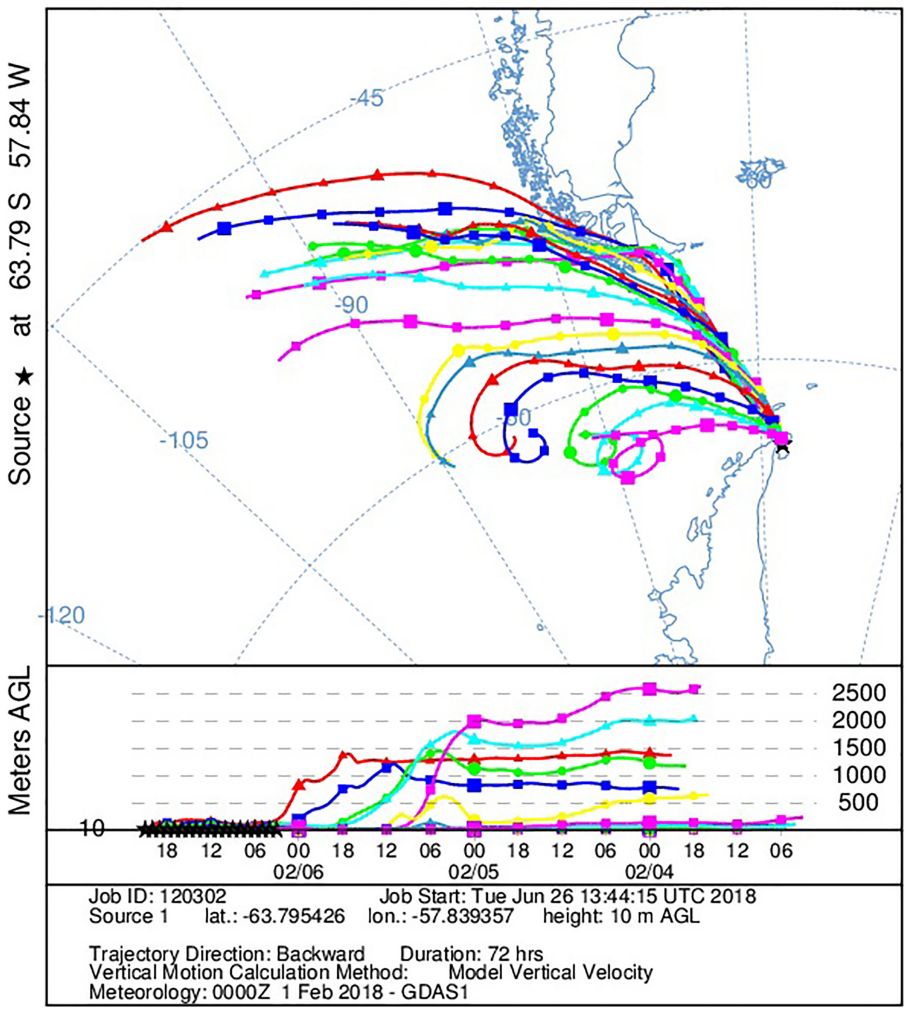

FIGURE 10 | NOAA HYSPLIT model backward trajectories for beginning of February 2018 (ending at 21:00 UTC 6 February, 2018); source: NOAA Air Resources Laboratory.

areas that experience harsh conditions, such as in Antarctica. The LOAC instrument performed quite well in such conditions, and provided valuable PM measurements for background as well as high aerosol concentration conditions for the period January-March 2018. Mean mass concentrations of the PM_{10} and $PM_{2.5}$ were similar to what has been reported from the Larsemann Hills (Budhavant et al., 2015), but lower than reported from the Maitri station (Chaubey et al., 2011). Mean values from JRI were higher than from McMurdo station in 1995–1997 (Mazzera et al., 2001), the Antarctic Peninsula in the late 1980s (Artaxo and Rabello, 1992), as well as Marambio station in the Antarctic Peninsula in 2013–2015 (Asmi et al., 2018). In a global context, a mean PM_{10} value of 6.4 μgm^{-3} from the Antarctic Peninsula is also comparable to two stations in Norway (annual mean of 7.5 $\mu g\ m^{-3}$), but higher than the annual mean of 4.4 $\mu g\ m^{-3}$ in Sevettijarvi, Finland (Putaud et al., 2010). The mean $PM_{2.5}$ value presented here is, however, lower than stations in Northern Europe. Dust events caused during high wind events over barren areas impair the air quality in Antarctica significantly. There is no available literature reporting PM_{10} concentrations exceeding 50 $\mu g\ m^{-3}$ from Antarctica. The frequency of dust events (15 events during 2 months) demonstrates the importance of HLD sources and their contribution to the global dust cycle (Bullard et al., 2016), provided that measurements can give a better estimate of the erosion activity and dust production from Antarctica ice-free zones.

The observed mean wind speed during the study period (5.2 m s^{-1}) corresponds well to the general spatial pattern of Antarctic surface wind streamlines and the position of JRI in

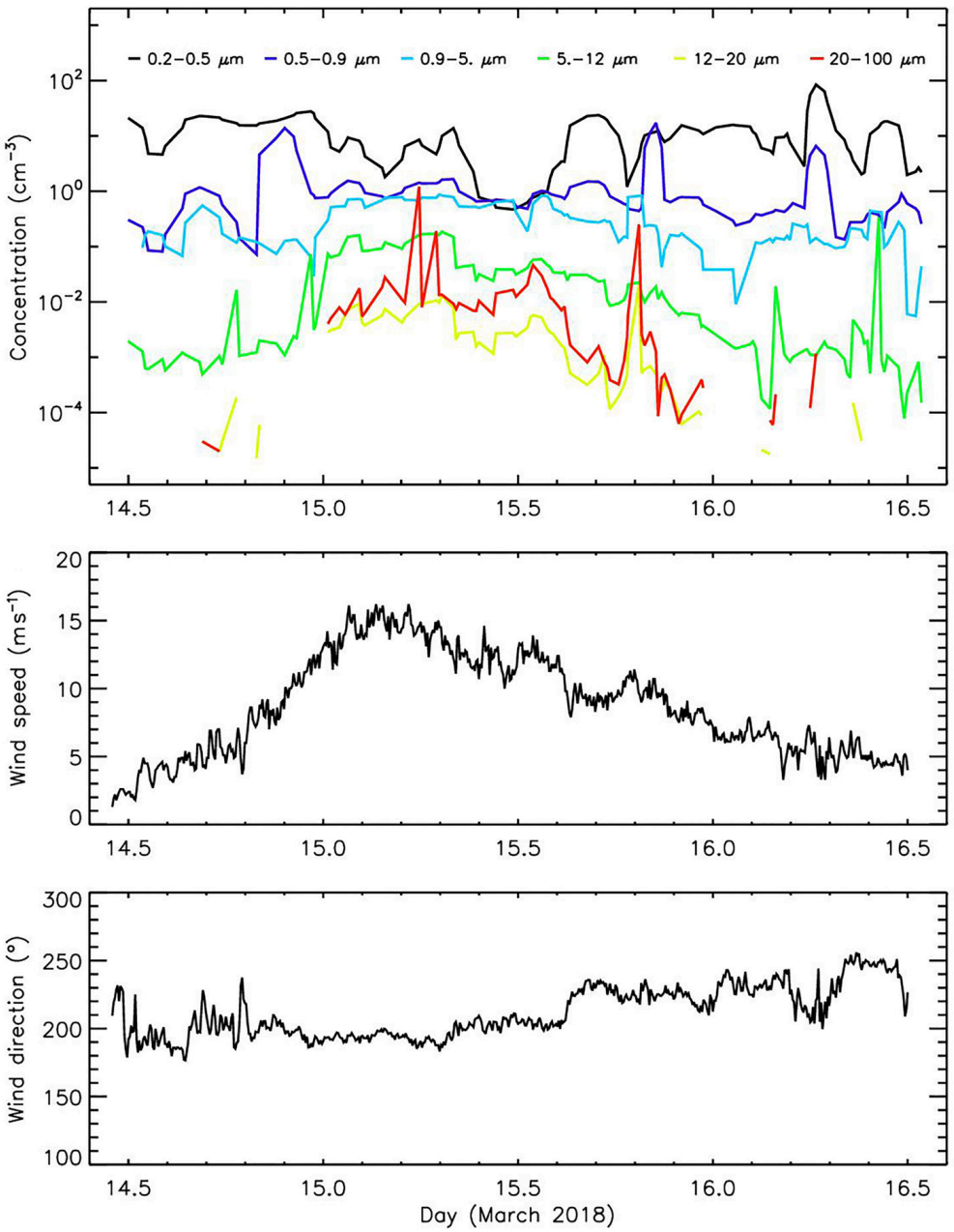

FIGURE 11 | Event 2 – wind conditions and aerosol concentration.

the Antarctic Peninsula region. Ramesh and Soni (2018) report a mean wind speed for the summer months at Maitri station as approximately 7.2 m s^{-1}, and Lancaster (2002) observed mean wind speed ranging from 2.7 to 5.3 m s^{-1} at different sites in Taylor Valleys. Aristidi et al. (2005) observed a mean wind speed at Dome C of 2.9 m s^{-1}, Lazzara et al. (2012) reported mean wind speeds of around 2 m s^{-1} in the summer rising to around 4–5 m s^{-1} at Amundsen Scott station at the South Pole (continent interior). The mean wind speed in the area of Antarctic Peninsula typically ranges from 4.3 m s^{-1} at Faraday/Vernadsky station to 6.6 m s^{-1} at Arctowski Station on King George Island (King and Turner, 1997; Marsz and Styszyńska, 2000). Mean wind speed data are summarized in **Table 2**. The observed wind speed and direction coincide well with the surface wind analysis from Johnson Mesa (3 km southwest of JGM station) that southerly and westerly winds were the most frequent in 2008–2010 and the strongest wind was found during a southerly flow (Zvěřina et al., 2014; Bohuslavová et al., 2018). Average wind speeds at Marambio station (the closest to JGM Station) reaches 5–7 m s^{-1} during the summer season (Asmi et al., 2018). This represents well the general pattern of low mean wind speed in the interior of the continent and

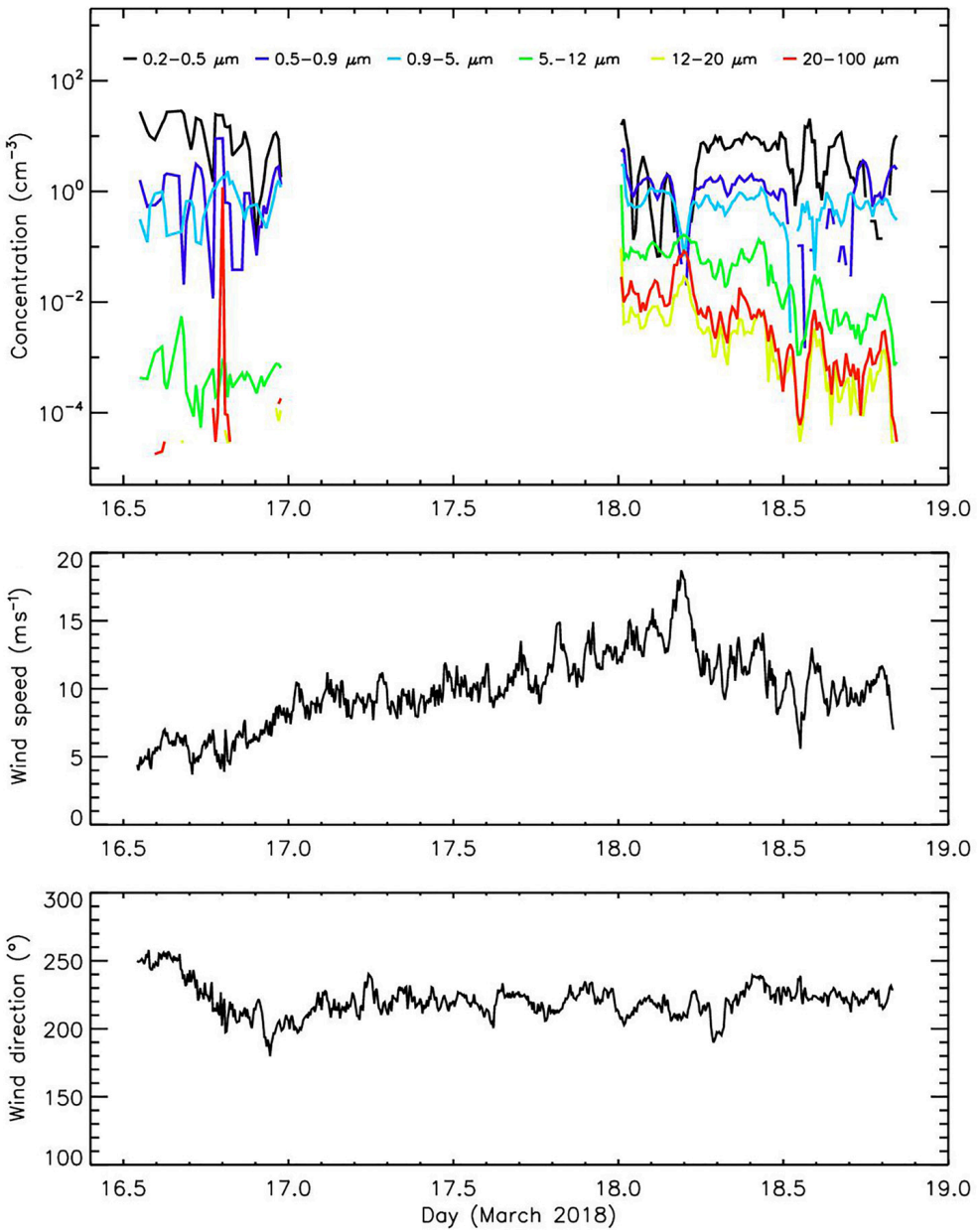

FIGURE 12 | Event 3 – wind conditions and aerosol concentration.

high on the continent edges. The observed critical value of wind speed around 10 m s^{-1} when local material sources are activated differs dramatically among different sites [e.g., 20 m s^{-1} for Taylor Valleys in Šabacká et al. (2012)]. However, the wind speed threshold value for activating local sources depends on the particle size of the material, its availability (Lancaster, 2002) and also on the ground surface moisture conditions (Wiggs et al., 2004). Crusius et al. (2011) similarly observed the high frequency of dust events in autumn when the water level is low and fluvial sediments are exposed. A rapid increase of larger particles in the air is observed when a critical value of wind speed is exceeded, as confirmed also from the typology of aerosol (detection of mineral particles). The prevailing southerly winds, especially during the high wind speed events, bring material from distant (approximately 15 km) bare unglaciated surfaces of weathered rocks and sediments (e.g., Abernethy Flats). Horizontal sediment deposition on the surface level reaches an average of 4.95 g m^{-2} d^{-1} (1471 g m^{-2} $year^{-1}$), showing very high deposition rates compared to other HLD areas (Bullard, 2013; Bullard et al., 2016). Such values are significantly higher than those reported by Atkins and Dunbar (2009) of 7.8–24.5 g m^{-2} $year^{-1}$, or Chewings et al. (2014) of 0.2–55 g m^{-2} $year^{-1}$ in the McMurdo Valleys, West Antarctica. Higher deposition rate of dust particles on Ulu Peninsula can be considered as an important factor contributing

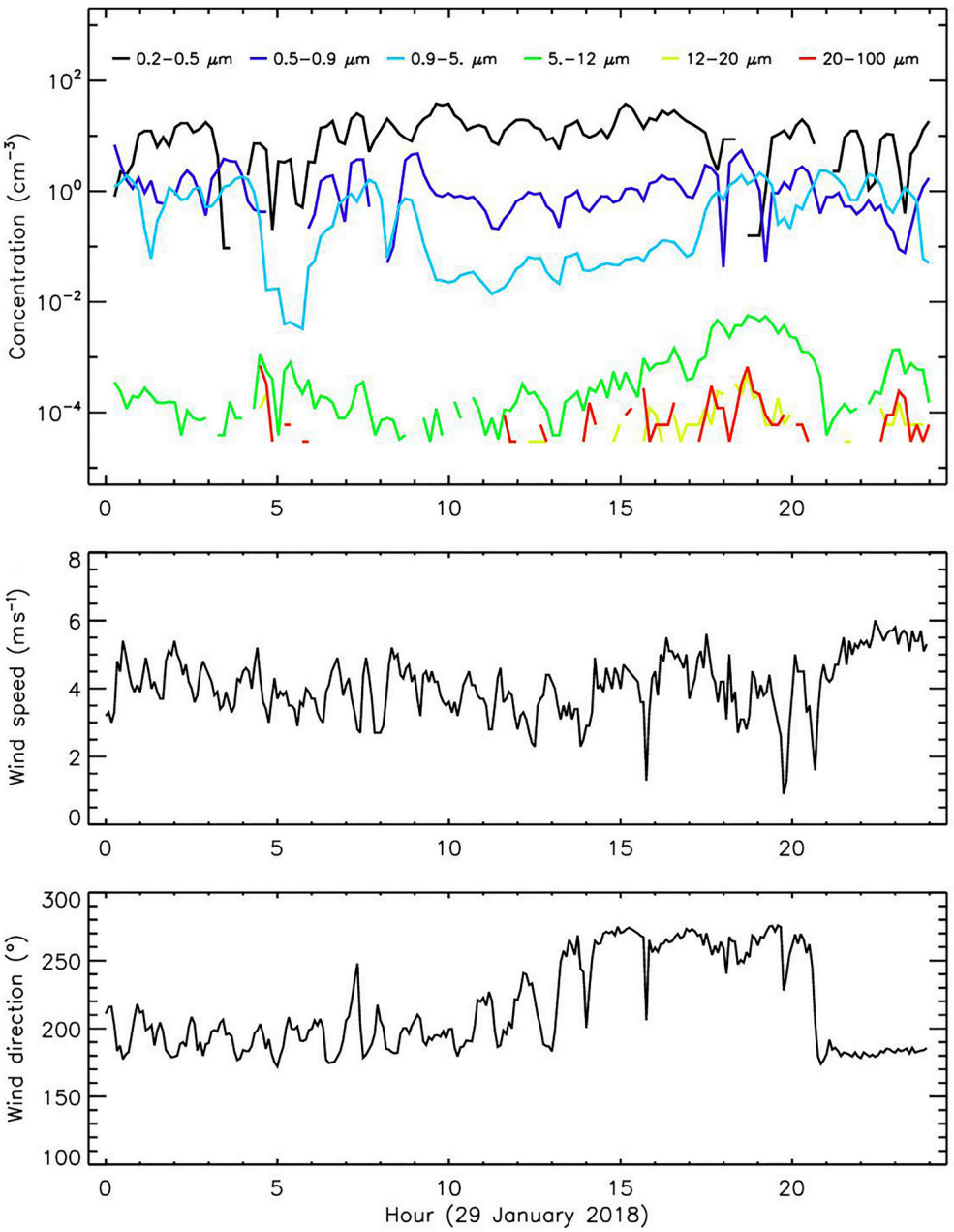

FIGURE 13 | 29 January 2018 wind conditions and aerosol concentration.

to changes of physical and optical properties of the snow. This can have further consequences for energy exchange between glaciers and atmosphere, enhanced snow melt and negative surface mass balance on several mountain glaciers in the investigated area (Engel et al., 2012; Láska et al., 2018).

The aerosols optical properties measured by the Microtops II sun photometer showed high interdiurnal variation of AOT with the mean value of 0.139 ± 0.142 at a wavelength of 500 nm. The mean AOT was influenced by two Events with values above 0.300 (15 January and 18 March 2018), while the mean AOT in the rest of the period was 0.090. The observed AOT at 500 nm are higher than those measured during summer at Maitri station (123 m a.s.l.), which reached 0.034 ± 0.005 (Chaubey et al., 2011), or those being reported near to the Antarctic coast (south of 60°S) which reach values as low as 0.03–0.05 (Gadhavi and Jayaraman, 2004; Vinoj et al., 2007). This clearly confirms that local geographical features (i.e., altitude, distance of the study site from the coastline and size of the ice-free area) can significantly affect the AOT level and the range of its seasonal variation. An increase of the AOT up to 0.545 was documented during the third dust event on 18 March, which had the highest recorded PM_{10} and $PM_{2.5}$ values. However, a major problem with AOT and

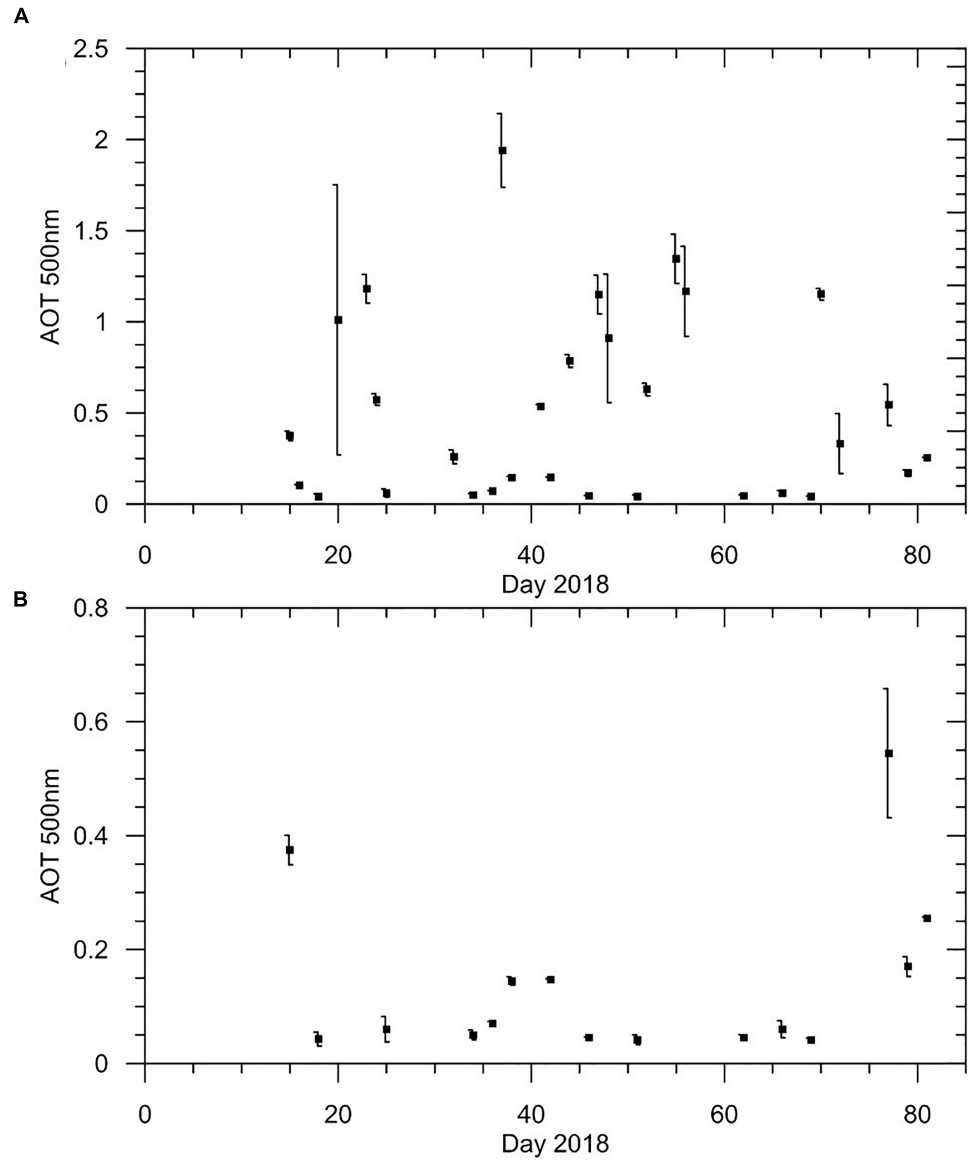

FIGURE 14 | Mean AOT for 500 nm with standard deviation for each day **(A)** all measurements **(B)** when water vapor column was ≤0.8 cm.

TABLE 2 | Mean wind speed (m s^{-1}) observed at different Antarctic location.

Site	Mean wind speed	Reference
Maitri	7.2	Ramesh and Soni, 2018
Taylor Valleys	2.7–5.3	Lancaster, 2002
Dome C	2.9	Aristidi et al., 2005
Amundsen Scott	2.0–5.0	Lazzara et al., 2012
Faraday/Vernadsky	4.3	King and Turner, 1997
Arctowski	6.6	Marsz and Styszyńska, 2000
Marambio	5.0–7.0	Asmi et al., 2018
JGM Station	5.2	This study

LOAC data comparison in the Antarctic coastal areas was cloud cover and the fact that aerosol optical measurements can only be carried out during clear sky days. This reduced significantly the number of days suitable for comparison as well as possibilities to capture the dust event in the AOT observations.

CONCLUSION

Aerosol measurements in Antarctica are rare, especially for particles >1 μm. Most of the research on aeolian processes are concentrated to a few areas – the McMurdo Dry Valleys (e.g., Lancaster, 2002; Fortner et al., 2011; Šabacká et al., 2012), the Antarctic Peninsula (e.g., Artaxo and Rabello, 1992; Asmi et al., 2018), or at the edge of the continent (e.g., Weller et al., 2008; Chaubey et al., 2011; Budhavant et al., 2015). This study sheds new insight into aeolian transport in the eastern Antarctic Peninsula region. It relates the measured aerosol concentration

to local atmospheric conditions and also to surface horizontal aeolian deposition.

A two-month summer campaign demonstrated that ice-free areas in Antarctica provide material supply, which is frequently suspended during high wind speed events. Over 15 dust events were measured with PM_{10} concentrations exceeding 20 $\mu g\ m^{-3}$ and a maximum of up to 57 $\mu g\ m^{-3}$. This study demonstrates that dust becomes suspended at wind speeds $>10\ m\ s^{-1}$ in the coastal zones of the largest ice-free area in the Antarctic Peninsula. Particles $>20\ \mu m$ can be lifted >3 m above surface and transported for long distances. Submicron particles do not contribute to increased PM concentrations during dust events, showing the predominance of coarse material available for suspension.

Our measurements show that PM_{10} concentrations on JRI are higher than in natural areas in the Northern Europe. Antarctica is an important HLD source contributing to the global dust budget, and more long-term measurements are needed to quantify how much material is transported. Local dust sources can play a significant role in the enrichment of Antarctic marine environment (Crusius et al., 2011), with iron as an important micronutrient in marine biota (Prospero et al., 2012). The uniquely large ice-free area of Ulu Peninsula has great potential for further study of aeolian processes.

AUTHOR CONTRIBUTIONS

JK was responsible for the study design, field installation of LOAC, and writing and editing the manuscript. PD-W was responsible for interpretation of the results and partly writing the manuscript. JR processed the LOAC data and helped with interpretation of the results. KL and KA were in charge of wind properties + AOT measurements and preparation of the data also with contribution to the manuscript.

FUNDING

This work was in part funded by the Icelandic Research Fund (Rannis) Grant No. 152248-051; by the Czech Science Foundation project GC16-14122J and projects no. LM2015078, CZ.02.1.01/0.0/0.0/16_013/0001708; and the Masaryk University project MUNI/A/1251/2017. The LOAC instruments were funded by the French Labex VOLTAIRE. Field work was carried out with help of staff of the Johann Gregor Mendel Station.

ACKNOWLEDGMENTS

We would like to thank Ewan O'Connor from the Finnish Meteorological Institute and Santiago Gassó from the NASA for providing us with supporting data. We also would like to thank to Yoav Y. Yair and Lucas Alados-Arboledas for useful comments and remarks during the review process. Many thanks also to Stephen Jennings for language corrections and improving the formal aspect of the paper.

REFERENCES

Ambrožová, K., and Láska, K. (2016). "The air temperature change on james ross island within the context of the Antarctic Peninsula," in *Proceedings of the Conference on Czech Geographical Society, 5-7 September 2016*, ed. A. Novacek (Ceske Budejovice: Jihoceska univerzita).

Aristidi, E., Agabi, K., Azouit, M., Fossat, E., Vernin, J., Travouillon, T., et al. (2005). An analysis of temperatures and wind speeds above Dome C, Antarctica. *Astron. Astrophys.* 430, 739–746. doi: 10.1051/0004-6361:20041876

Arnalds, O., Olafsson, H., and Dagsson-Waldhauserova, P. (2014). Quantification of iron-rich volcanogenic dust emissions and deposition over the ocean from Icelandic dust sources. *Biogeosciences* 11, 6623–6632. doi: 10.5194/bg-11-6623-2014

Arnalds, O., Thorarinsdottir, E. F., Thorsson, J., Dagsson-Waldhauserova, P., and Agustdottir, A. M. (2013). An extreme wind erosion event of the fresh Eyjafjallajökull 2010 volcanic ash. *Sci. Rep.* 3:1257. doi: 10.1038/srep01257

Artaxo, P., and Rabello, M. L. C. (1992). Trace elements and individual particle analysis of atmospheric aerosols from the Antarctic Peninsula. *Tellus B* 44, 318–334. doi: 10.1034/j.1600-0889.1992.00010.x

Asmi, E., Neitola, K., Teinilä, K., Rodriguez, E., Virkkula, A., Backman, J., et al. (2018). Primary sources control the variability of aerosol optical properties in the Antarctic Peninsula. *Tellus B Chem. Phys. Meteorol.* 70:1414571. doi: 10.1080/16000889.2017.1414571

Atkins, C. B., and Dunbar, G. B. (2009). Aeolian sediment flux from sea ice into southern McMurdo sound, Antarctica. *Global Planet. Change* 69, 133–141. doi: 10.1016/j.gloplacha.2009.04.006

Ayling, B. F., and McGowan, H. A. (2006). Niveo-eolian sediment deposits in coastal South Victoria Land, Antarctica: indicators of regional variability in weather and climate. *Arc. Antarct. Alp. Res.* 38, 313–324. doi: 10.1657/1523-0430(2006)38[313:NSDICS]2.0.CO;2

Ballantyne, C. K. (2002). Paraglacial geomorphology. *Q. Sci. Rev.* 21, 1935–2017. doi: 10.1016/S0277-3791(02)00005-7

BAS (2005). *Antarctic Factsheet, Geographical Statistics*. Available at: https://www.bas.ac.uk/wp-content/uploads/2015/05/factsheet_geostats_print.pdf

Basile, I., Grousset, F. E., Revel, M., Petit, J. R., Biscaye, P. E., and Barkov, N. I. (1997). Patagonian origin of glacial dust deposited in East Antarctica (Vostok and Dome C) during glacial stages 2, 4 and 6. *Earth Planet. Sci. Lett.* 146, 573–589. doi: 10.1016/S0012-821X(96)00255-5

Bockheim, J. (1995). Permafrost distribution in the southern circumpolar region and its relation to the environment: a review and recommendations for further research. *Permafrost Periglacial Process.* 6, 27–45. doi: 10.1002/ppp.3430060105

Bohuslavová, O., Macek, P., Redčenko, O., Láska, K., Nedbalová, L., and Elster, J. (2018). Dispersal of lichens along a successional gradient after deglaciation of volcanic mesas on northern James Ross Island, Antarctic Peninsula. *Polar Biol.* 41, 2221–2232. doi: 10.1007/s00300-018-2357-7

Bory, A., Wolff, E., Mulvaney, R., Jagoutz, E., Wegner, A., Ruth, U., et al. (2010). Multiple sources supply eolian mineral dust to the Atlantic sector of coastal Antarctica: evidence from recent snow layers at the top of Berkner Island ice sheet. *Earth Planet. Sci. Lett.* 291, 138–148. doi: 10.1016/j.epsl.2010.01.006

Bristow, C. S., Jol, H. M., Augustinus, P., and Wallis, I. (2010). Slipfaceless 'whaleback' dunes in a polar desert, Victoria valley, Antarctica: insights from ground penetrating radar. *Geomorphology* 114, 361–372. doi: 10.1016/j.geomorph.2009.08.001

Budhavant, K., Safi, P. D., and Rao, P. S. P. (2015). Sources and elemental composition of summer aerosols in the Larsemann Hills (Antarctica). *Environ. Sci. Pollut. Res.* 22, 2041–2050. doi: 10.1007/s11356-014-3452-0

Bullard, J. E. (2013). Contemporary glacigenic inputs to the dust cycle. *Earth Surf. Process. Landf.* 38, 71–89. doi: 10.1002/esp.3315

Bullard, J. E., and Austin, M. J. (2011). Dust generation on a proglacial floodplain, West Greenland. *Aeolian Res.* 3, 43–54. doi: 10.1016/j.aeolia.2011.01.002

Bullard, J. E., Baddock, M., Bradwell, T., Crusius, J., Darlington, E., Gaiero, D., et al. (2016). High-latitude dust in the Earth system. *Rev. Geophys.* 54, 447–485. doi: 10.1002/2016RG000518

Chaubey, J. P., Moorthy, K. K., Babu, S. S., and Nair, V. S. (2011). The optical and physical properties of atmospheric aerosols over the Indian Antarctic stations during southern hemispheric summer of the international Polar Year 2007–2008. *Ann. Geophys.* 29, 109–121. doi: 10.5194/angeo-29-109-2011

Chewings, J. M., Atkins, C., Dunbar, G., and Golledge, N. R. (2014). Aeolian sediment transport and deposition in a modern high-latitude glacial marine environment. *Sedimentology* 61, 1535–1557. doi: 10.1111/sed.12108

Crusius, J., Schroth, A. W., Gassó, S., Moy, C. M., Levy, R. C., and Gatica, M. (2011). Glacial flour dust storms in the Gulf of Alaska: hydrologic and meteorological controls and their importance as a source of bioavailable iron. *Geophys. Res. Lett.* 38:L06602. doi: 10.1029/2010GL046573

Dagsson-Waldhauserova, P., Arnalds, O., and Ólafsson, H. (2014). Long-term variability of dust events in Iceland (1949–2011). *Atmos. Chem. Phys.* 14, 13411–13422. doi: 10.5194/acp-14-13411-2014

Delmonte, B., Paleari, C. I., Andò, S., Garzanti, E., Andersson, P. S., Petit, J. R., et al. (2017). Causes of dust size variability in central East Antarctica (Dome B): atmospheric transport from expanded South American sources during marine isotope stage 2. *Q. Sci. Rev.* 168, 55–68. doi: 10.5194/acp-14-13411-2014

Elliot, C. (2003). Rock weathering processes in antarctica: a comparison of some recent studies with those from the Northern Hemisphere. *N. Z. Geog.* 59, 50–60. doi: 10.1111/j.1745-7939.2003.tb02113.x

Engel, Z., Nývlt, D., and Láska, K. (2012). Ice thickness, areal and volumetric changes of davies dome and whisky glacier (James Ross Island, Antarctic Peninsula) in 1979-2006. *J. Glaciol.* 58, 904–914. doi: 10.3189/2012JoG11J156

Fortner, S. K., Lyons, W. B., and Olesik, W. B. (2011). Eolian deposition of trace elements onto taylor valley Antarctic glaciers. *Appl. Geochem.* 26, 1897–1904. doi: 10.1016/j.apgeochem.2011.06.013

Fountain, A. G., Nylen, T. H., Monaghan, A., Basagic, H. J., and Bromwich, D. (2009). Snow in the McMurdo dry valleys, Antarctica. *Int. J. Climatol.* 30, 633–642. doi: 10.1002/joc.1933

Gadhavi, H., and Jayaraman, A. (2004). Aerosol characteristics and aerosol radiative forcing over Maitri. *Antarct. Curr. Sci.* 86, 296–304. doi: 10.1002/joc.1933

Ganor, E. (1975). *Atmospheric Dust in Israel. Sedimentological and Meteorological Analysis of Dust Deposition*. PhD. thesis, Hebrew University of Jerusalem, Israel.

Global Modeling and Assimilation Office. (2015). *MERRA-2 tavg1_2d_slv_Nx:2d,1-Hourly, Time-Averaged, Single-Level, Assimilation, Single-Level Diagnostics V5.12.4*. Greenbelt, MD: Goddard Earth Sciences Data and Information Services Center (GES DISC), doi: 10.5067/VJAFPLI1CSIV

Hedding, D. W., Nel, W., and Anderson, R. L. (2015). Aeolian processes and landforms in the sub-Antarctic: preliminary observations from Marion Island. *Polar Res.* 34:26365. doi: 10.3402/polar.v34.26365

Hrbáček, F., Vieira, G., Oliva, M., Balks, M., Guglielmin, M., de Pablo, M. A., et al. (2018). Active layer monitoring in Antarctica: an overview of results from 2006 to 2015. *Polar Geogr.* 41, 1–16. doi: 10.1080/1088937X.2017.1420105

Hugenholtz, C. H., and Wolfe, S. A. (2010). Rates and environmental controls of aeolian dust accumulation, Athabasca River Valley, Canadian rocky mountains. *Geomorphology* 121, 274–282. doi: 10.1016/j.geomorph.2010.04.024

Kavan, J., and Nývlt, D. (2018). "Blowing in the wind – where does the Antarctic fluvial suspended load come from?," in *Proceedings of the Polar 2018 – SCAR & IASC Conference*, Davos. doi: 10.1080/04353676.2016.1257914

Kavan, J., Ondruch, J., Nývlt, D., Hrbáček, F., Carrivick, J. L., and Láska, K. (2017). Seasonal hydrological and suspended sediment transport dynamics in proglacial streams, James Ross Island, Antarctica. *Geogr. Ann.* 99, 38–55. doi: 10.1080/04353676.2016.1257914

King, J. C., and Turner, J. (1997). *Antarctic Meteorology and Climatology*. Cambridge: Cambridge University Press, 409.

King, J. C., Turner, J., Marshall, G. J., Connolley, W. M., and Lachlan-Cope, T. A. (2003). "Antarctic peninsula climate variability and its causes as revealed by analysis of instrumental records," in *Antarctic Peninsula Climate Variability: A Historical and Paleoenvironmental Perspective*, eds E. W. Domack, A. Burnett, A. Leventer, P. Conley, M. Kirby, and R. Bindschadler (Washington, D.C: American Geophysical Union). doi: 10.1080/15230430.2002.12003500

Lancaster, N. (2002). Flux of eolian sediment in the McMurdo Dry Valleys, Antarctica: a preliminary assessment. *Arct. Antarct. Alp. Res.* 34, 318–323. doi: 10.1080/15230430.2002.12003500

Láska, K., Engel, Z., Nývlt, D., Stachoň, Z., Kavan, J., Smolíková, J., et al. (2018). Is the positive mass balance of north-eastern Antarctic peninsula glaciers persistent after 2015? *Geophys. Res. Abstr.* 20.

Lazzara, M. A., Keller, L. M., Markle, T., and Gallagher, J. (2012). Fifty-year Amundsen–Scott South Pole station surface climatology. *Atmos. Res.* 118, 240–259. doi: 10.1016/j.atmosres.2012.06.027

Lurton, T., Renard, J.-B., Vignelles, D., Jeannot, M., Akiki, R., Mineau, J.-L., et al. (2014). Light scattering at small angles by atmospheric irregular particles: modelling and laboratory measurements. *Atmos. Meas. Tech.* 7, 931–939.

Marsz, A. A., and Styszyńska, A. (2000). "Główne cechy klimatu rejonu polskiej stacji antarktycznej," in *Antarktyka Zachodnia, Szetlandy Południowe, Wyspa Króla Jerzego*, ed. H. Arctowskiego (Gdynia: WSM). doi: 10.1016/S1352-2310(00)00409-X

Mazzera, D. M., Lowenthal, D., Chow, J. C., Watson, J. G., and Grubisic, V. (2001). PM10 measurements at McMurdo station, Antarctica. *Atmos. Environ.* 35, 1891–1902. doi: 10.1016/S1352-2310(00)00409-X

McConnell, J. R., Aristarain, A. J., Banta, J. R., Edwards, P. R., and Simoes, J. C. (2007). 20th-Century doubling in dust archived in an Antarctic peninsula ice core parallels climate change and desertification in South America. *Proc. Natl. Acad. Sci. U.S.A.* 104, 5743–5748. doi: 10.1029/2001JD900103

Morys, M., Mims, F. M. III, Hagerup, S., Anderson, S. E., Baker, A., Kia, J., et al. (2001). Design, calibration, and performance of microtops II handheld ozone monitor and sun photometer. *J. Geophys. Res. Atmos.* 106, 14573–14582. doi: 10.1002/2015JD023304

Neff, P. D., and Bertler, N. A. N. (2015). Trajectory modeling of modern dust transport to the Southern Ocean and Antarctica. *J. Geophys. Res. Atmos.* 120, 9303–9322. doi: 10.1002/2015JD023304

Nylen, T. H., Fountain, A. G., and Doran, P. T. (2004). Climatology of katabatic winds in the McMurdo dry valleys, southern Victoria Land, Antarctica. *J. Geophys. Res.* 109:D03114. doi: 10.1029/2003JD003937

Pereira, K. C. D., Evangelista, H., Pereira, E. B., Simões, J. C., Johnson, E., and Melo, L. R. (2004). Transport of crustal microparticles from chilean patagonia to the Antarctic peninsula by SEM-EDS analysis. *Tellus B* 56, 262–275. doi: 10.3402/tellusb.v56i3.16428

Prospero, J. M., Bullard, J. E., and Hodgkins, R. (2012). High-latitude dust over the north atlantic: inputs from icelandic proglacial dust storms. *Science* 335, 1078–1082. doi: 10.1126/science.1217447

Putaud, J.-P., Van Dingenen, R., Alastuey, A., Bauer, H., Birmili, W., Cyrys, J., et al. (2010). A European aerosol phenomenology e 3: physical and chemical characteristics of particulate matter from 60 rural, urban, and kerbside sites across Europe. *Atmos. Environ.* 44, 1308–1320. doi: 10.1016/j.atmosenv.2009.12.011

Ramesh, K. J., and Soni, V. K. (2018). Perspectives of Antarctic weather monitoring and research efforts. *Polar Sci.* (in press). doi: 10.1016/j.polar.2018.04.005

Renard, J.-B., Dulac, F., Berthet, G., Lurton, T., Vignelles, D., Jégou, F., et al. (2016a). LOAC, a light aerosols counter for ground-based and balloon measurements of the size distribution and of the main nature of atmospheric particles, 1. Principle of measurements and instrument evaluation. *Atmos. Meas. Tech.* 9, 1721–1742. doi: 10.5194/amt-9-1721-2016

Renard, J.-B., Dulac, F., Berthet, G., Lurton, T., Vignelles, D., Jégou, F., et al. (2016b). LOAC, a light aerosols counter for ground-based and balloon measurements of the size distribution and of the main nature of atmospheric particles, 2. First results from balloon and unmanned aerial vehicle flights. *Atmos. Meas. Tech.* 9, 3673–3686. doi: 10.5194/amt-9-3673-2016

Renard, J.-B., Dulac, F., Durand, P., Bourgeois, Q., Denjean, C., Vignelles, D., et al. (2018). In situ measurements of desert dust particles above the western mediterranean sea with the balloon-borne light optical aerosol counter/sizer (LOAC) during the ChArMEx campaign of summer 2013. *Atmos. Chem. Phys.* 18, 3677–3699. doi: 10.5194/acp-18-3677-2018

Šabacká, M., Priscu, J. C., Basagic, H. J., Fountain, A. G., Wall, D. H., Virginia, R. A., et al. (2012). Aeolian flux of biotic and abiotic material in Taylor

Valley, Antarctica. *Geomorphology* 15, 102–111. doi: 10.1016/j.geomorph.2011.12.009

Truzzi, C., Lambertucci, L., Illuminati, S., Annibaldi, A., and Scarponi, G. (2005). Direct gravimetric measurements of the mass of the antarctic aerosol collected by high volume sampler: PM10 summer seasonal variation at terra nova bay. *Ann. Chim.* 95, 867–876. doi: 10.1002/adic.20059 0099

van Lipzig, N. P. M., King, J. C., Lachlan-Cope, T. A., and van der Broeke, M. R. (2004). Precipitation, sublimation and snow drift in the Antarctic peninsula region from a regional atmospheric model. *J. Geophys. Res.* 109:D24106. doi: 10.1029/2004JD004701

Vinoj, V., Anjan, A., Sudhakar, M., Satheesh, S. K., Srinivasan, J., and Moorthy, K. K. (2007). Latitudinal variation of aerosol optical depths from northern Arabian Sea to Antarctica. *Geophys. Res. Lett.* 34:L10807. doi: 10.1029/2007GL029419

Weller, R., Wöltjen, J., Piel, C., Resenberg, R., Wagenbach, D., König-Langlo, G., et al. (2008). Seasonal variability of crustal and marine trace elements in the aerosol at neumayer station, Antarctica. *Tellus B* 60, 742–752. doi: 10.1111/j.1600-0889.2008.00372.x

Wiggs, G., Baird, A., and Atherton, R. (2004). The dynamic effects of moisture on the entrainment and transport of sand by wind. *Geomorphology* 59, 13–30. doi: 10.1016/j.geomorph.2003.09.002

Zvěřina, O., Láska, K., Červenka, R., Kuta, J., Coufalík, P., and Komárek, J. (2014). Analysis of mercury and other heavy metals accumulated in lichen Usnea antarctica from james ross island, Antarctica. *Environ. Monit. Assess.* 186, 9089–9100. doi: 10.1007/s10661-014-4068-z

Conflict of Interest Statement: The authors declare that the research was conducted in the absence of any commercial or financial relationships that could be construed as a potential conflict of interest.

frontiers in Earth Science

ORIGINAL RESEARCH
published: 09 January 2019
doi: 10.3389/feart.2018.00245

A 60 Year Examination of Dust Day Activity and Its Contributing Factors From Ten Icelandic Weather Stations From 1950 to 2009

Miye Nakashima[1] and Pavla Dagsson-Waldhauserová[2,3]*

[1] Department of Atmospheric and Oceanic Sciences, University of California, Los Angeles, Los Angeles, CA, United States, [2] Agricultural University of Iceland, Hvanneyri, Iceland, [3] Faculty of Environmental Sciences, Czech University of Life Sciences Prague, Prague, Czechia

High latitude dust is an important contributor to the global dust cycle, which affects the radiative balance of the atmosphere. The frequency and severity of dust events are driven by variables such as wind speed, precipitation, temperature, surface cover type, and volcanic activity. The extent of impact of glacial retreat is yet to be determined, but glacial outburst floods, known as jökulhlaups, have been suggested to be a significant factor in the seasonal pattern of dust activity, with major jökulhlaups being attributed as a cause for an increase in dust activity in their subsequent year. However, in examination of ten meteorological stations from 1950 to 2009, there does not appear to be sufficient evidence that jökulhlaups are a significant driver of Iceland's dust activity. Additionally, taking into account a larger range of dust codes, contributions from Icelandic dust plumes are found to be greater than previously assumed, with an average of 128 dust days per year as compared to a previously determined average of 34 dust days annually.

Keywords: high-latitude, jökulhlaups, *sandur*, Iceland, dust aerosol, dust haze

OPEN ACCESS

Edited by:
Yuh-Lang Lin,
North Carolina A&T State University, United States

Reviewed by:
Jose M. Baldasano,
Universitat Politecnica de Catalunya, Spain
Henrique De Melo Jorge Barbosa,
University of São Paulo, Brazil

****Correspondence:***
Miye Nakashima
nakashimamiye@gmail.com

Specialty section:
This article was submitted to Atmospheric Science, a section of the journal Frontiers in Earth Science

Received: *17 August 2018*
Accepted: *18 December 2018*
Published: *09 January 2019*

Citation:
Nakashima M and Dagsson-Waldhauserová P (2019) A 60 Year Examination of Dust Day Activity and Its Contributing Factors From Ten Icelandic Weather Stations From 1950 to 2009. Front. Earth Sci. 6:245. doi: 10.3389/feart.2018.00245

INTRODUCTION

High latitude regions such as Iceland, Greenland, Canada, Patagonia, and New Zealand have been acknowledged as sizeable contributors to the global dust cycle (Prospero et al., 2012; Bullard, 2013; Bullard et al., 2016). Unlike dry mid-latitude regions such as the Sahara and Gobi Deserts, some high latitudes regions may be exposed to high levels of precipitation, humidity, and vegetation. Iceland, in particular, has low vegetation and high wind speeds, which enhance active dust transport, in spite of relatively high annual precipitation and seasonal snow cover. Additionally, the presence of volcanoes and glaciers contribute to the creation of several types of barren, sandy landscapes, including *sandurs* (glacial outwash plains), which serve as major dust plume sources (Arnalds, 2010).

The potential impacts of glacial activity on dust emissions occur through two main events: glacial retreat and jökulhlaups. The process of glacial retreat contributes sediment supply by reworking flood paths (Maizels, 1997) and through the process of glacier basal sliding abrasions, which is especially effective during the melting of warm-based glaciers like those of Iceland (Bullard, 2013). The correlation between glacier meltwater discharge rates and sediment concentration flux is not linear, and is therefore difficult to predict (Bullard, 2013).

Jökulhlaups are glacial outburst floods and consist of two main types: subglacial and proglacial (Björnsson, 1992). Subglacial jökulhlaups are due to a breach in lakes that formed under glaciers through geothermal heating, and can be triggered periodically as a result of gradual melting over time, or by sudden volcanic or seismic activity (Björnsson, 2002). Proglacial jökulhlaups are the result of the overflow of proglacial lakes, which are created from glacial melt runoff which collects along the margins of the glacier extent. Both types of jökulhlaups carry sediment to *sandur*, where it can then be entrained into the atmosphere. It has been speculated that summer temperatures increase jökulhlaup activity and is responsible for the seasonal increase of dust activity, and additionally that major jökulhlaups may be responsible for sizeable increases of dust activity in their subsequent year (Prospero et al., 2012).

The main objectives of this study are to investigate whether changes in the frequency of dust activity can be attributed to glacial activity, and to reassess whether dust activity in Iceland is comparable to that in mid-latitude deserts. As no published official record of minor jökulhlaup activity is available, this study does not aim to prove or disprove the direct impact of minor jökulhlaups on dust activity, but rather aims to draw to attention other variables such as temperature, wind speed, and precipitation, which may hold more significant influence over dust activity. This study further investigates the impact of jökulhlaups by placing three major jökulhlaups (1955, 1996, 1999) in the context of long-term dust activity fluctuations.

MATERIALS AND METHODS

Synoptic observations were taken from meteorological stations run by the Icelandic Meteorological Office over the years of 1950–2009 from a total of ten different stations across Iceland as seen in **Figure 1**, grouped into three regions:

(1) Northeast (NE): Grímsstaðir, Raufarhöfn, Egilsstaðir;
(2) Southwest (SW): Reykjavik, Eyrarbakki, Hæll;
(3) South: Stórhöfði, Vatnsskarðshólar, Vík í Mýrdal, Kirkjubæjarklaustur.

Note that Raufarhöfn, Reykjavik, Eyrarbakki, Vatnsskarðshólar, Vík í Mýrdal, and Stórhöfði are situated close to the shoreline, while Grímsstaðir, Egilsstaðir, Hæll, and Kirkjubæjarklaustur are located further inland.

At all stations, synoptic dust observations were made every day of the year, 3–8 times a day. Many stations stopped reporting the present weather observations after the year 2009. A dust day is considered to be any day during which at least one observation of dust activity is observed, using synoptic dust codes as defined in the World Meteorological Organization Report (WMO, 2009). SYNOP codes of the present weather used in this study are 6 (dust in suspension, not raised by wind at or near the station at the time of observation), 7 (blowing dust raised by wind at time of observation, without the development of whirls or storms), 8 (developed dust whirls, but no storm), 9 (dust storm within sight within the past hour of observation), 30–32 (slight or moderate dust or sand storms), 33–35 (severe dust or sand storms), and additionally codes 4–5, which are used for the visibility reduced by volcanic ash resuspension and dust haze in Iceland. Codes 4–6 were omitted from the dust frequency studies published by Dagsson-Waldhauserová et al. (2013, 2014).

Average monthly temperature, wind speed, and precipitation were gathered from each of the stations via the Icelandic Meteorological Office[1]. Volcanic eruption records from 1950 to 2009 were taken from the Smithsonian Institution Global Volcanism Program[2]. These include the non-glacial volcanic activity in the Northeast (Askja and Krafla) and South (Hekla and Vestmannaeyjar's Eldfell and Surtsey), as well as subglacial activity for Vatnajökull (Grímsvötn) and Mýrdalsjökull (Katla). *Sandur* and dust plume locations, as seen in **Figure 2**, were

[1]http://en.vedur.is/climatology/data/

[2]http://volcano.si.edu/database/search_eruption_results.cfm

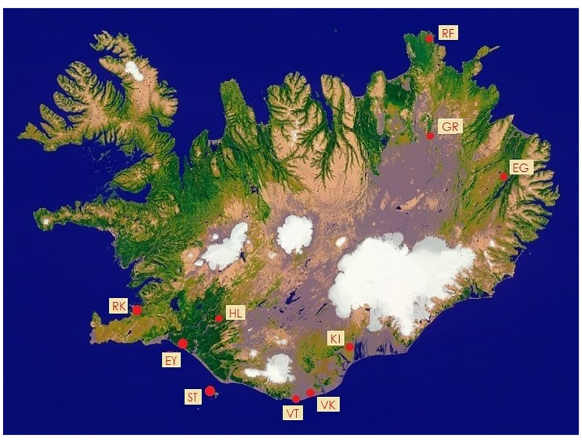

FIGURE 1 | Vegetation map of Iceland. Source: Based on data from National Land Survey of Iceland (http://www.lmi.is/en/okeypis-kort/). *Station locations added: Grímsstaðir (GR), Raufarhöfn (RF), Egilsstaðir (EG), Reykjavik (RK), Eyrarbakki (EY), Hæll (HL), Stórhöfði (ST), Vatnsskarðshólar (VT), Vík í Mýrdal (VK), Kirkjubæjarklaustur (KI).

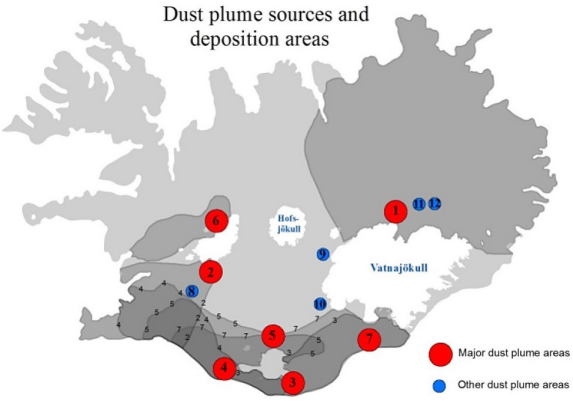

FIGURE 2 | Major dust plume sources and estimated regions of deposition (Arnalds, 2010): (1) Dyngjusandur, (2) Hagavatn, (3) Mýrdalssandur, (4) Landeyjasandur, (5) Mælifellssandur, (6) Flosaskarð, (7) Skeiðarársandur.

acquired from Arnalds (2010) by using Landsat and Moderate Resolution Imaging Spectroradiometer (MODIS).

RESULTS

Meteorological Observations at Each Station

Figure 3 takes an average of the temperature, precipitation, and wind speed at each station for each month over the 60 year period. It shows that the general annual trends in temperature follow the same pattern at all stations, with the Northeast colder than the Southwest, and the Southwest colder than the South, though with Kirkjubæjarklaustur temperatures more in line with Southwestern stations than Southern ones. A line is drawn at 5°C, above which the months will be referred to as "warm season" and below which will be "cold season." Months falling between 5 ± 0.7°C will be considered "transitional," sometimes acting as a warm season month while other times acting as a cold season month.

Like temperature, precipitation ranges are distinguishable by region, though here, Kirkjubæjarklaustur aligns with the Southern stations instead of the Southwestern ones. Vík í Mýrdal precipitation records also far exceed the other stations. Grímsstaðir is the only station with warm season precipitation rising over cold season precipitation. Note that these precipitation records do not distinguish between types, such as rain or snow. No consistent, long-term record of snowfall exists for this time period.

Unlike temperature and precipitation, wind speed does not segregate by region, but rather by proximity to the coast or mountains. Coastal stations Raufarhöfn, Reykjavik, Eyrarbakki, and Vatnsskarðshólar tend to group together with a trend of higher wind speeds, while inland stations of Egilsstaðir, Hæll, and Kirkjubæjarklaustur group together with lower wind speeds. Grímsstaðir, despite also being an inland station, has moderate wind speeds, while Vík í Mýrdal, another coastal station, has

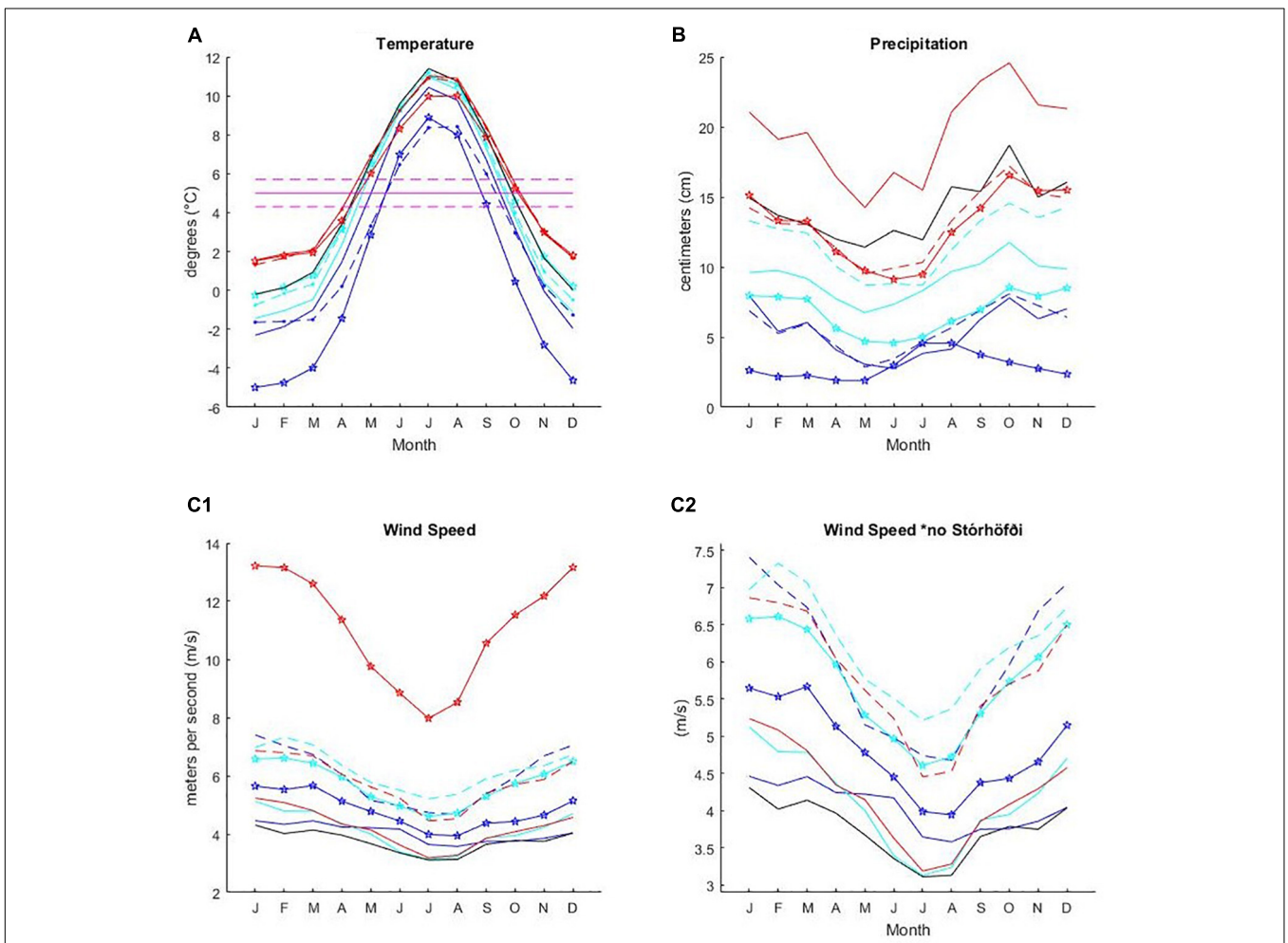

FIGURE 3 | Sixty year average **(A)** Temperature (°C), **(B)** Precipitation (cm), and **(C1)** Wind speed (m/s) at each station for each month. **(C2)** provides a closer look at station wind speed disparities without Stórhöfði. Grímsstaðir (blue ☆), Raufarhöfn (blue – – –), Egilsstaðir (blue —), Reykjavik (cyan ☆), Eyrarbakki (cyan – – –), Hæll (cyan —), Stórhöfði (red ☆), Vatnsskarðshólar (red – – –), Vík í Mýrdal (red —), Kirkjubæjarklaustur (black —).

wind speeds that are more similar to the inland stations, likely due to its location being sheltered by surrounding mountain terrain. Stórhöfði, the only separate island station, stands as an outlier, with its average wind speed exceeding the other stations' maximums.

Dust Day Frequency at Each Station

Figure 4 shows the average number of dust days per month over the 60 year period at each station, with the final plot showing the average for the whole of Iceland. Each station peaks in dust day frequency (DDF) at the beginning of the warm season. Overall, dust activity is greatest in the summer, May through July, and lowest in the winter, December and January. Shown in **Figure 5**, Stórhöfði leads in average number of dust days per year with over 40, while also leading in wind speed at around 11 m/s, which is about 5 m/s above the next highest wind speed. Vík í Mýrdal, with the greatest amount of precipitation averaging at almost 20 cm/year,

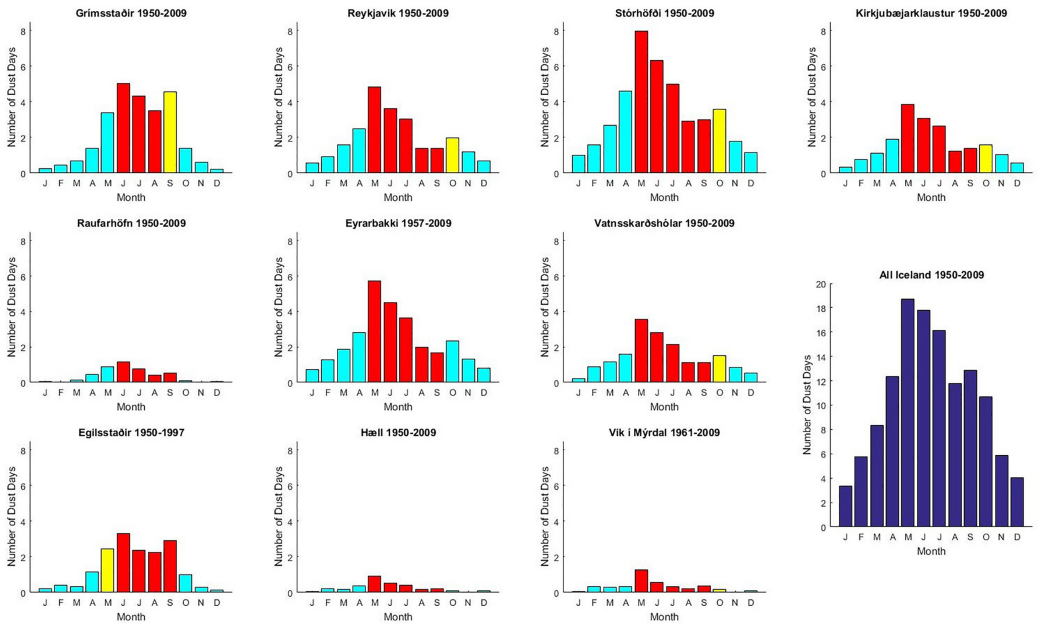

FIGURE 4 | Average number of dust days per year, with cold season (cyan), warm season (red), and transitional (yellow). NE stations in the first column, SW stations in the second column, and South stations in the third and fourth column. The bottom-right graph depicts the average number of dust days per year for all of Iceland.

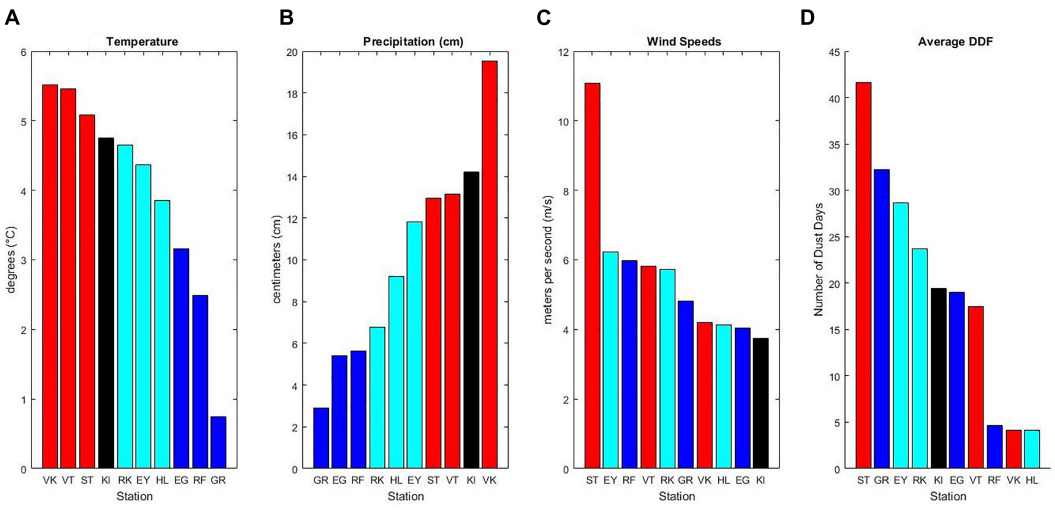

FIGURE 5 | Average annual **(A)** Temperature, **(B)** Precipitation, and **(C)** Wind Speed over 60 year period. **(D)** Average number of dust days per year at each station: Grímsstaðir (GR), Raufarhöfn (RF), Egilsstaðir (EG), Reykjavik (RK), Eyrarbakki (EY), Hæll (HL), Stórhöfði (ST), Vatnsskarðshólar (VT), Vík í Mýrdal (VK), Kirkjubæjarklaustur (KI). NE stations in blue, SW stations in cyan, and South stations in red, with Kirkjubæjarklaustur black.

is among the three lowest DDFs, next to Raufarhöfn and Hæll.

Figure 6 depicts the annual DDF for each region across the 60-year period. Included are vertical lines indicating volcanic eruptions and major jökulhlaups with the potential of affecting annual dust activity. Three major jökulhlaups are indicated in the figure, two from Mýrdalsjökull (located in South Iceland) in 1955 and 1999, and one in 1996 at Grimsvötn Gjalp (from Vatnajökull, which is bordered by Dyngjusandur on its north end and Skeiðarársandur on its south end). In South stations, the 1999 Mýrdalsjökulhlaup is followed by an increase in DDF the next year, but the 1955 Mýrdalsjökulhlaup is followed by a drop in DDF the next year. There is an increase in DDF seen in several stations the year following the Grimsvötn jökulhlaup, but greater peaks are seen throughout the 60 year period. However, the nearest weather stations from the jökulhlaup-affected areas are not always on the main dust plume paths and many dust events remain unreported. This occurs especially in South Iceland where dust plumes from the Mýrdalssandur and Skeiðarársandur areas head directly toward the ocean. The number of dust events after the jökulhlaups can therefore be underestimated.

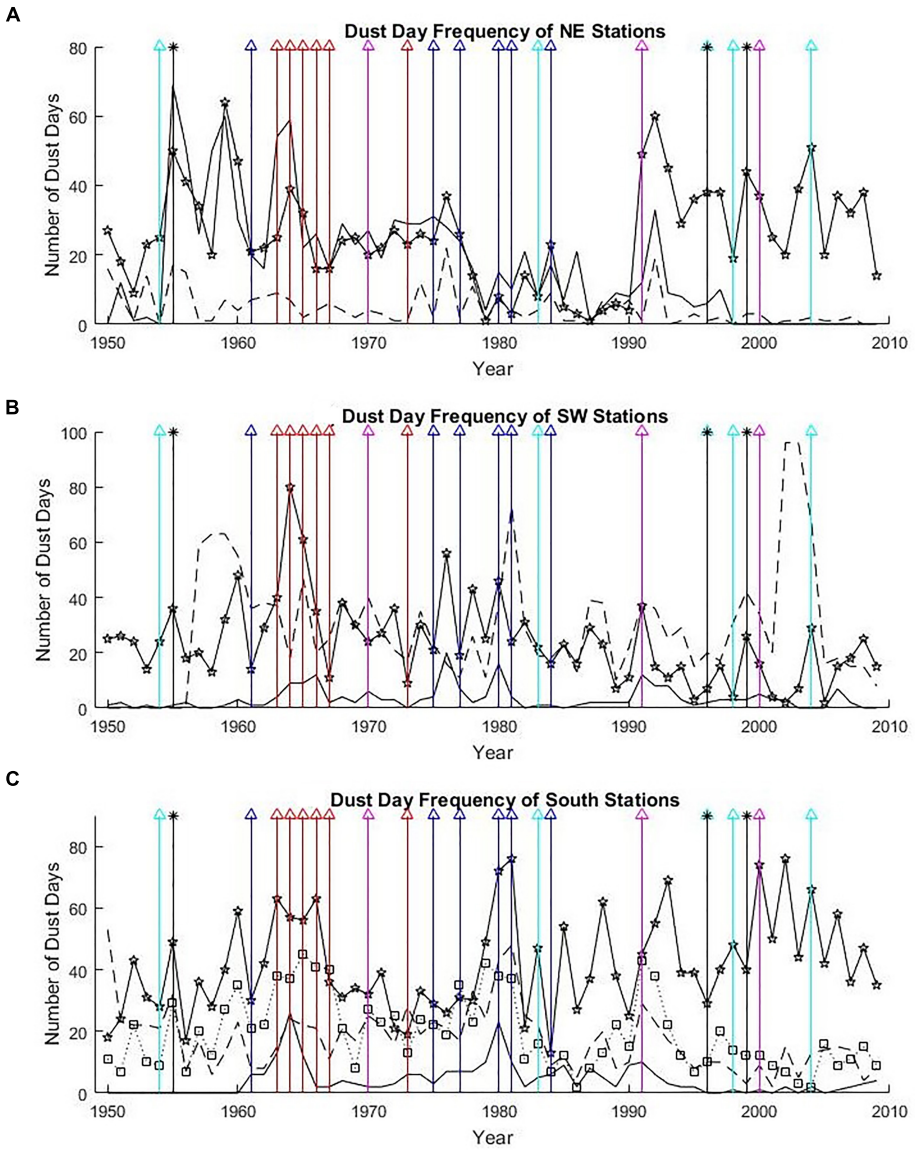

FIGURE 6 | The line graphs along the *y*-axis indicate the number of dust days each year, separated by region. **(A)** NE stations: Grímsstaðir (☆), Raufarhöfn (– – –), Egilsstaðir (—), **(B)** SW stations: Reykjavik (☆), Eyrarbakki (– – –), Hæll (—), **(C)** South stations: Stórhöfði (☆), Vatnsskarðshólar (– – –), Vík í Mýrdal (—), Kirkjubæjarklaustur (☐ dotted line). Volcanic eruptions (△) and major jokulhlaups (black *) depicted with vertical lines. In southern Iceland, there are eruptions in Vestmannaeyjar (red △) and Hekla (magenta △); in NE Iceland, there are eruptions in Askja and Krafla (blue △) and Grimsvötn (cyan △). The jökulhlaup (black *) in 1996 occured at Grimsvötn Gjalp, while the other two lines (black *) indicate Mýrdalsjökulhlaups in the South.

The most consistent dust activity occurs in South stations, but stations in other regions, such as Grímsstaðir and Eyrarbakki, experienced sharp increases in DDF that at times matched that of Stórhöfði. As seen in **Figure 5**, this contributes to their high number of average dust days per year. Overall though, Stórhöfði had the highest number of dust days, with a total of just under 2500 dust days from 1950 to 2009, as compared to 118 dust days previously reported at Stórhöfði from 1949 to 2011 (Dagsson-Waldhauserová et al., 2014).

DISCUSSION

Seasonal Dust Day Variability

In each station, during the cold season, DDF increases as average temperature rises toward the warm season. It peaks at the start of the warm season, but dips before the return of the cold season. The drop that occurs after the start of the warm season may be because the increased temperature is accompanied by decreased wind speeds. There is likely a threshold temperature around 5°C, below which temperature acts as the limiting factor, as warmer temperatures are necessary in order to evaporate moisture between sediments and reduce particle adhesion for entrainment. Above 5°C, the rate of dessication may be sufficient for the frequency of entrainment to be determined mostly by wind speeds.

Other variance within the warm season may be due to precipitation. If DDF was only determined by wind speeds, it would increase as wind speed picks up after July. Instead, DDF drops even more sharply, coinciding with the sharp increase in precipitation after July. Though precipitation increases up through October, wind speeds also steadily increase, surpassing a threshold at which it outcompetes the effects of heavy precipitation. Once the cold season starts after September or October, entrainment is once again limited by desiccation rate, despite continually increasing wind speeds.

Dagsson-Waldhauserová et al. (2014) reported 1965 to be the driest year for SW Iceland in 100 years, and it is during that same year that Reykjavik peaks in DDF, further indicating a relationship between moisture and entrainment frequency. Furthermore, Dagsson-Waldhauserová et al. (2014) reported that almost half of the dust events in the south part of Iceland occurred in the winter or at subzero temperatures. Though including the dust haze synoptic code increased the number of dust days observed during warmer temperatures, the presence of cold-weather dust activity indicates greater connection of dust events to moisture as opposed to temperature.

Annual Dust Day Variability

Volcanic eruptions that took place within this time period do not appear to have a significant long-term effect extending more than a year beyond the time of eruption, though they may have sizeable impacts on short-term dust activity. For instance, the Eyjafjallajökull eruption in 2010 had increased the dust storm frequency in South Iceland significantly during the 6–9 months following the start of the eruptive explosion (Arnalds et al., 2013; Dagsson-Waldhauserová et al. (2014), though this eruption year is not included in the presented analysis, as it is outside the examined time frame.

While records of minor seasonal jökulhlaups are not present for the observation of seasonal impacts, major jökulhlaups do not appear to have a consistent impact on annual DDF. Prospero et al. (2012) attributes the increase of dust concentration at Stórhöfði in 1997 potentially to the 1996 jökulhlaup, but the total dust days for Stórhöfði in 1997 was 40, which is just below Stórhöfði's 60 year annual mean of 41.6 (standard deviation of 15.8). They additionally linked the increase in dust concentration at Stórhöfði in 2000 to the 1999 Mýrdalsjökulhlaup, and though the number of dust days in 2000 was relatively high at 74 (two standard deviations above the mean), there are two other spikes in annual dust day number (1981 and 2002) that are at least two standard deviations above the mean and not temporally proximal to a major jökulhlaup. It may be relevant to note that the year 2000 coincides with an eruption of Hekla, located in Southwest Iceland just north of Landeyjasandur. The DDF in 1956, the year following the 1955 Mýrdalsjökulhlaup, was 17, which is greater than a standard deviation below Stórhöfði's 60 year mean. Remaining South stations also did not reflect DDFs above their stations' annual mean in the year following each of the three jökulhlaups.

Variability of Dust Activity Between Stations

Variations in overall DDF between stations may be due to sediment availability and the downwind location of stations from the dust plume sources. While Stórhöfði's spot as the highest DDF can be attributed to its extraordinarily high wind speeds, other stations are not as simple. Vík í Mýrdal's spot among the lowest three DDFs can be attributed to its extraordinarily high precipitation, as well as the fact that synoptic codes for this station were only measured at 9 a.m. and 9 p.m., missing long periods during the day at which dust activity may have occurred. The placement of Hæll and Raufarhöfn among the bottom three alongside Vík í Mýrdal may be due to their location in more vegetative regions, as can be seen in **Figure 1**. Vegetation serves to prevent erosion by holding together ground sediment and acting as a buffer between entrainable particles and the atmosphere. Egilsstaðir, with unremarkable temperature and wind speeds, but somewhat low precipitation, also has some vegetative cover and, like Raufarhöfn, is a fair distance from a dust plume source. However, it manages a moderate DDF compared to Hæll and Raufarhöfn, mainly due to dust flowing in the northeast direction from the Dyngjusandur dust plume source (Arnalds et al., 2016).

Vatnsskarðshólar has moderate wind speeds and is located in proximity to the Mýrdalsjökull floodplain. Despite this, it experiences a fair amount of precipitation, which is likely responsible for limiting its resulting DDF. Kirkjubæjarklaustur, which has similar wind speeds and precipitation to Vatnsskarðshólar and is likewise situated near major floodplains (Skeiðarársandur and Mýrdalssandur), follows with a similar resulting DDF.

The remaining stations Reykjavik, Eyrarbakki, and Grímsstaðir may owe their DDFs to a combination of moderate

meteorological factors and unremarkable locational factors. Reykjavik has moderate temperature, precipitation, and wind speed, and is located a moderate distance from the Hagavatn dust plume source, but also receives dust from the South coast (Landeyjasandur) (Arnalds et al., 2016). As a result, its DDF falls in between the median three (Egilsstaðir, Vatnsskarðshólar, Kirkjubæjarklaustur) and the top three (Eyrarbakki, Grímsstaðir, Stórhöfði). Eyrarbakki, though also with fairly moderate meteorological factors, is located more proximally to an intersection zone of dust plume sources from Hagavatn, Landeyjasandur, and Mælifellssandur. Finally Grímsstaðir, with moderate wind speeds but extraordinarily low precipitation, is located within the dust plume region of Dyngjusandur, surrounded by barren desert.

Grímsstaðir in Northeast Iceland was originally the station with the highest reported frequency of dust storms in Iceland (Dagsson-Waldhauserová et al., 2013, 2014). Inserting all the dust codes into the analyses shows that the highest frequency of dust codes is now reported from South Iceland, at Stórhöfði. This describes the general situation in South Iceland, where many dust plume sources are located close to the seashore and dust plumes can only be captured on satellite images (Dagsson-Waldhauserová et al., 2014). Monitoring stations floating on the sea south of Iceland could possibly record the highest rates of airborne dust observations.

CONCLUSION

The analysis of dust day variability reveals correlation to location and wind speed. Location, such as proximity to dust plume sources and sandurs, determines whether there is ample exposed sediment supply, while high wind speeds enhance the transport of that accessible supply. Wind direction and gust, precipitation type, and duration of daylight exposure have yet to be accounted for, and may explain discrepancies in the relationship between meteorological variables and DDF.

The volcanic eruptions alone seem not to correspond to the frequent spikes in DDF year to year. There is an average of one eruption every 3–4 years in Iceland (Thordarson and Höskuldsson, 2008). Jökulhlaups in Iceland occur more frequently than explosive volcanic eruptions, and large jökulhlaups can bring >5 million tons of fine deposits (grain size < 0.05 mm) available for suspension every year (Jensen et al., 2018). Yet it appears that even the largest jökulhlaups do not directly lead to a significant increase in dust activity. This might be because jökulhlaups increase supply in active sandur regions that are not limited by sediment supply. If this is the case, minor jökulhlaups also may not be significantly accountable for seasonal DDF variability. The areas of main jökulhlaups are, however, poorly monitored, because the weather stations are not located in the main pathways of dust plumes from such places. This can cause the underestimation in number of dust SYNOP codes (O'Loingsigh et al., 2010; Arnalds et al., 2016).

Potential long-term impacts of glacier retreat must then reside primarily in the expansion of erodible surface area that was once covered by glaciers, thereby increasing the extent of areas rich in sediment supply. However, floodpaths and vegetation cover may also shift over time to balance this. A possible outcome is that floodplains initially expand as the rate of melting and magnitude of flooding increase; then, as the size of the glacier decreases and the size of its floods follow suit, the floodplains will subsequently be subjected to vegetation succession, especially in the lowland areas. This may eventually reduce the size of sediment supply areas, though many of the most active sand surfaces are hostile to vegetative succession due to abrasion (Vilmundardóttir, 2014).

Overall, we find that the frequency of dust day activity is higher than previously suggested, with an average of about 128 dust days annually for all Iceland, as compared to the previous annual mean of 34 dust days. Dust particles need to be further quantified and qualified in terms of their size and type for a better prediction of the potential impact of future fluctuations in dust activity on global radiative balance.

AUTHOR CONTRIBUTIONS

The analysis of dust day frequency, meteorology, volcanic eruptions, and jokulhlaups was made by MN. MN and PD-W contributed to writing the manuscript. PD-W coordinated the writing of the paper.

FUNDING

This work was funded by the SIT (School for International Training) Study Abroad Program, a Program for World Learning, Iceland, and Greenland: Climate Change and the Arctic. The preparation of this manuscript was funded by the Icelandic Research Fund (Rannis) Grant No. 152248-051.

ACKNOWLEDGMENTS

We would like to acknowledge SIT Program Coordinator Mr. Daniel Govoni and Ms. Alexandra Tyas. We would also like to thank professor Olafur Arnalds for helping with the manuscript preparation.

REFERENCES

Arnalds, O. (2010). Dust sources and deposition of aeolian materials in Iceland. *Icel. Agric. Sci.* 23, 3–21.

Arnalds, O., Dagsson-Waldhauserová, P., and Olafsson, H. (2016). The icelandic volcanic aeolian environment: processes and impacts–A review. *Aeolian Res.* 20, 176–195. doi: 10.1016/j.aeolia.2016.01.004

Arnalds, O., Thorarinsdottir, E. F., Thorsson, J., Dagsson-Waldhauserova, P., and Agustsdottir, A. M. (2013). An extreme wind erosion event of the fresh Eyjafjallajokull 2010 volcanic ash. *Nat. Sci. Rep.* 3:1257. doi: 10.1038/srep01257

Björnsson, H. (1992). Jökulhlaups in Iceland: prediction, characteristics, and simulation. *Ann. Glaciol.* 16, 95–106. doi: 10.3189/1992AoG16-1-95-106

Björnsson, H. (2002). Subglacial lakes and jökulhlaups in Iceland. *Glob. Planet. Change* 35, 255–271. doi: 10.1016/S0921-8181(02)00130-3

Bullard, J. E. (2013). Contemporary glacigenic inputs to the dust cycle. *Earth Surf. Process. Landf.* 38, 71–89. doi: 10.1002/esp.3315

Bullard, J. E., Baddock, M., Bradwell, T., Crusius, J., Darlington, E., Gaiero, D., et al. (2016). High-latitude dust in the Earth system. *Rev. Geophys.* 54, 447–485. doi: 10.1002/2016RG000518

Dagsson-Waldhauserová, P., Arnalds, O., and Olafsson, H. (2013). Long-term frequency and characteristics of dust storm events in Northeast Iceland (1949-2011). *Atmos. Environ.* 77, 117–127. doi: 10.1016/j.atmosenv.2013.04.075

Dagsson-Waldhauserová, P., Arnalds, O., and Olafsson, H. (2014). Long-term variability of dust events in Iceland (1949-2011). *Atmos. Chem. Phys.* 14, 13411–13422. doi: 10.5194/acp-14-13411-2014

Jensen, E. H., Egilson, D., Pagneux, E., Björnsson, B. B., Zóphóníasson, S., Snorrason, S. P., et al. (2018). *Hættumat Vegna Jökulhlaupa í Skaftá. Mat á Setflutningi Með Sögulegu Yfirliti*. Reykjavík: Veðurstofa Íslands.

Maizels, J. (1997). Jökulhlaup deposits in proglacial areas. *Q. Sci. Rev.* 16, 793–819. doi: 10.1016/S0277-3791(97)00023-1

O'Loingsigh, T., Mc Tainsh, G., Tapper, N., and Shinkfield, P. (2010). Lost in code: a critical analysis of using meteorological data for wind erosion monitoring. *Aeolian Res.* 2, 49–57. doi: 10.1016/j.aeolia.2010.03.002

Prospero, J. P., Bullard, J. E., and Hodgkins, R. (2012). High latitude dust over the North Atlantic: inputs from Icelandic proglacial dust storms. *Science* 335, 1078–1082. doi: 10.1126/science.1217447

Thordarson, T., and Höskuldsson, A. (2008). Postglacial volcanism in Iceland. *Jökull* 58, 197–228.

Vilmundardóttir, O. K. (2014). Early stage development of selected soil properties along the proglacial moraines of Skaftafellsjökull glacier. SE Iceland. *Catena* 121, 142–150. doi: 10.1016/j.catena.2014.04.020

WMO (2009). *Manual on Codes: International Codes,* Vol. 1 *(Part A – Alphanumeric Codes)*. Available at: http://www.wmo.int/pages/prog/www/WMOCodes.html [accessed November 6, 2014].

Conflict of Interest Statement: The authors declare that the research was conducted in the absence of any commercial or financial relationships that could be construed as a potential conflict of interest.

frontiers in Earth Science

REVIEW
published: 11 January 2019
doi: 10.3389/feart.2018.00250

Light-Absorbing Impurities in Snow: A Personal and Historical Account

*Stephen G. Warren**

Department of Atmospheric Sciences, University of Washington, Seattle, WA, United States

The ability of light-absorbing impurities (LAI) to darken snow had been known for decades, even inspiring practical applications, but quantification of the radiative forcing awaited radiative-transfer modeling in 1980 and measurement of soot in Arctic snow in 1983-4. Climate-modeling interest in this forcing began in 2004, spurring a modern explosion of research on several topics: methods to measure black carbon (BC) and other LAI, Arctic air pollution, measurement of BC mixing ratio in snow over large areas, and radiative transfer modeling of this forcing and its climatic and hydrological effects. The BC-content of snow in large remote regions of the northern hemisphere is on the order of 20 parts per billion, causing albedo reductions of ∼1–2%. This reduction is climatically significant but difficult to detect by remote sensing, so quantification requires fieldwork to collect and analyze snow samples. This review is a personal account of early research at the National Center for Atmospheric Research and the University of Washington, followed by a brief summary of recent work by the author and his colleagues.

Keywords: snow, light-absorbing impurities in snow, snow albedo, Arctic, radiative transfer

OPEN ACCESS

Edited by:
Pavla Dagsson-Waldhauserova, Agricultural University of Iceland, Iceland

Reviewed by:
Outi Meinander, Finnish Meteorological Institute, Finland
Jeff Dozier, University of California, Santa Barbara, United States
Tami Bond, University of Illinois at Urbana–Champaign, United States

***Correspondence:**
Stephen G. Warren
sgw@uw.edu

Specialty section:
This article was submitted to Atmospheric Science, a section of the journal Frontiers in Earth Science

Received: *24 July 2018*
Accepted: *20 December 2018*
Published: *11 January 2019*

Citation:
Warren SG (2019) Light-Absorbing Impurities in Snow: A Personal and Historical Account. Front. Earth Sci. 6:250. doi: 10.3389/feart.2018.00250

BEGINNINGS

That the albedo of snow is reduced by light-absorbing impurities (LAI) is obvious to the eye when the LAI arrive in a massive deposition event, for example when volcanic ash falls out onto Icelandic glaciers (e.g., Wittmann et al., 2017). Such observations have no doubt been made for centuries, and the consequences for snowmelt rate were probably also sometimes noticed long before any scientific study was undertaken. But the discovery that most snow in the northern hemisphere contains enough LAI to reduce its albedo by climatically significant, yet invisible, amounts was a surprise; it resulted from field measurements and modeling in the 1970s and 1980s, described below.

How I developed a research focus on LAI in snow takes some explaining. I was trained as a physical chemist, then got into biophysics research with my Ph.D. project to solve the three-dimensional atomic structure of an enzyme using X-ray crystallography (Warren et al., 1973). I continued in that field as a *post doc* in Germany, on the fascinating structural-biology problem of a virus that infects tobacco plants (Stubbs et al., 1977). Although the work was interesting, my mind kept wandering to thoughts of geography and climate.

The opportunity to change careers came when I was accepted as a *post doc* at the National Center for Atmospheric Research (NCAR) in Boulder, Colorado, for retraining in atmospheric physics. My sponsor was Steve Schneider. On my arrival at NCAR in January 1978 I told Steve that I was interested in the ice ages, so he introduced me to Warren Wiscombe, his colleague in the Climate Section. Steve knew that Wiscombe shared an interest in the ice ages, although there was no

published evidence of that interest; Wiscombe's focus was on developing methods for computing atmospheric radiative transfer, and he had become the world leader in that field. When I met him, I was ignorant of the fame of his great accomplishments; I was even unfamiliar with the term "radiative transfer." He told me "We won't solve the ice-age problem, but we'll chip away at it. We'll solve one small but important part of the ice-age problem – we'll explain the albedo of snow."

My 1st year at NCAR I worked with Steve Schneider on energy-balance climate modeling (Warren and Schneider, 1979); meanwhile I enrolled in a graduate course on radiative transfer taught by Gary Thomas at the University of Colorado (also in Boulder). Professor Thomas distributed his handwritten notes to the students, which were later published as an authoritative textbook (Thomas and Stamnes, 1999). After that training I was ready to start working with Wiscombe. [I'm using surnames here because their given names can cause confusion: my two mentors at NCAR were named "Steve" and "Warren"].

RADIATIVE TRANSFER MODEL FOR SNOW

We used one of the radiative-transfer models that Wiscombe had invented, the delta-Eddington method, to compute the variation of snow albedo with wavelength (Wiscombe and Warren, 1980). The single-scattering computation, using Wiscombe's (1980) implementation of Mie theory, required as input the complex refractive index of ice, which I had to compile from numerous published laboratory measurements, and which I eventually published (Warren, 1984b) and more recently have updated (Warren and Brandt, 2008). At any given wavelength, the albedo depends on the snow grain size, the solar zenith angle, the partitioning of direct and diffuse irradiance, and the snow depth.

We modeled the snowpack as a pack of ice spheres, and argued that what really mattered was the area-to-mass ratio of the snow grains (now called "specific surface area"; I wish we had thought of that name!). The radius of the spheres in our model snowpack would then be three times the volume-to-area ratio of the real non-spherical snow grains. The errors in this spherical representation were later quantified for various snow-crystal shapes (Grenfell and Warren, 1999; Neshyba et al., 2003; Grenfell et al., 2005). The extinction efficiency and single-scattering albedo are well-represented by the equivalent spheres. The scattering asymmetry factor for the spheres is too large, but its effect can be compensated by reducing the model's grain size (Dang et al., 2016).

The modeling showed that the most important variable determining snow albedo is the size of the snow grains. Physically, a photon traveling in a snowpack has a chance to change direction at each air/ice interface, and has a chance to be absorbed while traveling through ice. In coarse-grained snow, a photon travels a longer distance through ice between opportunities for scattering than in fine-grained snow, so it is more likely to be absorbed, and therefore a snowpack of coarse grains has lower albedo. The area/mass ratio normally decreases with snow age by "destructive metamorphism" (LaChapelle, 1969), leading to the "equilibrium form" (Colbeck, 1982), so the radiatively effective grain size increases, and the albedo drops.

We tested the model against measurements of near-infrared (near-IR) reflectance by O'Brien and Munis (1975), who had collected natural snow in the back yard of the United States Army's Cold Regions Research and Engineering Laboratory (CRREL) in New Hampshire. They had brought the snow into a cold-room laboratory for radiation measurements (they did not measure the grain size). The introduction of their report tells their motivation for this research: "The probability of detecting [military equipment and personnel] depends upon the contrast in reflection of solar radiation from objects compared with that from snow-covered backgrounds."

To match the measurements of O'Brien and Munis for new snow and 2-day-old snow, we needed grain radii r = 50 μm and r = 200 μm, respectively. Our model, using grain radius as a free parameter, agreed well enough with the measurements, considering that the measurements were actually not of albedo but rather of bidirectional reflectance at a particular pair of angles (source 0°, detector 30°).

WHAT'S WRONG WITH THE MODEL?

At shorter wavelengths we ran into trouble. The most accurate measurements of visible albedo were those of Grenfell and Maykut (1977; hereafter GM) for snow at a research camp on Ice Island T-3 in the Arctic Ocean. [Tom Grenfell made the measurements in 1974, and Gary Maykut helped with the analysis; both worked at the University of Washington (UW)]. At visible wavelengths, the absorption by ice is extremely weak. For example, the absorption length (e-folding depth, reciprocal of the absorption coefficient) for blue light is ∼200 m, and even for red light it is 2 m (Warren and Brandt, 2008). Photons entering a snowpack of 100-μm spheres should experience numerous refraction events and eventually escape upward, having traveled much less than 2 m through ice. Correspondingly, the albedo across the visible spectrum should be 95–100% for all grain radii 50–1500 μm. But that was not what GM had found. At the blue wavelength 400 nm, their albedo for dry new snow was 92%, and for old melting snow it was much lower, ∼82%. We considered what our model had neglected: the non-sphericity of snow grains, and the shadowing caused by close-packing in high-density snow. But we showed that those defects of the model would actually have caused more error at near-IR wavelengths than at visible wavelengths. So we concluded that the snow measured by GM had contained something in addition to ice, something that absorbs visible radiation. What could it be?

ATMOSPHERIC AEROSOLS CAN GET INTO SNOW

In my first few months at NCAR I had become aware that there were some scientists who had actually made a career of studying dust in the atmosphere (e.g., Patterson and Gillette, 1977). Dale Gillette was a friendly fellow, and I enjoyed his company. But

I was astonished at his choice of research topics; I could hardly imagine anything more boring than atmospheric dust. But of course dust can fall out into snow, and now it looked to be important for snow albedo, so to my surprise I myself became fascinated with dust.

I consulted the literature, back as far as the 1920s. Dust from Oklahoma had reached Vermont in the "brown snowfall" of 1936; pinkish-colored snow in New Zealand in 1928 was attributed to red dust from Australia. Haeberli (1977) had written a nice review of Saharan dust in the Alps. Dirmhirn (1960) had measured the effect of a dust-fall event on the albedo of alpine snow: a reduction of 10% in broadband albedo and 16% in visible albedo. The champion for brevity of title headed a Russian paper by Khromov (1931), "Zhyoltyy Sneg," which simply means "yellow snow."

I got optical constants of red Saharan dust from Dale Gillette (Patterson et al., 1977). When we incorporated them into our radiative transfer model, the snow, not surprisingly, turned red. But the snow measured by Tom Grenfell in the Arctic Ocean was not visibly colored; if it had been he probably would not have measured it. And his spectral plots were flat across the visible spectrum, so what we needed was a gray absorber. One day when Wiscombe and I were walking down a corridor at NCAR, we bumped into Bob Charlson from UW. Wiscombe asked him, "What's that light-absorber you're finding in the atmospheric aerosol?" Bob revealed his not-yet-published secret, whispering in our ears: "It's carbon!"

Some of the papers describing dirty snow did have enough soot to produce visible gray bands (Elgmork et al., 1973), and others had actually experimented with the use of black carbon to promote snowmelt in Japan, China, and Colorado (e.g., Meiman, 1973). A long paper in the *Journal of Applied Meteorology* by Professor Bill Gray of Colorado State University (Gray et al., 1976) advocated the use of carbon dust for weather modification, including speeding up snowmelt. His Figure 5 is a drawing of an airplane spewing carbon dust from its engines: after a B-52 airplane reaches cruising altitude it no longer needs all eight engines for power, so four of them can be switched to soot-production. This was apparently what some scientists in the 1970s thought to be the role of black carbon in the climate system, but now Gray's paper is rarely cited; it was missing from the authoritative 173-page treatise by Tami Bond et al. (2013).

That literature-search was fun, but to make progress on research what we really needed was to find optical constants and size distributions for atmospheric soot, and to incorporate them into our radiative transfer model of snow. When we did that, to match Grenfell's measurements we had to say that his snow at T-3 contained 150–200 nanograms of carbon per gram of snow (ng/g) (Warren and Wiscombe, 1980; Warren, 1982). These amounts of soot, reducing the visible albedo by nearly 20% without coloring it, would not make the snow visibly darker because the eye is a logarithmic detector, adapting to changes in illumination over a factor of 500,000 (judging from our ability to read a printed page illuminated by either the overhead Sun or the overhead full moon).

In our model, the addition of soot reduced the albedo only at wavelengths where the albedo of pure snow is very high (UV and visible). It did not reduce the near-IR albedo, where ice itself is moderately absorptive, so that trace amounts of impurities cannot do much.

We were left with two important unanswered questions. (1) Can we trust the model? We had not tested our model against measurements for snow known to be clean. (2) How much soot does the Arctic snow actually contain? The source of soot over wide areas would be fallout from the atmospheric "Arctic haze" (Rahn and McCaffrey, 1980; Cess, 1983), but Grenfell's measurements had been made close to the T-3 research station where the snow was probably affected by local pollution and did not represent the wider area.

WHAT IS THE SOOT CONTENT OF ARCTIC SNOW?

Answering both questions benefited from my move to UW. In 1981 Ed LaChapelle retired, and I was lucky to be hired as his successor. As part of my job interview I gave a seminar, "Reflection of sunlight by snow." In the audience was Tony Clarke, a graduate student in Charlson's lab. Tony was inspired by my talk to try to quantify the soot in Arctic snow. Tony had invented the "integrating sandwich" filter method to greatly increase the sensitivity for quantifying the small amounts of soot in clean remote air (Clarke, 1982). His fellow student John Ogren had developed methods to collect soot from rainwater, and Tony adapted John's method for snow. In April 1983 Tony and I drove up to Mount Rainier on a Sunday to practice snow-collection. Tony's wife Joan came along, but she became bored watching us discussing our snow-pit. She pulled out a cigarette and was just about to light it when it dawned on her that maybe she shouldn't.

Tony got on the phone to researchers who were going to the Arctic, and many of them volunteered to collect snow for him. Tony instructed them on snow-sampling procedures (Please don't smoke!). They shipped their still-frozen snow to Seattle, from Alaska, Canada, Greenland, Svalbard, and Scandinavia. A Masters student, Kevin Noone, worked with Tony to process the samples. Their measurements of filter transmission at four wavelengths allowed them to separate the absorption by soil dust from the absorption by BC. They found BC values in the range 5–50 ng/g (Clarke and Noone, 1985). Using our radiative-transfer results, they estimated that this soot content would reduce snow albedo by 0–4%, depending on the snow grain size, with radiative forcing similar to that of Arctic haze in the atmosphere (Cess, 1983; Warren and Clarke, 1986). An albedo reduction of 1–2% sounds small, and is often within the measurement uncertainty, but it is climatically important. For a typical daily average solar irradiance of 400 W m^{-2} in the Arctic during late spring and early summer, a 1% reduction of broadband snow albedo causes a positive forcing of 4 W m^{-2} locally, similar to the forcing caused by doubling CO_2.

The Arctic haze exhibits a dramatic seasonal cycle, with high values in winter and low values in summer (e.g., Sharma et al., 2004). A chance conversation of Tony with Björn Holmgren at the IUGG meeting in 1983 led to an invitation for Kevin to investigate the transfer of soot from air into snow at the Abisko research station in northern Sweden. For his Master's

thesis, Kevin documented the springtime decline of Arctic soot, measuring BC in both air and falling snow at Abisko (Noone and Clarke, 1988).

WHERE CAN WE FIND CLEAN SNOW?

Being at UW in the same department with Tom Grenfell gave me the opportunity to get involved in fieldwork. In 1982 Tom and I wrote a proposal to NSF to go to the interior plateau of Antarctica, to measure the spectral albedo of snow we could be sure was clean, to see if the visible albedo was as high as the model predicted. Our proposal was rejected, by reviewers saying "Albedo has already been measured in Antarctica." We needed to emphasize that it was spectral albedo, not broadband albedo, that was required, and that Tom was the world expert for measuring spectral albedo of polar surfaces. Our resubmitted proposal was approved by the NSF Program Manager, Ben Fogle, and in December 1985 we arrived at the South Pole Station, together with a graduate student, Peter Mullen. We spent 2 months there.

The Antarctic snow is extremely clean, but we were based at a station that burned diesel fuel and experienced 100 landings and takeoffs of C-130 airplanes every summer. So while Tom and Peter made numerous albedo measurements, under various sky conditions for both new and old snow, I conducted a soot survey. Tony and Kevin had given me a filtering apparatus and had instructed me on their procedures. I walked out along 3-km lines in all directions from the station, collecting snow at regular intervals, until I was able to make a contour map of soot-pollution (Warren and Clarke, 1990). The wind at the South Pole is strongly directional, and just 500 m upwind of the station, in the Clean Air Sector, at a site we had already chosen for albedo measurements, the soot content was only 0.3 ng/g, far too small to measurably affect snow albedo at the most sensitive wavelength. The albedo exceeded 0.98 across the UV and visible, in agreement with our model for pure snow. We showed this result in a brief report (Warren et al., 1986); we eventually published the full paper after we had also made similar measurements at Vostok Station (Grenfell et al., 1994).

TANGENTIAL TOPICS FROM THE EARLY YEARS

Soot Can Lower Snow Albedo; Why Not Cloud Albedo?

Black carbon can get into snow by being attached to ice nuclei in clouds or scavenged by falling snow crystals, as well as by dry deposition. BC in snow reduces the snow albedo; what does it do to clouds? Cindy Twohy, another of Charlson's students, had developed the Counterflow Virtual Impactor (CVI) for measurements from an airplane flying through a cloud, to separately quantify LAI inside cloud droplets and LAI in the interstitial air between cloud droplets. She asked me to compute the effect of the LAI on the visible albedo of the clouds she had sampled over the Pacific Ocean between California and Hawaii. The effect was insignificant. Our calculation (Twohy et al., 1989) showed that to achieve a given reduction of visible albedo in a cloud or in snow, the required mixing ratio of soot in the cloud (ng/g) would have to be 300 times the mixing ratio in snow, because of two differences between clouds and snow that determine their interaction with sunlight: (1) cloud particles are smaller, with effective radii $\sim$10 μm as opposed to 100 μm or more for snow, so photons can escape upward from the cloud without passing through much water; and (2) typical cloud optical thicknesses at visible wavelengths are only 15–30, whereas snow is effectively semi-infinite (just 1 cm of snow has an optical thickness of $\sim$40), so much of the light incident on a cloud escapes out the bottom without encountering impurity particles.

But now I have to back off from our categorical conclusion about the ineffectiveness of soot in clouds. Over the ocean off the southwest coast of India, Andy Ackerman showed that the clouds can be so polluted by smoke that they do absorb significant sunlight, enough to cause the clouds to heat up and evaporate (Ackerman et al., 2000).

CO_2-Snow in the Polar Caps of Mars, Where the Impurity Is Water

In February 1981 Wiscombe returned to NCAR from a conference about climate change on Mars, and asked me to apply our model to CO_2-snow in the seasonal polar caps, using some newly measured optical constants of CO_2-ice that had been reported at the meeting. We calculated the visible spectral albedo and how it is lowered by Martian dust, but our primary motivation was to explain some strange satellite observations of low brightness temperature in the thermal infrared. Because absorption by CO_2-ice is extremely weak between the 4.3- and 15-μm bands, the thermal emissivity of CO_2-snow is sensitive to trace amounts of water-ice, whose absorption coefficient in the interband region is 2–3 orders of magnitude higher than that of CO_2-ice. So in the radiative transfer model, our specification of the "impurity" became, to our amusement, not dust or BC but rather water-ice (Warren et al., 1990).

THE MODERN ERA

After the pioneering work of Clarke and Noone was published in 1985, Tony and I expected that climate modelers would take notice. But for many years they ignored it, so Tony and I pursued work on other topics (Tony worked on atmospheric aerosol studies; I worked on cloud climatology, sea-ice albedo, longwave radiation spectra, and sea-glaciers on Snowball Earth).

Finally, nearly 20 years later, interest in LAI in snow was renewed by Jim Hansen, who thought that soot-in-snow might be the missing radiative forcing in his modeled global warming of the 20th century, so he incorporated that process into the GISS climate model (Hansen and Nazarenko, 2004; hereafter HN). He asked me and Tony to review his paper, hoping to persuade us to return to our former research topic.

The HN paper generated wide interest, including among funding agencies. Tom Grenfell, Tony Clarke, and I got a grant from the NSF Arctic Program, and we were joined in the work by Sarah Doherty and Rich Brandt. We carried out large-area

FIGURE 1 | Photos from fieldwork. **(a)** In the Kolyma lowland, Yakutia. **(b)** Rich Brandt on a frozen lake in Arctic Canada. **(c)** Cheng Dang and Sarah Doherty in Manitoba. **(d)** With Sarah Doherty, finding buried summer melt-layers near Dye-2 in the percolation zone of South Greenland (photo by Rich Brandt). **(e)** Tom Grenfell filtering snowmelt in a hotel room in Tiksi near the Lena Delta. [Written informed consent has been obtained from him to publish this picture]. **(f)** Making artificial snowpacks in the Adirondack Mountains (Rich Brandt).

surveys of LAI in snow in the Arctic (Doherty et al., 2010) and North America (Doherty et al., 2014). Professor Qiang Fu in my department at UW established a collaboration with Lanzhou University so that we could carry out a similar survey across northern China (Huang et al., 2011). We carried out these large-area surveys as field trips because it is difficult to detect small yet climatically important amounts of LAI in snow by remote sensing, especially in the Arctic where the snow is often thin and patchy (Warren, 2013). [Also, those trips gave me the opportunity to travel in some exotic remote regions!] On trips where we were driving, we could specify the sampling interval. We typically collected samples every 100 km, and this seemed adequate, as evidenced for example in the smooth plot of BC versus latitude in northeast China (Figure 6 of Huang et al., 2011).

Tom built our laboratory photometer for analyzing filters (Grenfell et al., 2011). Sarah developed a spectroscopic method to separate the absorption by BC from that of other LAI, showing that typically ∼40% of the absorption by impurities was by non-BC LAI. [In some regions, BC is actually a minor contributor to the LAI; Tom Painter leads a group studying snow in mid-latitude mountain regions near deserts, where soil dust dominates the absorption (e.g., Painter et al., 2007)].

Hansen and Nazarenko's paper also generated interest in the remote-sensing community. For several years after 2004 I was sometimes asked to review proposals that promised to quantify BC in Arctic snow by remote sensing from satellites or unmanned aerial vehicles (UAVs). One of those proposals requested several million dollars from NASA to accomplish a goal I considered impossible. To forestall such proposals, I wrote a paper to explain

why I thought that such projects, if undertaken, were destined to fail (Warren, 2013). A particular problem is that much of the Arctic snowpack in spring is thin and patchy, and the spectral signature of thin snow resembles that of BC in snow. [However, in some other parts of the world the snow is so heavily loaded with LAI that remote sensing can be useful. Painter et al. (2012) used MODIS to infer radiative forcing by dust contamination of snow in the Himalaya and in southwest Colorado, checked with ground-truth measurements in Colorado. The snow was grossly contaminated, with concentrations in the parts-per-thousand range rather than parts per billion. The MODIS retrieval found an astonishingly large mean dust-in-snow forcing of $\sim$250 W m^{-2} in these regions].

Figure 1 shows some pictures from our fieldwork. **Table 1** gives a global summary of our BC mixing ratios. They range over four orders of magnitude, from 0.2 ng/g in Antarctica to 2000 ng/g in northeast China. The values in this table all come from the same method of measurement that was developed by Clarke and Noone (1985). An alternative method using controlled combustion and measurement of CO_2 release ("thermal-optical method") tends to give smaller values (e.g., Forsström et al., 2013), possibly because of undercatch by the quartz fiber filter (Torres et al., 2014).

Our Arctic survey found lower BC mixing-ratios than those of Clarke and Noone (1985), in regions that both studies had sampled. This result was anticipated by some measurements that Tom Grenfell had made in 1998 at the SHEBA site in the Beaufort Sea (Grenfell et al., 2002) and during an Arctic Ocean transect in 2005. Our lower BC mixing ratios were consistent with results from the continuous monitoring of BC in air since 1989 at the Alert station on Ellesmere Island (82°N) by Sangeeta Sharma and her coworkers (Gong et al., 2010). They showed that the Arctic atmosphere has become cleaner in the past 30 years, which they attributed to the demise of the Soviet Union. We concluded that BC in snow and ice of the Arctic Ocean is probably not contributing to the rapid decline of sea ice in recent decades, so other causes must be sought.

TABLE 1 | Global summary of black-carbon mixing-ratios in snow before the onset of melt (winter in midlatitudes; spring in the Arctic and Antarctic).

Region	Black carbon (ng/g); median values in snowpits	Reference
Greenland	1–4	Doherty et al., 2010
Arctic Ocean	4–10	Doherty et al., 2010
Arctic Canada	8–14	Doherty et al., 2010
Arctic Russia	10–60	Doherty et al., 2010
Scandinavia	20–60	Doherty et al., 2010
Northeast China	30–2000	Wang et al., 2013
Northwest China (Xinjiang)	20–600	Ye et al., 2012
Western North America	5–70	Doherty et al., 2014
Antarctic Plateau *(South Pole, Vostok, Dome C)*	0.2–0.6	Warren and Clarke, 1990; Grenfell et al., 1994; Warren et al., 2006
Antarctic sea ice	0.2–0.4	Zatko and Warren, 2015

We studied the vertical redistribution of BC in melting snow in Greenland and Alaska, and also in Norway in a collaboration with Sanja Forsström (Doherty et al., 2013). This work was a follow-on to the study by Conway et al. (1996), who had spread artificial soots, both hydrophobic and hydrophilic, onto melting snow, and quantified the vertical redistribution. Because BC is largely hydrophobic, much of it gets left behind at the surface as the snow melts, enhancing the albedo reduction.

Rich Brandt tested our radiative-transfer modeling of BC-in-snow by making artificial snowpacks containing large amounts of soot (Brandt et al., 2011). Dean Hegg, a chemist just down the hall from me in the UW cloud-physics group, got interested in our project; he led a study on source-attribution of BC by looking for fingerprints in the pattern of 24 chemicals that he measured in our meltwater (Hegg et al., 2009, 2010). He surprised us by showing the dominance of biomass burning over industrial sources in most parts of the Arctic. A graduate student, Cheng Dang, worked with us to quantify the radiative effects of the LAI found in our large-area surveys (Dang et al., 2015, 2017).

BROADER IMPACTS

Ice-core records show enhanced dust fallout during glacial maxima, as first shown by Lonnie Thompson (1977). The albedo-lowering effect of dust was suggested by Will Kellogg to cause a negative feedback on ice-sheet growth (Figure 8 of Kellogg, 1975), as discussed by Warren (1984a). Indeed, climate modeling of ice-age cycles now finds this albedo-lowering effect of dust necessary for deglaciation (Willeit and Ganopolski, 2018). And on a shorter time-scale, within the present interglacial, the "Little Ice Age" in the Alps is hypothesized to have been terminated by deposition of BC from the 19th-century industrialization of Europe (Painter et al., 2013).

THE FUTURE

I have been amazed to see the expansion of research by many groups worldwide, in Europe, North America, South America, Japan, China, and India, on all aspects of this problem, with sessions every year at EGU and AGU, and the publications in this special issue. Here are just a few suggested topics for future research that link to our recent measurements.

(1) Determine wet-deposition rates of particles, following on to the work of Noone and Clarke (1988). Riding the cable-car from Ny-Ålesund up to the Zeppelin Station on Svalbard stimulated our thinking on one way to do this, resulting in the paper by Hegg et al. (2011).

(2) Investigate lofting and deposition of dust on small scales that are currently missing from climate models, for example the transport of dust to shallow patchy snow from nearby soil (centimeter-scale), and to glaciers from mountain-walls (kilometer-scale). This problem became apparent to us in Inner Mongolia, where sheep grazing through thin snow would kick up soil that then fell on top of the neighboring snow.

(3) Further quantify the biases in our filter method (ISSW) and in the single-particle soot photometer (SP2) for snow samples containing BC mixed with organic carbon and/or mineral dust (Schwarz et al., 2012), and the capture-efficiency of the filter for the thermal-optical method (Torres et al., 2014).

AUTHOR CONTRIBUTIONS

The author confirms being the sole contributor of this work and has approved it for publication.

ACKNOWLEDGMENTS

This work was made possible by collaborations with many colleagues: Warren Wiscombe, Tony Clarke, Tom Grenfell, Rich Brandt, Sarah Doherty, Dean Hegg, Qiang Fu, Cheng Dang, Rudong Zhang, Peter Mullen, Steve Hudson, and Sanja Forsström. Others who collected snow or participated in other ways include (from the United States) Matthew Sturm, Mike Steele, Angel Adames, Jamie Morison, Ron Sletten, Mike Town, Kat Huybers, Ryan Eastman, Maria Zatko, Ignatius Rigor, and Lora Koenig; (from China) Jianping Huang and Hao Ye; (from Russia) Vladimir Radionov, Sergei Zimov, Viktor Boyarsky, and Stas Kogan; and (from Europe) Carl Bøggild, Sebastian Gerland, Christina Pedersen, Johan Ström, Jane Carlsen, Koni Steffen, Kevin Noone, and Sebastian Simonsen. Thanks to OM, PD-W, Marie Dumont, and Biagio Di Mauro for inviting me to give this talk at their session of the EGU meeting (April 2018), and to write this paper. Helpful comments on the manuscript were provided by Sarah Doherty, Tony Clarke, Tom Grenfell, OM, Tom Painter, JD, and Tami Bond. Richard Brandt assisted in the preparation of **Figure 1**.

REFERENCES

Ackerman, A. S., Toon, O. B., Stevens, D. E., Heymsfield, A. J., Ramanathan, V., and Welton, E. J. (2000). Reduction of tropical cloudiness by soot. *Science* 288, 1042–1047. doi: 10.1126/science.288.5468.1042

Bond, T. C., Doherty, S. J., Fahey, D. W., Forster, P. M., Berntsen, T., DeAngelo, B. J., et al. (2013). Bounding the role of black carbon in the climate system: a scientific assessment. *J. Geophys. Res.* 118, 1–173. doi: 10.1002/jgrd.50171

Brandt, R. E., Warren, S. G., and Clarke, A. D. (2011). A controlled snowmaking experiment testing the relation between black carbon content and reduction of snow albedo. *J. Geophys. Res.* 116:D08109. doi: 10.1029/2010JD015330

Cess, R. D. (1983). Arctic aerosols: model estimates of interactive influences upon the surface-atmosphere clear-sky radiation budget. *Atmos. Environ.* 17, 2555–2564. doi: 10.1016/0004-6981(83)90083-5

Clarke, A. D. (1982). Integrating sandwich: a new method of measurement of the light absorption coefficient for atmospheric particles. *Appl. Opt.* 21, 3011–3020. doi: 10.1364/AO.21.003011

Clarke, A. D., and Noone, K. J. (1985). Soot in the arctic snowpack: a cause for perturbations in radiative transfer. *Atmos. Environ.* 19, 2045–2053. doi: 10.1016/0004-6981(85)90113-1

Colbeck, S. C. (1982). An overview of seasonal snow metamorphism. *Rev. Geophys. Space Phys.* 20, 45–61. doi: 10.1029/RG020i001p00045

Conway, H., Gades, A., and Raymond, C. F. (1996). Albedo of dirty snow during conditions of melt. *Water Resour. Res.* 32, 1713–1718. doi: 10.1029/96WR00712

Dang, C., Brandt, R. E., and Warren, S. G. (2015). Parameterizations for narrowband and broadband albedo of pure snow, and snow containing mineral dust and black carbon. *J. Geophys. Res.* 120, 5446–5468. doi: 10.1002/2014JD022646

Dang, C., Fu, Q., and Warren, S. G. (2016). Effect of snow grain shape on snow albedo. *J. Atmos. Sci.* 73, 3573–3583. doi: 10.1175/JAS-D-15-0276.1

Dang, C., Warren, S. G., Fu, Q., Doherty, S. J., and Sturm, M. (2017). Measurements of light-absorbing particles in snow across the Arctic, North America, and China: effects on surface albedo. *J. Geophys. Res.* 122, 10149–10168. doi: 10.1002/2017JD027070

Dirmhirn, I. (1960). Starke absorptionsschichten auf den schneeoberflächen der alpengletscher. *Wetter Leben* 12, 152–153.

Doherty, S. J., Dang, C., Hegg, D. A., Zhang, R., and Warren, S. G. (2014). Black carbon and other light-absorbing particles in snow of central North America. *J. Geophys. Res.* 119, 12807–12831. doi: 10.1002/2014JD022350

Doherty, S. J., Grenfell, T. C., Forsström, S., Hegg, D. L., Brandt, R. E., and Warren, S. G. (2013). Observed vertical redistribution of black carbon and other insoluble light-absorbing particles in melting snow. *J. Geophys. Res.* 118, 5553–5569. doi: 10.1002/jgrd.50235

Doherty, S. J., Warren, S. G., Grenfell, T. C., Clarke, A. D., and Brandt, R. E. (2010). Light-absorbing impurities in Arctic snow. *Atmos. Chem. Phys.* 10, 11647–11680. doi: 10.5194/acp-10-11647-2010

Elgmork, K., Hagen, A., and Langeland, A. (1973). Polluted snow in southern Norway during the winters 1968-1971. *Environ. Pollut.* 4, 41–52. doi: 10.1016/0013-9327(73)90030-X

Forsström, S., Isaksson, E., Skeie, R. B., Ström, J., Pedersen, C. A., Hudson, S. R., et al. (2013). Elemental carbon measurements in European Arctic snow packs. *J. Geophys. Res. Atmos.* 118, 13614–13627. doi: 10.1002/2013JD019886

Gong, S. L., Zhao, T. L., Sharma, S., Toom-Sauntry, D., Lavoue, D., Zhang, X. B., et al. (2010). Identification of trends and inter-annual variability of sulphate and black carbon in the Canadian High Arctic: 1981 to 2007. *J. Geophys. Res.* 115:D07305. doi: 10.1029/2009JD012943

Gray, W. M., Frank, W. M., Corrin, M. L., and Stokes, C. A. (1976). Weather modification by carbon dust absorption of solar energy. *J. Appl. Meteor.* 15, 355–386. doi: 10.1175/1520-0450(1976)015<0355:WMBCDA>2.0.CO;2

Grenfell, T. C., Doherty, S. J., Clarke, A. D., and Warren, S. G. (2011). Light absorption from particulate impurities in snow and ice determined by spectrophotometric analysis of filters. *Appl. Opt.* 50, 2037–2048. doi: 10.1364/AO.50.002037

Grenfell, T. C., Light, B., and Sturm M. (2002). Spatial distribution and radiative effects of soot in the snow and sea ice during the SHEBA experiment. *J. Geophys. Res.* SHE 7-1–SHE 7-7. doi: 10.1029/2000JC000414

Grenfell, T. C., and Maykut, G. A. (1977). The optical properties of ice and snow in the Arctic basin. *J. Glaciol.* 18, 445–463. doi: 10.1017/S0022143000021122

Grenfell, T. C., Neshyba, S. P., and Warren, S. G. (2005). Representation of a nonspherical ice particle by a collection of independent spheres for scattering and absorption of radiation: 3, hollow columns and plates. *J. Geophys. Res. (Atmospheres)* 110:D17203. doi: 10.1029/2005JD005811

Grenfell, T. C., and Warren, S. G. (1999). Representation of a nonspherical ice particle by a collection of independent spheres for scattering and absorption of radiation. *J. Geophys. Res.* 104, 31697–31709. doi: 10.1029/1999JD900496

Grenfell, T. C., Warren, S. G., and Mullen, P. C. (1994). Reflection of solar radiation by the Antarctic snow surface at ultraviolet, visible, and near-infrared wavelengths. *J. Geophys. Res.* 99, 18669–18684. doi: 10.1029/94JD01484

Haeberli, W. (1977). Sahara dust in the Alps – A short review. *Z. Gletscher. Glazialgeol.* 13, 206–208.

Hansen, J., and Nazarenko, L. (2004). Soot climate forcing via snow and ice albedos. *Proc. Natl. Acad. Sci. U.S.A.* 101, 423–428. doi: 10.1073/pnas.2237157100

Hegg, D. A., Clarke, A. D., Doherty, S. J., and Ström, J. (2011). Measurements of black carbon aerosol washout ratio on Svalbard. *Tellus B* 63, 891–900. doi: 10.1111/j.1600-0889.2011.00577.x

Hegg, D. A., Warren, S. G., Grenfell, T. C., Doherty, S. J., and Clarke, A. D. (2010). Sources of light-absorbing aerosol in Arctic snow and their seasonal variation. *Atmos. Chem. Phys.* 10, 10923–10938. doi: 10.5194/acp-10-10923-2010

Hegg, D. A., Warren, S. G., Grenfell, T. C., Doherty, S. J., Larson, T. V., and Clarke, A. D. (2009). Source attribution of black carbon in arctic snow. *Environ. Sci. Technol.* 43, 4016–4021. doi: 10.1021/es803623f

Huang, J., Fu, Q., Zhang, W., Wang, X., Zhang, R., Ye, H., et al. (2011). Dust and black carbon in seasonal snow across northern China. *Bull. Am. Meteor. Soc.* 92, 175–181. doi: 10.1175/2010BAMS3064.1

Kellogg, W. W. (1975). "Climatic feedback mechanisms involving the polar regions," in *Climate of the Arctic*, eds G. Weller and S. A. Bowling (Fairbanks, AK: University of Alaska, Geophysical Institute), 111–116.

Khromov, S. (1931). Zhyoltyy sneg (Yellow snow). *Mirovedenie* 20, 106–107.

LaChapelle, E. R. (1969). *Field Guide to Snow Crystals*. Seattle, WA: University of Washington Press, 101.

Meiman, J. (1973). "Snow surface modification," in *The Role of Snow and Ice in Hydrology*, ed. I. C. Brown (London: International Association of Hydrological Sciences Publ. No. 107), 1376–1381.

Neshyba, S. P., Grenfell, T. C., and Warren, S. G. (2003). Representation of a nonspherical ice particle by a collection of independent spheres for scattering and absorption of radiation: II. Hexagonal columns and plates. *J. Geophys. Res.* 108:4448. doi: 10.1029/2002JD003302

Noone, K. J., and Clarke, A. D. (1988). Soot scavenging measurements in Arctic snowfall. *Atmos. Environ.* 22, 2773–2778. doi: 10.1016/0004-6981(88)90444-1

O'Brien, H. W., and Munis, R. H. (1975). Red and near-infrared spectral reflectance of snow. *CRREL Res. Rep.* 332:18.

Painter, T. H., Barrett, A. P., Landry, C. C., Neff, J. C., Cassidy, M. P., Lawrence, C. R., et al. (2007). Impact of disturbed desert soils on duration of mountain snow cover. *Geophys. Res. Lett.* 34:L12502. doi: 10.1029/2007GL030284

Painter, T. H., Bryant, A. C., and Skiles, S. M. (2012). Radiative forcing by light absorbing impurities in snow from MODIS surface reflectance data. *Geophys. Res. Lett.* 39:L17502. doi: 10.1029/2012GL052457

Painter, T. H., Flanner, M., Marzeion, B., Kaser, G., VanCuren, R., and Abdalati, W. (2013). End of the little ice age in the alps forced by black carbon. *Proc. Nat. Acad. Sci. U.S.A.* 110, 15216–15221. doi: 10.1073/pnas.1302570110

Patterson, E. M., and Gillette, D. A. (1977). Commonalities in measured size distributions for aerosols having a soil-derived component. *J. Geophys. Res.* 82, 2074–2082. doi: 10.1029/JC082i015p02074

Patterson, E. M., Gillette, D. A., and Stockton, B. H. (1977). Complex index of refraction between 300 and 700 nm for Saharan aerosols. *J. Geophys. Res.* 82, 3153–3160. doi: 10.1029/JC082i021p03153

Rahn, K. A., and McCaffrey, R. J. (1980). On the origin and transport of the winter Arctic aerosol. *Ann. N. Y. Acad. Sci.* 338, 486–503. doi: 10.1111/j.1749-6632.1980.tb17142.x

Schwarz, J. P., Doherty, S. J., Li, F., Ruggiero, S. T., Tanner, C. E., Perring, A. E., et al. (2012). Assessing single particle soot photometer and integrating sphere/integrating sandwich spectrophotometer measurement techniques for quantifying black carbon concentration in snow. *Atmos. Meas. Tech.* 5, 2581–2592. doi: 10.5194/amt-5-2581-2012

Sharma, S., Lavoué, D., Cachier, H., Barrie, L. A., and Gong, S. L. (2004). Long-term trends of the black carbon concentrations in the Canadian Arctic. *J. Geophys. Res.* 109:D15203. doi: 10.1029/2003JD004331

Stubbs, G., Warren, S., and Holmes, K. (1977). Structure of RNA and RNA binding site in tobacco mosaic virus from a 4-A map calculated from X-ray fibre diagrams. *Nature* 267, 216–221. doi: 10.1038/267216a0

Thomas, G. E., and Stamnes K. (1999). *Radiative Transfer in the Atmosphere and Oceans*. Cambridge: Cambridge Univ. Press, 517. doi: 10.1017/CBO9780511613470

Thompson, L. G. (1977). "Variations in microparticle concentration, size distribution and elemental composition found in camp century, greenland, and byrd station, antarctica, deep ice cores," in *Isotopes and Impurities in Snow and Ice*, Vol. 118, ed. H. Oeschger (London: International Association of Hydrological Sciences), 351–364.

Torres, A., Bond, T. C., Lehmann, C. M. B., Subramanian, R., and Hadley, O. L. (2014). Measuring organic carbon and black carbon in rainwater: evaluation of methods. *Aerosol. Sci. Tech.* 48, 239–250. doi: 10.1080/02786826.2013.868596

Twohy, C. H., Clarke, A. D., Warren, S. G., Radke, L. F., and Charlson, R. J. (1989). Light-absorbing material extracted from cloud droplets and its effect on cloud albedo. *J. Geophys. Res.* 94, 8623–8631. doi: 10.1029/JD094iD06p08623

Wang, X., Doherty, S. J., and Huang, J. (2013). Black carbon and other light-absorbing impurities in snow across Northern China. *J. Geophys. Res. Atmos.* 118, 1471–1492. doi: 10.1029/2012JD018291

Warren, S. G. (1982). Optical properties of snow. *Rev. Geophys. Space Phys.* 20, 67–89. doi: 10.1029/RG020i001p00067

Warren, S. G. (1984a). Impurities in snow: effects on albedo and snowmelt. *Ann. Glaciol.* 5, 177–179. doi: 10.1017/S0260305500003700

Warren, S. G. (1984b). Optical constants of ice from the ultraviolet to the microwave. *Appl. Opt.* 23, 1206–1225. doi: 10.1364/AO.23.001206

Warren, S. G. (2013). Can black carbon in snow be detected by remote sensing? *J. Geophys. Res.* 118, 779–786. doi: 10.1029/2012JD018476

Warren, S. G., and Brandt, R. E. (2008). Optical constants of ice from the ultraviolet to the microwave: a revised compilation. *J. Geophys. Res.* 113:D14220. doi: 10.1029/2007JD009744

Warren, S. G., Brandt, R. E., and Grenfell, T. C. (2006). Visible and near-ultraviolet absorption spectrum of ice from transmission of solar radiation into snow. *Appl. Opt.* 45, 5320–5334. doi: 10.1364/AO.45.005320

Warren, S. G., and Clarke, A. D. (1986). "Soot from Arctic haze: radiative effects on the Arctic snowpack," in *Proceedings of the Snow Watch Workshop 1985: Glaciological Data*, Vol. 18 (Boulder, CO: NSIDC, University of Colorado Boulder), 73–77.

Warren, S. G., and Clarke, A. D. (1990). Soot in the atmosphere and snow surface of Antarctica. *J. Geophys. Res.* 95, 1811–1816. doi: 10.1029/JD095iD02p01811

Warren, S. G., Edwards, B. F. P., Evans, D. R., Wiley, D. C., and Lipscomb, W. N. (1973). Aspartate transcarbamylase from *Escherichia coli*: electron density at 5.5 A resolution. *Proc. Nat. Acad. Sci. U.S.A.* 70, 1117–1121. doi: 10.1073/pnas.70.4.1117

Warren, S. G., Grenfell, T. C., and Mullen, P. C. (1986). Optical properties of antarctic snow. *Antarct. J. U.S.* 21, 247–248.

Warren, S. G., and Schneider, S. H. (1979). Seasonal simulation as a test for uncertainties in the parameterizations of a Budyko-Sellers zonal climate model. *J. Atmos. Sci.* 36, 1377–1391. doi: 10.1175/1520-0469(1979)036<1377:SSAATF>2.0.CO;2

Warren, S. G., and Wiscombe, W. J. (1980). A model for the spectral albedo of snow. II: Snow containing atmospheric aerosols. *J. Atmos. Sci.* 37, 2734–2745. doi: 10.1175/1520-0469(1980)037<2734:AMFTSA>2.0.CO;2

Warren, S. G., Wiscombe, W. J., and Firestone, J. F. (1990). Spectral albedo and emissivity of CO2-snow in martian polar caps: model results. *J. Geophys. Res.* 95, 14717–14741. doi: 10.1029/JB095iB09p14717

Willeit, M., and Ganopolski, A. (2018). The importance of snow albedo for ice sheet evolution over the last glacial cycle. *Clim. Past* 14, 697–707. doi: 10.5194/cp-14-697-2018

Wiscombe, W. J. (1980). Improved mie scattering algorithms. *Appl. Opt.* 19, 1505–1509. doi: 10.1364/AO.19.001505

Wiscombe, W. J., and Warren, S. G. (1980). A model for the spectral albedo of snow, I: pure snow. *J. Atmos. Sci.* 37, 2712–2733. doi: 10.1175/1520-0469(1980)037<2712:AMFTSA>2.0.CO;2

Wittmann, M., Zwaaftink, C. D. G., Schmidt, L. S., Guðmundsson, S., Pálsson, F., Arnalds, O. et al. (2017). Impact of dust deposition on the albedo of Vatnajökull ice cap, Iceland. *Cryosphere* 11, 741–754. doi: 10.5194/tc-11-741-2017

Ye, H., Zhang, R., Shi, J., Huang, J., Warren, S. G., and Fu, Q. (2012). Black carbon in seasonal snow across northern Xinjiang in northwestern China. *Environ. Res. Lett.* 7, 1–9. doi: 10.1088/1748-9326/7/4/044002

Zatko, M. C., and Warren, S. G. (2015). East Antarctic sea ice in spring: spectral albedo of snow, nilas, frost flowers, and slush; and light-absorbing impurities in snow. *Ann. Glaciol.* 56, 53–64. doi: 10.3189/2015AoG69A574

Conflict of Interest Statement: The author declares that the research was conducted in the absence of any commercial or financial relationships that could be construed as a potential conflict of interest.

frontiers in Earth Science

ORIGINAL RESEARCH
published: 02 April 2019
doi: 10.3389/feart.2019.00049

Local Emissions and Regional Wildfires Influence Refractory Black Carbon Observations Near Palmer Station, Antarctica

Alia L. Khan[1,2], Andrew G. Klein[3], Joseph M. Katich[4,5] and Peng Xian[6]*

[1] Department of Environmental Sciences, Western Washington University, Bellingham, WA, United States, [2] National Snow and Ice Data Center, Cooperative Institute for Research in Environmental Sciences, University of Colorado Boulder, Boulder, CO, United States, [3] Department of Geography, Texas A&M University, College Station, TX, United States, [4] Chemical Sciences Division, NOAA Earth System Research Laboratory (ESRL), Boulder, CO, United States, [5] Cooperative Institute for Research in Environmental Sciences (CIRES), University of Colorado Boulder, Boulder, CO, United States, [6] Atmospheric Properties and Effects Section, Marine Meteorology Division, United States Naval Research Laboratory, Monterey, CA, United States

Antarctica is often regarded as the most pristine continent on Earth. However, local human activity can be significant point sources of production of contaminants, as well as light absorbing aerosols, such as black carbon (BC). In May 2015, over the Austral fall season (at the beginning of the accumulation season), surface snow was sampled at eight sites along a 1.7 km transect extending from Palmer Station, Antarctica. Two additional sites were sampled on Biscoe Point 14 km from the station. Snow samples were analyzed for refractory black carbon (rBC) with a Single Particle Soot Photometer (SP2). rBC concentrations increased with proximity to the Palmer Station 1.2–16.5 μg-rBC/L-H_2O (4.7 ± 4.9 μg-rBC/L-H_2O) and were higher than other studies of rBC in snow, such as in the McMurdo Dry Valleys, Antarctica (MDV) and the Clean Air Sector of the South Pole Station (CAS-SP), except on the more remote Biscoe Island, 0.4–1.2 μg-rBC/L-H_2O, which had similar background concentrations to the MDV and CAS-SP, 0.3–1.2 (0.6 ± 0.3 μg-rBC/L-H_2O) and (0.14–0.80 μg-rBC/L-H_2O), respectively. However, concentrations were lower than previous observations at South Pole Station downwind of the generator and long the runway (6.6–7000 μg-rBC/L-H_2O). Palmer Station is located on the southwestern coast of Anvers Island which lies off the western coast of the Antarctic Peninsula at 64° 46′S, 64° 03′W. Comparison with the Navy Aerosol Analysis Prediction System (NAAPS) model show that wildfire smoke may have reached this region of the Antarctic continent during the time period of the deposition of this seasonal snow, suggesting the increase in rBC may be a combination of local combustion of fossil fuels and regional wildfires. Although significant increases in rBC concentrations are found within a km of Palmer Station, like the South Pole Station, rBC is limited to a few kms from the station. Additionally, these measurements of rBC, which may be the only BC measurements in snow on the Antarctic Peninsula, show that background levels are similar to other locations on the continent.

Keywords: black carbon, snow, Antarctica, local impact, wildfires and biomass burning, fossil fuel emissions

OPEN ACCESS

Edited by:
Outi Meinander, Finnish Meteorological Institute, Finland

Reviewed by:
Henrique De Melo Jorge Barbosa, University of São Paulo, Brazil
Paulina Wong, Lingnan University, China

****Correspondence:***
Alia L. Khan
alia.khan@wwu.edu

Specialty section:
This article was submitted to Atmospheric Science, a section of the journal Frontiers in Earth Science

Received: *31 August 2018*
Accepted: *28 February 2019*
Published: *02 April 2019*

Citation:
Khan AL, Klein AG, Katich JM and Xian P (2019) Local Emissions and Regional Wildfires Influence Refractory Black Carbon Observations Near Palmer Station, Antarctica. Front. Earth Sci. 7:49. doi: 10.3389/feart.2019.00049

INTRODUCTION

Palmer Station is the smallest of the three permanent scientific research stations operated by the United States Antarctic Program (USAP). It is located on the southwestern coast of Anvers Island which lies off the western coast of the Antarctic Peninsula at 64° 46′S, 64° 03′W (**Figure 1**). The current station, which was commissioned on 20 March 1968 supports U.S. scientific research in the Antarctic Peninsula Region. It replaced "Old Palmer Station" which was established in 1965 on Amsler Island adjacent to the British Antarctic Survey's Base N, which was built in 1955 and abandoned in 1958. Palmer Station currently comprises two major and three smaller buildings, a boat dock and pier. Its maximum capacity is 44 individuals in the summer and approximately 20 people in winter. The R/V Laurence M. Gould regularly services the station. It is located within and supports research for the Palmer Long Term Ecological Research (LTER) site, which was established in the Fall of 1990.

Black carbon (BC) is a light-absorbing aerosol generated from the incomplete combustion of biomass burning and fossil fuels (Goldberg, 1985). BC influences atmospheric radiation and air quality (Bond et al., 2013) and the deposition of BC on snow/ice reduces the surface albedo (Warren and Wiscombe, 1980) and can lead to earlier and more rapid snow/ice melt (Xu et al., 2009). Previous studies have confirmed the presence of BC in snow and ice on the Antarctic continent (Warren and Wiscombe, 1980; Bisiaux et al., 2011, 2012; Bauer et al., 2013; Khan et al., 2016, 2017, 2018; Casey et al., 2017). The primary sources of BC to the southern hemisphere has been identified as biomass burning in Australia, South America, and Africa (Crutzen and Andreae, 1990). Variations in seasonal and decadal long-range BC transport to Antarctica have been observed to be due to changes in climate and the resulting influence on biomass burning in the Southern Hemisphere. Ice cores from Law Dome and the West Antarctic Ice Sheet (WAIS) showed significant annual to decadal variability (Bisiaux et al., 2012) where rBC transport to Antarctica was affected by ENSO climate patterns due to changes in biomass burning as a result of arid conditions.

Despite the perception that the Antarctic environment is pristine, it is subjected to diverse anthropogenic impacts on local to regional scales and these impacts are of concern (e.g., Tin et al., 2009). Over the past 25 years, the chemical signature of BC in the surface waters of McMurdo Dry Valley (MDV) lakes has shifted toward modern anthropogenic sources of BC (Khan et al., 2016), whereas a BC chemical signature of ancient biomass burning has been preserved in the lake bottom waters. The recent shift may be due to local combustion of fossil fuels from combustion toilets, diesel generators, all-terrain vehicles, and helicopters, which contribute 3.4×10^5 g aerosol elemental carbon annually in the MDV (Lyons et al., 2000). Additionally, previous studies on the Antarctic continent have found the South Pole Station creates enough local pollution to reduce the surface albedo of snow downwind of the station (Warren and Wiscombe, 1980; Warren and Clarke, 1990) and along the runway, leading to refractory black carbon (rBC) concentrations of (6.6–7000 μg-rBC/L-H_2O) (Casey et al., 2017). rBC is defined

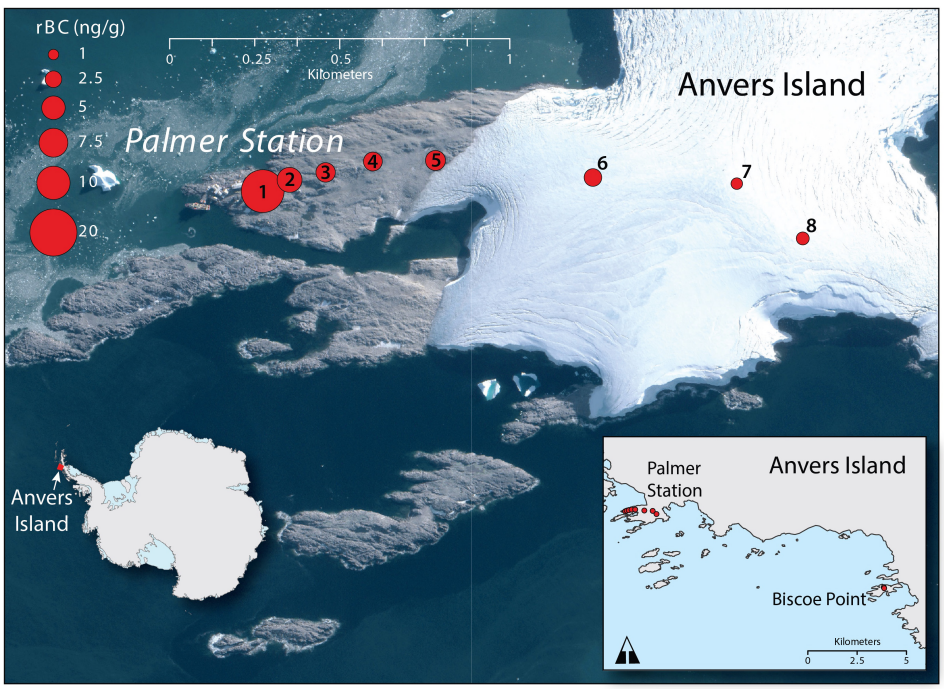

FIGURE 1 | Surface snow-sampling locations. On the main map the size of the symbol is proportional to the concentration of rBC. The background image is a WorldView2 satellite image from March 24, 2013 courtesy of the Polar Geospatial Center, University of Minnesota.

TABLE 1 | rBC concentrations in snow collected along a transect away from Palmer Station.

Site	Date of collection	Latitude	Longitude	Elevation (m)	Distance from station center (m)	rBC (μg-rBC/L-H_2O)
1	5-5-15	−64.774308	−64.051365	14	101	16.5
2	5-5-15	−64.774024	−64.049693	10	182	5.6
3	5-5-15	−64.773842	−64.047456	20	280	3.4
4	5-5-15	−64.773575	−64.044523	23	431	3.2
5	5-5-15	−64.773576	−64.040653	19	614	3.6
6	5-5-15	−64.774092	−64.030936	92	1072	2.8
7	5-5-15	−64.774315	−64.022048	121	1495	1.2
8	5-5-15	−64.775788	−64.018024	101	1695	1.5
9	5-1-15	−64.810521	−63.776677	10	13760	0.4
10	5-1-15	−64.810972	−63.776185	15	13800	1.2

rBC concentrations are the average of three sample duplicates.

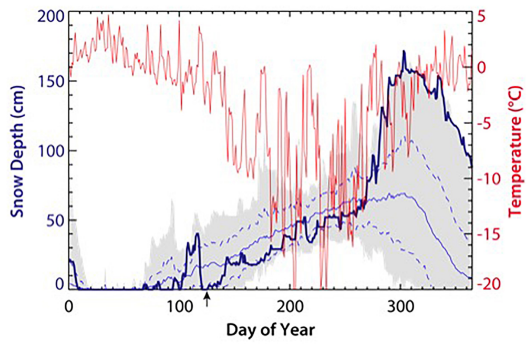

FIGURE 2 | Snow depths and temperature at Palmer Station for 2015. Daily snow depths (cm) during 2015 are shown as the thick blue line while the thin red line indicates corresponding average daily temperatures. The minimum and maximum daily snow depths recorded during the period of record (1991–2015) are indicated by the gray envelope. The light solid blue line indicates the average snow depth for each day while the dotted blue lines are +/– 1 standard deviation from the mean. The arrow pointing to day 125 indicates May 5th the major sampling day.

as BC detected via laser-induced incandescence via Single Particle Soot Photometer (SP2) (Petzold et al., 2013).

Environmental protection of Antarctica is internationally recognized and documented in the Antarctic Treaty (Watts, 1992). The Treaty and its annexes set forth national responsibilities to protect the environment. Individual treaty nations then enact national legislation, which regulates each country's nationals while in Antarctica. The Treaty's environmental protection practices were clarified and enhanced by the Protocol on Environmental Protection (often referred to as the Madrid Protocol), which entered into force in 1998 (Stokke and Vidas, 1998). The Protocol recognized that effective management of human impact on the continent required the monitoring of human activities. The snow samples in this study collected were collected as part of a program to design a long-term environmental monitoring program for Palmer Station similar to the program implemented for USAP's much larger McMurdo Station (Kennicutt et al., 2010; Klein et al., 2014). While the spatial extent of anthropogenic impacts around Antarctic research stations varies by contaminant or type of impact, these impacts are generally limited to a few hundred meters or few kilometers from the station. This study provides an initial estimate of the spatial extent of Palmer Station's BC emissions on the local environment.

MATERIALS AND METHODS

Site Description

As with other USAP facilities, Palmer Station operates on petroleum and station activities produce hydrocarbon emissions. For Fiscal Years 2006–2010, fuel consumption at Palmer Station averaged 104,792 gallons annually. Of this, 80% was consumed by the station's power plant, 19% for heating and hot water and 1% for vehicles (RSA Engineering, 2011). Two 250 kW Caterpillar engine generators (circa 1998) supply power to Palmer Station and heat to the building in which they are located. Oil boilers provide hot water for the other buildings. Machinery and small boats, at the time of this study, primarily inflatable Zodiacs, are also operated on station. A small incinerator is operated sporadically to incinerate poultry waste and a small wood-burning stove operates in one of Palmer's two main buildings. Palmer Station has ∼20% of the population of the South Pole at its maximum.

The Research/Vessel (R/V) Laurence M. Gould (LMG), operated by Lockheed Martin, supports Science and operations at Palmer Station. The LMG is a 230 foot long ice-classed ABS-A1 research and resupply vessel on a long-term charter from Offshore Service Vessels LLC. The LMG has two main engines (Caterpillar 3606) and three generators (Caterpillar 3508). USAP's larger vessel, the Nathaniel B. Palmer, services Palmer Station occasionally and approximately a dozen cruise vessels visit the station each year.

The LMG typically averages 8–9 visits to Palmer Station each year (RSA Engineering, 2011). During the period of snow accumulation in this study, the LMG made three cruises to Palmer Station LMG 15-02 (2/13-3/16), 15-03 (3/20-4/4), and 15-04 (4/7-5/11). Based on analysis of the LMGs navigational data (Aronson, 2015; O'Brien et al., 2015) and cruise history (United States Antarctic Program[USAP], 2018), the LMG spent

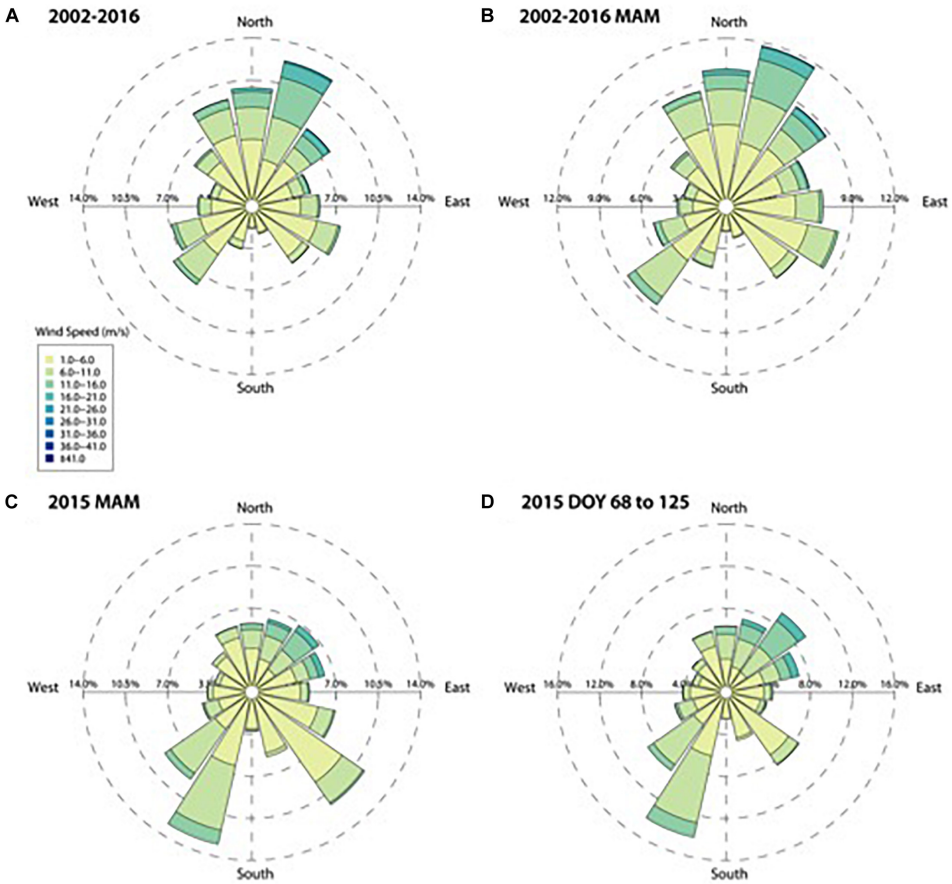

FIGURE 3 | Four wind roses indicating the number of observations from a particular direction and wind speed. The data is from the Palmer Station Automated Weather Station and represent 10-min average wind speeds. **(A)** All observations inclusive from 1/1/2002 to 12/31/2016, **(B)** All March, April, and May (MAM) observations from 1/1/2002 to 12/31/2016, **(C)** All March, April, and May (MAM) observations for 2015 (when samples were collected), and **(D)** Observations from the beginning of snow (March 9) to sample date (May 5th), 2015.

approximately 13 days docked at Palmer Station from the first day of snow accumulation March 9th through sample collection on May 5th.

Snow Measurements

On 5 May 2015, during a period without recent snowfalls, surface snow samples were collected for rBC analysis at eight sites along a 1.7 km transect extending eastward from Palmer Station. These sites were augmented by samples collected from two more remote sites located approximately 14 km from Palmer Station on Biscoe Point (now an island) situated within the Biscoe Point Antarctic Specially Protected Area (ASPA) No. 139 on 1 May 2015. Entry to an ASPA requires special permitting to sample these pristine sites (**Figure 1**).

At each site three replicate sample duplicates were collected. rBC concentrations reported in **Table 1** are the average of the three sample duplicates. Snow was collected in 500 ml glass jars which were pre-cleaned to meet Environmental Protection Agency (EPA) Protocol A Level 1 standards for contaminants. Samples were obtained by placing the opening of the glass jar perpendicular to the horizontal surface of the snowpack and pressing the jar through the snowpack until the snow completely filled the jar. Care was taken so the surface was only sampled once per replicate.

After collection, snow samples were kept frozen at Palmer Station, during their transport to Punta Arenas, Chile and onward to Texas A&M University until they were shipped to the Institute of Arctic and Alpine Research (INSTAAR) in Boulder, CO and then transferred to the Earth System Research Laboratory at the National Oceanic and Atmospheric Administration for rBC analysis. Snow samples were then melted for the first time immediately before analysis. The thirty surface snow samples were analyzed for rBC mass mixing ratios (MMR). Briefly, snow samples were melted, then immediately aerosolized with a carefully calibrated nebulizer and sampled with an SP2 following the approach of Schwarz et al. (2012). The SP2 has excellent sensitivity and selectivity for rBC with minimal interference from non-BC materials and was calibrated with fullerene soot (Alfa Aesar, Woodbridge, MA, United States, Lot F12S011). Here, a CETAC Marin-5 nebulizer interfaced with the SP2, following the same protocol as Katich et al. (2017). The size-dependent nebulization efficiency was characterized

with concentration standards of polystyrene latex spheres (PSLs) in the size range 220–3000 nm diameter, confirming low sensitivity to particle size over this range, consistent with recent results with concentric pneumatic nebulizers (Lim et al., 2014; Wendl et al., 2014; Mori et al., 2016; Katich et al., 2017). Size distributions were measured for samples with higher concentrations, and these indicated no appreciable contribution to rBC mass above 0.7 μm. Hence no size dependent corrections were applied for nebulizer size dependence. Background rBC contamination levels were bounded by measuring blank samples. Deionized water was used to flush the nebulization system between snow samples to reduce line contamination. Further, measurements of rBC concentrations in blank water samples were interspersed amongst snow samples to bound background contamination levels in the system. This averaged 0.43 μg/L over 15 blank water measurements, indicating a low enough background to avoid significant interference with the rBC MMR measurements. The blanks provide an upper bound on possible contaminants associated with the estimated 60% uncertainty for rBC MMR in the snow, which conservatively accounts for uncertainties dominated by calibration issues (Schwarz et al., 2012).

Local Meteorological Observations

Information on local meteorological conditions during the period of early snow accumulation in 2015 was obtained from two sources. Local Daily Summaries provided daily weather observations including snow depth and accumulation measurements recorded by Palmer Station personnel and were obtained from the Antarctic Meteorological Research Center (AMRC) at the University of Wisconsin (Antarctic Meteorological Research Center [AMRC], 2018) 2-min observations from the Palmer Automated Weather System (PALMOS) available from the Palmer Station Antarctica LTER (Long Term Ecological Research Network-Network Data Portal [LTER-NDP], 2017) were used to investigate wind speed and directions during the period of snow accumulation. Analysis of the weather observations was accomplished using the Anaconda Scientific Python Distribution. The wind roses are produced using IDL software (Fanning, 2019). All mapping was accomplished using ArcMap or ArcGIS Pro.

Aerosol Transport Modeling

Smoke aerosol optical depth (AOD) and concentrations from biomass burning comes from the Navy Aerosol Analysis and Prediction System (NAAPS) reanalysis (Lynch et al., 2016), which was developed and validated at the Naval Research Laboratory. The NAAPS model was used to explore regional and long-range biomass burning smoke transport events during the study period. It is a global 1°×1° decade-long 6-hourly aerosol reanalysis product. It utilizes a modified version of the NAAPS as its core and assimilates quality controlled retrievals of AOD from Moderate Resolution Imaging Spectroradiometer (MODIS) on Aqua and Terra, as well as the Multi-angle Imaging Spectroradiometer (MISR) on Terra (Zhang and Reid, 2006; Hyer et al., 2011; Shi et al., 2014). NAAPS characterizes anthropogenic and biogenic fine aerosol (including primary and secondary organic aerosols and sulfate), biomass burning smoke, dust, and marine sea salt aerosols. Biomass burning smoke is derived from near-real time thermal anomaly satellite based data used to construct smoke source functions (Reid et al., 2009), with orbital corrections on MODIS-based regional tunings and emissions. The fine and coarse mode reanalysis AOD at 550 nm is shown to be in agreement with the ground-based global scale sun photometer network Aerosol Robotic Network AOD (Holben et al., 1998).

RESULTS AND DISCUSSION

rBC Concentrations

rBC concentrations in surface snow decrease with increasing distance from Palmer Station (**Figure 1** and **Table 1**). Elevated rBC concentrations were found near the station, 16.5–1.5 μg-rBC/L-H_2O, especially as compared to the low concentrations found on Biscoe Island, 0.4 and 1.2 μg-rBC/L-H_2O. This suggests that the station's influence on rBC extends at least 1 km from

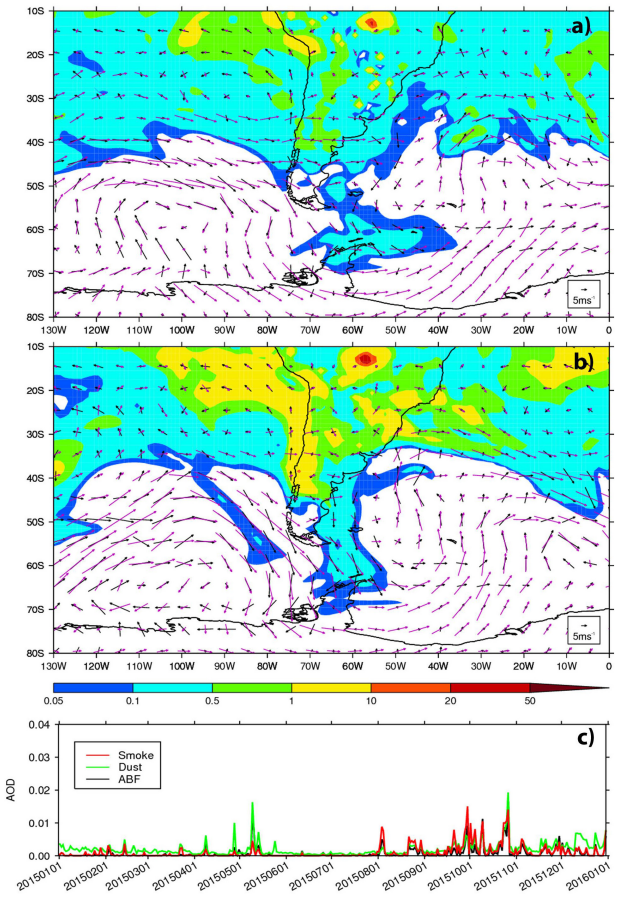

FIGURE 4 | NAAPS surface concentration of biomass burning smoke (μg/m^3), surface (black vector) and 700 hpa wind (magenta vector) at **(a)** 18Z April 9th **(b)** 18Z April 28th 2015. **(c)** Time series of NAAPS aerosol optical depths (AOD) from anthropogenic and biogenic fine (ABF), biomass-burning smoke and dust aerosols for Palmer Station over 2015.

the station. rBC concentrations in this study near Palmer station were higher than other studies of rBC in snow on the Antarctic continent, such as in the MDV, 0.3–1.2 μg-rBC/L-H_2O, except on the more remote Biscoe Island, 0.4 and 1.2 μg-rBC/L-H_2O, which like the MDV, has restrictions to entry, and had similar background concentrations indicative of long-range atmospheric transport. However, concentrations in this study were less than previous findings downwind of the generator and along the runway at the South Pole Station (6.6–7000 μg-rBC/L-H_2O) (Casey et al., 2017). It should be noted that Palmer Station has ∼20% of the population of the South Pole at its maximum. Additionally, samples from the clean air sector at the South Pole (0.14–0.80 μg-rBC/L-H_2O) (Casey et al., 2017) contained similar background concentrations of rBC as found in this study and in the MDV. Although, significant increases in rBC concentrations are found within a km of Palmer Station, like the South Pole Station, rBC is limited to a few kms from station.

During 2015, Palmer Station recorded some of its highest snow depths over the period of record (**Figure 2**). The period preceding snow sampling on May 1st and 5th saw intermittent snow on the ground from March 9 to April 5 after which snow was continuously present at the station. It reached a depth of 40 cm in late April. However, April 28–30 saw air temperatures remaining above freezing and maximum air temperatures exceeding 4° causing snow to disappear at the Palmer snow stake on May 1st. Therefore, the snow sampled on May 1st and 5th represent the snow that remained in patches or on the glacier from the early period of well-above average snow accumulation.

The wind roses illustrated in **Figure 3** show that surface winds during the snow accumulation period of the sampling differ from long-term averages for the entire year and the March to May (MAM) period. The period of snow accumulation captured by the sampling was characterized by a much higher occurrence of SSW surface winds than is typical.

NAAPS Model Results

According to the NAAPS analysis, a small amount of biomass burning smoke was transported southward from South America to Palmer Station on April 9, 2015 (**Figure 4a**) and on April, 28, 29, 2015 (**Figure 4b**). As evidenced by the NAAPS model plots, when there is southward wind blowing from South America, there is possible smoke transport to the Antarctic Peninsula (**Figures 4a,b**). Thus, it is possible that biomass burning smoke was deposited on the sampled snow layer. However, AOD time series of the study site for the whole year of 2015 (**Figure 4c**) show that the amount of smoke transported over the study period is smaller compared to the peak biomass season (September–October) transport. Palmer Station is located in the roaring circumpolar strong westerly wind belt; therefore sea salt is excluded in the time series plot, as it dominates the AOD signal.

SUMMARY AND CONCLUSION

These first observations of black carbon in seasonal snow on the Western Antarctic Peninsula show that rBC concentrations are similar to other pristine regions of the continent, including the MDV and the South Pole. This study provides a preliminary quantification of the Palmer Station "emissions or black carbon footprint" (Brooks et al., 2018). rBC concentrations in surface snow decrease with increasing distance from the Palmer Station. Elevated rBC concentrations near the station appear to show the station's local impact extends at least 1 km, as similarly found downwind of the South Pole station (Warren and Wiscombe, 1980; Casey et al., 2017). NAAPS model results show that smoke from regional wildfires occurring on the South American continent may have transported biomass burning derived rBC to the study site prior to sample collection. However, the AOD smoke signal over the Austral fall, when the samples were collected, is smaller than the peak southern hemisphere wildfire season in the Austral spring. Although the NAAPS AOD signal is smaller over the snow sample collection period than in the Austral spring, the background rBC concentrations found near Palmer Station and on Biscoe Island are likely a mix of locally produced BC and regional transport of smoke from wildfires.

In the future, this dataset can be improved by expansion both temporally and spatially, along Anvers Island, as well as the entire Antarctic Peninsula. Additionally, samples in this study were collected from snow remaining after an abnormally high early-season snowfall, followed by rapid and nearly total snow melt. Collection of samples over the entire snow season and immediately after snowfall would be an improvement, as well as over a larger spatial range. This is one of a small number of studies to look at the spatial footprint of airborne pollution around scientific installations on the continent. It demonstrates that for a station with a population of 44 the spatial footprint is somewhat limited and beyond 1 km the concentrations the pristine snow concentrations of the Western Antarctic Peninsula are similar to other pristine regions of the continent.

DATA AVAILABILITY

All measurement data generated are included in the manuscript, but further questions can be directed to alia.khan@wwu.edu.

AUTHOR CONTRIBUTIONS

AK and AGK conceived of the study. AGK conducted the sampling. AK and JK conducted the refractory black carbon analysis. PX conducted the NAAPS analysis. All authors contributed to the development, data analysis, and writing on the manuscript.

FUNDING

Funding for this work came from DOD-ARMY-COE-Cold Region Research Award W913E5-16-C-0006. The authors appreciate the support of the University of Wisconsin-Madison Antarctic Meteorological Research Center for the data set, data display, and information, NSF grant number ANT-1535632. PX was supported by the Office of Naval Research Code 322.

REFERENCES

Antarctic Meteorological Research Center [AMRC] (2018). *Antarctic Meteorological Research Center at the University of Wisconsin (AMRC-UW)*. Available at: https://amrc.ssec.wisc.edu.

Aronson, R. (2015). *Processed Ship-Based Navigation Data from the Southern Ocean Acquired During the Laurence M. Gould expedition LMG1502 (2015)*. Punta Arenas: Integrated Earth Data Applications (IEDA), doi: 10.1594/IEDA/321907

Bauer, S. E., Bausch, A., Nazarenko, L., Tsigaridis, K., Xu, B., Edwards, R., et al. (2013). Historical and future black carbon deposition on the three ice caps: ice core measurements and model simulations from 1850 to 2100. *J. Geophys. Res. Atmos.* 118, 7948–7961. doi: 10.1002/jgrd.50612

Bisiaux, M. M., Edwards, R., McConnell, J. R., Curran, M. A. J., Van Ommen, T. D., Smith, A. M., et al. (2011). Large scale changes in 20th century black carbon deposition to Antarctica. *Atmos. Chem. Phys.* 11, 27815–27831. doi: 10.5194/acpd-11-27815-2011

Bisiaux, M. M., Edwards, R., McConnell, J. R., Curran, M. A. J., Van Ommen, T. D., Smith, A. M., et al. (2012). Changes in black carbon deposition to Antarctica from two high-resolution ice core records, 1850-2000 AD. *Atmos. Chem. Phys.* 12, 4107–4115. doi: 10.5194/acp-12-4107-2012

Bond, T. C., Doherty, S. J., Fahey, D. W., Forster, P. M., Berntsen, T., DeAngelo, B. J., et al. (2013). Bounding the role of black carbon in the climate system: a scientific assessment. *J. Geophys. Res. Atmos.* 118, 5380–5552. doi: 10.1002/jgrd.50171

Brooks, S. T., Jabour, J., and Bergstrom, D. M. (2018). What is ' footprint ' in Antarctica: proposing a set of definitions. *Antarct. Sci.* 30, 227–235. doi: 10.1017/S0954102018000172

Casey, K. A., Kaspari, S. D., Skiles, S. M., Kreutz, K., and Handley, M. J. (2017). The spectral and chemical measurement of pollutants on snow near South Pole, Antarctica. *J. Geophys. Res. Atmos.* 122, 6592–6610. doi: 10.1002/2016JD026418

Crutzen, P., and Andreae, M. O. (1990). Biomass burning in the tropics: impact on atmospheric chemistry and biogeochemical cycles. *Science* 250, 1669–1678. doi: 10.1126/science.250.4988.1669

Fanning, D. (2019). *Last updated 2015, 03-27. Coyote Graphics Routines for cgwindrose.pro*. Available at: http://www.idlcoyote.com/idldoc/cg/cgwindrose.html

Goldberg, E. D. (1985) *Black Carbon in the Environment: Properties and Distribution*. New York, NY: Wiley.

Holben, B. N., Eck, T. F., Slutsker, I., Tanré, D., Buis, J. P., Setzer, A., et al. (1998). AERONET — a federated instrument network and data archive for aerosol characterization. *Remote Sens. Environ.* 66, 1–16. doi: 10.1016/S0034-4257(98)00031-5

Hyer, E. J., Reid, J. S., and Zhang, J. (2011). An over-land aerosol optical depth data set for data assimilation by filtering, correction, and aggregation of MODIS Collection 5 optical depth retrievals. *Atmos. Meas. Tech.* 4, 379–408. doi: 10.5194/amt-4-379-2011

Katich, J. M., Perring, A. E., and Schwarz, J. P. (2017). Optimized detection of particulates from liquid samples in the aerosol phase: focus on black carbon. *Aerosol Sci. Technol.* 51, 543–553. doi: 10.1080/02786826.2017.1280597

Kennicutt II, M. C., Klein, A., Montagna, P., Sweet, S., Wade, T., Palmer, T., et al. (2010). Temporal and spatial patterns of anthropogenic disturbance at McMurdo Station, Antarctica. *Environ. Res. Lett.* 5:034010. doi: 10.1088/1748-9326/5/3/034010

Khan, A. L., Jaffé, R., Ding, Y., and McKnight, D. M. (2016). Dissolved black carbon in Antarctic lakes: chemical signatures of past and present sources. *Geophys. Res. Lett.* 43, 5750–5757. doi: 10.1002/2016GL068609

Khan, A. L., McMeeking, G. R., Schwarz, J. P., Xian, P., Welch, K. A., Berry Lyons, W., et al. (2018). Near-surface refractory black carbon observations in the atmosphere and snow in the mcmurdo dry valleys, antarctica, and potential impacts of foehn winds. *J. Geophys. Res. Atmos.* 123, 2877–2887. doi: 10.1002/2017JD027696

Khan, A. L., Wagner, S., Jaffe, R., Xian, P., Williams, M., Armstrong, R., et al. (2017). Dissolved black carbon in the global cryosphere: concentrations and chemical signatures. *Geophys. Res. Lett.* 44, 6226–6234. doi: 10.1002/2017GL073485

Klein, A. G., Sweet, S. T., Kennicutt II, M. C., Wade, T. L., Palmer, T. A., and Montagna, P. (2014). "Long-term monitoring of human impacts to the terrestrial environment at McMurdo Station," in *Antarctic Futures,* eds T. Tin, D. Liggett, P. Maher, and M. Lamers (Dordrecht: Springer), 213–227.

Lim, S., Faïn, X., Zanatta, M., Cozic, J., Jaffrezo, J. L., Ginot, P., et al. (2014). Refractory black carbon mass concentrations in snow and ice: method evaluation and inter-comparison with elemental carbon measurement. *Atmos. Meas. Tech.* 7, 3549–3589. doi: 10.5194/amtd-7-3549-2014

Long Term Ecological Research Network-Network Data Portal [LTER-NDP] (2017). *Published 2017-04-17. 2-minute PALMOS Automatic Weather Station Meteorological Measurements (precipitation, radiation, cloud base, temperature, etc.) From Palmer Station Antarctica, 2001 - March 2017*. Available at: https://portal.lternet.edu/nis/mapbrowse?packageid = knb-lter-pal.214.3.

Lynch, P., Reid, J. S., Westphal, D. L., Zhang, J., Hogan, T. F., Hyer, E. J., et al. (2016). An 11-year global gridded aerosol optical thickness reanalysis (v1.0) for atmospheric and climate sciences. *Geosci. Model Dev.* 9, 1489–1522. doi: 10.5194/gmd-9-1489-2016

Lyons, W. B., Nezat, C. A., Welch, K. A., Kottmeier, S. T., and Doran, P. T. (2000). Fossil fuel burning in taylor valley, southern victoria land, antarctica: estimating the role of scientific activities on carbon and nitrogen reservoirs and fluxes. *Environ. Sci. Technol.* 34, 1659–1662. doi: 10.1021/es990794l

Mori, T., Moteki, N., Ohata, S., Koike, M., Goto-Azuma, K., Miyazaki, Y., et al. (2016). Improved technique for measuring the size distribution of black carbon particles in liquid water. *Aerosol Sci. Technol.* 50, 242–254. doi: 10.1080/02786826.2016.1147644

O'Brien, K. (2015). Processed ship-based Navigation Data from the Antarctic Peninsula acquired during the Laurence M. Gould expedition LMG1504 (2015). *Interdiscip. Earth Data Appl.* doi: 10.1594/IEDA/321941

Petzold, A., Ogren, J. A., Fiebig, M., Laj, P., Li, S.-M., Baltens-perger, U., et al. (2013). Recommendations for reporting "Black Carbon" measurements. *Atmos. Chem. Phys.* 13, 8365–8379. doi: 10.5194/acp-13-8365-2013

Reid, J. S., Hyer, E. J., Winkler Prins, E. A., Westphal, D. L., Zhang, J., Christopher, S. F., et al. (2009). Global monitoring and forecasting of biomass-burning smoke: description of and lessons from the fire locating and modeling of burning emissions (FLAMBE) program. *IEEE J. Sel. Top. Appl. Earth Obs. Rem. Sens.* 2, 144–162. doi: 10.1109/JSTARS.2009.2027443

RSA Engineering (2011). *Palmer Station Major Systems Studies*. Anchorage, AK: Prepared for National Science Foundation by RSA Engineering Inc., 53. Available at: https://www.usap.gov/USAPgov/conferencesCommitteesAndWorkshops/userCommittees/documents/Palmer%20Major%20Systems%20Study122910.pdf

Schwarz, J. P., Doherty, S. J., Li, F., Ruggiero, S. T., Tanner, C. E., Perring, A. E., et al. (2012). Assessing recent measurement techniques for quantifying black carbon concentration in snow. *Atmos. Meas. Tech.* 5, 3771–3795. doi: 10.5194/amtd-5-3771-2012

Shi, Y., Zhang, J., Reid, J. S., Liu, B., and Hyer, E. J. (2014). Critical evaluation of cloud contamination in the MISR aerosol products using MODIS cloud mask products. *Atmos. Meas. Tech.* 7, 1791–1801. doi: 10.5194/amt-7-1791-2014

Stokke, O. S., and Vidas, D. (eds). (1998). *Governing the Antarctic: The Effectiveness and Legitimacy of the Antarctic Treaty System.* Cambridge: Cambridge University Press.

Tin, T., Fleming, Z. L., Hughes, K. A., Ainley, D. G., Convey, P., Moreno, C. A., et al. (2009). Impacts of local human activities on the Antarctic environment. *Antarct. Sci.* 21, 3–33. doi: 10.1017/S0954102009001722

United States Antarctic Program[USAP] (2018). *Last update 2018, December 18. RV LAURENCE M. GOULD Cruise History*. Available at: https://www.usap.gov/USAPgov/vesselScienceAndOperations/documents/lmg_history.pdf

Warren, S. G., and Clarke, A. D. (1990). Soot in the atmosphere and snow surface of Antarctica. *J. Geophys. Res.* 95, 1811–1816. doi: 10.1029/JD095iD02p01811

Warren, S. G., and Wiscombe, W. J. (1980). A model for the spectral albedo of snow. II: snow containing atmospheric aerosols. *J. Atmos. Sci.* 37, 2734–2745. doi: 10.1175/1520-0469(1980)037<2734:AMFTSA>2.0.CO;2

Watts, A. (1992). *International Law and the Antarctic Treaty System*. Cambridge: Sir Arthur Watts Grotius Publications Ltd, 480.

Wendl, I. A., Menking, J. A., Färber, R., Gysel, M., Kaspari, S. D., Laborde, M. J. G., et al. (2014). Optimized method for black carbon analysis in ice and snow using the single particle soot photometer. *Atmos. Meas. Tech.* 7, 3075–3111. doi: 10.5194/amtd-7-3075-2014

Xu, B., Cao, J., Hansen, J., Yao, T., Joswia, D. R., Wang, N., et al. (2009). Black soot and the survival of Tibetan glaciers. *Proc. Natl. Acad. Sci. U.S.A.* 106, 22114–22118. doi: 10.1073/pnas.0910444106

Zhang, J., and Reid, J. S. (2006). MODIS aerosol product analysis for data assimilation: assessment of over-ocean level 2 aerosol optical thickness retrievals. *J. Geophys. Res. Atmos.* 111, 1–17. doi: 10.1029/2005JD006898

Conflict of Interest Statement: The authors declare that the research was conducted in the absence of any commercial or financial relationships that could be construed as a potential conflict of interest.

frontiers in Earth Science

ORIGINAL RESEARCH
published: 03 July 2019
doi: 10.3389/feart.2019.00142

Can Volcanic Dust Suspended From Surface Soil and Deserts of Iceland Be Transferred to Central Balkan Similarly to African Dust (Sahara)?

Dragana Đorđević[1], Ivana Tošić[2], Sanja Sakan[1], Srđan Petrović[1], Jelena Đuričić-Milanković[3], David C. Finger[4,5] and Pavla Dagsson-Waldhauserová[6,7]*

[1] Institute for Chemistry, Technology and Metallurgy, Centre of Excellence in Environmental Chemistry and Engineering, University of Belgrade, Belgrade, Serbia, [2] Department of Meteorology, Faculty of Physics, University of Belgrade, Belgrade, Serbia, [3] Higher Medical and Business-Technological School of Applied Studies, Šabac, Serbia, [4] School of Science and Engineering, Reykjavik University, Reykjavik, Iceland, [5] Sustainability Institute and Forum (SIF), Reykjavik University, Reykjavik, Iceland, [6] Agricultural University of Iceland, Hvanneyri, Iceland, [7] Faculty of Environmental Sciences, Czech University of Life Sciences Prague, Prague, Czechia

OPEN ACCESS

Edited by:
Irina Alexandrovna Mironova, Saint Petersburg State University, Russia

Reviewed by:
Stefano Federico, Italian National Research Council (CNR), Italy
György Varga, Hungarian Academy of Sciences (MTA), Hungary

***Correspondence:**
Dragana Đorđević
dragadj@chem.bg.ac.rs

Specialty section:
This article was submitted to Atmospheric Science, a section of the journal Frontiers in Earth Science

Received: *30 July 2018*
Accepted: *16 May 2019*
Published: *03 July 2019*

Citation:
Đorđević D, Tošić I, Sakan S, Petrović S, Đuričić-Milanković J, Finger DC and Dagsson-Waldhauserová P (2019) Can Volcanic Dust Suspended From Surface Soil and Deserts of Iceland Be Transferred to Central Balkan Similarly to African Dust (Sahara)? Front. Earth Sci. 7:142. doi: 10.3389/feart.2019.00142

In this work we use chemical fingerprints as characteristics ratios of specific crustal elements Ca/Al, Fe/Al, K/Al, Mg/Al, Mn/Al, Ca/Fe, and Mg/Fe to investigate the long-range transport of volcanic aerosols from Iceland. Volcanic dust enters the atmosphere during suspension processes from Icelandic deserts, but mainly from the dust hot spots in remote areas in Iceland, and it is transmitted to the central Balkan area (Belgrade). For this purpose, backward trajectories from Belgrade ($\varphi = 44°48'$; $\lambda = 20°28'$) in 2012 and 2013, simultaneous with atmospheric aerosols measurements, were calculated by using the Hybrid Single-Particle Lagrangian Integrated Trajectory (HYSPLIT) model. We found that about 17% of air masses passed over Icelandic territory and arrived to Balkan area. In almost all of these episodes ratios of some investigated elements in suburban aerosols of Balkan area corresponded to the ratios of elements investigated in surface soil of the Rangárvellir area – South Iceland in the vicinity of volcanoes. We identified several episodes, such as August 6–8, 2012; June 2–6, 2013; June 26–28, 2013; and September 18–20, 2013; with the characteristic ratios of the highest number of investigated elements in atmospheric aerosol of central Balkan corresponding to ratios from Icelandic soil material. This study provides evidence that Icelandic dust can travel long distances showing the importance of High Latitude Dust sources.

Keywords: High Latitude Dust sources, backward trajectories, chemical fingerprints, atmospheric aerosol, long-range transport

INTRODUCTION

Charles Darwin described the phenomenon he noticed on the sailboat Beagle that the deck and all the equipment were covered with fine dust in the nineteenth century. Also, the sea was covered with a thin layer of dust as long as the sight was visible. This happened when it sailed to the Atlantic coast of West Africa in its famous expedition (Darwin, 1845). Today it is a well-known

phenomenon of long-range transport of dust and numerous side effects that have a great impact on the environment. Airborne particles, depending on their aerodynamic radius, can be transported from several hundred to even ten of thousand kilometers (Prospero, 1999; Husar, 2004). This mineral dust mostly comes from natural sources while the anthropogenic effect is far smaller (Mahowald et al., 2004; Tegen et al., 2004a,b). In recent years, increasing attention has been paid to this phenomenon because it has been shown that airborne particles contributing to dust have a major impact on atmospheric and meteorological phenomena through the absorption and scattering of solar radiation, and representing nucleation centers leading to the formation of clouds, rain and ice (Sokolik and Toon, 1999; Arimoto, 2001), while presenting chemical reaction centers for gaseous compounds by changing the mechanisms of chemical reactions in the atmosphere (Andreae and Rosenfeld, 2008). There is also a need to mention the significant degradation of soil from the sources of dust, while the deposition of dust leads to an increase in the nutrients of the soil, and therefore to the increase in the fertility of these areas (Swap et al., 1992). Long-range dust transport affects, to a large extent, animals as well as humans, and it can transmit different pathogens resulting in a direct threat to health (Kellogg and Griffin, 2006). Dust particles with aerodynamic diameter less than 2.5 μm, which mostly contain long-range transport, directly affect human and animal health because they smoothly penetrate the lungs and sensitive alveolar system causing various inflammatory processes, asthma and obstructive pulmonary disease (Prospero et al., 2008; De Longueville et al., 2010). Although this phenomenon of long-range dust transport is generally present, it is necessary to point out that North Africa, more precisely the Sahara, is the largest source of mineral dust, with about 0.8×10^9 tons per year, contributing with 20–70% of global mineral dust (Laurent et al., 2008). In the Sahara region, air currents lead to dust build-ups, which are then transported to the Mediterranean (Rodríguez et al., 2003; Querol et al., 2004) and further north to Arctic regions or west to the Atlantic and there by long-range transport all away across the ocean to the coast of America.

Chemical composition and complex refractive index, chemical and mineralogical particle analysis of airborne dust and size distribution of Sahara dust are well investigated (Kandler et al., 2007, 2009, 2011; Scheuvens et al., 2011, 2013), and the content of numerous mineral species (Illite, Albite, Quartz, Calcite, Dolomite, Halite, Hematite, etc.), as well as the concentration and ratio of cationic and anionic species that represent the "fingerprint" of Saharan dust (Rodríguez et al., 2003;

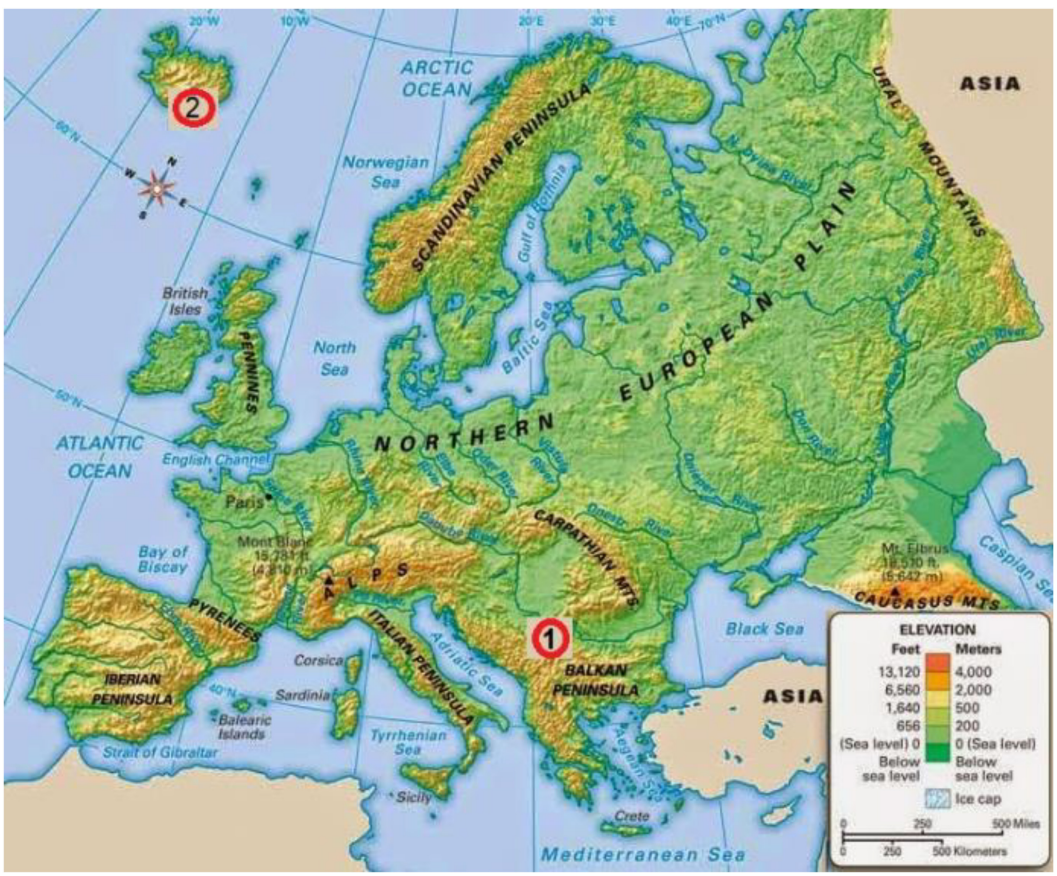

FIGURE 1 | Map of Europe and sampling sites for atmospheric aerosols: Belgrade ① and the Rangárvellir area ②. https://2.bp.blogspot.com/-LVlaPBN2nvA/VNECxS7jCPI/AAAAAAAAATc/Whc6_-9OKzc/s1600/Geography%2Bof%2BEurope.jpg.

Querol et al., 2004). The same concept is also used to determine the existence of long-range transports from other areas (marine aerosol, large cities, industrial areas, etc.) which can complement the complex picture of transmission and the impact of dust, whether natural or anthropogenic.

Iceland is the largest desert in Europe and Arctic with estimated dust deposition of 31–40 mil tons per year (Arnalds et al., 2014). This can represent about 7% of total global dust emissions and up to 21% of the Saharan dust emissions. About 3% of Icelandic dust is estimated to reach Europe (Groot Zwaaftink et al., 2017). Dust event frequency in Iceland is 34–135 dust days per year on average (Dagsson-Waldhauserova et al., 2014a). Icelandic dust is, however, different to crustal dust such as from Sahara. It is volcanic dust, dark in color, with >75% of volcanic glass with high proportions of FeO, Al_2O_3, and TiO_2 (Dagsson-Waldhauserova et al., 2014b; Arnalds et al., 2016). The identification of Icelandic dust particles transported to Europe, except for volcanic eruptions, is, however, sparse (Ovadnevaite et al., 2009).

Different approaches have been used to identify and characterize source areas of air masses. Backward trajectories are the most commonly calculated type, the HYSPLIT being the most widely used model and particulate matter being the kind of pollutant most frequently investigated (Pérez et al., 2015). The accuracy of trajectory models depends on the source of wind field data, resolution of available meteorological fields, trajectory type, etc (Fleming et al., 2012). Backward trajectories are typically estimated from archived wind field and pressure data and represent the approximate three-dimensional flow path of an air parcel. The HYSPLIT model was used to compute transport, mixing, chemical transformation, and deposition of pollutants and hazardous materials (Stein et al., 2015). It was extensively applied for research of the Fukushima accident and the Eyjafjallajökull volcano eruption, as well as several worldwide investigations of regional to local scale dust and air pollution transport (e.g., McGowan and Clark, 2008; Wang et al., 2010; Cristofanelli et al., 2011; Liu et al., 2013; Draxler et al., 2015; Leelõssy et al., 2017). The HYSPLIT backward trajectories have been frequently used also in long-range dust transportation and Saharan dust intrusions (Hamonou et al., 1999; Varga et al., 2013, 2014).

The main reason why the HYSPLIT model is widely used is that is freely available and prove extremely easy to apply (Pérez et al., 2015). The HYSPLIT model is accessed via web-based

TABLE 1 | Average content of elements in atmospheric aerosols of the suburban area of Belgrade (Serbia) and in the soil of the Rangárvellir area (Iceland).

		Aerosol in the suburban area of Belgrade (Serbia) [ng m^{-3}]						Rangárvellir area (Iceland) soil [mg kg^{-1}]
		$PM_{0.27-0.53}$	$PM_{0.53-1.06}$	$PM_{1.06-2.09}$	$PM_{2.09-4.11}$	$PM_{4.11-8.11}$	$PM_{8.11-16}$	
Al	Average	9.95	19.91	33.23	51.45	69.16	70.92	28923
	St. dev.	36.46	83.85	48.07	58.10	63.54	67.01	6559
	Min.	2.64	2.64	2.81	2.81	2.81	2.81	18642
	Max.	365.14	839.65	325.57	382.43	316.65	355.30	47271
Ca	Average	100.58	77.46	127.96	145.78	255.92	245.76	23404
	St. dev.	159.38	170.84	188.11	202.11	301.70	328.80	5889
	Min.	7.45	7.45	7.95	7.95	7.95	7.95	16702
	Max.	829.93	1115.87	868.60	1091.85	1811.18	1950.09	40676
Fe	Average	17.74	28.68	74.09	94.06	108.28	88.68	51361
	St. dev.	26.01	23.24	122.92	68.20	73.20	61.82	6315
	Min.	0.82	0.82	2.79	8.67	16.19	0.88	39012
	Max.	168.25	113.94	1183.13	417.20	381.44	266.32	66387
K	Average	78.61	68.67	30.63	17.88	24.27	23.86	1226
	St. dev.	93.84	93.40	43.34	27.81	29.11	32.67	322
	Min.	2.40	2.40	2.56	2.56	2.56	0.56	651
	Max.	420.44	514.19	251.67	132.23	133.32	188.76	1943
Na	Average	16.72	14.69	20.89	23.37	18.01	19.41	4810
	St. dev.	34.70	22.86	33.60	35.12	24.50	35.72	1296
	Min.	5.27	5.27	5.62	5.62	5.62	5.62	3319
	Max.	241.61	110.62	208.29	175.02	116.51	223.17	8035
Mg	Average	6.62	8.16	16.53	25.33	33.32	29.49	14111
	St. dev.	4.13	6.68	16.59	21.43	30.99	20.28	3116
	Min.	4.84	4.84	5.16	5.16	5.16	5.16	9938
	Max.	24.25	34.44	117.66	142.00	263.24	83.74	21562
Mn	Average	1.01	0.95	1.73	1.73	2.18	1.99	708
	St. dev.	3.37	0.52	4.05	1.24	1.36	1.33	116
	Min.	0.05	0.05	0.16	0.15	0.28	0.05	498
	Max.	32.61	2.28	41.01	7.47	6.91	5.73	954

Real-time Environmental Applications and Display sYstem (READY) developed by NOAA's Air Resources Laboratory (ARL) (Draxler et al., 2013).

In this work, we intend to use characteristic ratios of elements as fingerprints for identification of Icelandic volcanic dust particles in central Balkan. In addition, long-range transport of atmospheric aerosols entering the atmosphere by suspension of crustal element material from surface soil and deserts in Iceland is discussed. The large amount of the aerosols samples in suburban central Balkans' area and surface soil of the Rangárvellir area in Iceland and their analyses done are valuable unique dataset.

MATERIALS AND METHODS

Sampling

Atmospheric aerosols were measured in the suburban area (**Figure 1**) of Belgrade (φ= 44°48′; λ= 20°28′; 240 m elevation) as 48 h cumulative samples every 6 days, starting at 8 a.m. Low-pressure cascade impactors by Prof. Dr. Berner with vacuum pump with the flow rate of 25 l min^{-1} was used for sampling (Berner, 1972; Wang and John, 1988). Size segregated aerosols were collected on Tedlar foils with the following stages: $PM_{0.27-0.53}$, $PM_{0.53-1.06}$, $PM_{1.06-2.09}$, $PM_{2.09-4.11}$, $PM_{4.11-8.11}$, and $PM_{8.11-16}$. Samples and blanks were each stored in Petri cups in the freezer (−20°C) until processing.

Surface soil samples were collected in the Rangárvellir area in southern Iceland (63° N; 20° E; 50m elevation) in the vicinity of Mt Hekla, Iceland's most active volcano and under high erosion processes (Thorarinsdottir and Arnalds, 2012). Soil from this area consists of various materials originating from surrounding volcanoes and lava.

Daily composite means of geopotential heights and wind speed at specific isobaric levels were retrieved from the National Centers for Environmental Prediction/National Center for Atmospheric Research (NCEP/NCAR) reanalysis datasets for the study period (2012–2013).

Analytical Procedure

Samples of atmospheric aerosols were gravimetric measured in a glove box system with controlled nitrogen atmosphere (temperature 20 ± 5 °C and humidity 45 ± 5%). The digestions of collected aerosols were performed using Advanced Microwave

TABLE 2 | Average, standard deviation, minimum and maximum of characteristic ratios in atmospheric aerosol of suburban central Balkans' area and surface soil in South Iceland.

		Aerosol in the suburban area of Belgrade (Serbia)						Rangárvellir area (Iceland) soil
		$PM_{0.27-0.53}$	$PM_{0.53-1.06}$	$PM_{1.06-2.09}$	$PM_{2.09-4.11}$	$PM_{4.11-8.11}$	$PM_{8.11-16}$	
Ca/Al	Aver.	30.84	21.17	17.34	8.87	8.30	9.45	0.708
	St. dev.	55.73	51.00	40.23	21.18	15.27	21.34	0.079
	Min.	0.02	0.01	0.05	0.08	0.08	0.05	0.533
	Max.	314.85	315.73	251.19	150.75	89.80	148.50	0.772
Fe/Al	Aver.	5.22	5.90	7.26	5.25	4.24	4.02	1.621
	St. dev.	9.40	6.37	8.51	6.39	6.66	7.23	0.192
	Min.	0.03	0.02	0.10	0.20	0.47	0.31	1.281
	Max.	63.83	29.76	36.56	32.09	41.90	46.49	1.924
K/Al	Aver.	24.65	19.00	4.43	0.58	0.94	0.65	0.041
	St. dev.	35.01	32.50	8.65	0.70	2.73	1.27	0.010
	Min.	0.09	0.08	0.04	0.02	0.03	0.02	0.028
	Max.	159.51	195.07	49.57	3.68	21.44	8.71	0.060
Mg/Al	Aver.	1.86	1.65	1.83	1.26	1.11	1.12	0.395
	St. dev.	1.35	1.65	2.50	1.60	1.71	1.54	0.066
	Min.	0.01	0.01	0.03	0.03	0.10	0.09	0.269
	Max.	6.50	9.62	12.24	9.51	12.71	8.81	0.501
Mn/Al	Aver.	0.33	0.22	0.17	0.10	0.10	0.11	0.021
	St. dev.	1.28	0.19	0.19	0.14	0.16	0.22	0.004
	Min.	0.00	0.00	0.00	0.00	0.01	0.01	0.014
	Max.	12.37	0.84	0.79	0.65	0.89	1.87	0.024
Ca/Fe	Aver.	12.30	4.11	2.34	1.68	2.46	3.43	0.439
	St. dev.	24.46	12.03	3.55	2.74	2.87	3.45	0.052
	Min.	0.04	0.07	0.04	0.03	0.07	3.47	0.353
	Max.	150.72	102.69	18.04	18.99	12.82	3.48	0.505
Mg/Fe	Aver.	1.46	0.49	0.29	0.28	0.31	0.42	0.395
	St. dev.	1.93	0.82	0.23	0.13	0.16	0.58	0.066
	Min.	0.03	0.06	0.04	0.08	0.05	0.11	0.269
	Max.	5.86	5.86	1.85	0.65	1.07	5.86	0.501

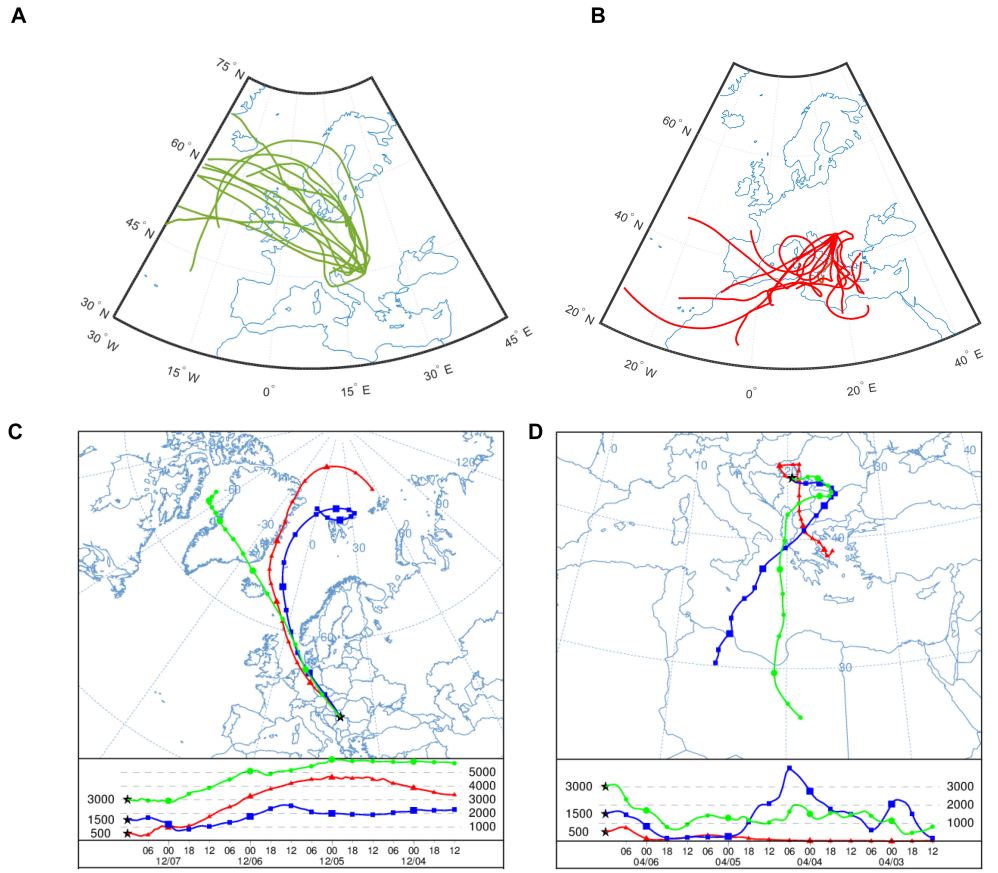

FIGURE 2 | Backward air trajectories approaching Belgrade for the arrival height of 3000 m from: **(A)** Iceland (17 cases) and **(B)** Sahara (18 cases) during the period 2012–2013. Selected 4 days backward trajectories ending in Belgrade at 500, 1500, and 3000 m on: **(C)** December 7, 2013 and **(D)** April 6, 2012.

Digestion System (ETHOS 1, Milestone, Italy) with HPR-1000/10S high pressure segmented rotor and pressure resistant PTFE vessels. Samples were transfered to the PTFE vessels, using HNO_3 (62%, UltraPure, Merck), H_2O_2 (30%, Sigma-Aldrich) and HF (UltraPure, Merck) and then heated with microwave energy for 50 min. The content of elements in solution samples of atmospheric aerosols was determined by inductively coupled plasma mass spectrometry (ICP-MS), using a Thermo Fisher Scientific iCAP Qc ICP-MS (Bremen, Germany) using EPA Method Standard, Low Level Elements Calibration Stock (10 mg L^{-1}) of elements. Every tenth sample was blank, collected using the same procedure as for the aerosol samples, but without use of the pump to draw air through the filter (Karanasiou et al., 2007; Đuričić-Milanković et al., 2018).

Inductively coupled plasma iCAP-6500 Duo (Thermo Scientific, United Kingdom) with an atomic emission spectrometer was used for determining element concentrations in the extracts of soil from Iceland. Laboratory quality assurance and quality control methods were used in element concentrations determination, including the standard operating procedures, calibration with standards, and analysis of both, reagent blanks and replicates. Elements concentrations are reported in mg kg^{-1} on a dry weight of soil (Sakan et al., 2016).

The HYSPLIT Model of Backward Trajectories

The HYSPLIT model is a complete system for computing trajectories complex dispersion and deposition simulations using either puff or particle approaches (Draxler and Hess, 1998). The HYSPLIT continues to be one of the most extensively used atmospheric transport and dispersion models in the atmospheric sciences community (Stein et al., 2015). The HYSPLIT model is widely used to generate backward trajectories in given starting locations (e.g., Rozwadowska et al., 2010; Freitag et al., 2014; Pérez et al., 2015; Su et al., 2015).

Four days backward trajectories were computed to trace the air history by means of the HYSPLIT model. The particle motion is defined as the superposition of a deterministic downwind term (advection) and a stochastic turbulent motion (Draxler and Hess, 1998). The deterministic term is interpolated to each particle position from the wind field provided by an input numerical weather prognostic (NWP) model. Input meteorological data is obtained from analysis of the Global Data Assimilation System (GDAS) data. The GDAS is run operationally 4 times a day (at 00, 06, 12, and 18 UTC) by the NOAA's National Centers for Environmental Prediction (NCEP). NCEP post-processing of the GDAS converts the data from spectral coefficient form

to 1 degree latitude-longitude (360 by 181) grids and from sigma levels to pressure levels. NOAA's ARL saves the successive analyses and 3-h forecast, four times each day to produce a continuous data archive. The decision to use these data was caused by enhanced data assimilation methods as well as the highest horizontal, vertical and temporal resolution. 4 days

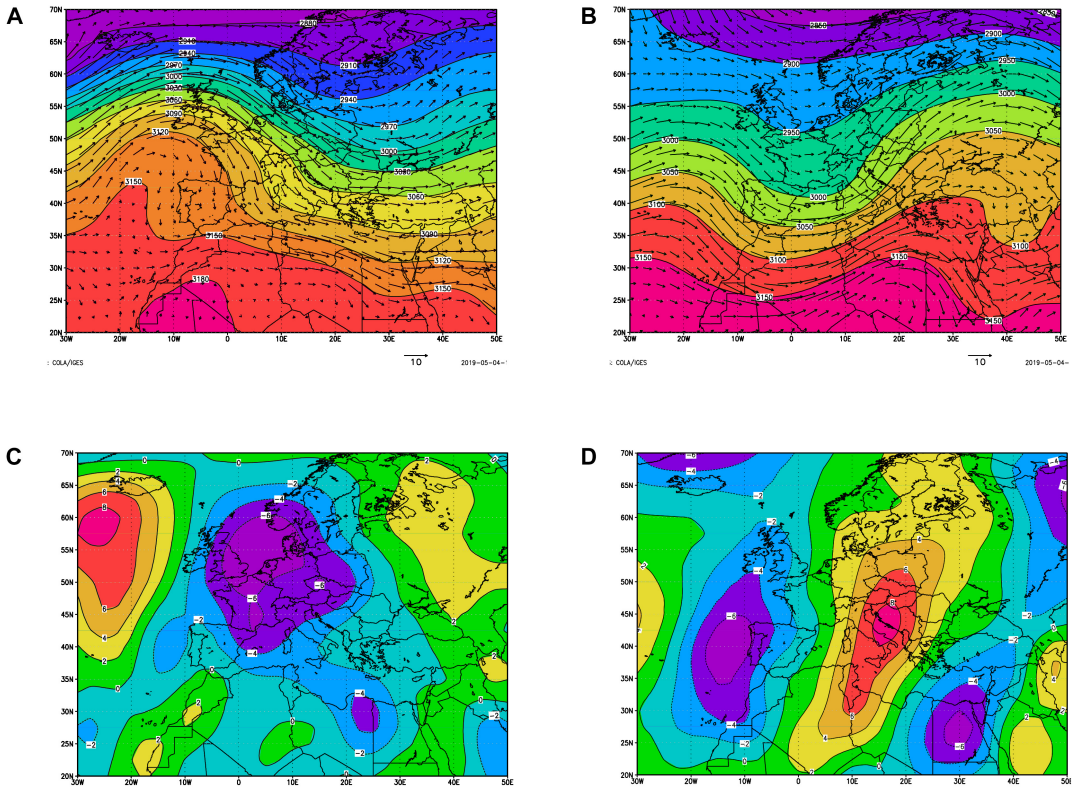

FIGURE 3 | A composite geopotential height (m) and wind flow (m/s) map **(A,B)**, and meridional wind component **(C,D)** for days of 17 and 18 events analyzed from March 2012 to December 2013 for trajectories represented in **Figure 2A** (left) and **Figure 2B** (right), respectively.

TABLE 3 | Elements ratio in suburban atmospheric aerosols of central Balkans' corresponding with their ratios in surface crustal material of Northern Africa (NA) for air masses coming from Northern Africa.

		Characteristic elements ratios						
Periods	**Air masses**	**Ca/Al**	**K/Al**	**Fe/Al**	**Mg/Al**	**Mn/Al**	**Ca/Fe**	**Mg/Fe**
1st – 3rd April 2012	SW	3.48					1.57	0.26
4th – 6th April 2012	S		0.50	1.15	0.36	0.03	1.50	0.35
24th – 26th August 2012	SW			1.21	0.45	0.03	2.25	0.34
17th – 19th October 2012	SW			1.07		0.03		0.52
10th – 12th November 2012	SW			1.22		0.04		0.90
4th – 6th March 2013	SW	0.51	0.22	0.89	0.39	0.03		0.47
16th – 18th March 2013	SW	0.49						0.22
3rd – 5th April 2013	SW		0.10	1.20	0.37	0.03	0.40	0.20
21st – 23rd April 2013	SW	0.35		0.75	0.29		0.49	0.37
27th – 29th April 2013	SW	0.31	0.45		0.26		0.48	0.38
15th – 17th May 2013	S	0.56			0.31			0.44
27th – 29th May 2013	S	0.61			0.51	0.03		0.27
8th – 10th June 2013	SW	0.59		0.98	0.31		2.75	0.48
6th – 8th October 2013	S	0.31	0.29		0.74			0.13
12th – 14th October 2013	SW	1.86	0.30		0.77	0.04	2.03	0.27
17th – 19th November 2013	S	7.59					1.18	0.23
24th – 26th December 2013	S	2.18					0.98	0.48

backward trajectories were selected because it is sufficient time to determine regional transport pathways. The trajectories were calculated every 1 h from March 14, 2012 to December 26, 2013 for four arrival heights: 500, 1500, 3000, and 5000 m above sea level. The selection of 500 m as the lowest level resulted from the orography around the station. To elucidate the effect of long-range transport, trajectories are analyzed at low and mid tropospheric altitudes, up to 5000 m (e.g., Ogawa et al., 2004; Sangeetha et al., 2018). The trajectories and composite maps are presented for 700 mb level as the most representative HYSPLIT backward trajectory level based on previous analyses of long-range dust transport episodes for Central European and Mediterranean case studies (Hamonou et al., 1999; Varga et al., 2013, 2014).

RESULTS

The contribution of mineral dust from high-latitude sources of the global dust cycle has not been sufficiently investigated yet (Baddock et al., 2017). In the near past there are some works relate to the atmospheric transport of Icelandic volcanic ash during eruption of Eyjafjallajökull (Langmann et al., 2012) as well as volcanic dusts during storm events (Dagsson-Waldhauserova et al., 2015; Taylor et al., 2015; Wilkins et al., 2016) but there are not yet sufficiently investigations relate to volcanic particles in atmospheric aerosols originated from dust storms occurrences in Iceland over continental part of Europe.

Elements Contents and Their Ratios

In this work we considered next elements Al, Ca, Fe, K, Na, Mg, and Mn and their characteristic ratios as fingerprints for Icelandic volcanic dust in suburban atmospheric aerosols of central Balkan. The contents of elements were shown in **Table 1** as distributions of average values with standard deviations, minimum and maximum in suburban aerosol segregated into six Dp fractions for samples measured and collected in Belgrade (Đuričić-Milanković et al., 2018) and for the soil of the Rangárvellir area (Iceland). The main difference between atmospheric aerosols of central Balkan and surface soil of the Rangárvellir area is that dominant mass contribution of Ca is in measured atmospheric aerosol while dominant element in surface soil of investigated area in Iceland is Fe.

The characteristic ratios that we considered in this work were Ca/Al, Fe/Al, K/Al, Mg/Al, Mn/Al, Ca/Fe, and Mg/Fe. **Table 2** presents the averages, standard deviations, minimums and maximums of investigated ratios in atmospheric aerosol of suburban central Balkans' area and in the surface soil of South Iceland. These ratios measured in PM of atmospheric aerosols vary up to several orders of magnitudes depending on the air mass origin while deviations from the mean values of elements ratios in surface soils of the Rangárvellir area in Iceland are significantly lower indicating the similarity in elements compositions of all investigated samples. The highest average ratios showed Ca/Al in atmospheric aerosols of central Balkan while the highest average ratios in surface soil of the Rangárvellir area in Iceland is for Fe/Al.

The Backward Trajectory Analysis

Backward trajectories at altitudes of 500, 1500, 3000, and 5000 m for 101 cases were traced for 96 h using the HYSPLIT model for Belgrade (φ= 44°48′; λ= 20°28′). The trajectories are classified in two groups if they meet the following criteria: their direction of approach and passage over potential source areas (Iceland or Sahara). Each of the two trajectory groups starting at 3000 m is displayed in **Figures 2A,B**, respectively. We analyzed 101 cases and found that there were 17 (18) cases in which trajectories approached Belgrade from Iceland (the Sahara). Nearly all trajectories from Iceland (**Figure 2A**) have a north/northwesterly direction, while those from the Sahara (**Figure 2B**) a south/southwesterly direction. An example of the horizontal and vertical backward air trajectories from Iceland toward Belgrade is shown in **Figure 2C**. The flow of air parcels in the layer up to 3000 m was from northwestern direction on December 7, 2013. It can be seen a lifting of air parcels at all levels. Selected case for the Saharan dust transport toward Belgrade on April 6, 2012 is presented in **Figure 2D**. Backward trajectories show a flow of air masses from the south and southwestern direction in the layer above 1500 m. A lowering of air parcels above 1500 m in the first day is followed by lifting and lowering in the last 2 days.

The HYSPLIT backward trajectories at different altitudes of 500, 1500, 3000, and 5000 m were counted as individual paths in the present study. The trajectory analyses of all cases indicate that the predominant flow regime is NW and SW. This is in accordance with the results for Belgrade during summer and autumn in 2008 by Mihajlidi-Zelić et al. (2015).

It is expected that each individual trajectory be associated with a synoptic pattern, since trajectories are constructed from wind fields. As a verification, a composite map of all those days when trajectories are assigned to a particular group (cluster) is plotted for the level of 700 hPa (∼3000 m) in **Figure 3**. Composites are obtained as the average of the geopotential height and wind fields, and meridional wind component of all the 17 events (**Figures 3A,C**), i.e., 18 events (**Figures 3B,D**) analyzed for the March 2012–December 2013 period. **Figure 3A** presents a composite geopotential height and wind flow pattern for the cluster of trajectories presented in **Figure 2A**, indicating flow to Belgrade from a northwest direction. Low pressure over Northern Europe with

TABLE 4 | Element ratios in suburban atmospheric aerosols of central Balkans' corresponding with volcanic soil in South Iceland.

Periods	Air masses	Characteristic elements ratios					
		Ca/Al	Mg/Al	Fe/Al	Mn/Al	Ca/Fe	Mg/Fe
6th – 8th August 2012	NW	1.01	0.39	1.46	0.03	0.42	0.31
26th – 28th June 2013	NW	0.90	0.32	1.06	0.02	0.39	0.31
18th – 20th September 2013	NW		0.47	1.72	0.08		0.35

TABLE 5 | Dust storm occurrence for selected periods in Iceland in 2012 and 2013.

SYNOP codes for dust observation in Iceland	Corresponding measured episode
2nd August and 8th August 2012: dust storm in North East Iceland	6th – 8th August 2012
20th June 2013: dust storm in South Iceland (Reykjavik) 18th June and 26th June 2013: dust storm in North East Iceland	26th – 28th June 2013
8th, 12th, and 14th September 2013: dust storm in North East Iceland 12th, 15th, 16th, and 17th September: dust storm in South Iceland	18th – 20th September 2013

a trough over Eastern Europe, and a high pressure system west from Europe produces northwesterlies over Serbia. In these synoptic situations, air from the Atlantic and also from Iceland can approach to Belgrade. The negative meridional wind components are located over Europe (**Figure 3C**), with the strongest values above the North Sea and France, suggesting dust intrusions from the northwest into central Europe and Serbia. **Figure 3B** shows the composite geopotential height and wind flow pattern for days of trajectories approaching Belgrade from Africa presented in **Figure 2B**. A very deep trough exists over Western Europe toward the central Algeria. Following this circulation, the dust was picked up from North Africa, and transported over Mediterranean toward Southeastern Europe, and also to Belgrade in corresponding circulation. The strongest meridional wind flows are located above the southern Adriatic Sea (**Figure 3D**), suggesting dust intrusions from the south-southwest into the Balkans. Synoptic situations with trajectories approaching Belgrade from Africa usually were characterized by a cyclone in lower troposphere, which developed over northern Italy and extended to the northern part of Africa and the Saharan desert (Vukmirović et al., 2004).

Chemical Fingerprints Model

In this work we analyzed of characteristic elements ratios corresponding with crustal material of Northern Africa (Kandler et al., 2007, 2009, 2011; Scheuvens et al., 2011, 2013), and with soil of volcanic origin in Iceland in atmospheric aerosols of suburban area of central Balkan of air masses coming from southern and

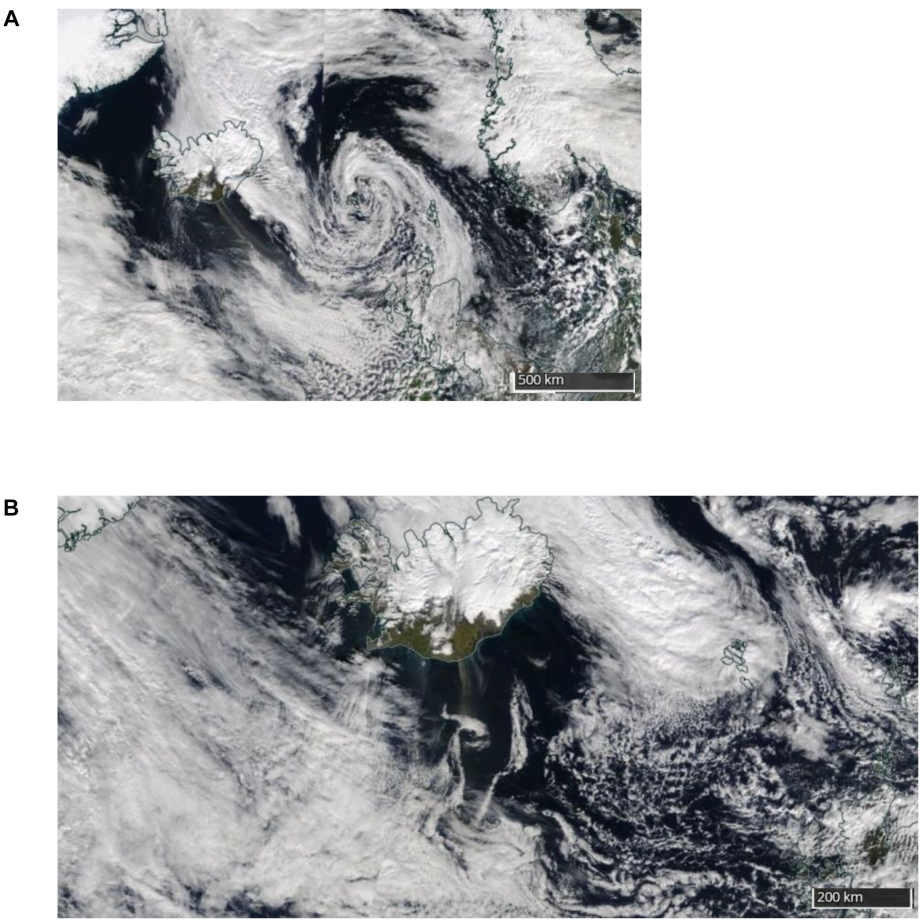

FIGURE 4 | Satellite images of dust storms in South Iceland on September 16 **(A)** and 17 **(B)** 2013 captured in true color by the Moderate Resolution Imaging Spectroradiometer (MODIS) flying on NASA's Terra satellite (Source: NASA/MODIS).

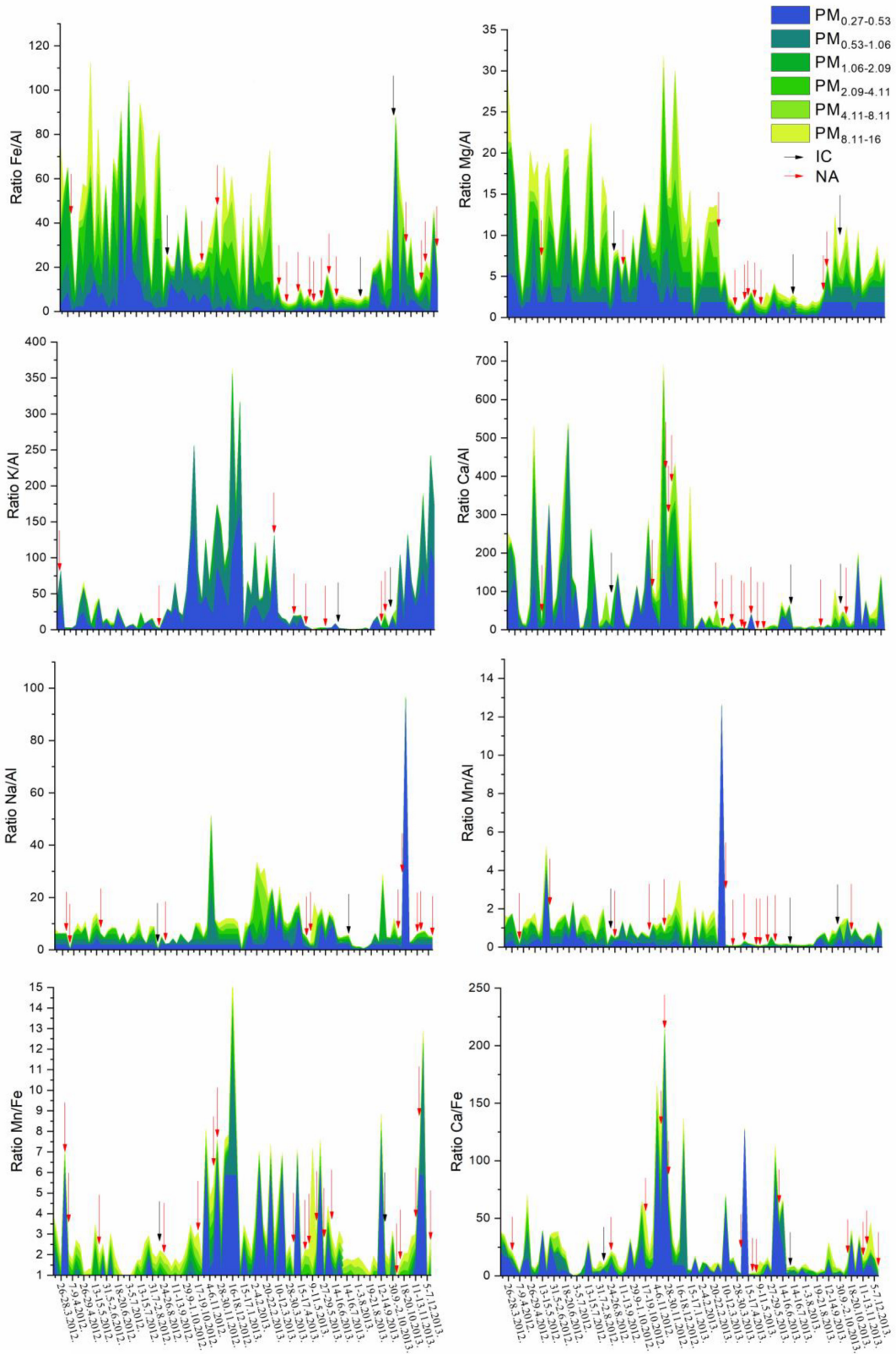

FIGURE 5 | Temporal variations of elements ratios with episodes of Icelandic dust (IC) and North Africa dust (NA).

west southern regions as well as air masses coming over Iceland from northwestern directions.

The Ca/Al ratio in soil from Iceland mainly is between 0.7 and 1.0 while in the African dust are varying. This ratio in Atlas region is >1.0, in some regions of Egypt and north Sudan <0.5 but in northern Mali the ratio Ca/Al ≈ 8. Ratio Mg/Al in African dust is >0.3 (Scheuvens et al., 2013) and also in soil of south Iceland Mg/Al > 0.3. In crustal material of Africa 0.1 < K/Al < 0.5 and we found the same ratio in aerosols from southern air masses. The ratio Fe/Al in crustal material of Africa were 0.2 and 1.2 while in crustal material from Iceland this ratio is between 1.0 and 3.0. Mn/Al < 0.03 in crustal material of Africa regions (Scheuvens et al., 2013) and also in investigated samples from Iceland this ratio is low and its value is about 0.03 and in some samples of river sediments it was approximately 0.06 while in volcano ash it was near 0.08.

Table 3 shows characteristic elements ratios in suburban atmospheric aerosols of central Balkan which are corresponding with the ratio in crustal material of North Africa in southern and south western air masses episodes.

Table 4 contains episodes of north western air masses passing over Iceland with element ratios corresponding with their ratios in surface soil of volcanoes origin in southern Iceland.

Table 5 shows dust storm occurrence in Iceland with the corresponding episodes of measured aerosols in central Balkan area.

Backward trajectories have calculated for each taken sample of atmospheric aerosol in central Balkan area – in total 101 backward trajectories that are corresponding with samples of atmospheric aerosols collected in suburban area of central Balkan. We found that 17 of total air masses were coming from the areas around Iceland. In 13 of them we found ratios of some elements that are corresponding to Iceland soil (volcano dust). We have chosen only those (1) which are passing over Iceland, (2) for which the characteristic elements ratios are corresponding to volcanic soil in South Iceland (**Table 5**), and (3) which are coinciding with dust storm occurrence in Iceland (**Figure 4**). According to this criterion we found 3 episodes for consideration as contribution of High Latitude Dust natural sources on central Balkan aerosol. Taking into account these criteria we can reliable claim that central Balkan area is under Icelandic dust affects. According to our results at least 3% air masses arriving from Iceland carrying suspended volcanic dust during storm occurrences in Iceland. It is demonstrated that dust storms occurrences on 16th and 17th September 2013 corresponding with backward trajectories of air masses reaching Belgrade calculated for the period from 18th to 20th September 2013 have documented (Beckett et al., 2017).

Most of the dust from the Icelandic desert originates from "dust hot-spots" which are in vicinity of glaciers and along the coastline. Such dust originates from abrasion underneath glaciers and deposited by glacio-fluvial processes. Further from the hot spots, dust can be also deposited on desert areas away from these hotspots and re-suspended again. The primary dust-hotspots contribute larger proportions of dust from Iceland than other areas combined (Arnalds et al., 2016).

Temporal variations of characteristic element ratios with episodes of Icelandic dust (IC) and North Africa dust (NA) have shown on **Figure 5**. Red arrows denote periods with characteristic elements ratios corresponding to African dust and black arrows indicate characteristic elements ratios with Icelandic volcanic soil measured in atmospheric aerosols in suburban area of Belgrade. Frequencies of air masses from NW and southern segments are almost the same with somewhat higher from NW segments. Nevertheless, a significantly larger number of cases with characteristic elements ratios in atmospheric aerosol of central Balkan corresponding to African crustal material were found in SW and S air masses (**Table 3**) than those which are corresponding to volcanic dust in air masses from NW segment (**Table 4**). This difference is consequence of more extensive dust storms on the North Africa than dust storm occurrence in Iceland.

CONCLUSION

Characteristic elements ratios corresponding with crustal material of Northern Africa and soil of volcanic origin in Iceland in atmospheric aerosols of suburban area of central Balkan were analyzed. We considered air masses coming from southern and southwestern regions as well as air masses coming over Iceland from northwestern directions. A total of 101 air parcel backward trajectories reaching Belgrade in Serbia were identified by means of a Lagrangian integrated trajectory (HYSPLIT) at four different ending altitudes of 500, 1500, 3000, and 5000 m. Large-scale atmospheric circulation features could be seen to be associated with two clusters of trajectories, from Iceland or Sahara. Air mass trajectories show that emissions from distant sources may cross boundaries and impact remote areas or places where the use of certain substances has been restricted. Three events meeting three set conditions were identified; air masses were passing over Iceland, the characteristic elements ratios corresponded to volcanic soil in South Iceland and these air masses coincide with dust storm occurrence in Iceland. We can conclude that central Balkan area is under influence of Icelandic dust originating from resuspended volcanic particles at least 3% of total air masses affecting central Balkan. This shows the importance of monitoring High Latitude Dust sources, particularly Iceland as the largest European and Arctic desert. Icelandic volcanic dust can contribute to impaired air quality in mainland Europe.

AUTHOR CONTRIBUTIONS

DĐ contributed in organization of measurements, interpretation of the results, and preparing the manuscript. IT contributed in trajectory calculation and preparing the manuscript. SS contributed in analyzing the soil and processing data. SP contributed in aerosol measuring and data processing. JĐ-M contributed in analyzing of the aerosol and data processing. DF contributing in organization of soil sampling and measuring in Iceland. PD-W contributing in dust observation in Iceland and preparing the manuscript.

FUNDING

This study was funded by the Ministry of Education, Science and Technological Development of Serbia (Projects: ON172001, ON176013, and III43007). The preparation of this manuscript was in part funded by the Icelandic Research Fund (Rannis) Grant No. 152248-051 and COST STSM Reference Number: COST-STSM-ES1306-34336 (Grant holder DĐ).

ACKNOWLEDGMENTS

The authors gratefully acknowledge the NOAA Air Resources Laboratory (ARL) for the provision of the HYSPLIT transport and dispersion model and READY website (http://ready.arl.noaa.gov), National Centers for Environmental Prediction/National Center for Atmospheric Research for providing the daily composite means used in this publication and to COST Action ES1306 – Connecteur.

REFERENCES

Andreae, M. O., and Rosenfeld, D. (2008). Aerosol–cloud–precipitation interactions. Part 1. The nature and sources of cloud-active aerosols. *Earth Sci. Rev.* 89, 13–41. doi: 10.1016/j.earscirev.2008.03.001

Arimoto, R. (2001). Eolian dust and climate: relationships to sources, tropospheric chemistry, transport and deposition. *Earth Sci. Rev.* 54, 29–42. doi: 10.1016/s0012-8252(01)00040-x

Arnalds, O., Dagsson-Waldhauserova, P., and Olafsson, H. (2016). The Icelandic volcanic aeolian environment: processes and impacts – a review. *Aeolian Res.* 20, 176–195. doi: 10.1016/j.aeolia.2016.01.004

Arnalds, O., Olafsson, H., and Dagsson-Waldhauserova, P. (2014). Quantification of iron-rich volcanogenic dust emissions and deposition over ocean from icelandic dust sources. *Biogeosci. Discuss* 11, 5941–5967. doi: 10.5194/bgd-11-5941-2014

Baddock, M. C., Mockford, T., Bullard, J. E., and Thorsteinsson, T. (2017). Pathways of high-latitude dust in the North Atlantic. *Earth Planet. Sci. Lett.* 459, 170–182. doi: 10.1016/j.epsl.2016.11.034

Beckett, F., Kylling, A., Sigurðardóttir, G., von Löwis, S., and Witham, C. (2017). Quantifying the mass loading of particles in an ash cloud remobilized from tephra deposits on iceland. *Atmos. Chem. Phys.* 17, 4401–4418. doi: 10.5194/acp-17-4401-2017

Berner, A. (1972). Praktische erfahrungen mit einem 20-stufen-impactor. *Staub Reinhalt. Luft* 32:315.

Cristofanelli, P., Calzolari, F., Bonafè, U., Lanconelli, C., Lupi, A., Busetto, M., et al. (2011). Five-year analysis of background carbon dioxide and ozone variations during summer seasons at the mario zucchelli station (Antarctica). *Tellus B: Chem.Phys. Meteorol.* 63, 831–842. doi: 10.1111/j.1600-0889.2011.00576.x

Dagsson-Waldhauserova, P., Arnalds, O., and Olafsson, H. (2014a). Long-term variability of dust events in iceland. *Atmos. Chem. Phys.* 14, 13411–13422. doi: 10.5194/acp-14-13411-2014

Dagsson-Waldhauserova, P., Arnalds, O., Olafsson, H., Skrabalova, L., Sigurdardottir, G. M., Branis, M., et al. (2014b). Physical properties of suspended dust during moist and low-wind conditions in iceland. *Icel. Agric. Sci.* 27, 25–39.

Dagsson-Waldhauserova, P., Arnalds, O., Olafsson, H., Hladil, J., Skala, R., Navratil, T., et al. (2015). Snow–dust storm: unique case study from iceland, March 6–7, 2013. *Aeolian Res.* 16, 69–74. doi: 10.1016/j.aeolia.2014.11.001

Darwin, C. (1845). *Journal of Researches into the Natural History and Geology of the Countries Visited During the Voyage of H.M.S. Beagle Round the World, Under the Command of Capt. Fitz Roy, R.N*, 2 Edn. London: John Murray.

De Longueville, F., Hountondji, Y.-C., Henry, S., and Ozer, P. (2010). What do we know about effects of desert dust on air quality and human health in west africa compared to other regions? *Sci. Total Environ.* 409, 1–8. doi: 10.1016/j.scitotenv.2010.09.025

Draxler, R., Arnold, D., Chino, M., Galmarini, S., Hort, M., Jones, A., et al. (2015). World meteorological organization's model simulations of the radionuclide dispersion and deposition from the fukushima daiichi nuclear power plant accident. *J. Environ. Radioact.* 139, 172–184. doi: 10.1016/j.jenvrad.2013.09.014

Draxler, R., Stunder, B., Rolph, G., Stein, A., and Taylor, A. (2013). *Hysplit4 User Guide*. Available at: http://www.arl.noaa.gov/documents/reports/hysplit_user_guide.pdf (accessed May 21, 2015).

Draxler, R. R., and Hess, G. D. (1998). An overview of the hysplit_4 modelling system for trajectories dispersion, and deposition. *Aust. Meteorol. Mag.* 47, 295–308.

Đuričić-Milanković, J., Anđelković, I., Pantelić, A., Petrović, S., Gambaro, A., Antonović, D., et al. (2018). Partitioning of particulate matter and elements of suburban continental aerosols between fine and coarse mode. *Environ. Sci. Poll. Res.* 25, 20841–20853. doi: 10.1007/s11356-018-2037-8

Fleming, Z. L., Monks, P. S., and Manning, A. J. (2012). Review: untangling the influence of air-mass history in interpreting observed atmospheric composition. *Atmos. Res.* 10, 1–39. doi: 10.1016/j.atmosres.2011.09.009

Freitag, S., Clarke, A. D., Howell, S. G., Kapustin, V. N., Campos, T., Brekhovskikh, V. L., et al. (2014). Combining airborne gas and aerosol measurements with HYSPLIT: a visualization tool for simultaneous evaluation of air mass history and back trajectory consistency. *Atmos. Meas. Tech.* 7, 107–128. doi: 10.5194/amt-7-107-2014

Groot Zwaaftink, C. D., Arnalds, Ó., Dagsson-Waldhauserova, P., Eckhardt, S., Prospero, J. M., and Stoh, A. (2017). Temporal and spatial variability of icelandic dust emissions and atmospheric transport. *Atmos. Chem. Phys.* 17, 10865–10878. doi: 10.5194/acp-17-10865-2017

Hamonou, E., Chazette, P., Balis, D., Dulac, F., Schneider, X., Galani, E., et al. (1999). Characterization of the vertical structure of saharan dust export to the mediterranean basin. *J. Geophys. Res.* 104, 22257–22270. doi: 10.1029/1999jd900257

Husar, B. R. (2004). "Transport of dust: historical and recent observational evidence," in *The Handbook of Environmental Chemistry*, eds D. Barceló and A. G. Kostianoy (Berlin: Springer).

Kandler, K., Benker, N., Bundke, U., Cuevas, E., Ebert, M., Knippertz, P., et al. (2007). Chemical composition and complex refractive index of saharan mineral dust at izana, tenerife (spain) derived by electron microscopy. *Atmos. Environ.* 41, 8058–8074. doi: 10.1016/j.atmosenv.2007.06.047

Kandler, K., Schütz, L., Deutscher, C., Ebert, M., Hofmann, H., JäCKEL, S., et al. (2009). Size distribution, mass concentration, chemical and mineralogical composition and derived optical parameters of the boundary layer aerosol at tinfou, morocco, during SAMUM 2006. *Tellus B Chem. Phys. Meteorol.* 61, 32–50. doi: 10.1111/j.1600-0889.2008.00385.x

Kandler, K., Schütz, L., Jäckel, S., Lieke, K., Emmel, C., Müller-Ebert, D., et al. (2011). Ground-based off-line aerosol measurements at praia, cape verde, during the saharan mineral dust experiment: microphysical properties and mineralogy. *Tellus B Chem. Phys. Meteorol.* 63, 459–474. doi: 10.1111/j.1600-0889.2011.00546.x

Karanasiou, A. A., Sitaras, I. E., Siskos, P. A., and Eleftheriadis, K. (2007). Size distribution and sources of trace metals and n-alkanes in the athens urban aerosol during summer. *Atmos. Environ.* 41, 2368–2381. doi: 10.1016/j.atmosenv.2006.11.006

Kellogg, C. A., and Griffin, D. W. (2006). Aerobiology and the global transport of desert dust. *Trends Ecol. Evol.* 21, 638–644. doi: 10.1016/j.tree.2006.07.004

Langmann, B., Folch, A., Hensch, M., and Matthias, V. (2012). Volcanic ash over europe during the eruption of eyjafjallajökull on iceland, April–May 2010. *Atmos. Environ.* 48, 1–8. doi: 10.1016/j.atmosenv.2011.03.054

Laurent, B., Marticorena, B., Bergametti, G., Léon, J. F., and Mahowald, N. M. (2008). Modeling mineral dust emissions from the sahara desert using new surface properties and soil database. *J. Geophys. Res.* 113:D14218.

Leelõssy, Â., Mészáros, R., Kovács, A., Lagzi, I., and Kovács, T. (2017). Numerical simulations of atmospheric dispersion of iodine-131 by different models. *PLoS One* 12:e0172312. doi: 10.1371/journal.pone.0172312

Liu, N., Yu, Y., He, J., and Zhao, S. (2013). Integrated modeling of urban–scale pollutant transport: application in a semi–arid urban valley, Northwestern China. *Atmos. Poll. Res.* 4, 306–314. doi: 10.5094/APR.2013.034

Mahowald, N. M., Rivera Rivera, G. D., and Luo, C. (2004). Comment on "relative importance of climate and land use in determining present and future global soil dust emission" by I. Tegen et al. *Geophys. Res. Lett.* 31:L24105.

McGowan, H., and Clark, A. (2008). Identification of dust transport pathways from lake eyre, Australia using Hysplit. *Atmos. Environ.* 42, 6915–6925. doi: 10.1016/j.scitotenv.2018.02.231

Mihajlidi-Zelić, D., Djordjević, D., Relić, D., Tošić, I., Ignjatović, L. J., Stortini, M. A., et al. (2015). Water-soluble inorganic ions in urban aerosols of the continental part of balkans (Belgrade) during the summer – autumn. *Open Chem.* 13, 245–256.

Ogawa, N., Yoshimura, K., Kikuchi, R., Adzuhata, T., Ozeki, T., and Kajikawa, M. (2004). Effect of long-range transport of air mass on the ionic components in radiation fog in northern Japan. *Analyt. Sci.* 20, 69–72. doi: 10.2116/analsci.20.69

Ovadnevaite, J., Ceburnis, D., Plauskaite-Sukiene, K., Modini, R., Dupuy, R., Rimselyte, I., et al. (2009). Volcanic sulfate and arctic dust plumes over the North Atlantic Ocean. *Atmos. Environ.* 43, 4968–4974. doi: 10.1016/j.atmosenv.2009.07.007

Pérez, A., Artuso, F., Mahmud, M., Kulshrestha, U., Luisa Sánchez, M., and Ángeles García, M. (2015). Applications of air mass trajectories. *Adv. Meteorol.* 2015:284213. doi: 10.1155/2015/284213

Prospero, J. M. (1999). Long-range transport of mineral dust in the global atmosphere: impact of African dust on the environment of the southeastern United States. *Proc. Natl. Acad. Sci. U.S.A.* 96, 3396–3403. doi: 10.1073/pnas.96.7.3396

Prospero, J. M., Blades, E., Naidu, R., Mathison, G., Thani, H., and Lavoie, M. C. (2008). Relationship between african dust carried in the atlantic trade winds and surges in pediatric asthma attendances in the caribbean. *Int. J. Biometeor.* 52, 823–832. doi: 10.1007/s00484-008-0176-1

Querol, X., Alastuey, A., Viana, M. M., Rodriguez, S., Artińano, B., Salvador, P., et al. (2004). Speciation and origin of PM10 and PM2.5 in Spain. *Aerosol Sci.* 35, 1151–1172. doi: 10.1016/j.jaerosci.2004.04.002

Rodríguez, S., Querol, X., Alastuey, A., Viana, M.-M., and Mantilla, E. (2003). Events affecting levels and seasonal evolution of airborne particulate matter concentrations in the western mediterranean. *Environ. Sci. Technol.* 37, 216–222. doi: 10.1021/es020106p

Rozwadowska, A., Zieliński, T., Petelski, T., and Sobolewski, P. (2010). Cluster analysis of the impact of air back-trajectories on aerosol optical properties at hornsund. *Spitsbergen. Atmos. Chem. Phys.* 10, 877–893. doi: 10.5194/acp-10-877-2010

Sakan, S., Popović, A., Anđelković, I., and Đorđević, D. (2016). Aquatic sediments pollution estimate using the metal fractionation, secondary phase enrichment factor calculation, and used statistical methods. *Environ. Geochem. Health* 38, 855–867. doi: 10.1007/s10653-015-9766-0

Sangeetha, S. K., Sivakumar, V., and Gebreslasie, M. (2018). Long-range transport of SO2 over South Africa: a case study of the calbuco volcanic eruption in April 2015. *Atmos. Environ.* 185, 78–90. doi: 10.1016/j.atmosenv.2018.04.056

Scheuvens, D., Kandler, K., Küpper, M., Lieke, K., Zorn, R., Ebert, M., et al. (2011). Individual-particle analysis of airborne dust samples collected over morocco in 2006 during SAMUM 1. *Tellus B Chem. Phys. Meteorol.* 63, 512–530. doi: 10.1111/j.1600-0889.2011.00554.x

Scheuvens, D., Schütz, L., Kandler, K., Ebert, M., and Weinbruch, S. (2013). Bulk composition of northern African dust and its source sediments — a compilation. *Earth Sci. Rev.* 116, 170–194. doi: 10.1016/j.earscirev.2012.08.005

Sokolik, I. N., and Toon, O. B. (1999). Incorporation of mineralogical composition into models of the radiative properties of mineral aerosol from UV to IR wavelengths. *J. Geophys. Res.* 104, 9423–9444. doi: 10.1029/1998jd200048

Stein, A. F., Draxler, R. R., Rolph, G. D., Stunder, B. J. B., Cohen, M. D., and Ngan, F. (2015). NOAA's HYSPLIT atmospheric transport and dispersion modeling system. *Bull. Am. Meteorol. Soc.* 12, 2059–2077. doi: 10.1175/bams-d-14-00110.1

Su, L., Yuan, Z., Fung, J. C., and Lau, A. K. (2015). A comparison of HYSPLIT backward trajectories generated from two GDAS datasets. *Sci. Total. Environ.* 50, 527–537. doi: 10.1016/j.scitotenv.2014.11.072

Swap, R., Garstang, M., Greco, S., Talbot, R., and Kallberg, P. (1992). Saharan dust in the amazon basin. *Tellus* 44B, 133–149. doi: 10.1034/j.1600-0889.1992.t01-1-00005.x

Taylor, I., Mackie, S., and Watson, M. (2015). Investigating the use of the saharan dust index as a tool for the detection of volcanic ash in SEVIRI imagery. *J. Volcanol. Geothermal Res.* 304, 126–141. doi: 10.1016/j.jvolgeores.2015.08.014

Tegen, I., Werner, M., Harrison, S. P., and Kohfeld, K. E. (2004a). Relative importance of climate and land use in determining present and future global soil dust emission. *Geophys. Res. Lett.* 31:L05105.

Tegen, I., Werner, M., Harrison, S. P., and Kohfeld, K. E. (2004b). Reply to comment by N.M. Mahowald et al. on "Relative importance of climate and land use in determining present and future global soil dust emission". *Geophys. Res. Lett.* 31:L24106.

Thorarinsdottir, E. F., and Arnalds, O. (2012). Wind erosion of volcanic materials in the hekla area. South Iceland. *Aeol. Res.* 4, 39–50. doi: 10.1016/j.aeolia.2011.12.006

Varga, G., Kovács, J., and Újvári, G. (2013). Analysis of saharan dust intrusions into the carpathian basin (Central Europe) over the period of 1979-2011. *Glob. Planet. Change* 100, 333–342. doi: 10.1016/j.gloplacha.2012.11.007

Varga, G., Újvári, G., and Kovács, J. (2014). Spatiotemporal patterns of Saharan dust outbreaks in the Mediterranean Basin. *Aeol. Res.* 15, 151–160. doi: 10.1016/j.aeolia.2014.06.005

Vukmirović, Z., Unkašević, M., Lazić, L., Tošić, I., Rajšić, S., and Tasić, M. (2004). Analysis of the saharan dust regional transport. *Met. Atmos. Phys.* 85, 265–273. doi: 10.1007/s00703-003-0010-6

Wang, F., Chen, D. S., Cheng, S. Y., Li, J. B., Li, M. J., and Ren, Z. H. (2010). Identification of regional atmospheric PM10 transport pathways using HYSPLIT, MM5-CMAQ and synoptic pressure pattern analysis. *Environ. Modell. Softw.* 25, 927–934. doi: 10.1016/j.envsoft.2010.02.004

Wang, H.-C., and John, W. (1988). Characteristics of the berner impactor for sampling inorganic ions. *Aerosol Sci. Technol.* 8, 157–172. doi: 10.1080/02786828808959179

Wilkins, K. L., Benedetti, A., Kristiansen, N. I., and Lange, A. C. (2016). Chapter 13 - applications of satellite observations of volcanic ash in atmospheric dispersion modeling. *Volcanic Ash* 2016, 233–246. doi: 10.1016/b978-0-08-100405-0.00019-7

Conflict of Interest Statement: The authors declare that the research was conducted in the absence of any commercial or financial relationships that could be construed as a potential conflict of interest.

frontiers in Earth Science

ORIGINAL RESEARCH
published: 05 July 2019
doi: 10.3389/feart.2019.00178

Aerosol Optical Depth Over the Nepalese Cryosphere Derived From an Empirical Model

Bikas Chandra Bhattarai, John Faulkner Burkhart, Frode Stordal and Chong-Yu Xu*

Department of Geosciences, University of Oslo, Oslo, Norway

In the Himalayan region, aerosols received much attention because they affect the regional as well as local climate. Aerosol Optical Depth (AOD) observation from satellite are limited in the Himalayan region mainly due to high surface reflectance. To overcome this limitation, we have conducted a multivariate regression analysis to predict the AOD over the cryospheric portion of Nepalese Himalaya. Prediction using three meteorological variables from ERA-Interim: relative humidity, wind velocity components (U10 and V10) were taken into account for model development as independent variables, while the longest time series AOD observation at Pokhara station is used as dependent variable. Model coefficients were found significant at 95 percent level with 0.53 coefficients of determination for daily values. Correlation coefficients between model output and AERONET observations were found to be 0.68, 0.73, 0.75, 0.83, and 0.82 at Lumbini, Kathmandu Bode (KTM-BO), Kathmandu University (KTM-UN), Jomson, and Pyramid laboratory/observatory (EVK2CNR) AERONET stations, respectively. Model overestimate AOD at Jomsom, and EVK2CNR AERONET stations while slightly underestimates AOD in Lumbini, KTM-UN, and KTM-BO AERONET station, respectively. Both model output and MODIS observation showed that the highest AOD over Nepal is observed during winter and pre-monsoon season. While lowest AOD is observed during monsoon, and post-monsoon season. The result of this research supports that the use of linear regression model yields good estimation for daily average AOD in Nepal. The model that we have presented could possibly be used in other mountain regions for climate research.

Keywords: Himalaya, MODIS aerosol optical depth, AERONET aerosol optical depth, empirical model, cryosphere

OPEN ACCESS

Edited by:
Pavla Dagsson-Waldhauserova, Agricultural University of Iceland, Iceland

Reviewed by:
Prasenjit Acharya, Vidyasagar University, India
Shubha Verma, Indian Institute of Technology Kharagpur, India
Tommaso Zanca, University of Helsinki, Finland

****Correspondence:***
Bikas Chandra Bhattarai
b.c.bhattarai@geo.uio.no

Specialty section:
This article was submitted to Cryospheric Sciences, a section of the journal Frontiers in Earth Science

Received: *11 July 2018*
Accepted: *24 June 2019*
Published: *05 July 2019*

Citation:
Bhattarai BC, Burkhart JF, Stordal F and Xu C-Y (2019) Aerosol Optical Depth Over the Nepalese Cryosphere Derived From an Empirical Model. Front. Earth Sci. 7:178. doi: 10.3389/feart.2019.00178

1. INTRODUCTION

Aerosols are a focal point of climate research due to their role, and significant uncertainty, in atmospheric processes. Atmospheric aerosol particles scatter, reflect, and absorb incoming solar radiation (as a direct effect) (Chylek and Wong, 1995; Solomon et al., 2007), and modify cloud properties (as an indirect effect) (Charlson et al., 1992; Kim et al., 2014). The uncertainty associated with these processes thusly is considered as one of the huge gaps in current climate prediction capabilities (Parry et al., 2007; Istomina et al., 2011; Alexandrov et al., 2016). Considering the significant role of aerosol in climate processes in the Himalaya (Ramanathan, 2001; Meehl et al., 2008; Nair et al., 2013), different studies have evaluated this region (Ramanathan and Ramana, 2005; Ramanathan et al., 2007; Srivastava et al., 2012) focusing on aerosol emissions,

optical–physical properties, and its climatic implications (Tripathi et al., 2007; Srivastava et al., 2012; Lau, 2014; Soni, 2015; Paliwal et al., 2016; Zhang et al., 2017) as well as impacts for regional hydrology (Matt et al., 2018). These research showed that the aerosols over the Himalayan region are in increasing trend, which is mainly detected during the winter and post-monsoon seasons and are forced by the high anthropogenic emissions, composed of bio and fossil fuel combustions (Acharya and Sreekesh, 2013). Ramanathan and Carmichael (2008) state that aerosols (particularly black carbon) in the high Himalayas likely play significant role in the snow and glacier melt by increasing solar heating. Li et al. (2016) claim the Himalayan region should be considered as the most vulnerable due to the impact of black carbon. Aerosol deposition and its transport over the Himalaya is attracting more attention due to its impact on the transformation of hydrological processes, and regional energy balance, affecting billions of people living downstream (Nepal et al., 2014).

Satellites offer a global perspective on many atmospheric variables, including AOD (Kaufman et al., 2002). Remotely sensed data from satellites has potential to account the highly variable black carbon aerosol properties on global as well as on regional scales and to provide repeated observations over long periods. A well-known example is the MODerate resolution Imaging Spectroradiometer (MODIS) instrument which can provide daily aerosol and its different properties with nearly global coverage at the resolution of 10 and 3 km (Remer et al., 2013). Several works provide an overview of MODIS aerosol retrieval algorithms and products (Kaufman et al., 1997; Chu et al., 2002; Remer et al., 2005; Martonchik et al., 2009; de Leeuw et al., 2011). The basis of MODIS AOD retrievals is that two independent algorithms are used to derive aerosol, one over ocean, and a second to derive over land. The land algorithm is mainly based on the dark target approach (Kaufman et al., 1997; Remer et al., 2005). However, there are some limitations over brighter surface. In both Govaerts et al. (2010) and Mei et al. (2012) the snow and glacier covered surfaces are identified as a great challenge for aerosol retrieval from remote sensing due to the fact the high surface reflectance makes it difficult to separate radiation at the top of atmosphere due to reflection from the snow and from atmospheric scattering by aerosol particles. As Mei et al. (2012), indicate that the crucial issue with using satellite for AOD retrieval over brighter surface is due to very high spectral albedo of the brighter surface like snow at wavelengths in the visible region.

To fully understand the effect of aerosols over the Himalayan region, detailed knowledge regarding the spatio-temporal distributions of aerosols, and their seasonal variability in the atmosphere are required (Bonasoni et al., 2012). Several methods have been used to retrieve AOD over pure snow (Istomina et al., 2009; Mei et al., 2012, 2013), but all these algorithms are restricted to the Arctic region in order to meet the requirement of having a sufficient snow BRDF model (Mei et al., 2013). To date, no algorithm exists to retrieve AOD products over Himalayan cryospheric region (snow and ice surfaces). A more detailed understanding of spatial, and temporal variations of aerosols is required in order to quantify the dynamic influence on the regional climatic conditions.

The objective of this research is to develop an empirical proxy model by using multiple regression, to increase the present understanding of spatio-temporal variability of AOD over the cryospheric portion of Nepal. Three meteorological variables from ERA-interim reanalysis dataset: relative humidity, wind velocity components (U10 and V10) (describe in section 3.3) and observed AERONET AOD from Pokhara AERONET station are used to develop our proxy en empirical model. Our study region is presented in section 2, while the dataset used in this research, and the proposed methods to retrieve AOD is explained in section 3. Results and discussion are presented in section 4, and finally conclusions are presented in section 5.

2. STUDY AREA

The domain of our analysis is the country of Nepal (see **Figure 1**), with our results applicable to the cryospheric portion of the country. Nepal is between India and China, and extends 885 km east-west and 145–248 km north-south. Within this small geographical range, the altitude varies from ∼60 m above sea level (m asl.) in the southern plain, tropical Terai, to the highest peak on the earth in the northeast. Along a south-north transect, Nepal is divided into three ecological belts: Mountain in the northern range, the mid range is called Hill, and the low elevated southern range called Terai (CBS, 2014). Area of the country is 147,181 km^2, out of which about 15% is comprised of high Himalaya, 68% covers by mid hill regions, and the remaining 17% flat valley floor Terai. Around 50% of the total population lives in Terai region, 43% of country population lives in the Hill region, and 7% in the Himalayan region (CBS, 2012). Predominant economic (and aerosol producing) activities (farming, industrial establishment) are conducted in Terai region.

Rapid changes in elevation within a short north-south distance creates a wide range of climatic conditions, from subtropical to alpine/arctic within a span of <200 km. The temperature variation in Nepal is mainly related with the seasons. Within a season temperature varies with topographic variations along north to south direction. Eighty percent of the total precipitation in Nepal occurs during the monsoon (June to September) season (Nayava, 1974; Shrestha et al., 2000) with winter (5%) (December to February) rains more common in the western hills (Ichiyanagi et al., 2007). Pre-monsoon (March-May) season receives about 10% of rainfall while 5% of rainfall occurs during Post-Monsoon (October to November) (Nayava, 1974).

3. DATASETS AND METHODS

3.1. AERONET Data

The Aerosol Robotic NETwork (AERONET) is a federation of ground-based sun photometers which derive total column AOD and other aerosol characteristics based on a radiative transfer inversion algorithm. The network requires standardized instruments, calibration, and processing (Holben et al., 1998). AERONET stations provide measurements every 15 min from a spectral radiometer with a 1.2° field of view, and eight solar

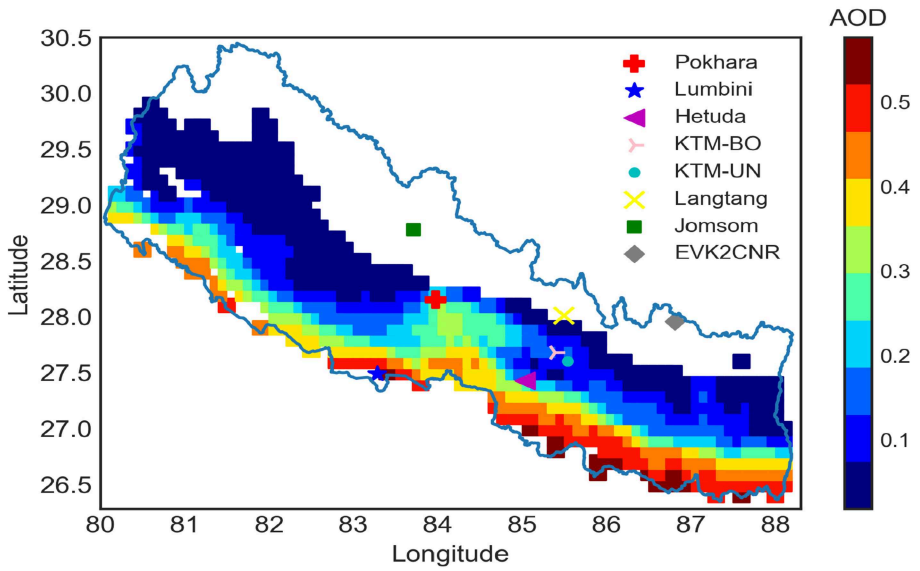

FIGURE 1 | Spatial average dry AOD from daily MODIS observation (2000–2015) over Nepal. Markers in map represent the location of AERONET station.

spectral bands from 340 to 1020 nm are used to calculate, for each wavelength, the AOD, with an accuracy of ±0.01–0.02 (Eck et al., 1999). There are eight AERONET stations in Nepal. The longest time series data come from Pokhara (2010–2016) and the EVK2CNR (2006–2015) station while data from other stations are less comprehensive and for relatively short periods from different years.

The mean AOD at 550 nm from the AERONET stations at different locations is presented as boxplots in **Figure 2**. While we note an elevation dependence of AOD, it must be recognized some stations have limited data. **Figure 2** shows that the Lumbini station located in lowest elevation has highest AOD mean followed by the Hetuda, while the lowest AOD mean value is observed at EVK2CNR at the highest altitude. Systematically the mean are greater than the median indicating that the positive skewed distributions are characteristic of naturally occurring phenomena as indicated by Sriram et al. (2004). Since the number of observed data points are limited in Hetuda and Langtang (up to 2016), further analysis does not include the data from these stations. AERONET datasets were screened for outliers, and these values were removed using a mean ± 3 standard deviation conventional approach (Miller, 1991; Leys et al., 2013). As in prior studies, to provide an effective comparison and analysis, AERONET data are interpolated from 500 to 550 nm using the following computation (Kaskaoutis et al., 2007; Prasad and Singh, 2007; Alam et al., 2014).

$$AOD_{550_{nm}} = AOD_{500_{nm}} \left(\frac{550}{500}\right)^{-\alpha} \tag{1}$$

where $AOD_{500_{nm}}$ in Equation (1) is the AOD measured in 500 nm wavelength. Here α is the Ångstrom exponent from the wavelength of 440–870 nm (Sayer et al., 2013):

$$\alpha = -\frac{\ln(\tau_1/\tau_2)}{\ln(\lambda_1/\lambda_2)} \tag{2}$$

where τ_1, and τ_2 are the AOD at wavelengths λ_1, and λ_2.

As explained below, in section 3.5, our empirical proxy aerosol model performs better with dry than wet aerosols. To derive dry AOD from wet AOD we use the approach of Zhang et al. (2017) to account for hygroscopic growth.

$$AOD_{dry} = \frac{AOD}{f(RH)} \tag{3}$$

where, RH is relative humidity, AOD_{dry} represents the AOD with a dehydration adjustment. $f(RH)$, the hygroscopic growth factor, denotes the ratio of the aerosol scattering coefficient in ambient with a certain relative humidity to that in the dry air condition (Li et al., 2014; Zheng et al., 2017). $f(RH)$ can be expressed as:

$$f(RH) = \frac{1}{(1 - RH/100)} \tag{4}$$

We have tested the different hygroscopic factors given by Li et al. (2014) to convert observed AOD in to a dry state and Equation (4) performed best to yield a higher correlation of AOD_{dry} with meteorological parameters. Hereinafter, all references to AERONET AOD denote AOD_{dry} at 550 nm from AERONET, unless otherwise indicated, and wavelength subscripts are not assigned for conciseness.

3.2. MODIS Data

In this study we use 16 years (2000–2015) of AOD data obtained from the MODIS instrument on-board, the NASA EOS satellites.

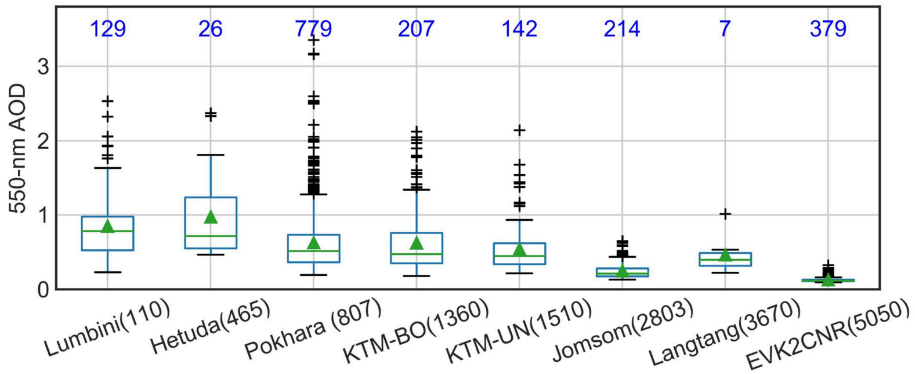

FIGURE 2 | Box plots for AERONET AOD observation at 550-nm in Nepal. The blue number in the figure represents the total number of AOD observation at each AERONET station. Along the abscissa numbers inside brackets after each name of the station are station elevation in m asl. Green triangle and lines inside boxplots are the mean and median values, respectively.

The MODIS products provide three processing levels of data: Level 1 (geolocated radiance, and brightness temperature), Level 2 (retrieved geophysical data products), and Level 3 (gridded averages of geophysical retrievals) data. There are two MODIS Aerosol data product files: `MOD04_L2`, containing data collected from the Terra platform; and `MYD04_L2`, containing data collected from the Aqua platform. Daily `Level_2` (Collection 6) data produced at the spatial resolution of a 10 km x 10 km (at nadir) from the Terra platform `MOD04_L2` is used in this study. The `MOD04_L2` product provides global AOD from the dark target (DT) (Kaufman et al., 1997; Levy et al., 2013), and deep blue (DB) algorithms (Huss, 2013). The DT algorithm is applied over the ocean and dark land surfaces, while the DB algorithm is used for brighter surfaces. The data analysis that follows uses AOD at 550nm to be consistent with the wavelength used by many climate transport and chemistry models (Kinne et al., 2013) and prior MODIS validation studies (Levy et al., 2007, 2010; Safarpour et al., 2014). MODIS scientific datasets (SDS) in Level 2, collection 06 is used to retrieve AOD for this study.

Table 1 provides the names for the relevant scientific datasets within the MODIS Level 2 aerosol products. In order to select the optimal MODIS scientific dataset for our purposes, we conducted a brief validation and evaluation of different scientific dataset performance in relation to the Pokhara AERONET observations. Validation of MODIS AOD with AERONET observed AOD (dry AOD from both observation) is carried out to find the best fit MODIS scientific dataset with AERONET datasets. For the validation, we followed the procedure described by Ichoku et al. (2002) and Li et al. (2009). Spatial and temporal variability of AOD distributions were taken into account. MODIS retrieval at 10 km x 10 km and AERONET measurement within ±30 min of MODIS overpass time and atleast 3 out of 9 MODIS retrieval in a square box of 30 × 30 km centered over AERONET site were used. After that mean values of co-located spatial and temporal values were used for calculating error statistics (i.e., RMSE, correlation coefficient). Scatter plots between mean AERONET and MODIS AOD for different scientific dataset are shown in **Supplementary Figure 1**. Although different datasets have different expected error (EE), $\pm(0.05+0.15AOD_{AERONET})$ is used for direct comparison (Remer et al., 2005). Validation results shows that the lowest RMSE (0.13), with highest correlation coefficient (0.75) and EE (71%) is found for aerosol optical depth estimated from deep blue algorithm. The correlation coefficient for the best estimate is higher (0.75), but MODIS has large underestimation. Large AOD underestimation by MODIS in the studied site does not affect the current study because MODIS AOD is only used in a relative sense to determine gradient along the mountain slope.

Using classical regression model evaluation statistics, we also calculated at the Pearson Correlation coefficient (Adler and Parmryd, 2010) for the different MODIS scientific dataset in two forms (i.e., dry (converted by using Equation 3) and normal) against the observations. The correlation coefficient between AERONET AOD and MODIS AOD in normal (0.75) as well as in dry form (0.87) are also highest for aerosol optical depth estimated from deep blue algorithm (**Table 1**). We selected this scientific datasets and hereinafter this is refers to as MODIS AOD.

3.3. ERA-Interim Data

We use the daily average ERA-Interim global atmospheric reanalysis dataset (Berrisford et al., 2011) to obtain the meteorologic parameters over Nepal. The data of this reanalysis are available from ECMWF website http:apps.ecmwf.int/datasets/. Nine variables are included in the analysis: albedo, 10m wind velocity components (U10 & V10), total columnar water vapor, total columnar water, 2m dew temperature, 2m surface temperature, sea level pressure, and surface level pressure. Obtained datasets are linearly interpolated to the resolution of 10 × 10 km. Additionally, we include relative humidity in our analysis, which is calculated using the equation given by Dingmann (2015):

$$Relative\ humidity(\%) = 100 \times \frac{exp\left[\frac{17.625\times TD}{243.04+TD}\right]}{exp\left[\frac{17.625\times T}{243.04+T}\right]} \quad (5)$$

TABLE 1 | Pearson correlation coefficients between daily average AERONET AOD with MODIS AOD in dehydrated (dry) and normal (without dehydration) form.

S.N.	MODIS scientific datasets	Pearson correlation coefficient (r)	
		Normal AOD	Dry AOD
1	Opital_Depth_Land_And_Ocean	0.68	0.85
2	AOD_550_Dark_Target_Deep_Blue_Combined	0.68	0.85
3	Corrected_Optical_Depth_Land	0.57	0.76
4	Deep_Blue_Aerosol_Optical_Depth_ 550_Land_Best_Estimate	0.75	0.87

where, T, and TD in Equation (5) are the 2 m air temperature, and dew point temperature in °C, respectively.

3.4. Digital Elevation Model (DEM)

A detailed map of land surface elevation was obtained from the Advanced Spaceborne Thermal Emission, and Reflection Radiometer (ASTER) (Fujisada et al., 2005) with 30 m resolution. The DEM is re-sampled to the ground resolution of 10 × 10 km using a nearestneighbor interpolation technique available in the re-sampling tools of spatial analyst in ESRI ArcGIS.

3.5. Regression Analysis

Multiple linear regression methods with Ordinary Least Square (OLS) assumptions (i.e., the model is linear in the parameter and error terms are identically and independently distributed) (Kleiber, 2001) are applied to develop an empirical model for dry AOD based on ERA-Interim predictors. Daily average AERONET AOD in dry form at Pokhara station (see **Figures 1**, **2**) is selected as the dependent variable, as the statistical significance was greatly improved compared to the use of the wet aerosols. We have selected Pokhara to develop our model as it has the longest time series (2010–2016) with consistent data quality. The nine aforementioned meteorological variables from ERA-Interim are initially used as independent variables and we conducted a step-wise multiple linear regression analysis (Bendel and Afifi, 1977).

All the data were linearly de-trended (Tanabe et al., 2002) and normalized ($\frac{X-\bar{X}}{S_X}$) before doing the statistical analysis. Scatter plots between the dependent and independent variables are presented in **Figure 3** with the resulting correlation coefficients (r).

To maximize the estimation power of the model using the minimum number of independent variables, forward step-wise regression process (Bendel and Afifi, 1977; Khatibi Bardsiri et al., 2014; Silhavy et al., 2017) is used to identify the independent variables. The selected regression model from the step-wise regression process, based on Pokhara AERONET data as a dependent variables, and average daily ERA-interim as independent variables is given by:

$$AOD_{sim} = -0.030 - 0.6035 \times RH + 0.2140 \times V10 + 0.3140 \times U10 + \epsilon \quad (6)$$

where, $\epsilon \sim N(0, \sigma^2)$ is an error term that is associated with the model prediction. AOD_{sim} is the simulated AOD in dry form.

We found that the coefficient of determination (R^2) of the model is 0.53 for daily values. Observed *P*-value for all the regression coefficients are <0.05 indicating that the model is statistically significant at 95% confidence level. In the developed empirical model given by Equation (6) simulated dry AOD (AOD_{sim}) is determinedly the relative humidity, and wind components (U10 and V10). Higher relative humidity is associated with removal of aerosols, reducing the AOD (loss term, negative coefficient), and aerosol sources are predominantly to the south, and west of Nepal, so southerly (V10 > 0), and westerly (U10 > 0) winds should bring higher aerosol content (source term, positive coefficients). Although Equation (6) is a proxy model only (as we have not considered emission flux and sources), this interpretation shows a relation to processes controlling the AOD.

3.6. Model Correction

Possible biases in simulated AOD due to the altitudinal gradients (see section 4.1) are corrected by three methods using:

- Model-1: average regression slope from MODIS,
- Model-2: monthly regression slope from MODIS data,
- Model-3: monthly regression slope calculated from the AERONET station data,

abbreviated as M1, M2, and M3, respectively. Now the correction equation for all models becomes Equation (7), except that the value of regression slope will change according to the model.

$$AOD_{corr} = AOD_{sim} + AOD_{sim} \times Exp(E_i - EB) \times Slope \quad (7)$$

where, E_i is the elevation of respective station, *EB* is the elevation of base station i.e., elevation of AERONET station at Pokhara.

3.7. Model Evaluation Statistics

We briefly describe three standard statistical metrics which were used throughout the analysis to evaluate the performance model results: Root Mean Square Error (RMSE), Pearson correlation coefficient (r), and percent bias (PBIAS). These are described below.

- Root Mean Square Error (RMSE): is the standard deviation of the residual (prediction errors). It is the distance, on average, of the fitted line for a data point to the observed value. Hence it is consistent in terms of measurement units and provides a metric that is easy to interpret: the smaller an RMSE value, the

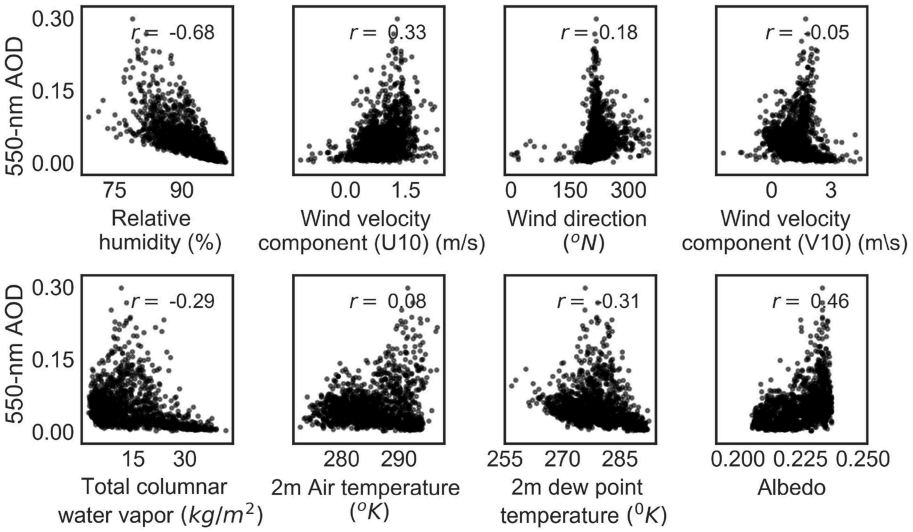

FIGURE 3 | Scatter plots between aerosol optical depth with meteorological variables. "r" represents Pearson correlation coefficient between aerosol optical depth and meteorological variables.

closer predicted values are to the observed. Mathematically it is describe by Chai and Draxler (2014)

$$RMSE = \sqrt{\frac{(AOD_{sim} - AOD_{aeronet})^2}{n}} \quad (8)$$

where n is the total number of observations, AOD_{sim} is the simulated AOD from the model, and $AOD_{aeronet}$ is the AERONET AOD, respectively.

- Pearson correlation coefficient (r): r (Pearson, 1896) measures the strength and the direction of a linear relationship between our observed and simulated AOD. The mathematical formula for computing r given in Pearson (1895) is used. The numerical value of the correlation coefficient can vary numerically between −1, and 1. The closer the correlation is to 1.0, the stronger the relationship between the two variables, whereas a negative value defines an anti-correlation.
- Percent bias (PBIAS): measures the average tendency of the simulated AOD to be larger or smaller than their observed counterparts (Moriasi et al., 2007). The optimal value of PBIAS is 0.0, with a low-magnitude value indicating accurate model performance. Positive values indicate model underestimation bias while negative values indicate overestimation bias.

$$PBIAS = \left[\frac{(AOD_{aeronet} - AOD_{sim}) \times 100}{\sum(AOD_{aeronet})}\right] \quad (9)$$

4. RESULTS AND DISCUSSION

4.1. Altitudinal Distribution of AOD

Shown in **Figure 1** is the spatial distribution of average observed AOD from MODIS over Nepal for the period of 2000–2015. It is clear that the spatial gradients of AOD are inversely related to the topography, i.e., higher AOD over the southern low land and lower AOD over the mountainous regions of Nepal. Scatter plots (**Figure 4**) show that the AOD non-linearly decreases with the altitude (steep negative gradient) up to ∼500 m asl. and thereafter varying more smoothly with the altitude. We found that the altitudinal distribution follows a semi-logarithmic form with a slope and coefficient of determination of −0.135 and 0.899, respectively (blue points in **Figure 4** is the linear transfer of elevation by taking natural log). Since the aerosol load over the region varies greatly with the seasons (Acharya and Sreekesh, 2013), slope coefficient of the regression equation on the monthly average MODIS and AERONET observations are calculated over Nepal. In **Figure 5** the blue points represent an average AOD per each grid cell with respective elevation in semi-logarithmic scale. The red triangles represent the monthly average AOD from the AERONET stations. As compare to AERONET AOD, MODIS underestimates AOD in all months. Monthly gradients from MODIS and AERONET observations are different. But from both observations, the strongest elevation gradients are observed during the winter season, while the weaker gradients are observed during the monsoon season.

4.2. Seasonal Variability and Spatial Distribution of MODIS AOD

We calculated a spatial average (2000–2015) of the MODIS AOD in the dry forms for each season to evaluate the seasonal variability. These are shown in **Figure 6**. The maps show average AOD retrievals over Nepal are concentrated toward lower elevations (Terai) where a high density of data pixels exists, and the retrievals are limited in higher elevation regions due to high surface reflectance. However, the seasonal spatial distribution of AOD over Nepal clearly shows typical cycle of AOD with high AOD in winter and pre-monsoon, and low in monsoon and post-monsoon seasons. We present a further discussion of the seasonal dynamics of AOD over Nepal in section 4.5.3.

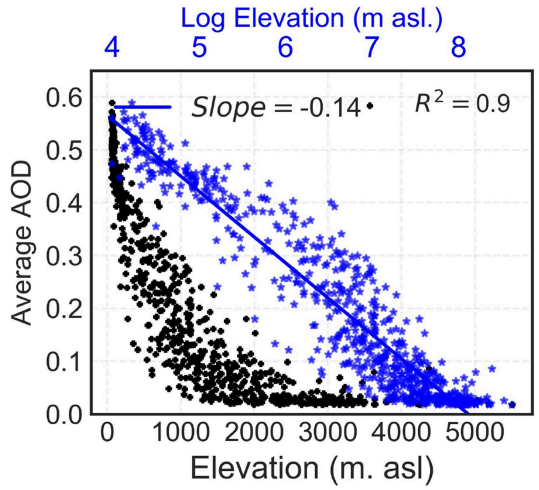

FIGURE 4 | Scatter plot for MODIS average AOD for the period of 2000–2015 with the altitude and log normally transferred altitude.

4.3. Validation of MODIS AOD With AERONET

Because of enormous altitude variation within a short south to north distance, Nepal has remarkable climatic variability (tropical to Arctic) (Li et al., 2017) which poses a challenge for satellite remote sensing of aerosol. Validation of remotely sensed AOD with ground based instruments (AERONET) is worthwhile in a region where such studies have not yet been completed. We followed the general way to validate MODIS AOD against AERONET AOD and the detailed procedure that we followed is explained in section 3.2. Scatter plots between mean AOD from MODIS and AERONET for different stations are plotted and shown in **Supplementary Figure 2**. The AERONET sites are located in different elevations ranging from 110 to 5,050 (m asl.) (**Figure 2**), but the validation is done in four AERONET stations (i.e., Lumbini, Pokhara, KTM-BO, and KTM-UN) with MODIS observations. The comparison is performed using co-located points. Seasonal analysis of these co-located AOD data shows that, most of these data points are from winter, and pre-monsoon season in all stations. In Pokhara, KTM-BO, and KTM-UN AERONET stations about 30, 55, and 41% of the co-located data are from winter season, while 55, 29, and 25% of the co-located data are from pre-monsoon season, respectively. The linear correlation coefficient, with RMSE, and regression slopes between AERONET, and MODIS observation over four station are given in **Table 2**. The regression slope, and intercept from **Table 2** shows that AOD observations from AERONET in all station are higher than from MODIS.

Chu et al. (2002) and Li et al. (2009) showed that the intercept of linear regression different from zero represents the errors in surface reflectance estimates, and the regression slope differing from 1.0 represents a systematic bias of MODIS AOD retrievals. We also tried to do similar comparison in our study. **Table 2** shows good correlation (0.75–0.91) between MODIS derived and AERONET observed average daily dry AOD with intercept values between 0.29 and 0.44, and a regression slope between 0.62 and 1.65. About 43, 74, and 69% of the observations fall inside expected error (EE) from KTM-BO, KTM-UN and Lumbini AERONET station. Lower percentage inside EE from KTM-BO might be due to fewer observation compared to KTM-UN and Pokhara (**Figure 2**). However, in comparison with global validation results (Levy et al., 2007), with intercept of 0.029, and slope of 1.009, MODIS C005 AOD retrieval has higher errors in Nepal. The relatively high positive offset of MODIS AOD in Nepal (e.g., intercept 0.29–0.44) is indicative of the poor estimates in surface reflectance (Li et al., 2009). Moreover, daily MODIS, and AERONET derived AOD are not concurrent in time. Therefore, the sampling time inconsistency for AERONET and MODIS AODs is also a source of uncertainty.

4.4. Average MODIS AOD Distribution With Inter Annual Variability, 2000–2015

Analysis of seasonal average dry AOD for Nepal shows the nature of the dynamics of aerosol concentration during the study period. **Figure 7** shows inter annual variability and 16 years AOD trends for each season from MODIS. It shows that the AOD exhibited an increasing trend in all seasons except in winter, but only the trend in monsoon season is statistically significant at 95% significant level (faint dashed lines in **Figure 7**). The highest average AOD throughout the period was in the pre monsoon, whereas the monsoon season showed an increasing trend after 2012. Between 2002–2004, and 2007–2010, the post-monsoon curves showed significant lowering of average AOD. The high AOD in pre-monsoon during 2001–2005 may be attributed to low rainfall over most parts of Nepal (Department of Hydrology and Meteorology Government of Nepal, 2017), which caused an increase in aerosol loading in the atmosphere. The winter decline in AOD (0.36–0.16) from 2000 to 2003 (0.046–0.01), and 2007 to 2010 (0.03–0.02) was possibly due to a reduction of aerosol load through higher precipitation observed over Nepal. Overall, significant increasing trend with slope of 0.0006, and *p*-value of 0.042 is observed for average AOD over Nepal. This weak but significant increasing trend may be attributed to annual decreasing trend in precipitation in Nepal (1.3 mm per year), although this precipitation decreasing trend is not significant (Department of Hydrology and Meteorology Government of Nepal, 2017).

In order to see the average inter-annual variability of AOD in Nepal, monthly average dry AOD from both MODIS and AERONET data are plotted in **Figure 8**. Standard deviation about the mean from corresponding nine cell MODIS observation is plotted as shaded part in the plot. From the seasonal AOD analysis, AERONET AOD is found higher than most of AOD observation from the MODIS. Although the seasonal AOD comparison between MODIS and multi wavelength radiometer (MWR) by Guleria et al. (2012), and between MODIS, and Multiangle Imaging Spectro-Radiometer(MISR) by Prasad and Singh (2007) over Indian subcontinent shows that MODIS is overestimating during summer, and underestimating during winter. But we found that in four stations MODIS AOD is lower

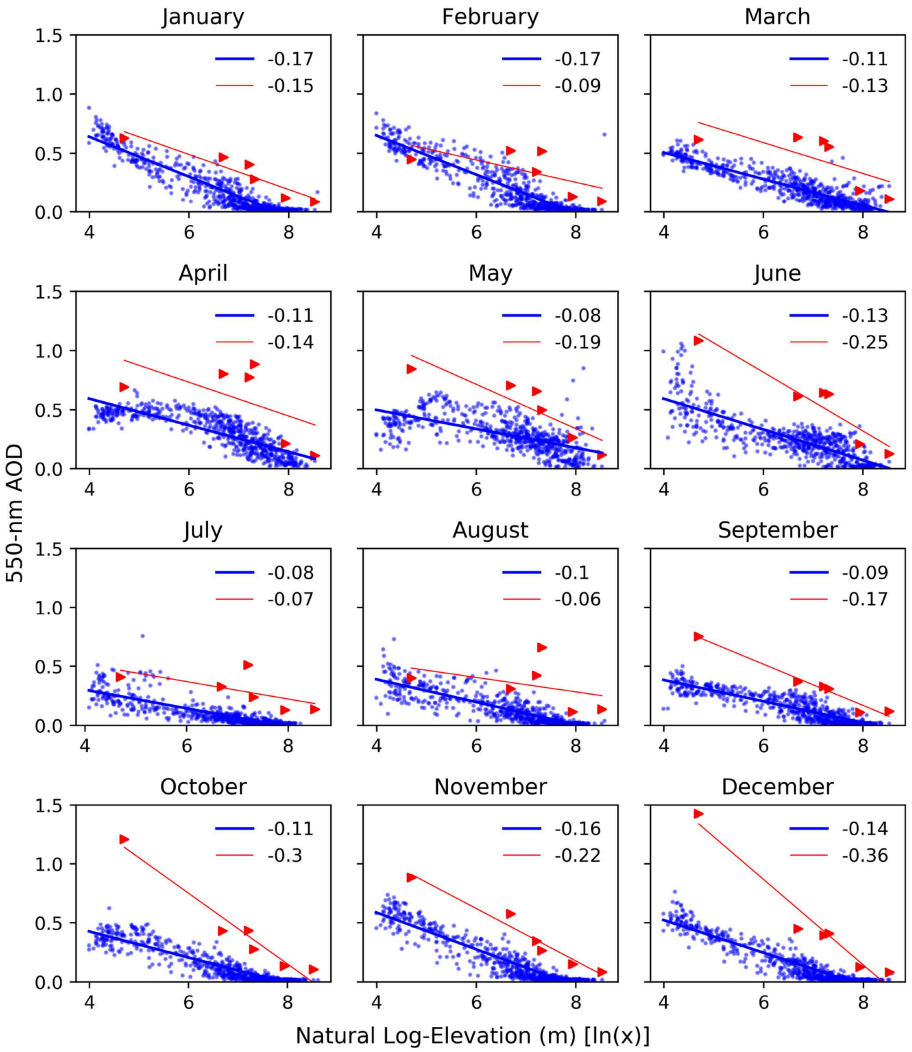

FIGURE 5 | Monthly average AOD at 550 nm from MODIS (blue) and AERONET (red) observation with log elevation. Blue and red lines show the best fit linear lines for each datasets. Numbers in each subplots show the slope for each best fit lines, respectively.

than AERONET AOD (**Figure 8**). From MODIS and AERONET observation, the highest AOD is observed during the period of March-May when Nepal experiences heavy spring dust from north-west a feature that might be attributed to the fact that we use dry aerosol in this analysis. The scavenging effect of the rain can be seen from both observations as the lowest AOD is observed during the period of July-August when the monsoon season initiates. The highest AOD observed is at Lumbini during November and December, and likely results from biomass burning for heating in the Terai region (Wang et al., 2013).

4.5. Model Result Analysis

The empirical model obtained from Equation (6) resulting from the multiple linear regression is used to simulate daily dry AOD at different AERONET stations in Nepal. Simulated daily dry AOD values with observed data are plotted in time in **Figure 9**. The time series can be effectively used to understand the predictability of the model. It is observed that the simulated dry AOD values are similar to the measured values except in Jomsom, and EVK2CNR station. The average bias (difference between observed mean with simulated mean) between simulated and observed value are found to be 0.0002, 0.034, 0.009, 0.013, −0.045, −0.043 for Pokhara, Lumbini, KTM-BO, KTM-UN, Jomsom, and EVK2CNR station, respectively. Results showed that the model underestimated when is used to simulate AOD in lower elevation region than Pokhara station, and overestimated AOD in Jomsom and EVK2CNR, which are located in higher altitude. The correlation coefficient between observed and modeled dry AOD (presented inside each plot) are found to be higher at stations in higher altitude indicating their higher similarity between observed and simulated values.

We found that the disagreement (i.e., highest PBIAS and RMSE) between the simulated, and observed AOD is due to the altitudinal dependencies (**Figure 5**), as it follows the topography

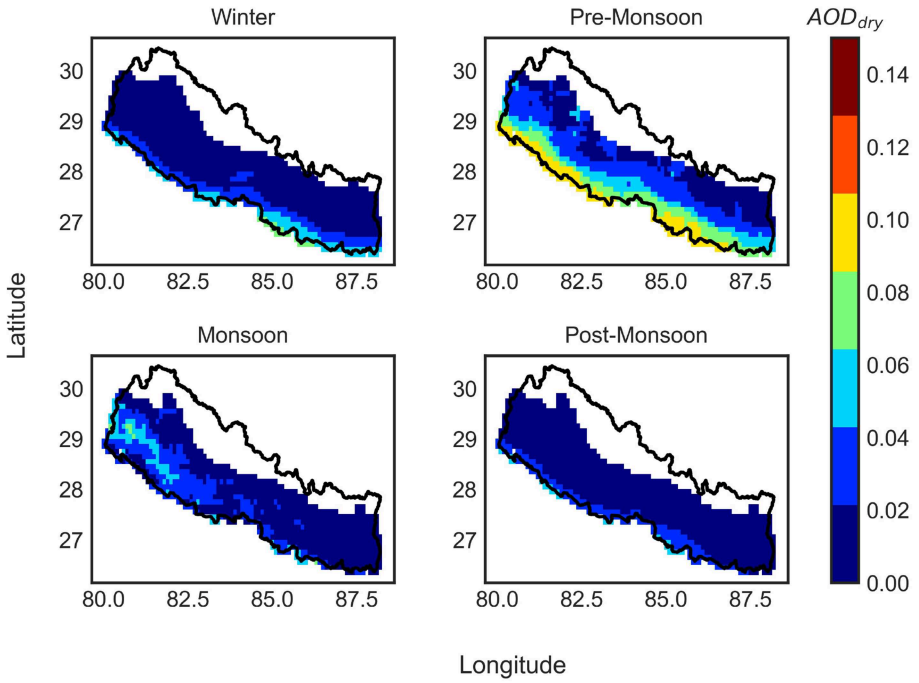

FIGURE 6 | Seasonal average MODIS AOD (2000–2015) over Nepal.

TABLE 2 | Different statistics calculated from daily average AERONET AOD and daily MODIS AOD for each station.

			Linear regression	
Station	**RMSE**	**Correlation coefficient**	**Slope**	**Intercept**
Lumbini	0.33	0.91	0.62	0.44
Pokhara	0.13	0.75	1.34	0.31
KTM-BO	0.39	0.75	1.65	0.29
KTM-UN	0.39	0.84	1.29	0.29

with higher AOD values over the low land than over the mountain area (**Figure 1**). Roux et al. (2008) showed that the lower aerosol load in French mountains are because of high wet deposition due to orographic effects, but in the case of Nepalese mountainous region, lower AOD observed from MODIS and AERONET might be lower anthropogenic activity in the region in addition. As we discussed in sections 4.2 and 4.4 that the aerosol distribution in Himalayan region are not only dependent upon altitude, but also dependent upon seasons, because the Hindu-Kush-Himalayan region is strongly influenced by large-scale atmospheric circulation, which alternates between the wet summer monsoon, and dry season. As the distribution of aerosols over time and space is determined by its type, size, and source (Cristofanelli et al., 2014), aerosols transported to Himalayas mainly from Indo-Gangetic plain during the pre-monsoon season (Ramanathan et al., 2007; Kopacz et al., 2011) are deposited differently over the space. Dhungel et al. (2016) mentioned that the different sources of AOD for the Himalayan region (especially to Nepal) are from biomass burning (mainly in mountain region) and fossil fuels combustion (in low land or Southern parts of Nepal).

To overcome biases between the model and observed AOD, monthly average regression slopes obtained from the linear regression between log elevation and AOD (**Figures 4**, **5**) are used to correct the simulated AOD values from the model over the different stations. Results from three different methods (see section 3.6) are discussed in section 4.5.1.

4.5.1. Model Performance Evaluation After Using Different Regression Slope Values

The three different slope correction models M1, M2, and M3 are compared with the daily average dry AOD values observed from respective AERONET stations. Model evaluation statistics were calculated, and presented in **Figure 10**. AERONET stations in **Figure 10** are arranged in such a way that the station elevations (**Figure 2**) are in increasing order from Lumbini to EVK2CNR in anticlockwise direction.

From the calculated error statistics (**Figure 10**), the models for the stations at the lower elevations are performing at a very close PBIAS, if we compare the PBIAS among all. With increasing station elevation, performance of the model decrease for M2, and M3. Performance difference can be clearly seen at EVK2CNR and Jomsom stations, where correlation coefficient of 0.1, 0.5, 0.82, RMSE of 0.018, 0.01, 0.002 with PBIAS of 136.8, −62.8, 4.9 are observed for the models M3, M2, and M1, respectively at EVK2CNR. Although a higher correlation

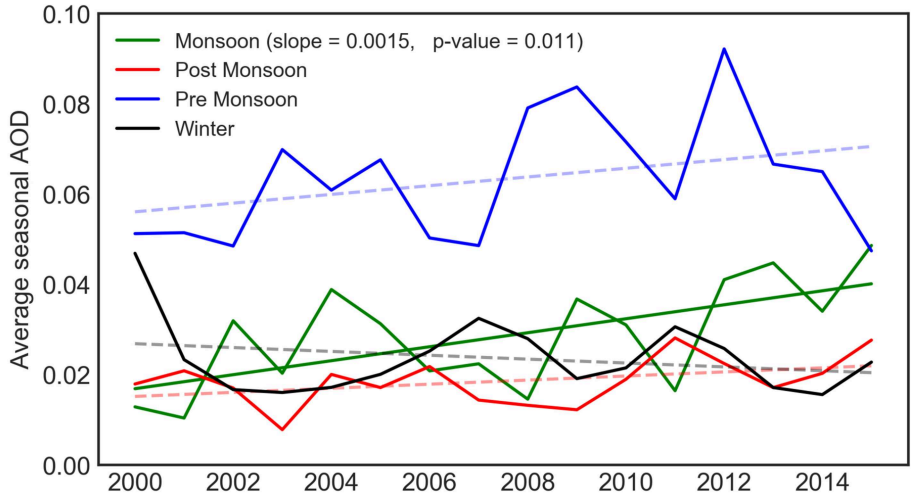

FIGURE 7 | MODIS average dry AOD (2000–2015) with seasonal trend over Nepal.

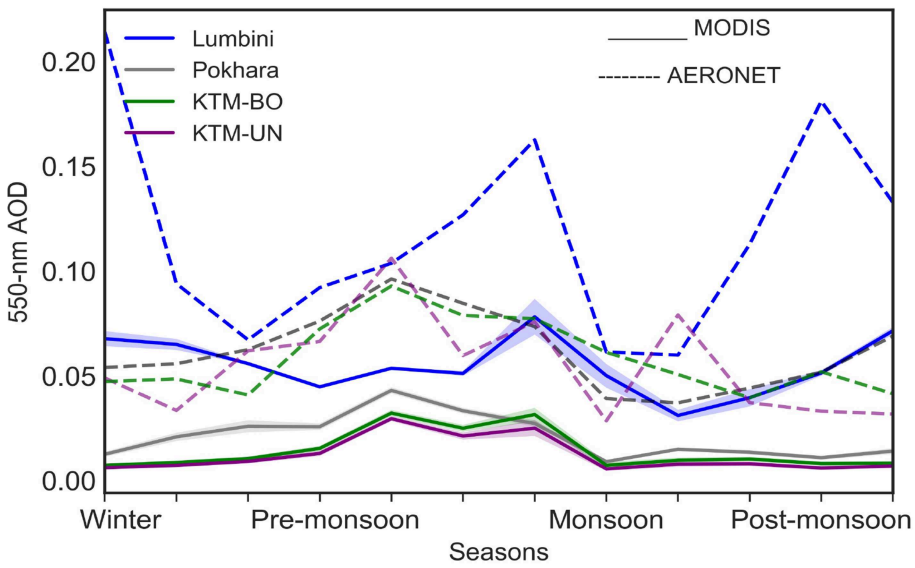

FIGURE 8 | Inter-annual variability of observed dry AOD from MODIS and different AERONET stations. Solid lines with shading are for the MODIS observations. Solid lines represent the mean values while shading represents the variance within nine cells of an AERONET station. Dotted lines are the respective observations from AERONET stations.

coefficient of 0.85 is observed in Jomsom station from the model M2 than model M1 (0.83), but the PBIAS and RMSE are better for model M1 (-68.2% and 0.014) compared to M2 (91% and 0.018). M3 performs similar to M1 and M2, however, it also tends to underestimate AOD with increasing elevation. Underestimation of AOD at EVK2CNR station from the model M3, is mainly due to the steeper regression slope obtained from the available monthly average AERONET data compared to the monthly regression slopes from the monthly MODIS AOD. Referring to **Figure 5**, monthly regression slopes mainly in Oct, Nov, Dec, April, May, and June are steeper when compared with monthly MODIS slope as well as average slope. These steeper slopes force the model M3 to predict relatively lower AOD values resulting overall underestimation and low predictability of the model M3.

Overall, our conclusion is that M1 performs the best of the three. In addition to the improved performance the correction is most simple, using an average regression slope from MODIS, and therefore M1 is recommended for the extrapolation of AOD in the Nepalese Himalaya region. But the selection of model might be different for the different purpose of study. In a study about seasonal patterns, model correction by monthly slope

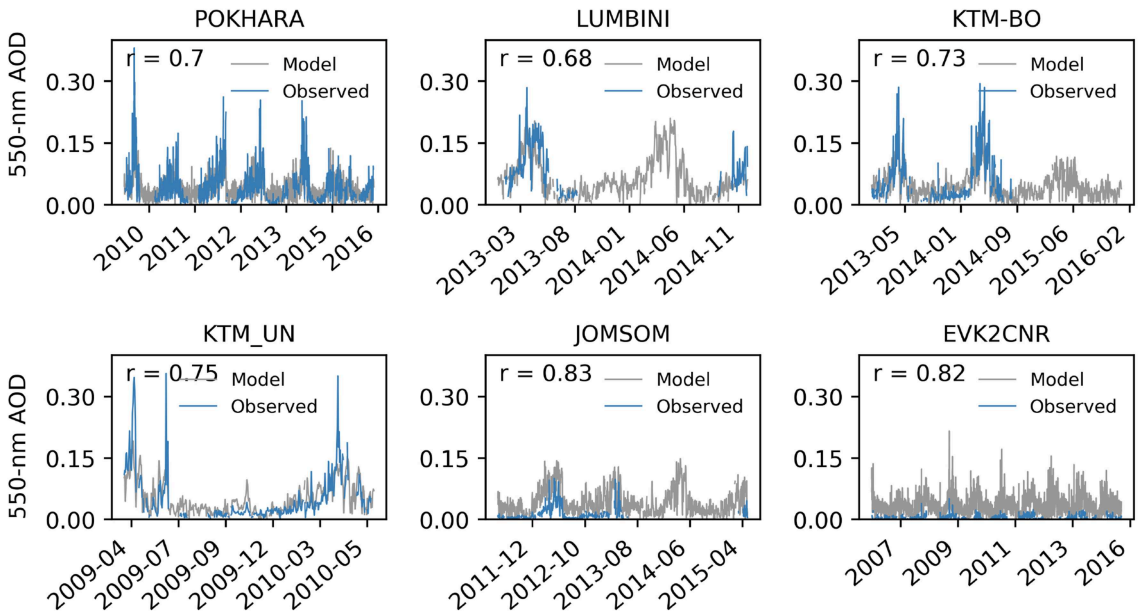

FIGURE 9 | Observed and model aerosol optical depth at different AERONET stations in Nepal. "r" represents the correlation coefficient between observed and model values.

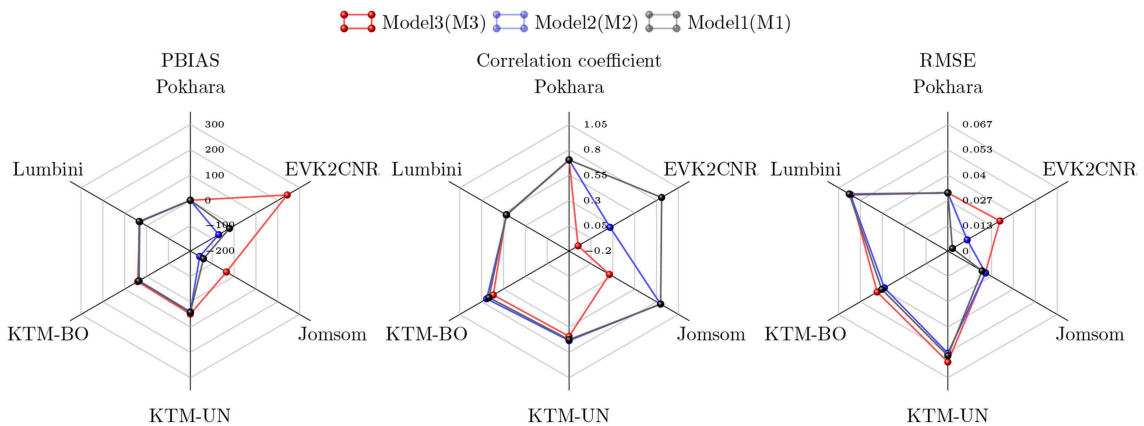

FIGURE 10 | Different model evaluation statistics. Names in each axis represents location of AERONET station and are in increasing station elevation (Lumbini to EVK2CNR) order. Color lines in each radar diagram is for error statistics (correlation, PBIAS, and RMSE) for different models: M1, M2, and M3.

might be appropriate, although the difference between these two models (M1 and M2) is not big. In **Figure 11**, observed and predicted AOD from M1 is presented. The correlation coefficient between the simulated AOD from model M1 and observed AOD from AERONET stations, Pokhara, Lumbini, KTM-BO, and KTM-UN are 0.7, 0.52, 0.72, and 0.67, respectively. We found that PBIAS in Pokhara, Lumbini, KTM-BO, and KTM-UN are 0.5, 34.4, 36.1, and 41.9%, respectively, indicating a general underestimation from the model. Highest RMSE (0.06) is calculated at Lumbini while the lowest is observed at Pokhara (0.03).

To better understand the seasonal predictability of the selected model, the longest time series of daily observed and simulated dry AOD data at Pokhara (2010–2016) and EVK2CNR AERONET stations (2006-2015) are taken in to account. During the monsoon season, the simulation give results that agree with measured dry AOD at Pokhara station where correlation coefficient of 0.89, with 0.019 RMSE, and lowest PBIAS of −0.6 were observed, and these values are better than in other seasons. In EVK2CNR, higher correlation coefficient between AERONET and simulated AOD were observed in winter (0.92), and in post-monsoon (0.89) season with RMSE of 0.002 and 0.0015, respectively. Low model performance (i.e., low correlation coefficient, large PBIAS and high RMSE) during the winter season at Pokhara is due to local air pollution. Since 87% of the energy requirement of the county

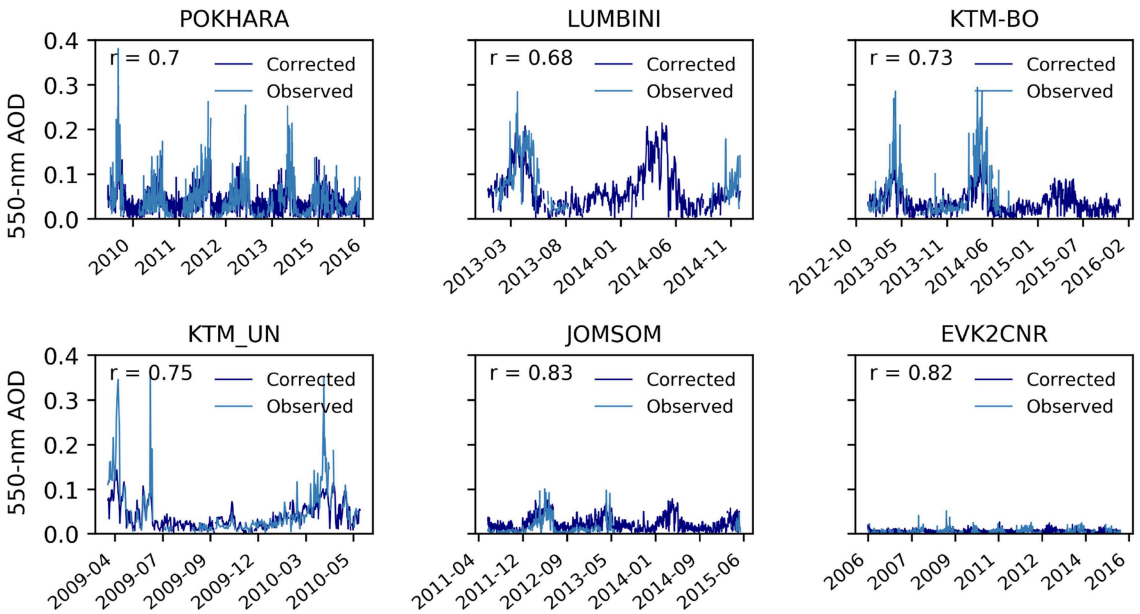

FIGURE 11 | Plot between dry AOD from AERONET and predicted AOD from M1 at different AERONET stations in Nepal. Inside each plot "r" represents the Pearson correlation coefficient.

is fulfilled by traditional sources like firewood, animal dung, and some paper residue leaves of trees to warm houses and as a kitchen fuels (Ranabhat et al., 2015), producing human-made aerosols in the form of smoke (Panday and Prinn, 2009). Higher model performance during the post-monsoon and winter season at EVK2CNR is due to the absence of local sources of pollution as compared to Pokhara station. Observed higher performance during the post-monsoon and winter season at EVK2VNR is also due to the number of sufficient observations during that season as the percentage of data point observations in post-monsoon and winter seasons are 35.63 and 26.24%, respectively.

4.5.2. AOD Simulation Compared With MODIS AOD

Since the simulation results from M1 is found better than the other models, it is further used to simulate dry AOD over all Nepal, and results are compared with the corresponding MODIS AOD observations. Comparison is made by calculating correlation coefficients between the simulated AOD with MODIS AOD. We found that the most of the correlation grid (see **Figures 13A,B**) shows that the values above 0.5 with some exception. We observed that the correlation coefficient between MODIS observation and model simulation is higher at lower elevations in Nepal. As the model is developed by using AERONET data, systematic error between MODIS observation and AERONET observation also leads to lower correlation coefficient. In addition to systematic errors between the two observations, the impact of clouds and coarse spatial resolution of MODIS (10 × 10 km) may also introduce other uncertainties. **Figure 12** shows the seasonal distribution of model AOD over Nepal. It follows the same seasonal distribution as we found from MODIS observation.

4.5.3. Seasonal AOD From MODIS and Model

Figures 6, **12** show the seasonal distribution of dry AOD from MODIS and model. From both, highest AOD is observed during winter and pre-monsoon season and lower AOD during the monsoon and post-monsoon season. In winter spatial distribution of dry AOD shows that for most of the southern part of Nepal, moderate to high values prevail. Cold surface conditions in winter, mostly in the southern plain region of Nepal, produces very dense mist, haze, and fog, through water vapor condensation on carbonaceous aerosol particles from biomass burning leading to elevated AOD, which is well-captured by MODIS observation. Higher average AOD values are observed over the Terai region which may be attributed to biomass burning activity during colder weather (Wang et al., 2013). Increased burning activity, in association with emission from industrial and fossil fuel burning (especially in Terai), also increases atmospheric AOD loading.

In pre-monsoon season, the shifting of the inter tropical convergence zone to Indo-Gangetic plain produces intense heating of the surface resulting in moderate to strong westerlies winds (Nayava, 1980). These westerlies are also associated with strong dust storms (Acharya and Sreekesh, 2013) occurring mostly over the southern part of Nepal, transferring large amounts of dust to the air leading to higher AOD in the atmosphere (**Figure 6**). The spatial variability of AOD is also controlled by the surface moisture content during this period. Intense temperature, in association with strong surface winds during pre-monsoon, plays an important role in heating and lifting the loose soil. The onset of gusty winds during the pre-monsoon (Shea et al., 2015) caused by convectional instability, produces a large amount of dust

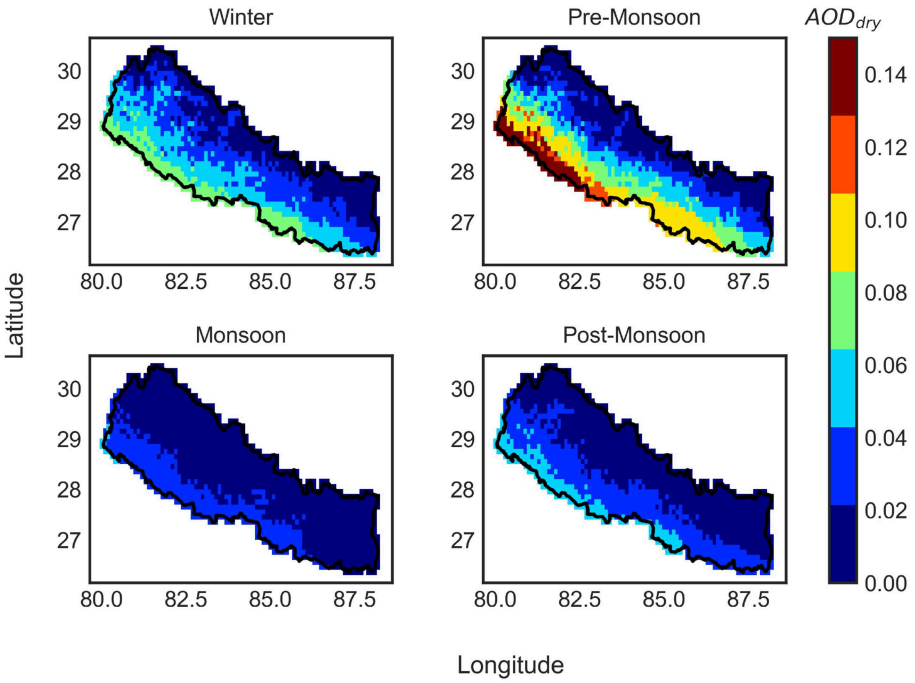

FIGURE 12 | Seasonal average AOD over Nepal from the M1.

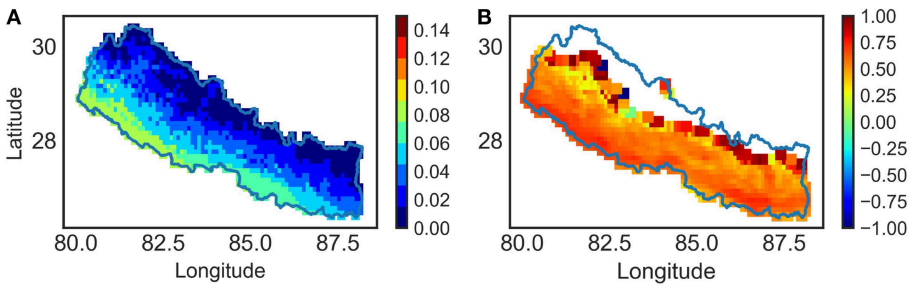

FIGURE 13 | (A) Spatial average dry AOD (2000–2015) from daily model simulation over whole Nepal. **(B)** Correlation coefficient between M1 output and AOD from MODIS satellite in dry form for each grid cell over Nepal.

aerosol locally leads to an increase in AOD during this season (Flossmann et al., 1985).

The monsoon climate over Nepal controls the seasonal aerosol concentration in the atmosphere. Lower AOD during monsoon is observed from model and MODIS observation (**Figures 6**, **12**). The lower AOD is due to the significant amount of rainfall which occurs during the monsoon, accounting for 60-90% of the total annual rainfall (Nayava, 1980). Higher amount of rainfall leads to higher relative humidity forcing model to predict lower AOD value. Therefore, the concentration of aerosol particles is reduced during this season as they are rapidly removed from the atmosphere through wet deposition (Gonçalves et al., 2010) which is well-captured by model and MODIS. Despite a strong dependence on the monsoon, interestingly the total average MODIS AOD value over Nepal during the monsoon season (0.02) is higher than during winter season (0.017). However, this potentially arises by choosing a fixed date for the monsoon season, rather than meteorological thresholds. Due to the fact that the timing for onset of monsoon in each year is not constant, the AOD values may be rather elevated if the monsoon rains have not yet initiated, leading to higher average values than in winter season. **Figures 6**, **12** clearly show that the AOD is higher in the western part than in eastern regions. This is a result due to the onset of monsoon from the east (Bhatt and Nakamura, 2005), and slowly moving toward the western region.

By the end of the monsoon, aerosol levels start to rise again during the post-monsoon seasons. It is the transition period between the wet and dry seasons. Retreat of the monsoon trough is accompanied by a high-pressure cell positioned over

the Tibetan plateau, generally called the Tibetan high. The cold north-easterly wind from this high-pressure cell spreads over southern Nepal, and makes the surface air relatively dense, restricting the effective convection mechanism. As a result, aerosols are closer to the surface, yielding a large backscattering fraction that increases AOD levels in Terai region (**Figures 6**, **12**). The spatial variability seen in the post-monsoon season shows typical AOD levels in the eastern and south-western parts of Nepal, respectively. As the eastern part of Nepal receives more precipitation compared to the western part (Department of Hydrology and Meteorology Government of Nepal, 2017), AOD distribution over this region is also different, as can be seen in **Figures 1**, **13**. Variability in weather patterns, as well as the nature, and intensity of emissions, produces such dramatic variation in the spatial profile.

After the simulated AOD from model are compared with the MODIS AOD data, model is further used to extrapolate AOD over the cryospheric portion of Nepal, and presented in **Figure 13A**. It is evident that the model is also able to predict relatively higher AOD value in river valleys (line toward north at around N29, E83.5 in **Figure 13A**) with settlements, as compared with surrounding mountainous peaks with snow, which was not detected from MODIS instrument, ascertaining its ability to predict with ground reality.

4.5.4. Uncertainty in the Model Prediction

Effective AOD prediction is a complex issue that is easily affected by various factors, including weather and climatic conditions, and emission fluxes. Different input factors as an independent variables also have different degree of impact on the regression results used for dry AOD prediction. In the studied region, AOD is highly seasonal and altitude dependent, inclusion of altitudinal correction factor improves the predictability of the model. However, this study only predicted dry AOD for Nepal, but did not take into consideration any regional differences in the atmospheric environment. Although the results were good, few uncertainties are remained. First, uncertainties in the AOD data sources: on the one hand, this was a reflection of the uneven spatial distribution and few monitoring AERONET station, which are mainly in lower elevation region. Second, uncertainties in the ERA Interim data which were more prone to generating random noise, which affected prediction accuracies. And the third is the uncertainties in the proposed model itself. This study only assumed a possible linear relationship between AOD and three meteorological variables but did not consider the emission fluxes and sources, which would have an impact on the effectiveness of the model. Depending on the region and time period, significant differences exist in dry AOD. The good predictions achieved by the model proposed here were limited to Nepal and over short duration. Further examination would be needed to determine whether the developed proxy model could be applied to dry AOD predictions at other mountain region with longer time periods.

5. CONCLUSIONS

This paper presented dry AOD retrieval methods over the cryospheric portion of Nepalese Himalayas. Multivariate regression analysis is carried out to develop proxy an empirical model to predict AOD in dry forms. Three meteorological variables (relative humidity and 10 m wind velocity components) from ERA-Interim, and AOD observation at Pokhara AERONET station (in dry forms) were taken into account for model development. We have presented the results from the model corrected using average regression slope from MODIS (M1). Simulated dry AOD from developed empirical proxy model is validated with AERONET observations. Results showed that the presented model (M1) is able to simulate dry AOD over the different regions of Nepal, indicating model adequacy and establishing the model as an efficient AOD prediction model for Himalayan region. From both MODIS and model, highest dry AOD are observed during winter and pre-monsoon seasons. There are some discrepancies between observed and model values. The possible reason behind this discrepancies are because of the observed AOD represent sample of the population whose mean should correspond to the values predicted by the model. In this empirical proxy model, emission flux and sources are not considered while developing model. Therefore, prediction from model have biases with observations, and also in the case of few measurement data, it is very difficult to validate model results with the fewer observation. With limited observed data, presented proxy model shows sufficient number of grid cells with higher correlation coefficients indicating its adequacy as proxy AOD prediction model for Himalayan region. Identifying the source of aerosol is beyond the scope of this study but as mention in several studies, aerosols over Nepal are transported from Indo-Gangetic plain. The repeated occurrence of forest fires (especially in hilly plain region during pre-monsoon season) contributed to AOD over Nepal. Thus, it can be concluded that the spatial variability of AOD depends upon weather condition, and emission sources, which are subject to change with seasons.

The results of this paper confirms that the use of even the simplest linear regression model will yield very good estimation results for daily average dry AOD data in Nepal. These simple models are indispensable prediction tools for scientist requiring AOD information in the data sparse Himalayan region. It is evident that the model from multivariate regression analysis has universality in statistics, and it can be able to predict most of the spatial AOD variability in the Himalayan regions. It is especially useful for the situation where we do not have explicit knowledge about the AOD. This includes modeling in very complex terrain where very limited observed data sources exist. We tested the model on a few available stations, but it can also be used for other regions for AOD estimation. Our proxy model only uses ASTER DEM and meteorological data from ECMWF, and therefore, these models could be easily applied to other regions with mountain environment, and in related climate research in mountain region.

AUTHOR CONTRIBUTIONS

BB and JB designed the analysis. BB performed the experiments, derived the models, and analyzed the data. BB and JB wrote the manuscript with input from FS and C-YX who also provided expertise on the statistical modeling.

FUNDING

This work was conducted within the Strategic Research Initiative Land Atmosphere Interaction in Cold Environments (LATICE) of the University of Olso and partially supported through the Norwegian Research Council's INDNOR program under the Hydrologic sensitivity to Cryosphere-Aerosol interaction in Mountain Processes (HyCAMP) project (NFR no. 222195).

ACKNOWLEDGMENTS

We were thankful to entire MODIS science team and NASA providing aerosol data.

SUPPLEMENTARY MATERIAL

The Supplementary Material for this article can be found online at: https://www.frontiersin.org/articles/10.3389/feart.2019.00178/full#supplementary-material

REFERENCES

Acharya, P., and Sreekesh, S. (2013). Seasonal variability in aerosol optical depth over India: a spatio-temporal analysis using the MODIS aerosol product. *Int. J. Rem. Sens.* 34, 4832–4849. doi: 10.1080/01431161.2013.782114

Adler, J., and Parmryd, I. (2010). Quantifying colocalization by correlation: the pearson correlation coefficient is superior to the Mander's overlap coefficient. *Cytometry* 77, 733–742. doi: 10.1002/cyto.a.20896

Alam, K., Us Sahar, N., and Iqbal, Y. (2014). Aerosol characteristics and radiative forcing during pre-monsoon and post-monsoon seasons in an urban environment. *Aerosol Air Qual. Res.* 14, 99–107. doi: 10.4209/aaqr.2013.05.0154

Alexandrov, M. D., Geogdzhayev, I. V., Tsigaridis, K., Marshak, A., Levy, R., and Cairns, B. (2016). New statistical model for variability of aerosol optical thickness: theory and application to MODIS data over ocean. *J. Atmos. Sci.* 73, 821–837. doi: 10.1175/JAS-D-15-0130.1

Bendel, R. B., and Afifi, A. A. (1977). Comparison of stopping rules in forward "Stepwise" regression. *J. Am. Stat. Assoc.* 72, 46–53.

Berrisford, P., Dee, D. P., Poli, P., Brugge, R., Fielding, K., Fuentes, M., et al. (2011). *The ERA-Interim Archive Version 2.0*. Reading: Shinfield Park.

Bhatt, B. C., and Nakamura, K. (2005). Characteristics of monsoon rainfall around the Himalayas revealed by TRMM precipitation radar. *Am. Meteorol. Soc.* 133:17. doi: 10.1175/MWR-2846.1

Bonasoni, P., Cristofanelli, P., Marinoni, A., Vuillermoz, E., and Adhikary, B. (2012). Atmospheric pollution in the Hindu Kush–Himalaya region. *Mount. Res. Dev.* 32, 468–479. doi: 10.1659/MRD-JOURNAL-D-12-00066.1

CBS (2012). *National Population and Housing Census 2011(National Report)*, Vol. 1. Kathmandu: Government of Nepal, National Planning Commission Secretariat, Central Bu reau of Statistics, 1–278.

CBS. (2014). *Nepal in Figures*. Technical report, Central Bureau of Statistics, Government of Nepal, National Planning Commission Secretariat, Kathmandu, Nepal.

Chai, T., and Draxler, R. R. (2014). Root mean square error (RMSE) or mean absolute error (MAE)?–Arguments against avoiding RMSE in the literature. *Geosci. Model Dev.* 7, 1247–1250. doi: 10.5194/gmd-7-1247-2014

Charlson, R. J., Schwartz, S. E., Hales, J. M., Cess, R. D., Coakley, J. A., Hansen, J. E., et al. (1992). Climate forcing by anthropogenic aerosols. *Science* 255, 423–30.

Chu, D. A., Kaufman, Y. J., Ichoku, C., Remer, L. A., Tanré, D., and Holben, B. N. (2002). Validation of MODIS aerosol optical depth retrieval over land. *Geophys. Res. Lett.* 29:8007. doi: 10.1029/2001GL013205

Chylek, P., and Wong, J. (1995). Effect of absorbing aerosols on global radiation budget. *Geophys. Res. Lett.* 22, 929–931.

Cristofanelli, P., Putero, D., Adhikary, B., Landi, T. C., Marinoni, A., Duchi, R., et al. (2014). Transport of short-lived climate forcers/pollutants (SLCF/P) to the Himalayas during the South Asian summer monsoon onset. *Environ. Res. Lett.* 9:084005. doi: 10.1088/1748-9326/9/8/084005

de Leeuw, G., Andreas, E. L., Anguelova, M. D., Fairall, C. W., Lewis, E. R., O'Dowd, C., et al. (2011). Production flux of sea spray aerosol. *Rev. Geophys.* 49:RG2001. doi: 10.1029/2010RG000349

Department of Hydrology and Meteorology Government of Nepal (2017). *Observed Climate Trend Analysis of Nepal (1971–2014)*. Kathmandu: Government of Nepal, Ministry of Population and Environment, Department of Hydrology and Meteorology.

Dhungel, S., Kathayat, B., Mahata, K., and Panday, A. (2016). Transport of regional pollutants through a remote trans-Himalayan valley in Nepal. *Atmos. Chem. Phys.* 18, 1–23. doi: 10.5194/acp-2016-824

Dingmann, L. S. (2015). *Physical Hydrology, 3rd Edn.* Long Grove, IL: Waveland Press, INC.

Eck, T. F., Holben, B. N., Reid, J. S., Dubovik, O., Smirnov, A., O'Neill, N. T., et al. (1999). Wavelength dependence of the optical depth of biomass burning, urban, and desert dust aerosols. *J. Geophys. Res. Atmos.* 104, 31333–31349.

Flossmann, A., Hall, W., and Pruppacher, H. (1985). A theoretical study of the wet removal of atmospheric pollutants. Part I: the redistribution of aerosol particles captured through nucleation and impaction scavenging by growing cloud drops. *J. Atmos. Sci.* 42, 583–606.

Fujisada, H., Bailey, G. B., Kelly, G. G., Hara, S., and Abrams, M. J. (2005). ASTER DEM performance. *IEEE Trans. Geosci. Rem. Sens.* 43, 2707–2713. doi: 10.1109/TGRS.2005.847924

Gonçalves, F. L. T., Beheng, K. D., Massambani, O., Vautz, W., and Klockow, D. (2010). Scavenging processes of atmospheric particulate matter: a numerical modeling of case studies. *Rev. Brasil. Meteorol.* 25, 437–447. doi: 10.1590/S0102-77862010000400003

Govaerts, Y. M., Wagner, S., Lattanzio, A., and Watts, P. (2010). Joint retrieval of surface reflectance and aerosol optical depth from MSG/SEVIRI observations with an optimal estimation approach: 1. Theory. *J. Geophys. Res.* 115:D02203. doi: 10.1029/2009JD011779

Guleria, R. P., Kuniyal, J. C., Rawat, P. S., Thakur, H. K., Sharma, M., Sharma, N. L., et al. (2012). Validation of MODIS retrieval aerosol optical depth and an investigation of aerosol transport over Mohal in north western Indian Himalaya. *Int. J. Rem. Sens.* 33, 5379–5401. doi: 10.1080/01431161.2012.657374

Holben, B., Eck, T., Slutsker, I., Tanré, D., Buis, J., Setzer, A., et al. (1998). AERONET–a federated instrument network and data archive for aerosol characterization. *Rem. Sens. Environ.* 66, 1–16.

Huss, M. (2013). Density assumptions for converting geodetic glacier volume change to mass change. *Cryosphere* 7, 877–887. doi: 10.5194/tc-7-877-2013

Ichiyanagi, K., Yamanaka, M. D., Muraji, Y., and Vaidya, B. K. (2007). Precipitation in Nepal between 1987 and 1996. *Int. J. Climatol.* 27, 1753–1762. doi: 10.1002/joc.1492

Ichoku, C., Chu, D. A., Mattoo, S., Kaufman, Y. J., Remer, L. A., Tanré, D., Slutsker, I., and Holben, B. N. (2002). A spatio-temporal approach for global validation and analysis of modis aerosol products. *Geophys. Res. Lett.* 29:MOD1-1. doi: 10.1029/2001GL013206

Istomina, L. G., von Hoyningen-Huene, W., Kokhanovsky, A. A., and Burrows, J. P. (2009). "The retrieval of aerosol optical thickness over snow using AATSR observations," in *American Geophysical Union, Fall Meeting 2009, Abstract NO. A11C-0112*.

Istomina, L. G., Von Hoyningen-Huene, W., Kokhanovsky, A. A., Schultz, E., and Burrows, J. P. (2011). Remote sensing of aerosols over snow

using infrared AATSR observations. *Atmos. Meas. Tech.* 4, 1133–1145. doi: 10.5194/amt-4-1133-2011

Kaskaoutis, D. G., Kambezidis, H. D., Hatzianastassiou, N., Kosmopoulos, P. G., and Badarinath, K. V. S. (2007). Aerosol climatology: dependence of the Angstrom exponent on wavelength over four AERONET sites. *Atmos. Chem. Phys. Discuss.* 7, 7347–7397. doi: 10.5194/acpd-7-7347-2007

Kaufman, Y. J., Tanre, D., and Boucher, O. (2002). A satellite view of aerosols in the climate system. *Nature* 419, 215–223. doi: 10.1038/nature01091

Kaufman, Y. J., Tanré, D., Remer, L. A., Vermote, E. F., Chu, A., and Holben, B. N. (1997). Operational remote sensing of tropospheric aerosol over land from EOS moderate resolution imaging spectroradiometer. *J. Geophys. Res. Atmos.* 102, 17051–17067.

Khatibi Bardsiri, V., Jawawi, D. N. A., Hashim, S. Z. M., and Khatibi, E. (2014). A flexible method to estimate the software development effort based on the classification of projects and localization of comparisons. *Emp. Softw. Eng.* 19, 857–884. doi: 10.1007/s10664-013-9241-4

Kim, D., Wang, C., Ekman, A. M. L., Barth, M. C., and Lee, D.-I. (2014). The responses of cloudiness to the direct radiative effect of sulfate and carbonaceous aerosols. *J. Geophys. Res. Atmos.* 119, 1172–1185. doi: 10.1002/2013JD020529

Kinne, S., O'Donnel, D., Stier, P., Kloster, S., Zhang, K., Schmidt, H., et al. (2013). MAC-v1: a new global aerosol climatology for climate studies. *J. Adv. Model. Earth Syst.* 5, 704–740. doi: 10.1002/jame.20035

Kleiber, C. (2001). Finite sample efficiency of OLS in linear regression models with long-memory disturbances. *Econ. Lett.* 72, 131–136. doi: 10.1016/S0165-1765(01)00423-2

Kopacz, M., Mauzerall, D. L., Wang, J., Leibensperger, E. M., Henze, D. K., and Singh, K. (2011). Origin and radiative forcing of black carbon transported to the Himalayas and Tibetan Plateau. *Atmos. Chem. Phys.* 11, 2837–2852. doi: 10.5194/acp-11-2837-2011

Lau, W. (2014). Atmospheric science: desert dust and monsoon rain. *Nat. Geosci.* 7, 255–256. doi: 10.1038/ngeo2115

Levy, R. C., Mattoo, S., Munchak, L. A., Remer, L. A., Sayer, A. M., Patadia, F., et al. (2013). The Collection 6 MODIS aerosol products over land and ocean. *Atmos. Meas. Tech.* 6, 2989–3034. doi: 10.5194/amt-6-2989-2013

Levy, R. C., Remer, L. A., and Dubovik, O. (2007). Global aerosol optical propertites and application to moderate resolution imaging spectroradiometer aerosol retrival over land. *J. Geophys. Res. Atmos.* 112, 1–15. doi: 10.1029/2006JD007815

Levy, R. C., Remer, L. A., Kleidman, R. G., Mattoo, S., Ichoku, C., Kahn, R., et al. (2010). Global evaluation of the Collection 5 MODIS dark-target aerosol products over land. *Atmos. Chem. Phys.* 10, 10399–10420. doi: 10.5194/acp-10-10399-2010

Leys, C., Ley, C., Klein, O., Bernard, P., and Licata, L. (2013). Detecting outliers: do not use standard deviation around the mean, use absolute deviation around the median. *J. Exp. Soc. Psychol.* 49, 764–766. doi: 10.1016/J.JESP.2013.03.013

Li, A., Deng, W., and Zhao, W. (2017). *Land cover change and its eco-environmental responses in Nepal*. Berlin; Heidelberg: Springer Berlin Heidelberg.

Li, B., Yuan, H., Feng, N., and Tao, S. (2009). Comparing MODIS and AERONET aerosol optical depth over China. *Int. J. Rem. Sens.* 30, 6519–6529. doi: 10.1080/01431160903111069

Li, C., Bosch, C., Kang, S., Andersson, A., Chen, P., Zhang, Q., et al. (2016). Sources of black carbon to the Himalayan–Tibetan plateau glaciers. *Nat. Commun.* 7:12574. doi: 10.1038/ncomms12574

Li, J., Han, Z., and Zhang, R. (2014). Influence of aerosol hygroscopic growth parameterization on aerosol optical depth and direct radiative forcing over East Asia. *Atmos. Res.* 140–141, 14–27. doi: 10.1016/j.atmosres.2014.01.013

Martonchik, J. V., Kahn, R. A., and Diner, D. J. (2009). "Retrieval of aerosol properties over land using MISR observations," in *Satellite Aerosol Remote Sensing Over Land*, eds A. A. Kokhanovsky and G. de Leeuw (Berlin; Heidelberg: Springer Berlin Heidelberg), 267–293.

Matt, F. N., Burkhart, J. F., and Pietikäinen, J.-P. (2018). Modelling hydrologic impacts of light absorbing aerosol deposition on snow at the catchment scale. *Hydrol. Earth Syst. Sci.* 22, 179–201. doi: 10.5194/hess-22-179-2018

Meehl, G. A., Arblaster, J. M., and Collins, W. D. (2008). Effects of black carbon aerosols on the Indian monsoon. *J. Clim.* 21, 2869–2882. doi: 10.1175/2007JCLI1777.1

Mei, L., Istomina, L., Von Hoyningen-Huene, W., Xue, Y., and Kokhanovsky, A. A. (2012). "Aerosol optical depth retrieval over Arctic region using AATSR data," in *International Geoscience and Remote Sensing Symposium (IGARSS)* (Munich), 2556–2559.

Mei, L., Xue, Y., Kokhanovsky, A. A., Von Hoyningen-Huene, W., Istomina, L., De Leeuw, G., Burrows, J. P., et al. (2013). Aerosol optical depth retrieval over snow using AATSR data. *Int. J. Rem. Sens.* 34, 5030–5041. doi: 10.1080/01431161.2013.786197

Miller, J. (1991). Short report: reaction time analysis with outlier exclusion: bias varies with sample size. *Quart. J. Exp. Psychol.* 13, 907–912.

Moriasi, D. N., Arnold, J. G., Van Liew, M. W., Bingner, R. L., Harmel, R. D., and Veith, T. L. (2007). Model evaluation guidelines for systematic quantification of accuracy in watershed simulations. *Trans. ASABE* 50, 885–900. doi: 10.13031/2013.23153

Nair, V. S., Babu, S. S., Moorthy, K. K., Sharma, A. K., Marinoni, A., and Ajai (2013). Black carbon aerosols over the Himalayas: direct and surface albedo forcing. *Tellus Chem. Phys. Meteorol.* 65, 0–14. doi: 10.3402/tellusb.v65i0.19738

Nayava, J. L. (1974). Heavy monsoon rainfall in Nepal. *Weather* 29, 443–450.

Nayava, J. L. (1980). Rainfall in Nepal. *Nepal Geogr. Soc.* 12, 1–18.

Nepal, S., Flügel, W.-A., and Shrestha, A. B. (2014). Upstream-downstream linkages of hydrological processes in the Himalayan region. *Ecol. Process.* 3:19. doi: 10.1186/s13717-014-0019-4

Paliwal, U., Sharma, M., and Burkhart, J. F. (2016). Monthly and spatially resolved black carbon emission inventory of India: uncertainty analysis. *Atmos. Chem. Phys.* 16, 12457–12476. doi: 10.5194/acp-16-12457-2016

Panday, A. K., and Prinn, R. G. (2009). Diurnal cycle of air pollution in the Kathmandu Valley, Nepal: observations. *J. Geophys. Res.* 114:D09305. doi: 10.1029/2008JD009777

Parry, M., Canziani, O., Palutikof, J., van der Linden, P., and Hanson, C. (2007). *Climate Change 2007: Impacts, Adaptation and Vulnerability*. Cambridge, UK: Intergovernmental Panel on Climate Change.

Pearson, K. (1895). Note on regression and inheritance in the case of two parents. *Proc. R. Soc. Lond.* 58, 240–242.

Pearson, K. (1896). The measurement of organs arise when indices are used in spurious correlation which may of theory of evolution–on a form mathematical contributions to the email alerting service. *Proc. R. Soc. Lond.* 1, 489–498.

Prasad, A. K., and Singh, R. P. (2007). Comparison of MISR-MODIS aerosol optical depth over the Indo-Gangetic basin during the winter and summer seasons (2000–2005). *Rem. Sens. Environ.* 107, 109–119. doi: 10.1016/j.rse.2006.09.026

Ramanathan, V. (2001). Aerosols, climate, and the hydrological cycle. *Science* 294, 2119–2124. doi: 10.1126/science.1064034

Ramanathan, V., and Carmichael, G. (2008). Global and regional climate changes due to black carbon. *Nat. Geosci.* 1, 221–227. doi: 10.1038/ngeo156

Ramanathan, V., and Ramana, M. V. (2005). Persistent, widespread, and strongly absorbing haze over the Himalayan foothills and the Indo-Gangetic Plains. *Pure Appl. Geophys.* 162, 1609–1626. doi: 10.1007/s00024-005-2685-8

Ramanathan, V., Ramana, M. V., Roberts, G., Kim, D., Corrigan, C., Chung, C., et al. (2007). Warming trends in Asia amplified by brown cloud solar absorption. *Nature* 448, 575–578. doi: 10.1038/nature06019

Ranabhat, C. L., Kim, C.-B., Kim, C.-S., Jha, N., Deepak, K. C., and Connel, F. A. (2015). Consequence of indoor air pollution in rural area of Nepal: a simplified measurement approach. *Front. Public Health* 3:5. doi: 10.3389/fpubh.2015.00005

Remer, L. A., Kaufman, Y. J., Tanré, D., Mattoo, S., Chu, D. A., Martins, J. V., et al. (2005). The MODIS aerosol algorithm, products, and validation. *J. Atmos. Sci.* 62, 947–973. doi: 10.1175/JAS3385.1

Remer, L. A., Mattoo, S., Levy, R. C., and Munchak, L. A. (2013). MODIS 3 km aerosol product: algorithm and global perspective. *Atmos. Meas. Tech.* 6, 1829–1844. doi: 10.5194/amt-6-1829-2013

Roux, L., Le Roux Ä, G., Pourcelot, L., Masson, O., Duffa, C., -oise Vray, F., et al. (2008). Open Archive TOULOUSE Archive Ouverte (OATAO) aerosol deposition and origin in French mountains estimated with soil inventories of 210 Pb and artificial radionuclides. *Atmos. Environ.* 42, 1517–1524. doi: 10.1016/j.atmosenv.2007.10.083

Safarpour, S., Abdullah, K., Lim, H. S., and Dadras, M. (2014). Accuracy assessment of Terra-MODIS aerosol optical depth retrievals. *IOP Conf. Series Earth Environ. Sci.* 20:012059. doi: 10.1088/1755-1315/20/1/012059

Sayer, A. M., Hsu, N. C., Bettenhausen, C., and Jeong, M.-J. (2013). Validation and uncertainty estimates for MODIS Collection 6 "Deep

Blue"aerosol data. *J. Geophys. Res. Atmos.* 118, 7864–7872. doi: 10.1002/jgrd.50600

Shea, J. M., Wagnon, P., Immerzeel, W. W., Biron, R., Brun, F., and Pellicciotti, F. (2015). A comparative high-altitude meteorological analysis from three catchments in the Nepalese Himalaya. *Int. J. Water Resour. Dev.* 31, 174–200. doi: 10.1080/07900627.2015.1020417

Shrestha, A. B., Wake, P. C., Dibb, J. E., Mayewski, P. A., Whitlow, S. I., Carmichael, G. R., et al. (2000). Seasonal variations in aerosol concentrations and compositions in the Nepal Himalaya. *Atmos. Environ.* 34, 3349–3363. doi: 10.1016/S1352-2310(99)00366-0

Silhavy, R., Silhavy, P., and Prokopova, Z. (2017). Analysis and selection of a regression model for the use case points method using a stepwise approach. *J. Syst. Softw.* 125, 1–14. doi: 10.1016/j.jss.2016.11.029

Solomon, S., Qin, D., Manning, M., Averyt, K., and Marquis, M. (2007). *Climate Change 2007-The Physical Science Basis: Working Group I Contribution to the Fourth Assessment Report of the IPCC.* Vol. 4. Cambridge, UK: Cambridge University Press.

Soni, A. K. (2015). *Mining in the Himalayas: An Integrated Strategy.* CRC Press

Sriram, G., Krishnamohan, N., and Gopalasamy, V. (2004). Analysis of skewness and kurtosis for ambient air quality monitoring data Neyveli thermal plants. *J. Sci. Ind. Res.* 63, 769–775.

Srivastava, A. K., Dey, S., and Tripathi, S. N. (2012). "Aerosol characteristics over the Indo-Gangetic basin: implications to regional climate," in *Atmospheric Aerosols-Regional Characteristics-Chemistry and Physics*, ed A.-R. Hayder (London, UK: InTech).

Tanabe, J., Miller, D., Tregellas, J., Freedman, R., and Meyer, F. G. (2002). Comparison of detrending methods for optimal fMRI preprocessing. *Neuroimage* 15, 902–907. doi: 10.1006/nimg.2002.1053

Tripathi, S. N., Pattnaik, A., and Dey, S. (2007). Aerosol indirect effect over Indo-Gangetic plain. *Atmos. Environ.* 41, 7037–7047. doi: 10.1016/j.atmosenv.2007.05.007

Wang, S.-Y., Yoon, J.-H., Gillies, R. R., Cho, C., Wang, S.-Y., Yoon, J.-H., et al. (2013). What caused the winter drought in western Nepal during recent years? *J. Clim.* 26, 8241–8256. doi: 10.1175/JCLI-D-12-00800.1

Zhang, Y., Forrister, H., Liu, J., Dibb, J., Anderson, B., Schwarz, J. P., et al. (2017). Top-of-atmosphere radiative forcing affected by brown carbon in the upper troposphere. *Nat. Geosci.* 10, 486–489. doi: 10.1038/ngeo2960

Zheng, C., Zhao, C., Zhu, Y., Wang, Y., Shi, X., Wu, X., et al. (2017). Analysis of influential factors for the relationship between PM2.5 and AOD in Beijing. *Atmos. Chem. Phys. Discuss. Chem. Phys.* 1170, 1–57. doi: 10.5194/acp-2016-1170

Conflict of Interest Statement: The authors declare that the research was conducted in the absence of any commercial or financial relationships that could be construed as a potential conflict of interest.

Advantages of publishing in Frontiers

OPEN ACCESS
Articles are free to read for greatest visibility and readership

FAST PUBLICATION
Around 90 days from submission to decision

HIGH QUALITY PEER-REVIEW
Rigorous, collaborative, and constructive peer-review

TRANSPARENT PEER-REVIEW
Editors and reviewers acknowledged by name on published articles

Frontiers
Avenue du Tribunal-Fédéral 34
1005 Lausanne | Switzerland

Visit us: www.frontiersin.org
Contact us: info@frontiersin.org | +41 21 510 17 00

REPRODUCIBILITY OF RESEARCH
Support open data and methods to enhance research reproducibility

DIGITAL PUBLISHING
Articles designed for optimal readership across devices

FOLLOW US
@frontiersin

IMPACT METRICS
Advanced article metrics track visibility across digital media

EXTENSIVE PROMOTION
Marketing and promotion of impactful research

LOOP RESEARCH NETWORK
Our network increases your article's readership